



**CHARACTERIZATION AND  
MEASUREMENT OF PASSIVE AND ACTIVE  
METAMATERIAL DEVICES**

THESIS

Christopher A. Lundell, Captain, USAF  
AFIT/GE/ENG/10-15

**DEPARTMENT OF THE AIR FORCE  
AIR UNIVERSITY**

***AIR FORCE INSTITUTE OF TECHNOLOGY***

**Wright-Patterson Air Force Base, Ohio**

APPROVED FOR PUBLIC RELEASE; DISTRIBUTION UNLIMITED.

The views expressed in this thesis are those of the author and do not reflect the official policy or position of the United States Air Force, Department of Defense, or the United States Government.

AFIT/GE/ENG/10-15

CHARACTERIZATION AND MEASUREMENT OF PASSIVE AND ACTIVE  
METAMATERIAL DEVICES

THESIS

Presented to the Faculty  
Department of Electrical and Computer Engineering  
Graduate School of Engineering and Management  
Air Force Institute of Technology  
Air University  
Air Education and Training Command  
in Partial Fulfillment of the Requirements for the  
Degree of Master of Science in Electrical Engineering

Christopher A. Lundell, B.S.E.E., M.B.A.  
Captain, USAF

March 2010

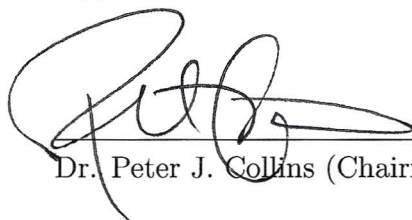
APPROVED FOR PUBLIC RELEASE; DISTRIBUTION UNLIMITED.

AFIT/GE/ENG/10-15

CHARACTERIZATION AND MEASUREMENT OF PASSIVE AND ACTIVE  
METAMATERIAL DEVICES

Christopher A. Lundell, B.S.E.E., M.B.A.  
Captain, USAF

Approved:



Dr. Peter J. Collins (Chairman)

26 FEB 10

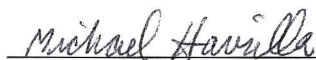
Date



Dr. Ronald A. Coutu, Jr. (Member)

26 Feb 10

Date



Dr. Michael J. Havrilla (Member)

03 Mar 2010

Date



## Abstract

Metamaterials are devices with embedded structures that provide the device with unique properties. While the metamaterials that have been proposed to date exhibit various types of phenomena, much of the current research focuses on their interaction with electromagnetic fields. Several exotic applications have been proposed for metamaterials including electromagnetic cloaks, lenses with much better resolutions than traditional lenses, improved antennas, and many more.

There are two major obstacles facing metamaterial development that this thesis addresses. The first is the uncertainty in the characterization of electromagnetic field behavior in metamaterial structures. This uncertainty centers on a particular type of metamaterial structure referred to as a double negative (DNG) metamaterial that has very unique properties many believe are impossible.

To address this obstacle, a new method to characterize and measure electromagnetic field behavior in a metamaterial structure is presented. This new method is a bistatic radar cross section (RCS) measurement technique of a metamaterial bulk sample. RCS measurements are well-suited to measuring bulk metamaterial samples because they show frequency dependence of scattering angles, a key determinant of resonant behavior. Furthermore, RCS measurements offer common postprocessing techniques that can be useful for visualizing the results.

In this thesis, RCS measurements are compared to the popular theories of field behavior in metamaterials. They are also compared to computational models run using CST Microwave Studio's® transient and frequency solvers. While both solvers show the same behavior seen in the measurements, the resonant band from the transient simulation is about 1 GHz below the transient band of the measurements. The

resonant band from the frequency simulation is very close to the measured band. Unfortunately, simulations with the frequency solver are more computationally intense.

The second major obstacle plaguing metamaterial development is the relatively small operational bandwidth of metamaterial structures. Metamaterials depend on the resonant features of the embedded structures that have their own resonant bands. Overlapping the bands causes the unique field behavior.

This thesis characterizes the effectiveness of a new adaptive metamaterial design. This design incorporates a microelectromechanical systems (MEMS) variable capacitor into a DNG metamaterial structure. The MEMS capacitor is mounted over the gap in the split ring resonator (SRR) of the DNG metamaterial. Applying voltages to the MEMS device changes the effective capacitance, which, in turn, changes the resonant frequency of the device. In this thesis, the behavior of electromagnetic fields in the presence of this metamaterial structure are characterized using computational models. Simulation results of passive metamaterial structures are compared to measurement results to validate the modeling process. They are found to be in agreement.

Computer models show that the metamaterial's responsiveness to changes in the MEMS capacitor is dependent on the size of the metamaterial structure. A larger-scale structure that is very responsive to changes in the MEMS capacitor is proposed. The resonant frequencies for a 4.0 scale structure vary with the MEMS capacitor from 2.17 to 0.680 GHz. The resonant frequencies for a 4.9 scale structure vary between 1.93 and 0.608 GHz. Fabrication of the MEMS capacitor for a larger structure can be accommodated by reducing the gap in the individual SRR elements. Other studies have shown that reducing the gap will have only minimal effect on the resonant frequency of the device.

## Acknowledgements

Many people have helped me complete this endeavor, and that especially includes my family. They have been instrumental in providing me with the support I needed. I would like to give a special thanks to my step-dad for his help proofreading many of the sections in this document. Also, I would like to recognize the special contributions from my wife. Her many hours of proofreading have been extremely helpful, but her biggest contributions have been her love and support. Without those, I surely would not have completed this effort.

I have received the help of many people at AFIT and beyond. I would like to give thanks to my thesis committee: Dr. Havrilla for his teachings about electromagnetics and materials; Dr. Coutu for his help with MEMS devices; and Dr. Collins for his support, guidance, discussions, and teachings. I need to thank the technical support crew at Sonnet Software for their help with CST Microwave Studio®. Also, I would like to thank my classmates for their support. Truly, I can say they have been their with me throughout my time at AFIT.

Finally, I would be remiss without giving special thanks to the Lord; for it was His guiding hand that led me down this path.

Christopher A. Lundell

# Table of Contents

	Page
Abstract . . . . .	iv
Acknowledgements . . . . .	vi
List of Figures . . . . .	x
List of Tables . . . . .	xviii
List of Symbols . . . . .	xix
List of Abbreviations . . . . .	xxvii
I. Introduction . . . . .	1
1.1 Problem Description . . . . .	1
1.2 Potential Applications for Metamaterials . . . . .	3
1.2.1 Perfect Lens . . . . .	4
1.2.2 Cloaking Device . . . . .	5
1.3 Research Goals . . . . .	8
1.3.1 Characterization of Field Behavior in Metamaterial Structures . . . . .	8
1.3.2 Analysis of an Active Metamaterial Structure . . . . .	10
1.4 Organization of Thesis . . . . .	11
II. Theory . . . . .	13
2.1 Chapter Overview . . . . .	13
2.2 Characterization of Metamaterials . . . . .	13
2.2.1 Negative Index of Refraction . . . . .	14
2.2.2 Realization of Negative Refractive Index . . . . .	17
2.2.3 Surface Waves in Metamaterials . . . . .	23
2.3 Computational Techniques . . . . .	25
2.3.1 Finite Integration Technique . . . . .	26
2.3.2 Boundary Conditions . . . . .	29
2.3.3 Farfield Calculations . . . . .	31
2.3.4 Computational Studies of Traditional Metamaterials . . . . .	36
2.3.5 Parameter Extraction . . . . .	43
2.4 Experimental Studies of Traditional Metamaterial Structures . . . . .	46
2.5 Achieving Frequency Adaptability . . . . .	52
2.5.1 Magnetic Circuits . . . . .	54
2.5.2 Varactor-Loaded Circuits . . . . .	55

2.5.3	Semiconductor Split Ring Resonators with Magnetostatic Fields . . . . .	58
2.5.4	SRRs with MEMS Switches . . . . .	60
2.5.5	Adaptive Metamaterial Literature Summary . . . . .	62
III.	Calculations and Computational Models . . . . .	64
3.1	Chapter Overview . . . . .	64
3.2	Calculation Time Studies . . . . .	65
3.3	Model Validation and Comparisons . . . . .	67
3.3.1	Modeling 2005 Smith et al. structure . . . . .	67
3.3.2	Modeling 2007 Hand and Cummer structure . . . . .	70
3.4	Metamaterial Wedge Models . . . . .	74
3.4.1	Unit Cell Model . . . . .	75
3.4.2	Predictions Using Effective Medium Theory . . . . .	76
3.4.3	Predictions Using Surface Wave Scattering Theory . . . . .	82
3.4.4	Simple Wedge Model . . . . .	83
3.4.5	Mid-Size Wedge Model . . . . .	85
3.4.6	Full 2-D Wedge Model . . . . .	96
3.4.7	Metamaterial Wedge Model Conclusions . . . . .	103
3.5	Basic AFIT Adaptive Metamaterial Models . . . . .	105
3.5.1	One Cell Periodic Model . . . . .	106
3.5.2	One Cell Non-Periodic Model . . . . .	109
3.5.3	Four Cell, Single Geometry Non-Periodic Model . . . . .	110
3.5.4	Four Cell, Double Geometry Non-Periodic Model . . . . .	113
3.6	Advanced AFIT Adaptive Metamaterial Structure Models . . . . .	114
3.6.1	Empty Stripline Model . . . . .	116
3.6.2	Original-Size AFIT Adaptive Metamaterial Models . . . . .	117
3.6.3	Larger-Scale AFIT Metamaterial Models . . . . .	121
3.6.4	Advanced AFIT Metamaterial Model Conclusions . . . . .	128
IV.	Experimental Measurements . . . . .	133
4.1	Chapter Overview . . . . .	133
4.2	RCS Measurement Procedures and Theory . . . . .	133
4.3	Initial Metamaterial Wedge RCS Measurements . . . . .	134
4.3.1	Calibration Verification . . . . .	134
4.3.2	Measurement Results . . . . .	138
4.3.3	Conclusions from the Initial Measurements . . . . .	145
4.4	Final Metamaterial Wedge RCS Measurements . . . . .	146
4.4.1	Calibration Verification . . . . .	146
4.4.2	Measurement Results . . . . .	147
4.4.3	Comparison of Measurement and Model Results . . . . .	151
4.5	Stripline Measurement Procedures and Theory . . . . .	153
4.6	AFIT Metamaterial Design Stripline Measurements . . . . .	156
4.6.1	Large Scale Non-adaptive Design . . . . .	156

	Page
4.6.2 Stripline Measurement Conclusions . . . . .	159
V. Conclusions and Recommendations . . . . .	160
5.1 Passive Metamaterial Characterization Summary . . . . .	160
5.2 Adaptive Metamaterial Summary . . . . .	161
5.3 Recommendations for Future Research . . . . .	163
5.3.1 Passive Metamaterial Characterization Recommendations . . . . .	163
5.3.2 Adaptive Metamaterial Recommendations . . . . .	165
Appendix A. Computation Mesh Figures and Statistics . . . . .	168
Appendix B. Radar Cross Section Measurement Data . . . . .	177
B.1 Initial Metamaterial Wedge Measurements . . . . .	177
B.2 Final Metamaterial Wedge Measurements . . . . .	181
Appendix C. Theory of Operation for Computer Scripts . . . . .	194
C.1 Material Parameter Extraction Script . . . . .	194
C.2 Time-Domain Reflectometry Script . . . . .	197
C.3 Farfield Data Export Script . . . . .	198
C.4 Farfield Data Import Script . . . . .	202
Bibliography . . . . .	207
Vita . . . . .	212

## List of Figures

Figure		Page
1	Typical negative refraction metamaterial unit cell . . . . .	2
2	Representations of two cloaking devices . . . . .	6
3	Simulation results for cloaking devices . . . . .	8
4	The metamaterial wedge sample . . . . .	10
5	AFIT-designed adaptive metamaterial unit cell . . . . .	11
6	Interface between a right-handed and left-handed material . . . . .	16
7	Comparison between negative and positive refraction . . . . .	18
8	Geometry of split ring resonator structure proposed in [32] . . . . .	20
9	Effective $\mu$ for the SRR structure in [32] . . . . .	22
10	Experimental transmission results for the double negative metamaterial structure discussed in [46] . . . . .	22
11	Example of the finite integration technique in the time- and frequency-domains . . . . .	30
12	Symmetric structure from [47] . . . . .	37
13	Published results from modeling structure of [47] . . . . .	38
14	Model and results of split ring resonator and wire structure simulation presented in [55] . . . . .	39
15	Parametric study results of split ring resonator and wire structure simulation presented in [55] . . . . .	41
16	Model and results for a metamaterial wedge modeled in [20] . . . . .	42
17	Experiment setup and results of a left-handed metamaterial measured in [44]. . . . .	47
18	Illustration of light transmission through a wedge made of lossy material . . . . .	48

Figure		Page
19	Setup for the measurement of a parallelogram-shaped slab . . . . .	50
20	Metamaterial structure and results from a measurement of parallelogram shaped slab . . . . .	50
21	Experiment setup and results of a left-handed metamaterial measured in [48]. . . . .	51
22	Dimensions of a SRR particle . . . . .	53
23	Unit cell structure that utilizes a magnetic layer . . . . .	54
24	Results from the analysis of the SRR structure with magnetic layer . . . . .	56
25	SRR structure proposed in [13] . . . . .	57
26	Measured transmission coefficients for structure in [13] . . . . .	57
27	Array of structures measured in [42] . . . . .	58
28	Measurement results for structure in [42] . . . . .	59
29	Geometry of structure in [16] . . . . .	60
30	Equivalent circuits for a SRR element with a series MEMS switch from [17] . . . . .	60
31	Equivalent circuits for a SRR element with a parallel MEMS switch from [17]. . . . .	61
32	Measurement results from [17] . . . . .	63
33	Ring resonator models used as time studies . . . . .	66
34	CST Microwave Studio® model of structure from [47] . . . . .	68
35	CST Microwave Studio® results of structure in [47] . . . . .	69
36	Published results of SRR circuit from [17] with no MEMS switch . . . . .	71
37	CST Microwave Studio® model of structure in [17] . . . . .	72
38	CST Microwave Studio® <i>S</i> -parameter results from structure in [17] . . . . .	73



Figure		Page
39	Dimensions of the metamaterial wedge's unit cell . . . . .	74
40	CST Microwave Studio® model for the metamaterial wedge unit cell . . . . .	75
41	Metamaterial wedge unit cell model $S$ -parameters . . . . .	76
42	Metamaterial wedge unit cell model refractive index . . . . .	77
43	Geometry for transmission into the metamaterial wedge . . . . .	78
44	Angle of reflection from lossless metamaterial wedge and metal plate . . . . .	80
45	Transmission vector angles for metamaterial wedge with losses . . . . .	82
46	Model for a simplified version of the metamaterial wedge . . . . .	84
47	Global bistatic RCS pattern of the simple metamaterial wedge model . . . . .	85
48	Model for a mid-size version of the metamaterial wedge . . . . .	86
49	Electric field amplitude from the mid-sized 2-D metamaterial wedge model . . . . .	87
50	Global bistatic RCS patterns of the mid-sized 2-D metamaterial wedge model . . . . .	88
51	Maximum return angles from mid-sized 2-D metamaterial wedge model . . . . .	89
52	Global range patterns of the mid-sized 2-D metamaterial wedge model at 10 GHz . . . . .	90
53	Global range patterns of the mid-sized 2-D metamaterial wedge model at 13.5 GHz . . . . .	91
54	Range plot for the mid-sized 2-D metamaterial wedge . . . . .	92
55	ISAR imagery from the mid-sized 2-D metamaterial wedge model . . . . .	93
56	Electric field amplitude from the mid-sized 2-D metamaterial wedge model without the metal plate . . . . .	94

Figure		Page
57	Global bistatic RCS pattern of the mid-sized 2-D metamaterial wedge model without the plate . . . . .	95
58	Model of the full width and depth of the metamaterial wedge . . . . .	96
59	Electric field amplitude from the full 2-D metamaterial wedge model . . . . .	97
60	Global bistatic RCS pattern of the full 2-D metamaterial wedge model . . . . .	98
61	Global range of the full 2-D metamaterial wedge model at 10 GHz . . . . .	99
62	Global range of the full 2-D metamaterial wedge model at 12.5 GHz . . . . .	100
63	Electric field amplitude from the full 2-D metamaterial wedge model without the metal plate . . . . .	101
64	Global bistatic RCS pattern of the full 2-D metamaterial wedge without plate model . . . . .	102
65	Model of single cell periodic structure . . . . .	107
66	<i>S</i> -parameter results from single cell periodic model . . . . .	108
67	Refractive index and impedance for single cell periodic structure . . . . .	108
68	Relative permittivity and permeability of single cell periodic structure . . . . .	109
69	<i>S</i> -parameter results from single cell non-periodic structure . . . . .	111
70	<i>S</i> -parameter results from four cell non-periodic model . . . . .	112
71	Resonant frequencies for four cell non-periodic structure with two additional capacitance values . . . . .	112
72	CST Microwave Studio® model of a double geometry, four cell, non-periodic device . . . . .	113
73	<i>S</i> -parameter results from four cell non-periodic model with two different geometries . . . . .	114
74	AFIT's large stripline . . . . .	115

Figure		Page
75	Model of the empty large stripline . . . . .	117
76	Results from the empty large stripline model . . . . .	118
77	Advanced model of the original scale AFIT metamaterial structure . . . . .	119
78	<i>S</i> -parameter results from the advanced model of the original scale AFIT metamaterial structure . . . . .	121
79	Resonant frequency as a function of scale . . . . .	122
80	Results from the large scale periodic model . . . . .	123
81	Advanced model of the 4.0 scale AFIT metamaterial structure . . . . .	124
82	Advanced AFIT large-scale non-adaptive metamaterial model results . . . . .	125
83	Advanced AFIT large-scale non-adaptive metamaterial four-strip model results . . . . .	126
84	Large-scale AFIT adaptive metamaterial model results . . . . .	127
85	Large-scale AFIT adaptive metamaterial four-strip model results . . . . .	128
86	Impact of MEMS capacitance on resonant frequencies for large scale AFIT adaptive metamaterial designs . . . . .	131
87	Setup for the initial metamaterial wedge measurements . . . . .	135
88	Calibration verification for the initial radar cross section measurements . . . . .	137
89	Global RCS patterns for the metal plate and metamaterial wedge from the initial measurements . . . . .	139
90	Radar cross section pattern for the metamaterial wedge and plate in and out of the resonance band from the initial measurements . . . . .	140
91	RCS frequency sweep from the initial measurements of the metamaterial wedge at 90° and 103° . . . . .	140

Figure		Page
92	Global RCS patterns for the 3 to 6 GHz frequency band from the initial measurements . . . . .	141
93	Global range patterns for the metal plate and metamaterial wedge from the initial measurements . . . . .	143
94	ISAR imagery centered at 13 GHz from the initial measurements . . .	144
95	ISAR imagery centered at 10 GHz from the initial measurements . . .	145
96	Setup for the final metamaterial wedge measurements . . . . .	146
97	Calibration comparison for the final metamaterial wedge RCS measurements in the $tt$ -polarization . . . . .	148
98	Global RCS patterns from the final metamaterial wedge measurements in the $tt$ -polarization . . . . .	149
99	Global RCS patterns from the final metamaterial wedge measurements without the metal plate in the $tt$ -polarization . . . . .	150
100	Global range patterns from the final metamaterial wedge measurements at $0^\circ$ incidence . . . . .	151
101	Equipment used for stripline measurements . . . . .	154
102	Fabrication of the passive large scale metamaterial test samples . . . . .	157
103	Testing of the passive large scale metamaterial samples . . . . .	157
104	Measurement results for large scale passive metamaterial samples . . . . .	158
105	Four-strip measurement results for large scale passive metamaterial samples . . . . .	159
106	Computational meshes generated for the comparison studies . . . . .	168
107	Computational mesh generated for the metamaterial wedge unit cell model . . . . .	168
108	Computational meshes generated for the metamaterial wedge models . . . . .	169

Figure		Page
109	Computational meshes generated for the AFIT adaptive metamaterial models . . . . .	170
110	Computational mesh generated for empty stripline model . . . . .	171
111	Computational meshes generated for the advanced AFIT adaptive metamaterial models . . . . .	171
112	Computational meshes generated for the advanced AFIT non-adaptive metamaterial models . . . . .	172
113	Computational meshes generated for the advanced AFIT adaptive metamaterial models . . . . .	173
114	Second calibration error for the initial metamaterial wedge measurement in the 3 to 6 GHz frequency range . . . . .	178
115	Histograms of the calibration error for the initial metamaterial wedge measurement in the $pp$ -polarization . . . . .	179
116	Global radar cross section patterns from the initial measurements of the metamaterial wedge in the $pp$ -polarization . . . .	180
117	Calibration histograms for the final metamaterial wedge radar cross section measurements in the $pp$ -polarization . . . . .	182
118	Calibration histograms for the final metamaterial wedge radar cross section measurements in the $tt$ -polarization . . . . .	183
119	Calibration comparison for the final metamaterial wedge radar cross section measurements in the $tt$ -polarization . . . . .	184
120	Global radar cross section patterns from the final metamaterial wedge measurements in the $pp$ -polarization . . . . .	185
121	Global radar cross section patterns from the final metamaterial wedge measurements without the metal plate in the $pp$ -polarization . . . . .	186
122	Global radar cross section patterns from the final measurements of the metal plate in the $tt$ -polarization . . . . .	187
123	Radar cross section patterns at 10 and 14 GHz for the final measurements of the wedge with plate . . . . .	188

Figure		Page
124	Global range patterns from the final measurements of the metamaterial wedge with plate at 15°, 30°, and 45° incidence . . . . .	189
125	Inverse synthetic aperture radar imagery from the final RCS measurements of the metamaterial wedge with the plate at 0° incidence. . . . .	190
126	Inverse synthetic aperture radar imagery from the final RCS measurements of the metamaterial wedge with the plate at 15° incidence. . . . .	191
127	Inverse synthetic aperture radar imagery from the final RCS measurements of the metamaterial wedge with the plate at 30° incidence. . . . .	192
128	Inverse synthetic aperture radar imagery from the final RCS measurements of the metamaterial wedge with the plate at 45° incidence. . . . .	193
129	Flow diagram for material parameter extraction script . . . . .	196
130	Flow diagram for time-domain reflectometry script . . . . .	199
131	Flow diagram for time-domain reflectometry script (cont.) . . . . .	200
132	Flow diagram for farfield data export script . . . . .	203
133	Flow diagram for farfield data import script . . . . .	206

## List of Tables

Table		Page
1	Dimensions of split ring resonator example in [32] . . . . .	21
2	Computational time for various model sizes . . . . .	66
3	Design parameters for structure in [17] . . . . .	71
4	Resonant frequencies in [17] versus those found with CST MWS® . . . . .	73
5	Metamaterial wedge principle scattering angles using FSS theory . . . . .	83
6	Simple metamaterial wedge model boundary conditions . . . . .	84
7	Mid-size metamaterial wedge model boundary conditions . . . . .	86
8	Non-periodic adaptive metamaterial model boundary conditions and spacing . . . . .	110
9	Measured capacitances for MEMS device . . . . .	120
10	Resonant frequencies for large-scale adaptive metamaterial models . . . . .	129
11	Initial metamaterial wedge measurement calibration statistics in dB . . . . .	136
12	Final metamaterial wedge measurement calibration statistics in dB . . . . .	147
13	Metamaterial wedge resonance bands . . . . .	152
14	Full 2-D metamaterial wedge model mesh summary . . . . .	169
15	Metamaterial wedge frequency-solver mesh statistics . . . . .	174
16	AFIT metamaterial design frequency-solver mesh statistics . . . . .	175
17	Solution time . . . . .	176
18	Test matrix for initial metamaterial wedge measurements . . . . .	177
19	Test matrix for final metamaterial wedge measurements . . . . .	181

## List of Symbols

Symbol		Page
<b><math>E</math></b>	electric field vector . . . . .	14
<b><math>H</math></b>	magnetic field vector . . . . .	14
<b><math>D</math></b>	electric flux density . . . . .	14
<b><math>B</math></b>	magnetic flux density . . . . .	14
$c$	speed of light in free space . . . . .	14
$\epsilon$	electric permittivity of a medium . . . . .	14
$\mu$	magnetic permeability of a medium . . . . .	14
$j$	imaginary unit ( $j = \sqrt{-1}$ ) . . . . .	15
$\omega$	angular frequency . . . . .	15
<b><math>k</math></b>	wave vector . . . . .	15
<b><math>S</math></b>	Poynting vector . . . . .	15
$\hat{n}$	surface normal unit vector . . . . .	16
$n$	index of refraction . . . . .	16
$p$	parameter indicating handedness of a material . . . . .	17
$\epsilon_0$	permittivity of free space . . . . .	17
$\mu_0$	permeability of free space . . . . .	17
$\varphi_t$	angle of transmission through a material . . . . .	17
$\varphi_i$	angle of incidence on a material . . . . .	17
$a$	separation length between wires . . . . .	18



Symbol		Page
$r_w$	wire radius . . . . .	18
$\omega_p$	plasmon angular frequency . . . . .	18
$\sigma$	electric conductivity . . . . .	18
$\lambda$	wavelength . . . . .	19
$r_{SRR}$	inner split ring resonator radius . . . . .	19
$w$	split ring resonator trace width . . . . .	19
$d$	gap between a split ring resonator pair . . . . .	19
$\ell$	separation length between split ring resonator layers . . . . .	19
$R_1$	split ring resonator resistance of unit length for metal sheets . . . . .	19
$\omega_0$	angular resonant frequency . . . . .	19
$d_m$	distance traveled by an wave in a medium . . . . .	23
$k_0$	freespace wavenumber . . . . .	23
$\hat{r}_{\pm}$	unit vector in direction of radiation from an infinite array . . . . .	24
$s_x$	incident plane wave propagation vector $x$ -component . . . . .	24
$s_z$	incident plane wave propagation vector $z$ -component . . . . .	24
$m_1$	Floquet mode for $x$ -direction . . . . .	24
$m_2$	Floquet mode for $z$ -direction . . . . .	24
$D_x$	interelement spacing in $x$ -direction . . . . .	24
$D_z$	interelement spacing in $z$ -direction . . . . .	24
$G$	primary grid for finite integration technique . . . . .	26
$\tilde{G}$	dual grid for finite integration technique . . . . .	26

Symbol		Page
$\mathbf{e}$	grid electric voltage vector . . . . .	26
$\mathbf{h}$	grid magnetic voltage vector . . . . .	26
$\mathbf{b}$	grid magnetic induction flux . . . . .	26
$\mathbf{d}$	grid electric displacement flux . . . . .	26
$q_{ev}$	electric charge density . . . . .	26
$L_i$	facet length of the $i$ th cell in $G$ . . . . .	27
$\tilde{L}_i$	facet length of the $i$ th cell in $\tilde{G}$ . . . . .	27
$A_i$	facet area of the $i$ th cell in $G$ . . . . .	27
$\tilde{A}_i$	facet area of the $i$ th cell in $\tilde{G}$ . . . . .	27
$\mathbf{J}$	electric current vector . . . . .	27
$\mathbf{C}$	support matrix operator $\oint_{\partial A} \cdot d\mathbf{s}$ for $G$ . . . . .	27
$\mathbf{S}$	support matrix operator $\oint_{\partial V} \cdot d\mathbf{A}$ for $G$ . . . . .	27
$\tilde{\mathbf{C}}$	support matrix operator $\oint_{\partial \tilde{A}} \cdot d\mathbf{s}$ for $\tilde{G}$ . . . . .	27
$\tilde{\mathbf{S}}$	support matrix operator $\oint_{\partial \tilde{V}} \cdot d\mathbf{A}$ for $\tilde{G}$ . . . . .	27
$\mathbf{M}_\epsilon$	spatial discretization of $\epsilon$ matrix . . . . .	28
$\mathbf{M}_\mu$	spatial discretization of $\mu$ matrix . . . . .	28
$\mathbf{M}_\sigma$	spatial discretization of $\sigma$ matrix . . . . .	28
$\mathbf{j}_s$	grid source electric current . . . . .	28
$\mathbf{J}_s$	equivalent electric surface current vector . . . . .	32
$\mathbf{M}_s$	equivalent magnetic surface current vector . . . . .	32
$\mathbf{N}$	farfield magnetic vector potential . . . . .	32
$\mathbf{L}$	farfield electric vector potential . . . . .	32

Symbol		Page
$ds'$	differential point on surface of bounding box . . . . .	32
$\mathbf{r}'$	position vector for point on surface . . . . .	32
$\hat{r}$	position unit vector for point in farfield . . . . .	32
$E_r$	$r$ component of $\mathbf{E}$ . . . . .	32
$E_\theta$	$\theta$ component of $\mathbf{E}$ . . . . .	32
$E_\phi$	$\phi$ component of $\mathbf{E}$ . . . . .	32
$H_r$	$r$ component of $\mathbf{H}$ . . . . .	32
$H_\theta$	$\theta$ component of $\mathbf{H}$ . . . . .	32
$H_\phi$	$\phi$ component of $\mathbf{H}$ . . . . .	32
$z$	intrinsic impedance . . . . .	33
$N_\theta$	$\theta$ component of $\mathbf{N}$ . . . . .	33
$N_\phi$	$\phi$ component of $\mathbf{N}$ . . . . .	33
$L_\theta$	$\theta$ component of $\mathbf{L}$ . . . . .	33
$L_\phi$	$\phi$ component of $\mathbf{L}$ . . . . .	33
$\sigma_{3D}$	radar cross section . . . . .	33
$E^i$	incident electric field strength . . . . .	33
$E^s$	scattered electric field strength . . . . .	33
$\sigma_{2D}$	scattering width . . . . .	33
$h$	actual height of a two-dimensional target . . . . .	34
$k$	wavenumber . . . . .	34
$\Delta R_d$	downrange resolution . . . . .	35
$B$	bandwidth . . . . .	35

Symbol		Page
$\Delta R_c$	cross range resolution . . . . .	36
$\lambda_{mid}$	wavelength at mid point of frequency band . . . . .	36
$\Theta$	angular extent of RCS data . . . . .	36
$d_s$	material slab thickness . . . . .	43
$m$	branch integer . . . . .	44
$f$	frequency . . . . .	46
$d_b$	distance of beam shift from centerline . . . . .	49
$L$	inductance . . . . .	52
$C$	capacitance . . . . .	52
$h$	split ring resonator thickness . . . . .	53
$l$	split ring resonator length . . . . .	53
$\delta$	split ring resonator gap width . . . . .	53
$\mu_r$	relative permeability . . . . .	54
$q$	volume fraction of frequency dependent magnetic material . . . . .	54
$\epsilon_r$	relative permittivity . . . . .	58
$\epsilon_\infty$	relative permittivity high-frequency limit . . . . .	58
$\omega_p$	plasma angular frequency . . . . .	58
$\gamma$	damping constant . . . . .	58
$C_s$	capacitance of the switch . . . . .	60
$R_s$	resistance of the switch . . . . .	60
$C_{eq}$	equivalent capacitance of a network . . . . .	70
$C_{VC}$	capacitance of a variable capacitor . . . . .	70

Symbol		Page
$S_{21}$	transmission coefficient from port 1 to port 2 in a scattering matrix . . . . .	71
$f_0$	resonant frequency ( $f_0 = \omega_0/2\pi$ ) . . . . .	73
$\varphi_{t1}$	angle of transmitted fields through first wedge boundary . . . . .	77
$n_w$	metamaterial wedge index of refraction . . . . .	77
$n_a$	free space index of refraction . . . . .	77
$\varphi_{i1}$	angle of incidence at first wedge boundary . . . . .	77
$\varphi_{i2}$	angle of incidence at boundary between metamaterial wedge and metal plate . . . . .	77
$\varphi_{r2}$	angle of reflection at boundary between metamaterial wedge and metal plate . . . . .	77
$\alpha$	angle formed by wedge . . . . .	77
$\beta$	rotation angle of wedge and plate . . . . .	77
$\varphi_{i3}$	angle of incidence at third wedge boundary . . . . .	77
$\varphi_{t3}$	angle of transmitted fields through third wedge boundary . . . . .	78
$\varphi_{tw}$	angle of fields from the wedge . . . . .	78
$\tilde{n}$	complex index of refraction . . . . .	79
$\kappa$	attenuation index . . . . .	79
$\psi_1$	angle of incident attenuation vector . . . . .	80
$\zeta_1$	angle of incident propagation vector . . . . .	80
$\psi_2$	angle of transmitted attenuation vector . . . . .	80
$\zeta_2$	angle of transmitted propagation vector . . . . .	80
$\alpha_{01}$	intrinsic attenuation constant of medium 1 . . . . .	80

Symbol		Page
$\beta_{01}$	intrinsic propagation constant of medium 1 . . . . .	80
$\alpha_2$	adjusted attenuation constant of medium 2 . . . . .	80
$\beta_2$	adjusted propagation constant of medium 2 . . . . .	80
$k_y$	wavenumber along $y$ -axis . . . . .	115
$\beta_{sl}$	propagation constant inside stripline . . . . .	115
$k_c$	cutoff wavenumber . . . . .	115
$b$	distance between outer conductors of stripline . . . . .	115
$f_c$	cutoff frequency . . . . .	115
$C_l$	capacitance per unit length between two SRR particles . . . . .	131
$\phi$	angle from $x$ -axis toward $y$ -axis in spherical coordinates . . . . .	133
$\theta$	angle from $z$ -axis in spherical coordinates . . . . .	133
$\sigma_{cb}$	measured radar cross section of calibration background . . . . .	133
$\sigma_c$	measured radar cross section of calibration device . . . . .	133
$\sigma_{tb}$	measured radar cross section of target background . . . . .	133
$\sigma_t$	measured radar cross section of target . . . . .	133
$\sigma_{tc}$	calibrated radar cross section of target . . . . .	133
$\sigma_{ce}$	exact radar cross section of calibration device . . . . .	133
$\theta_{ml}$	mainlobe beamwidth (null-to-null) . . . . .	140
$L_p$	length of plate . . . . .	141
$V_1^-$	impulse voltage response received at port 1 . . . . .	154
$V_2^-$	impulse voltage response received at port 2 . . . . .	154
$V_1^+$	impulse voltage response transmitted at port 1 . . . . .	154

Symbol		Page
$V_1^{sh}$	reflected signal at port 1 from electrical short . . . . .	155
$V_2^{th}$	transmitted signal at port 2 from empty stripline . . . . .	155
$V_1^s$	reflected signal at port 1 from material sample . . . . .	155
$V_2^s$	transmitted signal at port 2 from material sample . . . . .	155

## List of Abbreviations

Abbreviation	Page
DNG      double negative . . . . .	2
SRR      split ring resonator . . . . .	2
RCS      radar cross section . . . . .	8
FSS      frequency selective surfaces . . . . .	9
AFIT      Air Force Institute of Technology . . . . .	9
MEMS      microelectromechanical systems . . . . .	10
LHM      left-handed material . . . . .	15
RHM      right-handed material . . . . .	15
MWS      Microwave Studio . . . . .	25
FIT      finite integration technique . . . . .	25
FDTD      finite difference time-domain . . . . .	26
PEC      perfect electric conductor . . . . .	30
PMC      perfect magnetic conductor . . . . .	30
PML      perfectly matched layer . . . . .	31
RCS      radar cross section . . . . .	33
FFT      fast Fourier transform . . . . .	35
ISAR      inverse synthetic aperture radar . . . . .	35
FEM      finite element method . . . . .	37
TEM      transverse electromagnetic . . . . .	68



Abbreviation	Page
MOM	method of moments . . . . . 135
CI	confidence interval . . . . . 136
TDR	Time-Domain Reflectometer . . . . . 153
VB	Visual BASIC . . . . . 201

# CHARACTERIZATION AND MEASUREMENT OF PASSIVE AND ACTIVE METAMATERIAL DEVICES

## I. Introduction

### 1.1 Problem Description

Metamaterial devices have gained notoriety over the past decade. Government and industry expenditures have grown as researchers investigate the many different application areas. There are almost as many definitions for metamaterials as there are researchers studying them. For this research effort, a metamaterial is defined as “an arrangement of artificial structural elements designed to achieve advantageous and unusual properties” [22]. Despite the prominence of metamaterials, the science is not yet settled, and researchers are currently debating how metamaterials assume their unusual properties.

According to some scientists and engineers, metamaterials can be used to change the effective parameters of a medium. The metamaterials interact with incident electromagnetic fields much the same way a molecular lattice interacts with incident electromagnetic fields. The result is a structure that creates an effective electric permittivity and magnetic permeability. From the permittivity and permeability, quantities like the index of refraction and impedance are determined. These quantities dictate the behavior of electromagnetic fields inside a metamaterial and are what gives a metamaterial its unusual properties. This makes the accurate extraction of the effective parameters of a metamaterial structure both important and contentious.

The permittivity and permeability are controlled by the geometry of the struc-

ture's unit cell. With proper care, the engineer is able to create a medium with a specific permittivity and permeability. When both the permittivity and permeability are negative, the material is referred to as a double negative (DNG) material and takes on a negative index of refraction [10, 6-9]. The most common types of structures used to create a DNG material are wire lattices and a pair of split ring resonator (SRR) particles, like the structure shown in Figure 1. Other unit cell structures are possible and some are discussed in Chapter II. However, the unit cell shown in Figure 1 is the basis for the structures analyzed in this thesis.

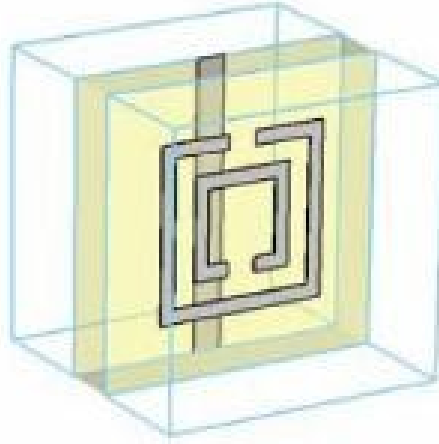


**Figure 1. A typical unit cell for a DNG metamaterial structure consists of a concentric SRR pair and wire lattice [20].**

Other scientists and engineers argue it is impossible for a metamaterial to achieve a negative index of refraction. Their arguments are usually based on causality and the physical implications of negative index of refraction. The theories behind both points-of-view are discussed in Chapter II. At this point in time, neither group of researchers is ready to accept their theories as wrong.

However, both groups acknowledge that the interesting phenomena that occur in metamaterials only happens over a small frequency bandwidth. As will be shown in Chapter II, the effective permittivity and permeability of the metamaterial is depen-

dent on the incident frequency. Unfortunately, the dispersive nature of metamaterials can limit their utility for certain applications. As a matter of practical application, expanding the resonant bandwidth would be very useful.

## 1.2 Potential Applications for Metamaterials

The ability to steer electromagnetic fields in a medium consisting of conventional materials is restricted by the fact that the electric permittivity and magnetic permeability are positive. While it has been known that there are many exciting possibilities for a medium where the effective material parameters could be made negative, the subject has only gained passing interest since the concept of negative material parameters was introduced by Veselago in 1968 [52]. However, with the rise of metamaterials, researchers are taking a harder look at the potential applications for devices that can guide electromagnetic waves.

Transformation optics is the science of bending electromagnetic fields based on coordinate transformations, rather than confining the fields to a particular portion of space like a waveguide or similar structure. Before the concept of negative refraction the ideas behind transformation optics were the stuff of science fiction. However, using negative refraction, effective media could be created that can steer electromagnetic fields.

The theory of transformation optics is based on the interaction of electromagnetic fields and the material parameters of a medium. The electromagnetic fields in a medium are guided by the electric permittivity and magnetic permeability through the constitutive relations (this is discussed in more detail in Chapter II). By transforming the coordinate system of the medium through the permittivity and permeability, electromagnetic fields encounter a different version of space-time than physical space-time. Thus, through Fermat's Principle, the electromagnetic fields continue to travel

in a straight line in their version of space-time. However, depending on the coordinate transformation involved, the electromagnetic fields can be made to bend around objects or towards points in physical space-time [23].

With the promise of transformation optics, metamaterials hit center stage of the scientific arena. In 2009, *Popular Mechanics* listed several everyday applications for metamaterials, most derived from transformation optics: cellphones with smaller antennas, detectors capable of detecting single molecules for use in finding weapons of mass destruction, microscope lenses capable of focusing beyond the diffraction limit, and fast metamaterial switching devices for photonic equipment [15]. Because of a metamaterial’s ability to compensate phase, it has been proposed that they be used to create electrically small cavity resonators and miniaturized waveguides [10, 21]. Their ability to compensate for dispersion have made metamaterials attractive to transmission line designers [10, 21-23]. Metamaterials have been proposed for creating small ring antennas for use in wireless telecommunications systems [9, 73-75].

The list of potential applications for metamaterials goes on and on, but perhaps the most controversial two applications commonly listed are the “perfect lens” and cloaking device. Here, those two potential applications are addressed in more detail.

### **1.2.1 Perfect Lens.**

The resolution of a conventional lens is constrained by the diffraction limit due to the decay of the evanescent modes that appear as the rays enter the conventional lens. The loss of the evanescent modes at the focal plane restrict focusing features less than about one wavelength in size [9, 119-120]. However, in 2000, Pendry published a paper claiming a DNG medium causes evanescent waves to grow instead of decay [31]. Thus, the image is reconstructed at the focal plane with contributions from both the evanescent and propagating modes. Therefore, the diffraction limit does not apply

and the focusing is only limited by aberrations and apertures [31].

There are limitations to the “perfect” lens. First, if the DNG material has any losses to it, the amplitude of the fields will decay and perfect focusing is lost [31]. Second, the DNG medium must be impedance matched to the surrounding medium (note that, unlike the index of refraction, the sign of the impedance is positive in a DNG material) so that there will be no reflected ray [31]. A final limitation is the placement of the lens. As Veselago pointed out in 1968 when he discussed negative refraction, a planar slab of DNG material does not behave like a true lens since it does not focus rays from infinity [52]. Furthermore, to achieve perfect focusing, the source must be very close to the lens, otherwise the evanescent modes will decay on their own. The lens must be in the source’s nearfield—about half of a wavelength away [9, 120].

Claims of perfect focusing with a DNG material have generated much controversy, and subsequent research has shown the limitations of the DNG lens are very difficult to overcome. However, research in this area is still ongoing.

### **1.2.2 Cloaking Device.**

In 2006, a pair of articles appeared in *Science* proposing the use of metamaterials to create electromagnetic cloaks [34], [23]. The cloaks worked on the principle of transformation optics. Inside the cloak, the electromagnetic fields would be guided around a central forbidden region. The required electric permittivity and magnetic permeability of the cloak are determined through conformal mapping [23]. The permittivity and permeability of the cloak change how the electromagnetic fields “experience” space-time. When the fields enter the cloak, they continue to travel in a straight line according to their perception of space-time. But, in physical space-time, the electromagnetic fields are guided around the forbidden region. The result is that

electromagnetic fields entering from outside the cloak never interact with the forbidden region. Similarly, electromagnetic fields radiated from the forbidden region can never escape the cloaking material [34]. Figure 2 depicts two such cloaks.

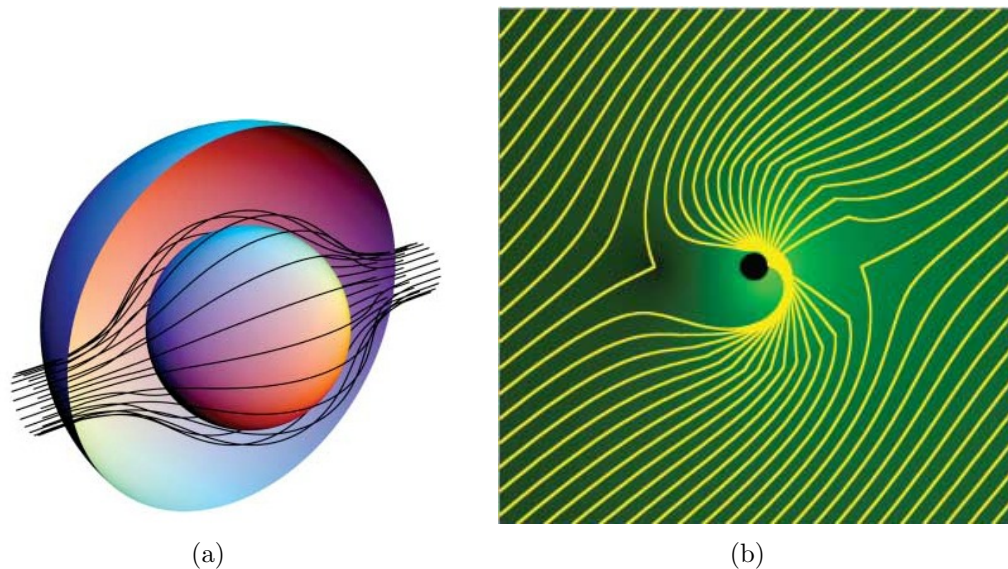


**Figure 2.** Representations of two cloaking devices. (a) The electromagnetic waves in the outer sphere are guided around the inner sphere such that none of the waves interact with the inner sphere [34]. (b) This cloaking device shows the electromagnetic fields following a different path, but the result is the same: the electromagnetic fields do not interact with the central black circle [23].

To create such a cloak, a material is needed where the permittivity and permeability can be spatially varied. Metamaterials offer the possibility of a material with changing material parameters. By engineering the metallic inclusions, a metamaterial could be designed such that the permittivity and permeability follow a pattern. However, a perfect cloak would require the permeability and permittivity be continuous, as any discontinuity in the index of refraction of the cloak would result in reflection. At its limit, this is impossible to achieve with metamaterials since the unit cells have non-zero dimensions. Furthermore, the cloaking device will require large values for the permittivity and permeability. This is not easily attainable with current metamaterial designs [34].

To determine the performance of non-ideal material parameters, Cummer et al. performed simulations on various configurations of the cloaking device [8]. The simulations were performed using COMSOL Multiphysics® finite element solver. The simulation results for four different configurations of the cloak are shown in Figure 3. The first configuration is a cloaking device with ideal, lossless parameters. In this configuration, the fields are smoothly bent around the forbidden region and there is little disturbance of the fields outside of the cloak. In the second configuration, loss is added to the smoothly-varying material parameters. Again, the fields are smoothly bent around the forbidden region, but the loss causes the cloak to cast a shadow in the forward-scatter region. The third configuration replaces the ideal parameters with an eight-layered design where the parameters are varied in a stair-step fashion. The layered design causes a degradation of the cloaking performance in all directions. The fourth configuration is an eight-layered design where the parameters have been limited to realizable values. Here, the cloaking performance is degraded in all directions, but the fields are still bent around the central forbidden region [8].

A metamaterial design for a cloak will involve losses, layers, and finite values for the permittivity and permeability. All of these factors will degrade the performance of the cloak. However, despite their shortcomings, it appears that metamaterials can still be used to create a device that offers some cloaking abilities.

Mentioning a cloaking device around the Air Force and quickly the conversation turns towards hiding aircraft. Unfortunately, there are a number of drawbacks to a metamaterial cloak, not the least of which include weight. As noted in a recent article in the *Air & Space Smithsonian*, metamaterials contain large amounts of metal, meaning that a cloak would add a significant weight to an airframe [2]. However, there are other applications for metamaterials that are of interest to the military. One such application is a cloaking device for the pylons used to mount targets in radar cross



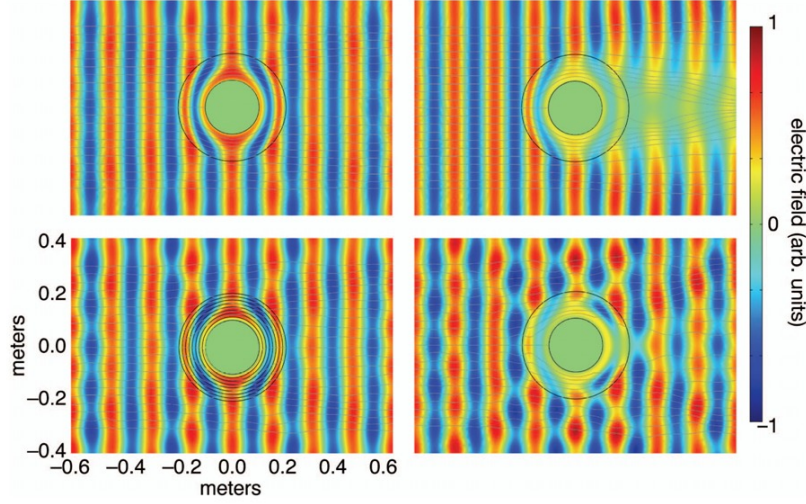


Figure 3. Simulation results for four different configurations of a cloaking device. Top left: in a perfect cloak, the electric fields smoothly bend around the central forbidden region and no disturbance of the electromagnetic fields are seen outside of the cloak. Top right: the electric field for a cloak with continuous parameters that include loss. The loss causes the cloak to cast a shadow in the forward scatter direction. Bottom left: the continuous parameters are approximated with an eight-layer shell. The cloaking performance is somewhat reduced in all directions. Bottom right: the material parameters are reduced to levels attainable with metamaterials. Cloaking performance is degraded in all directions, but the fields inside the cloak are still guided around the forbidden region [8].

section (RCS) measurements. This application is described in Chapter 1 of [24].

### 1.3 Research Goals

The goals of this research effort fall into two broad categories: characterization of field behavior in the presence of metamaterial structures and the analysis of an active metamaterial structure.

#### 1.3.1 Characterization of Field Behavior in Metamaterial Structures.

The first objective is to compare methods of characterizing and predicting the behavior of electromagnetic fields incident on a metamaterial structure. Two basic theories behind field behavior in the presence of metamaterial structure are presented: effective medium theory and frequency selective surface theory. In effective medium

theory, the metamaterial structures are said to act like a larger-scale molecular lattice. Therefore, media containing metamaterial structures have effective electric permittivities and magnetic permeabilities. This is described in more detail in Chapter II.

Using the other theory explaining field behavior in metamaterial structures, the metamaterial structures are modeled as periodic frequency selective surfaces (FSS). Electromagnetic fields incident on metamaterial structures create surface waves that cause radiation at the angles often attributed to an effective negative index of refraction. This theory is also described in more detail in Chapter II.

Also included in the characterization of the field behavior in metamaterial structures are advanced computational electromagnetic models. These models utilize frequency- and time-domain techniques to generate theoretical predictions of the field behavior in metamaterial structures. Since these models are entirely based on Maxwell's equations, they provide a view of metamaterials that is unbiased by either effective medium theory or FSS theory. The simulation techniques are described in detail in Section 2.3.

The accuracy of the theoretical results are best determined by comparing them to actual measurements. A large, bulk metamaterial sample in the form of a wedge was acquired by the Air Force Institute of Technology (AFIT) and is shown in Figure 4. Large, bulk samples are best accommodated by free-space measurements. The free-space measurements for this thesis are centered around RCS measurements. The RCS measurement technique presents a novel and straight-forward way to characterize the effects of metamaterials on electromagnetic waves. The measurement results are analyzed and compared to the theoretical results to determine the accuracy of the theory and models.

The RCS measurement technique introduced in this thesis has many advantages.



**Figure 4. This metamaterial wedge sample is characterized using modeling and free-space measurement techniques.**

One of the key advantages is that it makes use of equipment already in AFIT's possession. The RCS measurement technique also creates a new geometry that may help to distinguish between negative refraction and surface wave effects. Finally, the RCS measurement technique allows for expanded analysis using several common postprocessing techniques. The postprocessing techniques used in this thesis are discussed in Chapter II.

### **1.3.2 Analysis of an Active Metamaterial Structure.**

A novel metamaterial structure that achieves frequency adaptability was proposed in a previous AFIT research effort [39]. The structure is based on a basic DNG unit cell. The proposed structure incorporates a microelectromechanical systems (MEMS) variable capacitor across the gaps of the SRR particles. Figure 5 shows the proposed design. Varying the capacitance of the SRR particles has been shown to change the location of the resonant frequency of the device. The second main objective of this thesis is to continue the analysis of a slightly modified version of that structure. Computational models of the adaptive structure are created. The results are analyzed

to determine the effect of the SRR gap capacitance on the resonant frequency of the device.

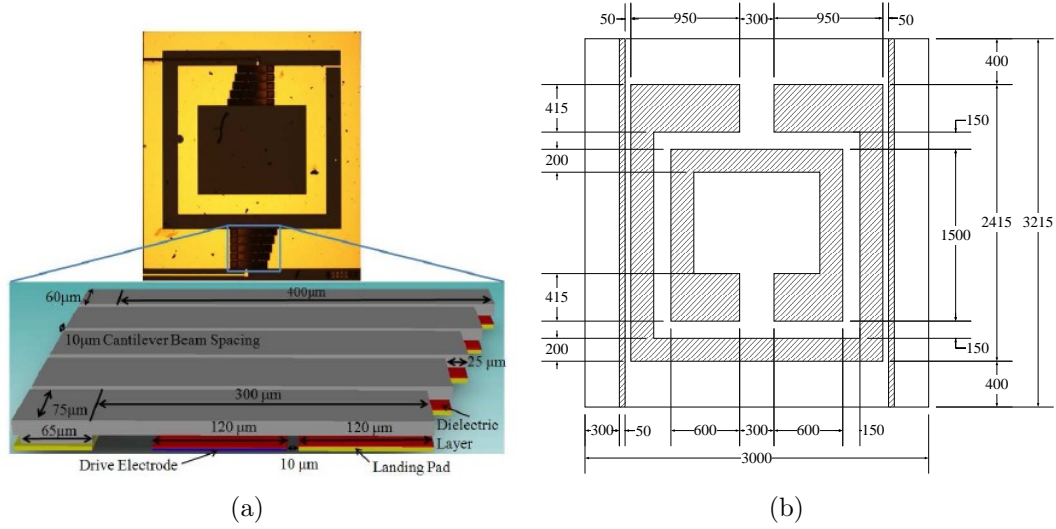


**Figure 5. AFIT-designed adaptive metamaterial structure. (a) A picture from a previous design iteration shows the basic structure and MEMS device [39, 52]. In the latest design, a few of the dimensions are slightly different. (b) The dimensions in  $\mu\text{m}$  for the latest design iteration of the basic unit cell.**

Like the results from the passive metamaterial structures, theoretical data are compared to laboratory measurements. The basic measurement effort for the active metamaterial structures incorporates guided-wave measurements performed using a stripline waveguide. The stripline measurements allow for the derivation of effective material parameters. This is particularly useful for characterizing the adaptive metamaterial structures. The movement of the resonance band is plainly visible in the stripline results.

#### 1.4 Organization of Thesis

This thesis is organized into 5 chapters and 3 appendices. Chapter II provides theoretical background information related to the concepts investigated through this research effort as well as a review of recent and ongoing efforts similar to this one.

Chapter III describes the creation, implementation, and results of computational models and other theory-based predictions for both passive and adaptive metamaterial structures. Chapter IV includes descriptions of the setup and results from laboratory measurements including RCS and stripline measurements. Chapter V includes the broad conclusions drawn from this research effort as well as proposed future endeavors to advance the science. Appendix A includes statistics and figures detailing the computational meshes used in the models of Chapter III. Data from the RCS measurement section not presented in Chapter IV are shown in Appendix B. Finally, computer scripts generated for this research effort are described in Appendix C.

## II. Theory

### 2.1 Chapter Overview

The purpose of this chapter is to present background information on the electromagnetic theory behind metamaterials and the techniques used to model, test, and evaluate their properties. Current research in the field of negative-index and adaptive metamaterials is presented.

The basic theory presented in this chapter addresses both of the research objectives laid out in Chapter I. First, the published methods of characterizing field behavior are described in detail. These theories will be used in later chapters to analyze both traditional and active metamaterial structures. Since this research effort makes heavy use of computational electromagnetics techniques, the relevant simulation methods are explained.

In addition to the basic theories, recently published research results are discussed in this chapter. In many cases the results illustrate the basic theories behind characterizing metamaterial structures. Moreover, the research findings presented in this chapter are directly tied to both research objectives. Efforts to characterize traditional and active metamaterials are discussed, and their relevance to the material presented in later chapters is outlined.

### 2.2 Characterization of Metamaterials

The interaction between metamaterials and electromagnetic fields is currently a critical issue in the scientific community. However, controversy exists relative to the proper explanation of the physical phenomena observed when these metamaterials are subjected to electromagnetic waves. A large number of researchers believe that these embedded structures can display effective material parameters and can be represented

by effective media. Others believe that this explanation is inadequate and argue that surface wave models are a more physically accurate description.

At the core of the controversy are the implications of materials that have negative permittivity and permeability values. This section provides background on effective mediums with negative permittivity and permeability frequency bands and describes how these media may be constructed. This section also looks at a particular counterclaim to the effective material parameters. Proponents of this specific argument believe that surface waves explain the observed properties of metamaterials.

### 2.2.1 Negative Index of Refraction.

The concept of materials with negative permittivity and permeability was first introduced by Veselago in [52]. In this work, Veselago explains the basic electromagnetic theory behind these materials. The concept of left-handed propagation is introduced. Maxwell's equations and the constitutive relations describe the behavior of electromagnetic fields in a material. Maxwell's curl equations for time harmonic fields in a source-free region and the constitutive relations are [1, 7-25]

$$\nabla \times \mathbf{E} = -j\omega\mathbf{B}, \tag{1a}$$

$$\nabla \times \mathbf{H} = j\omega\mathbf{D}, \tag{1b}$$

$$\mathbf{D} = \epsilon\mathbf{E}, \tag{1c}$$

$$\mathbf{B} = \mu\mathbf{H}, \tag{1d}$$

where  $\mathbf{E}$  and  $\mathbf{H}$  are the electric and magnetic field vectors respectively,  $\mathbf{D}$  and  $\mathbf{B}$  are the electric and magnetic flux densities respectively,  $c$  is the speed of light in free space,  $\epsilon$  is the electric permittivity of the medium,  $\mu$  is the magnetic permeability of

the medium, and  $j$  is the imaginary unit ( $j = \sqrt{-1}$ ). For an electromagnetic field with a single rotational frequency  $\omega$  and wave vector  $\mathbf{k}$ , Equation (1) simplifies for plane waves to [52]

$$\mathbf{k} \times \mathbf{E} = \frac{\omega}{c} \mu \mathbf{H}, \quad (2a)$$

$$\mathbf{k} \times \mathbf{H} = -\frac{\omega}{c} \epsilon \mathbf{E}. \quad (2b)$$

If the values of  $\epsilon$  and  $\mu$  are negative in Equation (2),  $\mathbf{E}$ ,  $\mathbf{H}$ , and  $\mathbf{k}$  will be a left-handed set of vectors [52]. Because of this property of materials with negative values of  $\epsilon$  and  $\mu$ , this type of material is referred to as a left-handed material (LHM). Conversely, a traditional material where  $\epsilon$  and  $\mu$  are positive is referred to as a right-handed material (RHM).

Veselago also notes in [52] that the Poynting vector ( $\mathbf{S}$ ),  $\mathbf{E}$ , and  $\mathbf{H}$  always form a right-handed set of vectors, regardless of the sign of  $\epsilon$  and  $\mu$ . The Poynting vector is defined by [1, 29]

$$\mathbf{S} = \frac{1}{2} \Re [\mathbf{E} \times \mathbf{H}^*], \quad (3)$$

where  $\Re$  denotes the real part and the  $*$  symbol denotes the complex conjugate. Equation (3) shows that  $\mathbf{S}$  does not depend on  $\epsilon$  and  $\mu$ . The direction of power flow will not change direction when the signs of  $\epsilon$  and  $\mu$  change. Thus, a LHM is said to have a negative group velocity. This also occurs in anisotropic or dispersive media [52].

An important property of a LHM is the impact negative refraction has on incident electromagnetic waves. This impact is readily seen from the boundary conditions of the interface between two media where there are no sources. The boundary conditions



of this interface are [1, 26]

$$\hat{n} \times (\mathbf{E}_2 - \mathbf{E}_1) = 0, \quad (4a)$$

$$\hat{n} \times (\mathbf{H}_2 - \mathbf{H}_1) = 0, \quad (4b)$$

$$\hat{n} \cdot (\epsilon_2 \mathbf{E}_2 - \epsilon_1 \mathbf{E}_1) = 0, \quad (4c)$$

$$\hat{n} \cdot (\mu_2 \mathbf{H}_2 - \mu_1 \mathbf{H}_1) = 0, \quad (4d)$$

where the 1 and 2 subscripts refer to the medium 1 and medium 2 respectively and  $\hat{n}$  refers to the boundary normal directed into medium 2. Figure 6 shows the interface between two materials. The top region is the RHM.

Equations (4a) and (4b) show that the tangential components of  $\mathbf{E}$  and  $\mathbf{H}$  remain the same in medium 1 and medium 2. However, according to Equations (4c) and (4d), the normal component reverses sign when it crosses the boundary between a RHM and LHM. As shown above, the normal component of  $\mathbf{k}$  also changes direction. These reversals combined with the boundary conditions and the requirement for  $\mathbf{E}$ ,  $\mathbf{H}$ , and  $\mathbf{k}$  to be left-handed mean that the electromagnetic field in the LHM will be on the same side of the  $z$ -axis as it is in the RHM [52]. This is opposite from the case of a boundary between two RHMs and will satisfy Snell's law provided that the index of refraction ( $n$ ) for a LHM is negative [52]. Thus, refraction at the boundary between

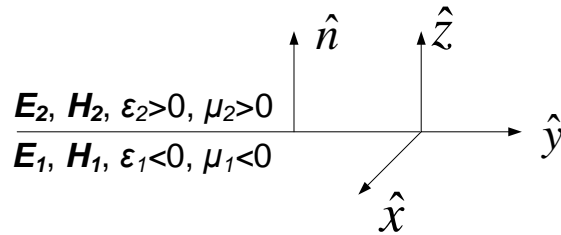


**Figure 6.** Boundary conditions for interface between a RHM and LHM. The medium above the interface (medium 2) is the RHM.

a RHM and LHM is referred to as negative refraction. Since the reflected ray is in the same medium as the incident ray, it will be in the same direction regardless of the second medium [52]. Figure 7 shows a comparison between positive and negative refraction.

In order to satisfy Snell's law, it is necessary to modify the definition of  $n$ . The parameter  $p$  is defined to be one if the material is a RHM and negative one if the material is a LHM. Thus,  $n$  can be calculated from  $\epsilon$  and  $\mu$  for the material as [52]

$$n = \frac{p_1}{p_2} \left| \sqrt{\frac{\epsilon\mu}{\epsilon_0\mu_0}} \right|, \quad (5)$$

where the subscripts 1 and 2 denote the materials on either side of the boundary and  $\epsilon_0$  and  $\mu_0$  are the permittivity and permeability of free space respectively.

Accounting for the difference in the sign of  $n$  between a RHM and LHM, Snell's law of refraction can be rewritten to give the angle of transmission ( $\varphi_t$ ) through the second material [10, 17]

$$\varphi_t = \frac{\text{sgn}(n_1)}{\text{sgn}(n_2)} \arcsin \left( \frac{|n_1|}{|n_2|} \sin \varphi_i \right), \quad (6)$$

where  $\varphi_i$  is the angle of incidence.

### 2.2.2 Realization of Negative Refractive Index.

When Veselago wrote his paper in the late 1960's, he admitted that there were no known substances that had both  $\epsilon < 0$  and  $\mu < 0$ . However, in the 1990's researchers discovered ways that would supposedly allow designers to create mediums with simultaneously negative effective  $\epsilon$  and  $\mu$  values. These effective parameters are created by embedding metallic structures in dielectric materials. The media appear continuous for wavelengths longer than the size and separation of the structures [53].

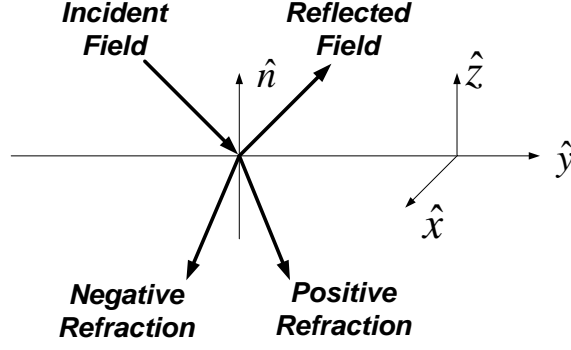


Figure 7. Comparison between negative and positive refraction. When an electromagnetic field crosses the boundary between a LHM and RHM, the refracted field appears in a different plate than an electromagnetic field that undergoes positive refraction. The reflected field is not affected by the second medium being a LHM as opposed to a RHM.

### 2.2.2.1 Negative Permittivity Metamaterials.

Pendry et al. show that a material containing a periodic lattice of metallic wires can have an effective permittivity [33]. The metallic wires serve to reduce the plasma frequency. Pendry et al. state this is because “by confining electrons to thin wires, we have enhanced their mass...” [33]. For a wire lattice with separation distance  $a$  and radius  $r_w$ , the plasmon frequency ( $\omega_p$ ) is reduced to [33]

$$\omega_p^2 = \frac{2\pi c_0^2}{a^2 \ln(a/r_w)}. \quad (7)$$

The plasma frequency is the frequency at which the electron density oscillates in a metal. Incident fields at a frequency higher than the plasma frequency penetrate the metal as if it were transparent; whereas fields below the plasma frequency are exponentially decayed as they enter the material [19, 130]. The plasma frequency of Equation (7) produces a dispersive expression for the effective  $\epsilon$  [33]

$$\epsilon = 1 - \frac{\omega_p^2}{\omega(\omega + \frac{j\epsilon_0 a^2 \omega_p^2}{\pi r_w^2 \sigma})}, \quad (8)$$

where  $\sigma$  is the conductivity of the metal used for the wires. Pendry et al. go on

to present detailed calculations that show agreement with their theory, but the key takeaway is that the results of Equation (8) will be negative when  $\omega < \omega_p$  [33].

### 2.2.2.2 Negative Permeability Metamaterials.

Pendry et al. show in [32] that by embedding certain microstructures into a material, a medium can be made to have an effective  $\mu$ . These microstructures are arranged in periodic arrays. Each element of the array makes up a cubic unit cell with dimension  $a$ . If  $a \ll \lambda$  where  $\lambda$  is the wavelength, the incident radiation will be largely unaffected by the internal structure of the cell and the medium can be characterized by an effective permeability [32].

In [32], Pendry et al. introduce three basic structures that offer some control of the magnetic permeability. However, the structure of interest here consists of two round, concentric SRR particles. The gap in the SRR particles prevent current from flowing around any one ring. However, the capacitance between the two rings allows current to circulate around the rings. This effective  $\mu$  of this structure is [32]

$$\mu = 1 - \frac{\frac{\pi r_{SRR}^2}{a^2}}{1 + j \frac{2\ell R_1}{\omega r_{SRR} \mu_0} - \frac{3dc^2}{\pi \omega^2 \ln \frac{2w}{d} r_{SRR}^3}}, \quad (9)$$

where  $r_{SRR}$  is the radius of the inner SRR,  $w$  is the width of the SRR traces,  $d$  is the difference between the outer radius of the inner SRR and the inner radius of the outer SRR,  $\ell$  is the separation length between the SRR layers, and  $R_1$  is the resistance of unit length of the metal sheets that make up the SRR particles measured around the circumference. Figure 8 illustrates the geometry of the structure. The frequency-dependence of Equation (9) has a resonant form, and the resonant angular frequency ( $\omega_0$ ) is of the form [32]

$$\omega_0 = \sqrt{\frac{3dc^2}{\pi^2 r_{SRR}^3}}, \quad (10)$$

where  $c$  refers to the speed of light in the substrate containing the SRR particles.

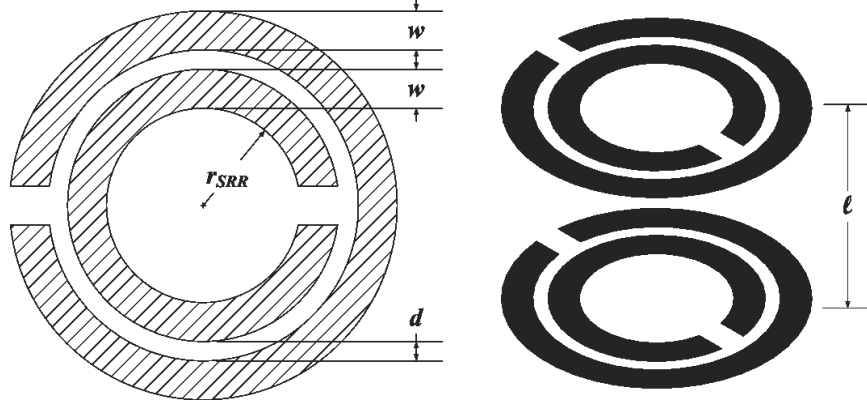


**Figure 8. The geometry of the SRR structure proposed in [32].**

In deriving Equation (9), some conditions are placed on the dimensions of the structure [32]

$$r_{SRR} \gg w, \quad (11a)$$

$$r_{SRR} \gg d, \quad (11b)$$

$$\ell < r, \quad (11c)$$

$$\ln \frac{w}{d} \gg \pi. \quad (11d)$$

To illustrate the behavior of this design, Pendry et al. provide an example calculation using the dimensions of Table 1 and  $R_1 = 200.0$ . Note that these values do not satisfy Equation (11), but “the inequalities are only important to the accuracy of [Equation (9)], not to the functioning of the structure” [32]. Figure 9 shows the effective  $\mu$  given by Equation (9). The effective  $\mu$  shows a resonant behavior at 13 GHz. Equation (9) also predicts a negative  $\mu$  band between approximately 13.5 and

14.5 GHz.

**Table 1. Dimensions for the SRR example given in [32].**

Parameter	Value (mm)
$a$	10
$w$	1.0
$d$	0.10
$\ell$	2.0
$r_{SRR}$	2.0

### 2.2.2.3 Double-negative metamaterials.

A medium with simultaneously negative  $\epsilon$  and  $\mu$  values is created by including a wire lattice and the SRR particles in the same structure. Smith et al. present this composite structure and experimentally measure its performance in [46]. Figure 10 shows the experimental results for a metamaterial structure consisting of just SRR particles (solid line) and a metamaterial structure consisting of SRR particles and a wire lattice (dashed line). The results show that the SRR particles by themselves generate a stop band near the resonance frequency where the theoretical effective  $\mu$  is negative. But, the combination of SRR and wire particles lead to a passband near the band where  $\mu < 0$ .

The analysis in [46] does not address the electric response of the SRR particles. This issue is addressed in [45], and Simovski et al. found that the interaction between the wire lattice and SRR particles does complicate the analysis. They show that the interaction between the two influences the effective permittivity due to the electric response of the SRR particles [45].

None of the analysis in this thesis looks at individual sheets of wires or SRR particles. Rather, all of the models include both components with the exception of one approximation made in Section 3.6.3 to show the impact of structure size on resonant frequency. That approximation is followed up with a numerical simulation.

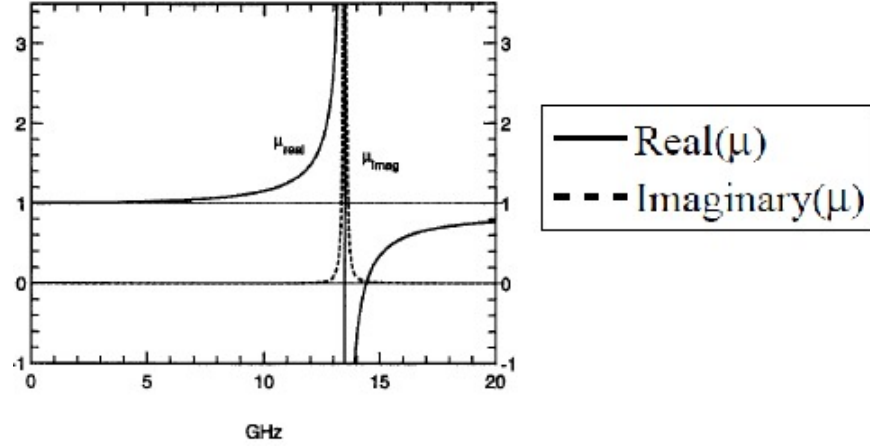


Figure 9. The effective  $\mu$  for the SRR example structure in [32]. The structure displays a resonant behavior near 13 GHz. Furthermore,  $\mu$  is negative between approximately 13.5 and 14.5 GHz.

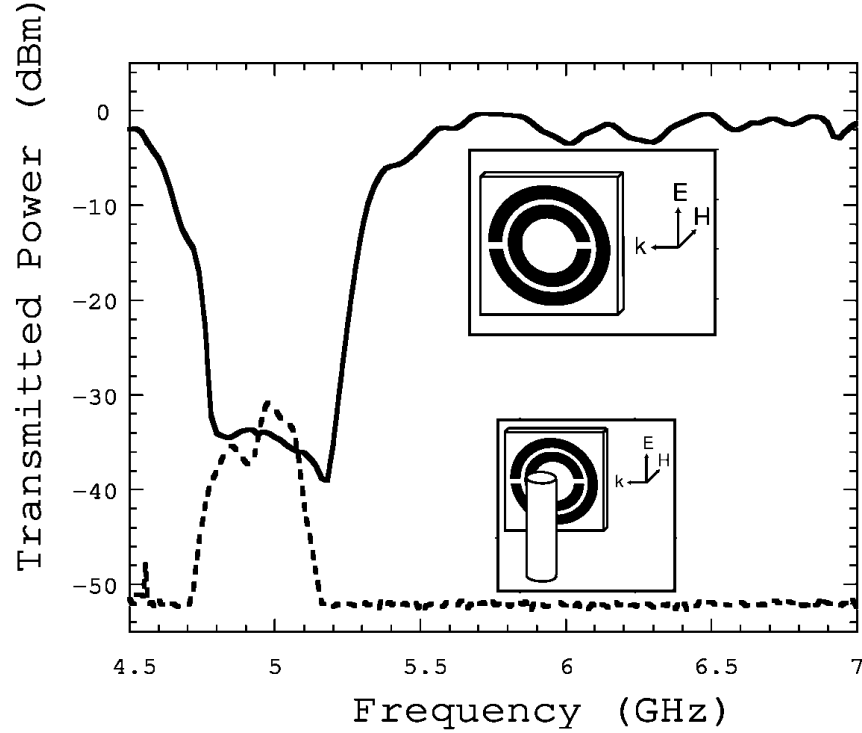


Figure 10. Experimental transmission results for a DNG metamaterial based on a SRR structure and a SRR with a wire array. The insets shows the geometry for each of the structures. The solid line shows that the transmitted power for the SRR metamaterial acts like a stop band. On the other hand, the dashed line indicates that the combination SRR and wire lattice metamaterial acts like a passband in the band where  $\epsilon$  and  $\mu$  are negative [46].

All of the numerical simulations in this thesis take into account the electric response of the SRR particles.

### 2.2.3 Surface Waves in Metamaterials.

Some researchers believe that negative refraction is impossible and that the radiation pattern from an illuminated metamaterial structure can be explained by surface waves. One of those researchers, Ben Munk, recently published a book describing his objections to the effective medium theory described in the sections above [27].

There are four basic theories about metamaterials that Munk disputes [27, 1]

1. certain metamaterial structures can have an effective negative index of refraction,
2. the phase of signal inside a medium with an effective negative index of refraction advances as it moves away from the source,
3. evanescent waves grow in amplitude as they propagate away from the source, and
4.  $\mathbf{E}$ ,  $\mathbf{H}$ , and  $\mathbf{k}$  form a left-handed triplet.

Munk notes that the concept of medium with negative effective values for permittivity and permeability and, thus, a negative effective index of refraction leads to the notion of negative time and violates causality. To illustrate his argument, he notes that the distance traveled by a wave in any medium ( $d_m$ ) is given by [27, 37]

$$d_m = \frac{\omega t}{n k_0}, \quad (12)$$

where  $k_0$  is the wavenumber for freespace. The quantities  $k_0$ ,  $d_m$ , and  $\omega$  in Equation (12) are taken to be positive. Therefore,  $n$  and  $t$  must be the same sign. The conclusion is that a medium with  $n < 0$  would require negative time [27, 37].



Rather than use an effective medium, Munk argues that the formulation for predicting scattering from FSS will work for metamaterial structures. Using this model, Munk states “the direction of refraction in air is determined solely by the interelement spacings  $D_x$  and  $D_z$  as well as the direction  $\hat{s}$  of the incident field, never by the element type” [27, 14].

For the metamaterial slab to be considered continuous, the interelemental spacing must be less than  $\lambda/2$  [27, 14]. This condition on the interelemental spacing also results in the suppression of grating lobes. Assuming the array is infinite, reradiation from the metamaterial slab is only possible in two directions: the forward direction (along same path as incident field) and specular reflection direction. This is because only Floquet currents are present in an infinite array [28]. For an infinite array in the  $x$ - and  $z$ -directions, the radiated fields will be in the direction of  $\hat{r}_\pm$  given by [26, 85]

$$\hat{r}_\pm = \hat{x} \left( s_x + m_1 \frac{\lambda}{D_x} \right) \pm \hat{y} r_y + \hat{z} \left( s_z + m_2 \frac{\lambda}{D_z} \right), \quad (13a)$$

$$r_y = \sqrt{1 - \left( s_x + m_1 \frac{\lambda}{D_x} \right)^2 - \left( s_z + m_2 \frac{\lambda}{D_z} \right)^2}, \quad (13b)$$

where  $s_x$  and  $s_z$  are the  $x$ - and  $z$ -components respectively of a vector pointing in the direction of propagation of the incident plane wave,  $m_1$  and  $m_2$  are the Floquet modes in the  $x$ - and  $z$ -directions respectively, and  $D_x$  and  $D_z$  are the interelemental spacings in the  $x$ - and  $z$ -directions respectively. Note that the waves radiated from the array are inhomogeneous.

The principle direction is given by the condition  $m_1 = m_2 = 0$  [27, 17]. In this case, Equation (13) reduces to  $\hat{r}_\pm = \hat{x} s_x \pm \hat{y} r_y + \hat{z} s_z$  and  $r_y = \sqrt{1 - s_x^2 - s_z^2} = s_y$ . The direction of the reflected field becomes  $r_- = \hat{x} s_x - \hat{y} s_y + \hat{z} s_z$  while the direction of the transmitted field becomes  $r_+ = \hat{x} s_x + \hat{y} s_y + \hat{z} s_z$ . As expected, the reflected

field will be in the specular direction. Furthermore, the direction of the transmitted field remains the same as the incident field.

For a finite array, the radiated fields take on a pattern where mainlobes are aligned along the forward and specular reflection directions. This pattern will also contain sidelobes due to the residual currents. The residual currents can be broken down into surface wave and end currents. Radiation from the end currents is typically much less than radiation from the surface waves. Radiation from surface waves is generally at least 14 to 20 dB lower than the mainbeam [27, 15]. These levels are similar to those found in many negative refraction experiments [27, 8].

The two competing theories for characterization of field behavior in metamaterials discussed in this chapter are key elements of this research effort. These theories have their ardent supporters and the debate continues. The next section discusses the computational techniques of the commercial full-wave electromagnetics solver used in this thesis. In later chapters, scattering predictions for a metamaterial wedge will be made using both theories presented above and tested against the results from the commercial solver, which are, in turn, validated by laboratory measurements. The full-wave solver depends on Maxwell's Equations and is not dependent on either of the two theories presented above.

### **2.3 Computational Techniques**

The main computational tool used to characterize the metamaterial structures presented in later chapters is CST Microwave Studio (MWS)®. CST MWS® is a commercial full-wave electromagnetics solver that primarily uses the finite integration technique (FIT). CST MWS® users have the option of employing the FIT in the time- or frequency-domains.

The results from the simulations are often provided in the form of scattering

parameters, or  $S$ -parameters. From these  $S$ -parameters, a set of effective material parameters can be calculated. Due to the complex (and controversial) nature of the material parameter extraction process, care must be taken in generating and interpreting the solutions.

This section describes basic background theory on the FIT, some recently published articles on modeling metamaterials, and the method used in this research to extract the effective material parameters.

### 2.3.1 Finite Integration Technique.

The FIT is of key interest because it is the main method for this study. The finite integration technique is similar to the finite difference time-domain (FDTD) technique. The computational domain is divided into two grids, denoted  $G$  and  $\tilde{G}$ . The grids are spaced so that the corner of a cell in one grid is collocated with the center of cell in the other grid [7]. The state variables of the FIT are referred to as the grid electric voltage vector ( $\mathbf{e}$ ), magnetic voltage vector ( $\mathbf{h}$ ), magnetic induction flux ( $\mathbf{b}$ ), and electric displacement flux ( $\mathbf{d}$ ). The quantities  $\mathbf{e}$ ,  $\mathbf{b}$ , and electric charge density ( $q_{ev}$ ) are defined on  $G$ ; while  $\mathbf{d}$ ,  $\mathbf{h}$ , and  $\mathbf{j}$  are defined on  $\tilde{G}$  [7]. The state variables for the  $i$ th grid cell are defined on both the edges or facets of the cells by [55]

$$e_i = \int_{L_i} \mathbf{E} \cdot d\mathbf{s}, \quad (14a)$$

$$b_i = \int_{A_i} \mathbf{B} \cdot d\mathbf{A}, \quad (14b)$$

$$d_i = \int_{\tilde{A}_i} \mathbf{D} \cdot d\mathbf{A}, \quad (14c)$$

$$h_i = \int_{\tilde{L}_i} \mathbf{H} \cdot d\mathbf{s}, \quad (14d)$$

$$j_i = \int_{\tilde{A}_i} \mathbf{J} \cdot d\mathbf{A}, \quad (14e)$$

where  $L_i$  and  $\tilde{L}_i$  are the lengths of the  $i$ th cell edges in  $G$  and  $\tilde{G}$  respectively,  $A_i$  and  $\tilde{A}_i$  are the areas of the  $i$ th cell facets in  $G$  and  $\tilde{G}$  respectively, and  $\mathbf{J}$  is the electric current vector.

The FIT is based on the integral form of Maxwell's equations. Assuming no magnetic source current, these equations are [55]

$$\oint_{\partial A} \mathbf{E} \cdot d\mathbf{s} = -\frac{d}{dt} \int_A \mathbf{B} \cdot d\mathbf{A}, \quad (15a)$$

$$\oint_{\partial A} \mathbf{H} \cdot d\mathbf{s} = \int_A \left( \frac{d}{dt} \mathbf{D} + \mathbf{J} \right) \cdot d\mathbf{A}, \quad (15b)$$

$$\oint_{\partial V} \mathbf{D} \cdot d\mathbf{A} = \int_V q_{ev} dV, \quad (15c)$$

$$\oint_{\partial V} \mathbf{B} \cdot d\mathbf{A} = 0. \quad (15d)$$

Support matrix operators ( $\mathbf{C} = \oint_{\partial A} \cdot d\mathbf{s}$ ,  $\mathbf{S} = \oint_{\partial V} \cdot d\mathbf{A}$ ) and ( $\tilde{\mathbf{C}} = \oint_{\partial \tilde{A}} \cdot d\mathbf{s}$ ,  $\tilde{\mathbf{S}} = \oint_{\partial \tilde{V}} \cdot d\mathbf{A}$ ) are defined for  $G$  and  $\tilde{G}$  respectively. The elements of  $\mathbf{C}$ ,  $\mathbf{S}$ ,  $\tilde{\mathbf{C}}$ , and  $\tilde{\mathbf{S}}$  can only take on values of -1, 1, or 0 [55]. Using these quantities and the definitions in Equation (14), Equation (15) can be transformed into [55]

$$\mathbf{C}\mathbf{e} = -\frac{d}{dt}\mathbf{b}, \quad (16a)$$

$$\tilde{\mathbf{C}}\mathbf{h} = \frac{d}{dt}\mathbf{d} + \mathbf{j}, \quad (16b)$$

$$\tilde{\mathbf{S}}\mathbf{d} = q_{es}, \quad (16c)$$

$$\mathbf{S}\mathbf{b} = 0. \quad (16d)$$

The constitutive relation describing the relationship between  $\mathbf{E}$ ,  $\mathbf{J}$ , and  $\sigma$  is [1, 7]

$$\mathbf{J} = \sigma\mathbf{E}. \quad (17)$$

The constitutive parameters  $\epsilon$ ,  $\mu$ , and  $\sigma$ , are discretized in both  $G$  and  $\tilde{G}$  and are represented by the matrices  $\mathbf{M}_\epsilon$ ,  $\mathbf{M}_\mu$ , and  $\mathbf{M}_\sigma$  respectively. Thus, the constitutive relations of Equations (1c), (1d), and (17) are converted to the discrete constitutive relations and become [41]

$$\mathbf{d} = \mathbf{M}_\epsilon\mathbf{e}, \quad (18a)$$

$$\mathbf{b} = \mathbf{M}_\mu\mathbf{h} \quad (18b)$$

$$\mathbf{j} = \mathbf{M}_\sigma\mathbf{e} + \mathbf{j}_s, \quad (18c)$$

where the source currents ( $\mathbf{j}_s$ ) have been included with  $\mathbf{j}$ . Equation (18) is where the first inaccuracies due to spatial discretization are introduced because the material parameters are spatially averaged [41].

Equations (16) and (18) form a complete system of equations that can be solved in the time-domain. Time-domain calculations are especially useful for broadband calculations. By defining a specific signal (e.g. Gaussian) for the frequency range of

interest, the corresponding time-domain signal can be found by computing the inverse Fourier transform. The time-domain signal is then used as the excitation signal and the time-domain solution is found using Equations (16) and (18). The solution can be transformed back into the frequency-domain using a Fourier transform [56]. While this procedure does involve transformations to and from the time-domain, it only requires one solution to Maxwell's equations. Generally speaking, solving Maxwell's equations takes considerably longer than Fourier transforms, so this procedure can produce results over a frequency band relatively quickly. A potential drawback is that in the time-domain Equations (16) and (18) have to be repeatedly computed until steady-state criteria are met. For resonant structures, this may become very computationally intensive. Since metamaterial structures are resonant by design, a frequency-domain implementation of Equations (16) and (18) is desirable.

For frequency domain calculations, Equation (16) can be re-written in the frequency-domain (assuming the time harmonic case) by substituting the complex frequency  $j\omega$  for  $d/dt$ . The frequency-domain version of Equation (16) along with Equation (18) are solved directly at individual frequency points. This implementation does not have the same steady-state requirement, so solutions for resonant structures can be found quickly. However, multiple solutions will be required for multiple frequencies. The number of solutions required can be reduced by using interpolation techniques on the results [56]. Figure 11 illustrates an example of the time- and frequency-domain calculations of  $S$ -parameters for a  $90^\circ$  coaxial connector.

### 2.3.2 Boundary Conditions.

Proper termination of the computational domain is a critical concern in the FIT. Like other solvers, CST MWS® employs several different boundary conditions. However, the boundary conditions of concern for this thesis are perfect electric conductor

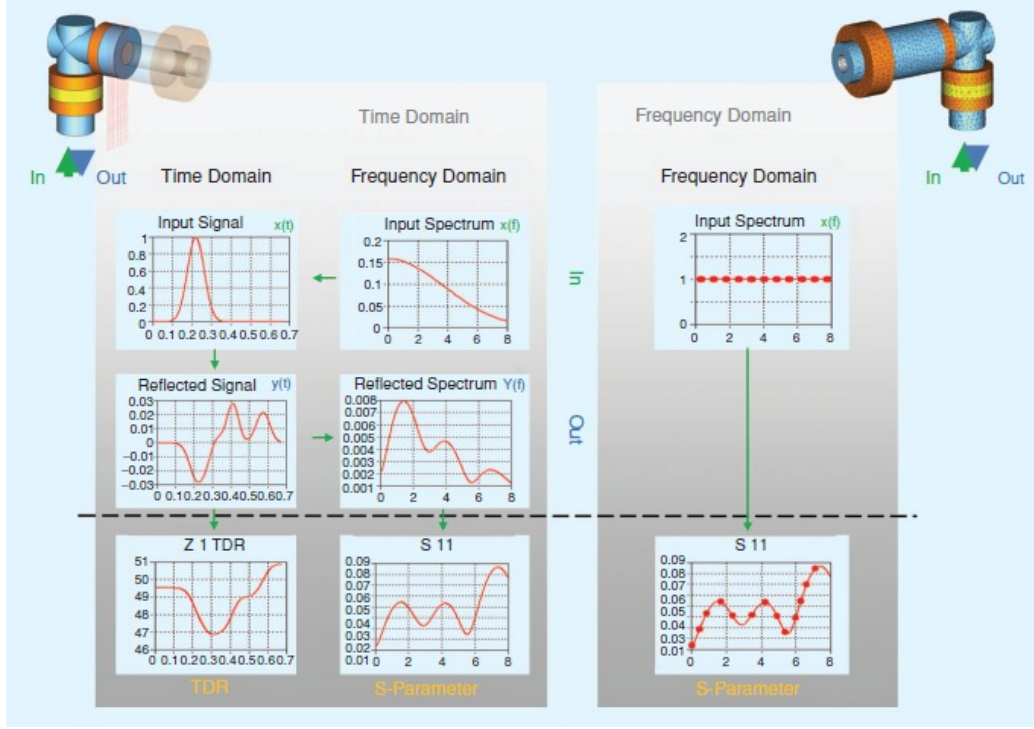


Figure 11. An example of the finite integration technique in the time- and frequency-domains. The  $S$ -parameters of a  $90^\circ$  coaxial connector are desired in the frequency-domain. Time-domain calculations require transformations from and to the frequency domain, but only one solution of Maxwell's equations. Frequency-domain calculations do not require the transformations, but multiple solutions of Maxwell's equations will be necessary [56].

(PEC), perfect magnetic conductor (PMC), open, and periodic or unit cell.

PEC and PMC boundary conditions are relatively straightforward. A PEC material has an infinite electric conductivity. Thus,  $\mathbf{E}$  inside a PEC material must be zero. PEC materials are often used to approximate good conductors, like metals. A PMC is the magnetic equivalent to a PEC material. That is, inside a PMC material  $\mathbf{H}$  must be zero. PEC and PMC boundary conditions are mathematically simple to realize. To create a PEC boundary, use  $\mathbf{E}_1 = 0$  in Equations (4a) and (4c). Likewise, for a PMC boundary, substitute  $\mathbf{H}_1 = 0$  into Equations (4b) and (4d).

An open boundary condition is more difficult to implement mathematically. An open boundary is meant to simulate an infinite amount of space in that direction. No energy incident on an open boundary should be reflected back into the computational

domain. CST MWS® realizes an open boundary with a form of the convolution perfectly matched layer (PML). The convolution PML is a robust mechanism that has very little numerical reflection, can be implemented with the standard FIT or FDTD formulation, and is computationally efficient[3].

Periodic and unit cell boundary conditions are very similar. A periodic boundary mirrors the computational domain along an axis. Unit cell boundary conditions mirror the computational domain along two axes. The result of either set of boundary conditions is a structure that is infinitely long in one dimension (in the case of periodic boundary conditions) or two dimensions (in the case of unit cell boundary conditions). These infinite arrays are created by assuming a known phase progression along the array. Thus, the response from the infinite array can be calculated using the appropriate phase shifts.

### **2.3.3 Farfield Calculations.**

The field solutions that result from the FIT are defined in the near field. However, many quantities of interest are defined in the farfield. So, a method for extending the results from the near field to the farfield is required. This section presents a technique for projecting the near field results to the farfield. Once the farfield values are computed, quantities like radar cross section can be determined. This section also discusses a few farfield quantities that is used in this thesis.

#### **2.3.3.1 Extension to the Farfield.**

The FIT solves for the fields inside the computational domain. However, to calculate the electromagnetic fields in the farfield region, either the computational domain needs to be extended to the farfield or additional calculations are required. Expanding the computational domain to an area large enough to approximate the farfield



would be too cumbersome. Therefore, implementations of FIT and FDTD like CST MWS® make use of a nearfield to farfield transformation.

The farfield values are computed from the fields present on the bounding box of the computational domain [11]. From the fields on the bounding box, the equivalent electric ( $\mathbf{J}_s$ ) and magnetic currents ( $\mathbf{M}_s$ ) are computed from [35, 518]

$$\mathbf{J}_s = \hat{n} \times \mathbf{H}, \quad (19a)$$

$$\mathbf{M}_s = -\hat{n} \times \mathbf{E}, \quad (19b)$$

where  $\hat{n}$  is outward directed. The farfields can be found using vector potentials. For the frequency-domain, the magnetic ( $\mathbf{N}$ ) and electric ( $\mathbf{L}$ ) vector potentials for the farfield are defined by [1, 286]

$$\mathbf{N} = \int \int_S \mathbf{J}_s e^{jk\hat{r} \cdot \mathbf{r}'} ds', \quad (20a)$$

$$\mathbf{L} = \int \int_S \mathbf{M}_s e^{jk\hat{r} \cdot \mathbf{r}'} ds', \quad (20b)$$

where  $ds'$  is a differential point on the surface of the bounding box,  $\mathbf{r}'$  denotes the position vector of a point on the surface, and  $\hat{r}$  is a unit vector directed towards the point of interest in the farfield. The electric and magnetic field vectors can be decomposed into their spherical components ( $E_r$ ,  $E_\theta$ ,  $E_\phi$ ,  $H_r$ ,  $H_\theta$ , and  $H_\phi$ ) and estimated in the farfield using [1, 288]

$$E_r \cong H_r \cong 0, \quad (21a)$$

$$E_\theta \cong -\frac{jke^{-jkr}}{4\pi r} (L_\phi + zN_\theta), \quad (21b)$$

$$E_\phi \cong \frac{jke^{-jkr}}{4\pi r} (L_\theta - zN_\phi), \quad (21c)$$

$$H_\theta \cong \frac{jke^{-jkr}}{4\pi r} \left( N_\phi - \frac{L_\theta}{z} \right), \quad (21d)$$

$$H_\phi \cong -\frac{jke^{-jkr}}{4\pi r} \left( N_\theta + \frac{L_\phi}{z} \right), \quad (21e)$$

where  $z$  is the intrinsic impedance and  $N_\theta$ ,  $N_\phi$ ,  $L_\theta$ , and  $L_\phi$  are the  $\theta$  and  $\phi$  components of  $\mathbf{N}$  and  $\mathbf{L}$  respectively.

### 2.3.3.2 Calculation of Radar Cross Section.

Once Equation (21) has been solved, farfield quantities can be computed. A farfield quantity of particular interest in this research effort is radar cross section (RCS). RCS ( $\sigma_{3D}$ ) is a measure of energy scattered off of an object in a particular direction and is mathematically defined as [21, 18]

$$\sigma_{3D} = \lim_{r \rightarrow \infty} 4\pi r^2 \frac{|E^s|^2}{|E^i|^2}, \quad (22)$$

where  $E^i$  denotes the incident electric field and  $E^s$  is the scattered electric field. Note that the incident and scattered magnetic fields can be substituted for  $E^i$  and  $E^s$ .

For objects that can be approximated as infinite in one dimension, the RCS problem can be simplified to two dimensions. The two-dimensional RCS, known as the scattering width ( $\sigma_{2D}$ ), is defined in terms a width instead of an area. It is defined mathematically by [21, 19]

$$\sigma_{2D} = \lim_{\rho \rightarrow \infty} 2\pi\rho \frac{|E^s|^2}{|E^i|^2}. \quad (23)$$

RCS is typically expressed in decibels per square meter (dBsm), while scattering width is usually expressed as decibels per meter (dBm). If the actual height of the two-dimensional object is known, the RCS can be approximated from the scattering width from [21, 19]

$$\sigma_{3D} = \frac{2\sigma_{2D}}{\lambda} |h \text{sinc}(kl \sin \theta)|^2, \quad (24)$$

where  $h$  is the actual height of the two-dimensional target,  $\theta$  is the azimuth angle of the incident propagation vector relative to the transverse plane of the object,  $k$  is the wavenumber of the incident field, and  $\text{sinc}(x) = \sin(x)/x$ . For geometries where the incident propagation vector is in the transverse plane of the object,  $\text{sinc}(kl \sin 0) = 1$  and Equation (24) simplifies to [1, 578]

$$\sigma_{3D} = \sigma_{2D} \frac{2h^2}{\lambda}. \quad (25)$$

Since the RCS and scattering widths are calculated using the magnitudes of the electric (or magnetic) fields, the phase information is lost. However, the phase information can be very useful for imaging. To get the phase quantity, the  $\sqrt{\sigma_{3D}}$  can be computed with [21, 19]

$$\sqrt{\sigma_{3D}} = \lim_{r \rightarrow \infty} 2\sqrt{\pi r} \frac{E^s}{E^i}. \quad (26)$$

Similarly, the  $\sqrt{\sigma_{2D}}$  can be found by taking the square root of Equation (23). Using this expression and Equation (24),  $\sqrt{\sigma_{3D}}$  can be estimated from  $\sqrt{\sigma_{2D}}$  with

$$\sqrt{\sigma_{3D}} = h \sqrt{\frac{2\sigma_{2D}}{\lambda}} \text{sinc}(kh \sin \theta). \quad (27)$$

### 2.3.3.3 Radar Cross Section Range Processing.

Range information can prove useful for determining scattering mechanisms. Range information is calculated from the RCS data by applying the inverse fast Fourier transform (FFT) to the frequency data. The FFT transforms the frequency data to the time-domain. Since the radar signal travels at the speed of light, the time-domain data are easily converted into spatial data. A drawback to this process, however, is that it introduces some extra information at the edges of the range cells which can be suppressed by applying a windowing technique. For the measurements presented in this thesis, a Hann window is used to suppress the excess information.

The amount of information contained in the RCS data determines the quality of the range images. A key factor is the downrange resolution ( $\Delta R_d$ ). The downrange resolution is related to the bandwidth ( $B$ ) by [25, 13]

$$\Delta R_d = \frac{c}{2B}. \quad (28)$$

The relationship between downrange resolution and bandwidth is a critical concern for this thesis. Many of the structures analyzed and measured are resonant. To see the effects of the resonance, the range information is analyzed over frequency windows. According to (28), this increases the downrange resolution making it harder to resolve scattering objects. The sizes of the range cells are calculated in the later chapters.

### 2.3.3.4 Inverse Synthetic Aperture Radar Image Processing.

In addition to range information, inverse synthetic aperture radar (ISAR) imagery is used to identify scattering mechanisms. ISAR information is calculated by using an

FFT on the angular data in addition to the frequency data. By doing this, ISAR information is able to convert the angular and frequency data into spatial data. Similar to the downrange resolution, the cross range resolution is determined by the amount of angular information contained in the RCS data. The cross range resolution ( $\Delta R_c$ ) is determined by [25, 16]

$$\Delta R_c = \frac{\lambda_{mid}}{2 \sin \Theta}, \quad (29)$$

where  $\lambda_{mid}$  is the wavelength of the mid point of the frequency band, and  $\Theta$  is the angular extent of the RCS data. The steps to set the resolution are:

1. determine the bandwidth of the RCS data,
2. use Equation (28) to determine the down range resolution,
3. set the cross range resolution equal to the down range resolution, and
4. solve Equation (29) for the angular extents.

Following this procedure results in square range cells. Again, because the structures in this thesis are resonant in frequency, they will be analyzed using frequency windows. This restricts the downrange resolution. For the analysis in this thesis, the angular data are also windowed to ensure square range cells in the ISAR images.

#### **2.3.4 Computational Studies of Traditional Metamaterials.**

Computational studies of metamaterials are currently being conducted in both academia and industry. This section provides a brief sampling of current efforts. Computational techniques are also described in later sections on adaptive metamaterials.

#### 2.3.4.1 Model of Left-Handed Material Using Finite Element Method.

Smith et al. model several metamaterial structures in [47], but the structure of interest here is the LHM shown in Figure 12. The structure consists of three particles. The first two particles are a pair of concentric SRR particles. The opening of the inside (smaller) SRR is on the opposite side as the opening of the outside (larger) SRR. The third particle is a wire that is embedded further into the substrate and runs down the center between the openings of the SRR particles. The substrate is FR4 with a relative permittivity of 4.4 and loss tangent of 0.02. The authors note that SRR particles are bianisotropic. The bianisotropy is avoided in their paper, however, by analyzing only one incident polarization. The authors state that the cross-coupling terms are small for this polarization, so their method provides an adequate characterization for the polarization of interest. A similar argument could be made to address the anisotropy of the FR4 substrate.

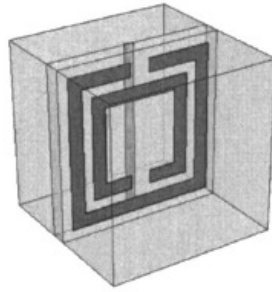


**Figure 12.** The symmetric structure from [47].

The modeling results published by Smith et al. for this structure are shown in Figure 13. To perform the modeling, the authors use Ansoft's HFSS<sup>TM</sup>. Ansoft HFSS<sup>TM</sup> is a commercial full-wave electromagnetics solver that uses the finite element method (FEM). The extraction of the refractive index, impedance, relative permittivity, and relative permeability are performed using a technique similar to the one described in Section 2.3.5. The results shown in Figure 12 demonstrate an effective

negative index band around 10 GHz. In fact, this negative band has both a negative permittivity and permeability [47].

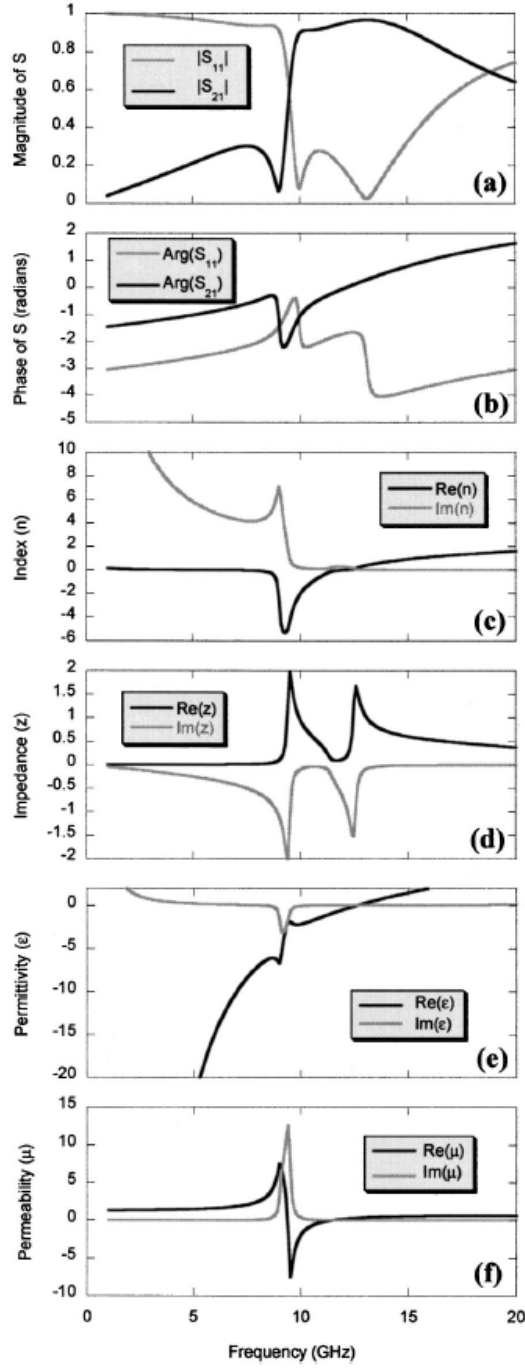
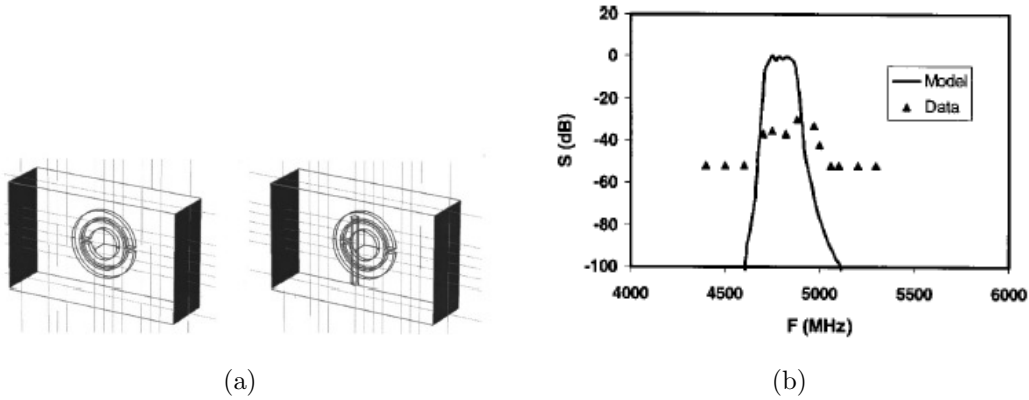


Figure 13. The published results from modeling the structure of Figure 12. The  $S$ -Parameters magnitude (a) and phase (b) are found. The index of refraction (c), impedance (d), permittivity (e), and permeability (f) are extracted [47].

### 2.3.4.2 Model of Left-Handed Material Using FIT.

Weiland et al. [55] present simulation and measurement results of the LHM structure presented in [46]. The structure consists of two concentric, round SRR particles and a single wire. Figure 14(a) shows the structure of the unit cell as well as the simulation results. CST MWS® was used to simulate the structure. The wire and rings are modeled as a PEC material. A plane wave source is introduced at the left face shown in Figure 14(a). The boundary conditions at the top and bottom faces are PEC, while the boundary conditions at the forward and rear faces are PMC. A symmetry plane parallel to the top and bottom faces is introduced in the center of the structure to cut the computational domain in half. The time-domain solver is used. The reported solution time was approximately 1/2 hour using an 800 MHz Pentium III processor [55]. The results are shown in Figure 14(b). The data from CST MWS® demonstrate the same passband behavior as the measured results in [46].



**Figure 14.** Simulation model and results of a metamaterial structure analyzed by Weiland et al. (a) The unit cell for the computer simulation consists of two concentric SRR particles and a wire. (b)  $S_{21}$  for an array of the metamaterial unit cells shows the expected bandpass behavior. The data from the CST Microwave Studio® (solid line) show the same behavior as the measured data (triangles) [55].

Weiland et al. also include a parametric study of their model in [55]. They show the dependence of the resonant frequency on the thickness of the SRR particles, radius



of the inner SRR, gap width of the SRR particles, gap between the SRR particles in a single unit cell, and the  $\epsilon$  and  $\mu$  of the substrate for the SRR particles and wire lattice. The results are shown in Figure 15. The thickness of the SRR particles, SRR radius, and gap width have only small impacts on the resonant frequency. The largest influence on the resonant frequency comes from varying  $\epsilon$  and  $\mu$  of the dielectric substrate [55].

#### 2.3.4.3 Model of Metamaterial Wedge Using FIT.

CST MWS® is used to analyze a couple of composite metamaterial structures in [20]. Of key interest is their model of a metamaterial wedge, as it closely matches part of this research effort. The model is shown in Figure 16. The unit cell of the metamaterial structure consists of a square SRR pair and wire trace, similar to the structure analyzed in by Smith et al. in [47]. A negative refraction band is said to occur between 8.5 and 9 GHz. The unit cells are arranged in a stair-step grid forming a 26.6° wedge. The wedge is fed by a waveguide port. The transient-solver in CST MWS® is used to perform the simulation [20].

The  $\mathbf{E}$ -field magnitudes resulting from the simulation in the negative refraction band are shown in Figure 16(c). The fields are transmitted at an angle of -22° relative to the wedge normal. Thus, the transmitted field is on the same side of the wedge normal as the incident field. Using this angle and solving Equation (6), the effective refractive index of the metamaterial wedge in the negative refraction band is  $n = -1.17$ . Similarly, the  $\mathbf{E}$ -field magnitudes outside of the negative refraction band are shown in Figure 16(d). The fields are transmitted at an angle of 5°, corresponding to  $n = 5.14$  [20].

The model of the metamaterial wedge is similar to the one analyzed in this thesis. However, the metamaterial wedge measured in this thesis forms a different angle and

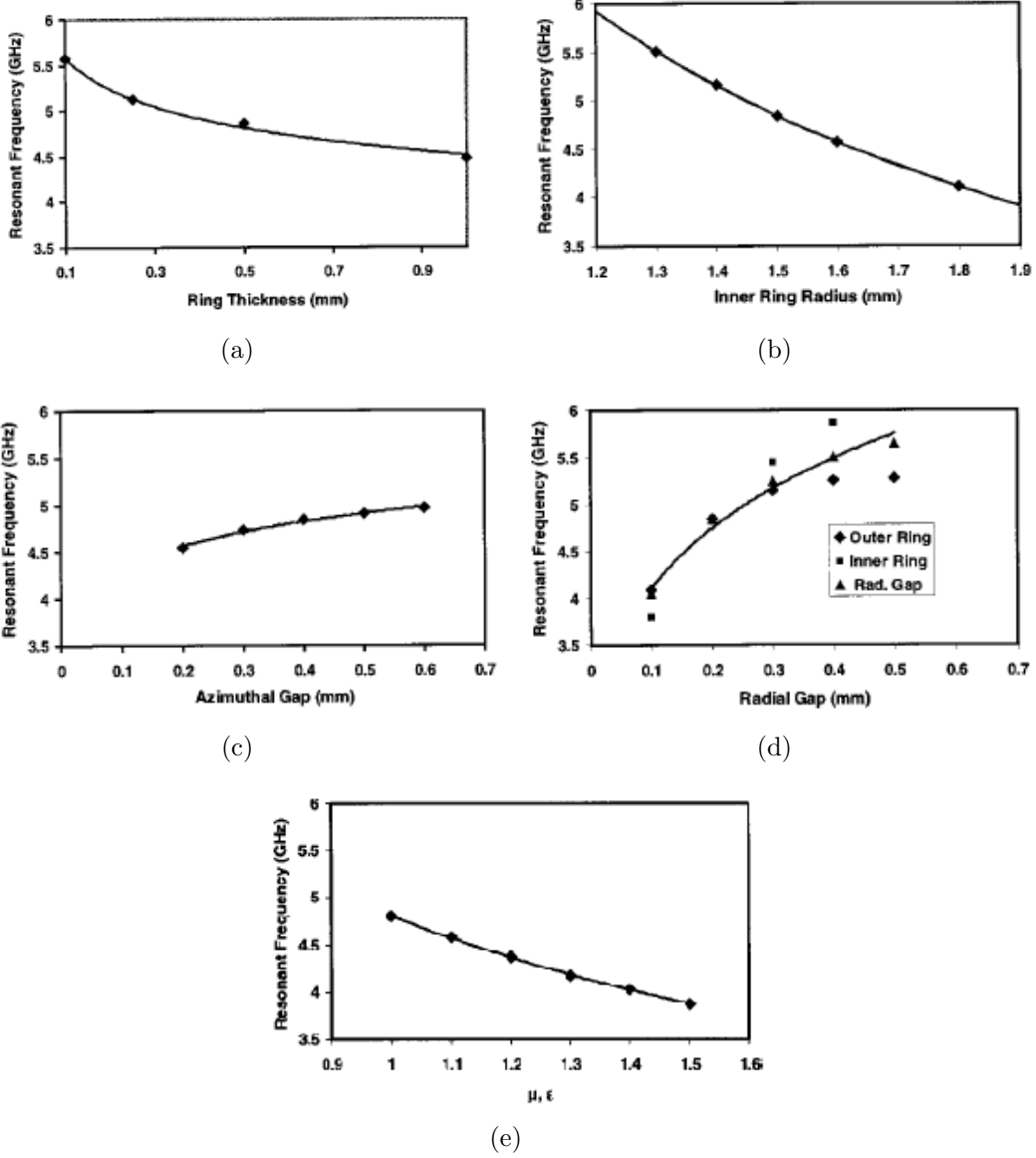
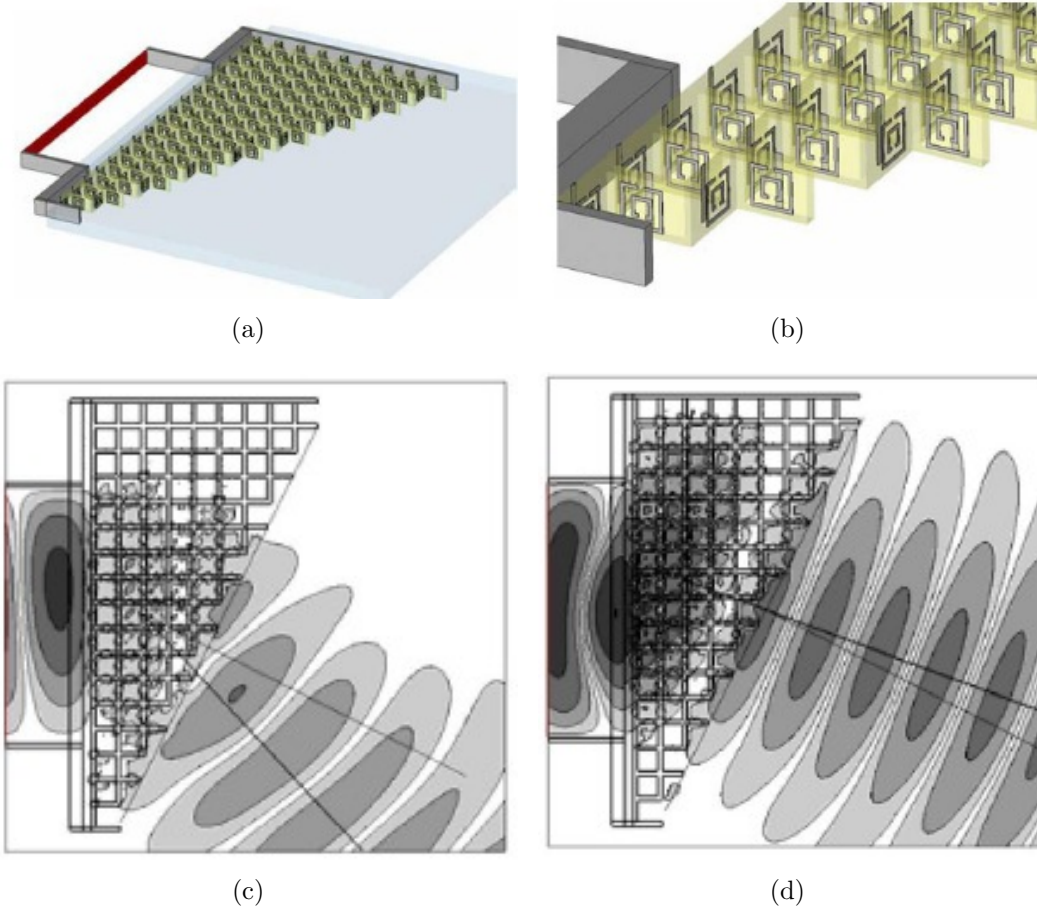


Figure 15. Results from the parametric study of the DNG structure from [55]. (a) Increasing the thickness of the SRR particles causes a slight decrease in the resonant frequency. (b) Increasing the radius of the SRR particles also decreases the resonant frequency slightly. (c) The width of the gap in the SRR particles has only a slight impact on the resonant frequency. (d) The gap between the SRR particles has a little more influence on the resonant frequency. (e) Only slight changes in the permittivity and permeability of the substrate can impact the resonant frequency [55].

does not have the criss-cross unit cells. Also, while the wedge in [20] is fed from behind and the transmission angle is measured directly, the wedge from this thesis is radiated with an electromagnetic field incident on the front of the wedge. The wedge



**Figure 16.** CST MWS® model and results for the metamaterial wedge analyzed in [20]. (a) The model consists of metamaterial unit cells arranged in a stair-step fashion forming a  $26.6^\circ$  wedge. The structure is fed by a waveguide port (the red plane). (b) A close-up view of the model shows that the metamaterial unit cells consist of a SRR pair and a wire trace. (c) Inside the negative refraction frequency band, the diffracted fields are seen emanating at an angle of about  $22^\circ$ . (d) Outside of the negative refraction frequency band, positive refraction occurs [20].

in this thesis has a metal plate behind it and the transmission angle is determined indirectly. Using the metal plate backing allows the wedge to be measured in the RCS range and eliminates the need for measurements in the back end of the range where the direct path from the transmitting antenna can interfere with the receiver. Finally, the metamaterial wedge analyzed in this thesis is many unit cells tall. This reduces the angular size of the scattering lobes in the vertical dimension.

### 2.3.5 Parameter Extraction.

Extraction of effective metamaterial parameters is a critical issue in the characterization of metamaterials, but it is a complicated process. Traditional methods tend to fail when the  $S$ -parameters are small in magnitude. Finding the roots of the impedance can be difficult. Further complicating matters is the behavior of the fields in the resonance band. Whether parameter extraction can be accomplished at all in the resonance band is a current topic of debate.

In light of these complexities, Chen et al. propose a more stable method for extracting the effective parameters of metamaterials [6]. While their method does not address the issue of field behavior in the resonance band, it is stable enough to work when the  $S$ -parameters are small and does pick the correct root for the impedance. The traditional methods calculate the impedance  $z$  and index of refraction  $n$  of a slab of thickness  $d_s$  with [6]

$$z = \pm \sqrt{\frac{(1 + S_{11})^2 - S_{21}^2}{(1 - S_{11})^2 - S_{21}^2}}, \quad (30a)$$

$$e^{jn k_0 d_s} = X \pm j\sqrt{1 - X^2}, \quad (30b)$$

$$X = \frac{1}{2S_{21}(1 - S_{11}^2 + S_{21}^2)}. \quad (30c)$$

The signs of the roots in Equations (30a) and (30b) are determined by [6]

$$\Re\{z\} \geq 0, \quad (31a)$$

$$\Im\{n\} \geq 0. \quad (31b)$$

The equations above treat  $n$  and  $z$  independently. However,  $n$  and  $z$  are related,

and Chen et al. exploit that relationship to find the appropriate roots. In the case of finding the roots for the impedance, their procedure uses the fact that the wave can not grow in amplitude. Therefore  $|e^{jnk_0d}| \leq 1$ ; where the left side is found with the relationship [6]

$$e^{jnk_0d_s} = \frac{S_{21}}{1 - S_{11}\frac{z-1}{z+1}}. \quad (32)$$

Chen et al. note that when finding the roots of Equation (30a), Equation (32) is only necessary when  $z$  is small. When  $z$  is large, Equation (31a) can be used. Throughout this thesis, however, the impedance will be calculated using the traditional method. The results from the traditional method of calculating  $z$  are found to be identical to the results from the more complicated procedure proposed by Chen et al.

Calculating index of refraction is more complex than finding the impedance. Solving Equation (30b) for  $n$  yields [6]

$$n = \frac{1}{k_0d_s} [\Im\{\ln(e^{jnk_0d_s})\} + 2m\pi - j\Re\{\ln(e^{jnk_0d_s})\}], \quad (33)$$

where  $m$  is the branch integer of  $n$ . From Equation (33) the imaginary part of  $n$  can be found with little trouble since Equation (33) gives a unique solution, but the real part of  $n$  will require making the proper branch choice. The proposed method is an iterative process that starts by determining which values of  $m$  are valid for the first frequency sample. By using the fact that imaginary parts of the relative permittivity and permeability must be positive, Chen et al. show for a branch choice to be valid it must satisfy

$$|\Re\{n\}\Im\{z\}| \leq \Im\{n\}\Re\{z\}. \quad (34)$$

If only one value of  $m$  satisfies Equation (34), then that value is the proper branch cut for all frequencies. If more than one value of  $m$  satisfies Equation (34) at the first frequency, then those solutions should be tested at the other frequencies. The value of  $m$  that satisfies at the other frequency values is the correct branch [6].

Note that there may exist a band of frequencies for which no values of  $m$  satisfy Equation (34). This is most likely the resonance band. As mentioned above, the process proposed by Chen et al. does not address this band. However, for the purposes of this research, the values of  $m$  that satisfy the most frequencies will be used as the correct value of  $m$ . Therefore, extracted results in the resonance band will be shown.

The extraction of the material parameters creates an effective medium, but the size of that effective medium has not yet been determined. Chen et al. present an algorithmic approach to solve for the location of the first boundary of the effective medium as well as its thickness. Their approach minimizes the difference in impedances between metamaterial structures of different thicknesses. However, after using the approach on different types of structures, they conclude that their algorithm is only necessary for two-dimensional and asymmetric one-dimensional metamaterials. For symmetric one-dimensional structures, like the one pictured in Figure 12, the first unit cell boundary is the first effective boundary, and the thickness of the metamaterial structure is the effective thickness [6]. The structures analyzed in this thesis closely resemble the structure shown in Figure 12. Thus, the first unit cell boundary and structure thickness are used for the effective first boundary and thickness.

The code used throughout this research to extract the parameters is described in Appendix C. As it will be shown later, the code does recreate the results found in published articles.

## 2.4 Experimental Studies of Traditional Metamaterial Structures

Many experiments have been conducted on non-adaptive LHM structures. One of the early experiments was carried out by Shelby et al. in [44]. In this experiment, a wedge, or prism, containing a lattice of two concentric SRR particles and wires is fabricated and then radiated with microwave energy. The transmission angle through the prism (i.e. the angle where the maximum forward scattering occurs) is measured. The results of the LHM measurements are compared to the results for a material known to be a RHM.

Figure 17 shows the structure, setup, and results of the measurements carried out in [44]. The transmitted power for the LHM and Teflon samples (Figure 17(c)) are normalized “such that the magnitude of the peaks are unity” [44]. The peaks show a discernible difference in the angle of transmission. For the metamaterial prism, the measured angle of transmission is  $-61^\circ$ ; whereas the Teflon prism shows a transmission angle of  $27^\circ$ . This corresponds to an index of refraction of  $-2.7$  and  $1.4$  for the LHM and Teflon samples, respectively. The refractive indices of the Teflon and LHM samples as a function of frequency ( $f$ ) (Figure 17(d)) show that, while the index of refraction for Teflon is flat across the frequency band, the LHM index shows strong dispersion characteristics. The dotted portion of the black line is the region where the wavelength inside the metamaterial sample became too long to use geometrical optics to characterize the scattering (occurs at  $f > 10.8$  GHz). The authors also note that anywhere  $|n| > 3$ , the electromagnetic wave undergoes total internal reflection. Thus,  $|n| > 3$  can not be measured using these samples [44]. The solid and dotted red lines show the real and imaginary parts of the LHM’s index of refraction calculated using theoretical values for  $\epsilon$  and  $\mu$  in Equation (5). A large imaginary component of  $n$  (i.e. losses) is shown near the resonance band [44].

The results of [44] have generated some controversy and other researchers dispute

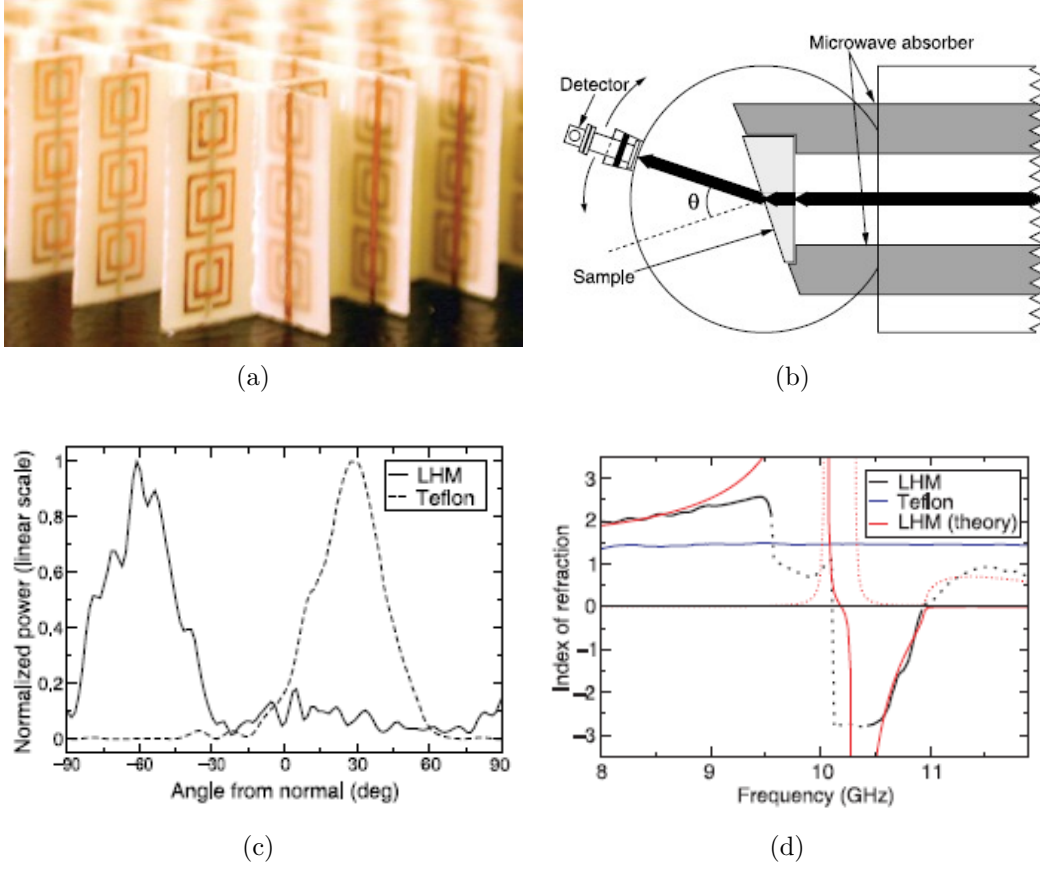


Figure 17. Setup and results of an experiment conducted in [44] to determine the index of refraction for a LHM. (a) The LHM is made up of a metamaterial array with two concentric SRR particles and a wire lattice. (b) The right face of the metamaterial prism is subjected to an incident electromagnetic field. The detector is placed on a pivot on the left face of the metamaterial prism and rotated to determine the refraction angle. The thick black line shows what the refraction through the prism would be if the prism index of refraction is positive. (c) At the metamaterial's resonant frequency of 10.5 GHz, the bulk of the power transmitted through the prism appears at an angle of approximately  $-61^\circ$ . A Teflon sample with a positive index of refraction shows peak transmission at approximately  $27^\circ$ . Note that the two curves are normalized. (d) The measured index of refraction of the Teflon sample (solid blue line) as compared to the measured index of the LHM (black line). The portions of the black line that are dotted are beyond the researchers' ability to accurately measure. Note that the LHM does show a negative index band near 10.5 GHz [44].

the interpretation of the results. Since the theoretical development of [44] does not account for losses in the material, some claim that the results do not show left-handed behavior [12]. Below 30 GHz, the permittivity of the metamaterial sample is largely imaginary, thus the metamaterial acts more like a metal than a dielectric. This will



lead to an inhomogeneous electromagnetic wave that complicates the analysis [12]. The losses due to dispersion are so great at microwave frequencies for this structure that they “swamp any characterization of a net negative real refractive index” [12].

In a later paper [40], these same researchers explain that the losses in the structure will cause the transmitted wave to appear to curve towards the thinner end of the wedge as shown in Figure 18. The transmitted field is stronger at the thinner edge of the wedge because it is attenuated less by the losses in the wedge. In effect, the transmitted field is no longer properly aligned with the center of the wedge complicating angle measurements. To show this, the researchers compare the transmission angle of light passing through a wedge of loss-free glass versus lossy gold. The results show that the beam transmitted through the wedge of lossy material bends toward the smaller end of the wedge and appears to show negative refraction despite the fact that the sample is known to have  $\Re\{n\} > 0$  [40]. To better show negative refraction experimentally, these researchers argue that a flat sample should be used instead of a wedge so that the losses will be uniform across the sample. They also note that increasing the radius of the wires in the metamaterial sample should reduce the amount of losses present [40].

Another group of researchers also performed the prism experiment, but then also

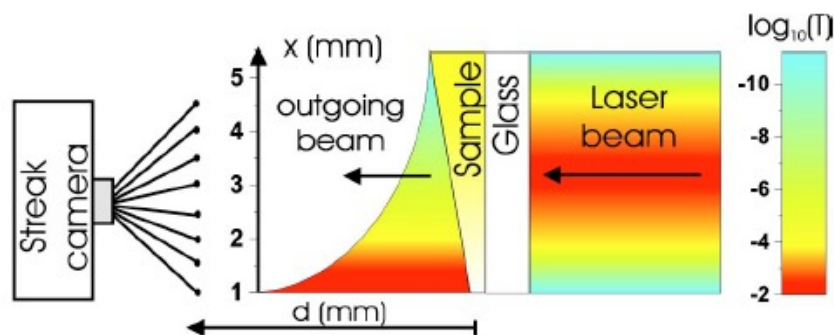


Figure 18. Illustration of light transmission through a wedge made of lossy material. The electromagnetic wave emerging from a wedge-shaped medium with losses will appear to curve towards the smaller end since there will be less losses in that part of the wedge [40].

measured a parallelogram-shaped slab [38]. The geometry of the measurement of the parallelogram-shaped metamaterial slab is shown in Figure 19. The advantage of this geometry is that it allows for an even distribution of loss along the wavefront. The incident electromagnetic field refracts twice—once at each boundary. This causes the beam to shift away from the centerline. This shift, denoted  $d_b$ , is dependent on the index of refraction for the metamaterial slab [38].

The measurement is conducted on different kinds of metamaterial structures: a non-concentric SRR and wire structure, two kinds of omega resonator structures, and a S-shaped resonator structure. The non-concentric SRR and wire structure is most like the structures to be analyzed in this thesis, so it is of prime interest. The metamaterial structure is shown in Figure 20(a). Figure 20(b) shows the results from the measurement. In the resonant frequency band (near approximately 8.7 GHz) the center of the beam shifts to -34 mm. Empty measurements give a reference point  $O$  of -13 mm. Thus the beam shifted -21 mm. The direction of the shift indicates that the index of refraction for the wedge is negative in the resonant frequency band [38].

Chinese researchers conducted free space measurements of a similar double-negative metamaterial structure [48]. The setup and some of the results are shown in Figure 21. For their measurements, alternating circuit boards with square SRRs and wires are arranged vertically (see Figure 21(a)). Horn antennas are used for transmission and reception and are placed on opposite sides of the sample (along the  $x$ -axis in Figure 21(a)). The circuit boards are measured at different rotation angles in the  $xz$ -plane:  $0^\circ$ ,  $30^\circ$ ,  $60^\circ$ , and  $90^\circ$ . The circuit boards are also rotated in the  $xy$ -plane at the same angles in another set of measurements. At each angle, measurements are made with alternating SRR/wire circuit boards, SRR circuit boards only, wire circuit boards only, and no circuit boards [48].

The results for the  $0^\circ$  rotation angle are shown in Figure 21(b). When only

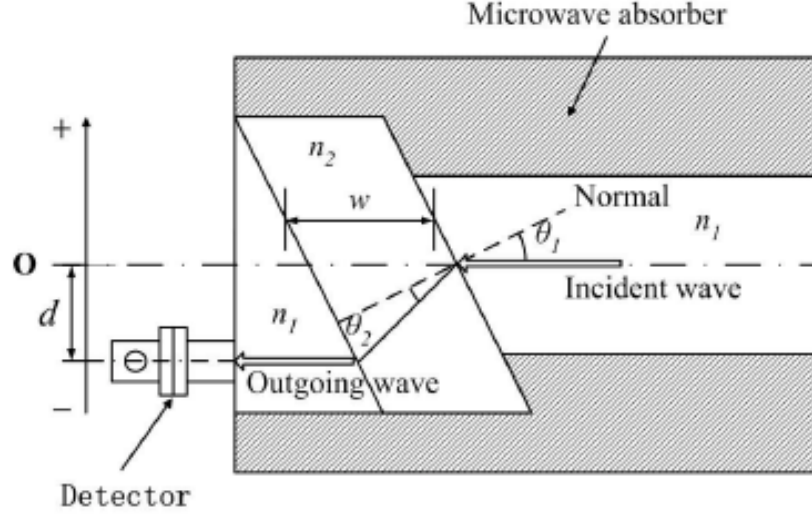


Figure 19. Setup for the measurement of a parallelogram-shaped metamaterial slab. Unlike the wedge-shaped prism, the parallelogram causes an even distribution of loss. The index of refraction for the sample can be determined by the distance the beam is shifted from the centerline [38].

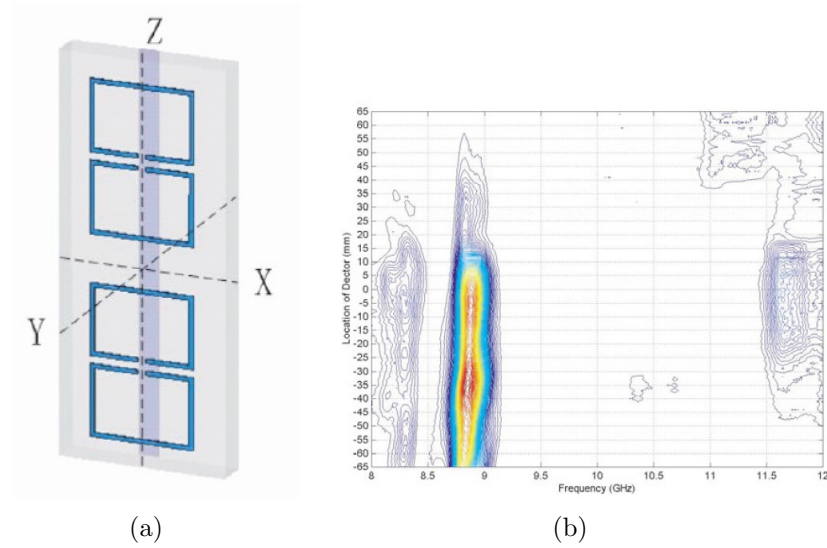
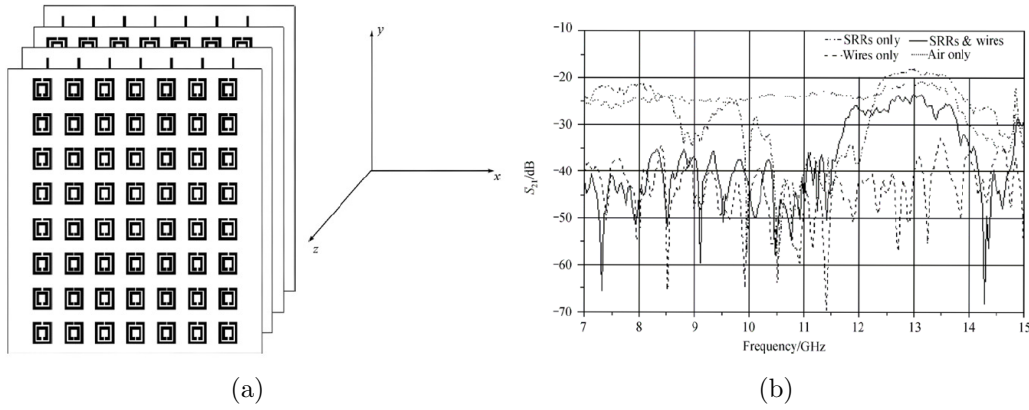


Figure 20. Basic metamaterial structure and results from the measurement of a parallelogram-shaped slab. (a) The basic unit cell consists of a single wire trace and two non-concentric SRR particles. (b) The results from the measurement show that in the resonant frequency band the beam center shifts to -34 mm (-21 mm from the reference point) [38].

the SRR circuit boards are measured, transmission is reduced by approximately 45 dB in the frequency band between 10.5 and 12.0 GHz. When only the wire circuit

boards are present, transmission is reduced throughout the entire frequency band. When both the wire and circuit boards are measured, transmission between 12.0 and 13.8 GHz is close to free space transmission, but reduced throughout the remaining frequency band [48]. The researchers interpret these results to mean that the bands that show reduced transmission in the cases of the SRR circuit boards only and wire circuit boards only indicate that either  $\epsilon$  or  $\mu$  are negative, but not both. They make this claim by stating that the electromagnetic wave can not propagate when only one of  $\epsilon$  and  $\mu$  are negative. In the case where both circuit boards are present, the band between 12.0 and 13.8 GHz can allow propagation because both  $\epsilon$  and  $\mu$  are negative. Outside of that band  $\mu$  is positive, but  $\epsilon$  is negative. Thus the wave can not propagate and transmission is reduced [48]. The results from the various angles shows that rotating the circuit boards affects the behavior of the SRR particles more than the behavior of the wire particles [48].



**Figure 21. Setup and transmission measurement results of a DNG metamaterial [48].** (a) The setup consists of separate circuit boards containing SRR particles and wire elements. The incident electric field propagates along the  $x$ -axis, and  $E$  is aligned along the  $y$ -axis. Measurements are made with the alternating SRR and wire circuit boards, SRR circuit boards only, wire circuit boards only, and no circuit boards. The angle of incidence is also varied. (b) The results for  $0^\circ$  incidence show reduced transmission in a frequency band for any of the configurations with one of the metamaterial circuit boards [48].

The research efforts presented in this section have generated many interesting results. However, they differ from the experiments conducted in this section for several

reasons. The experiments performed in [44] and [38] are performed in a guided-wave environment. The measurements in [48] include free-space measurements, but their analysis is limited to just beam shifting. All three papers focus on transmission results and do not look at reflection.

The measurements of traditional metamaterial structures in this paper utilize free space RCS measurements. The RCS measurement techniques used here allow for quick measurements at different incidence angles. With the addition of standard RCS postprocessing techniques, the results from the measurements in this thesis also reveal information about the phase, and, with further refinement, may be able to determine the location of the scattering centers. This will help to reveal the mechanism (for example, refraction or surface wave) causing the radiation pattern.

## 2.5 Achieving Frequency Adaptability

Many different methods for implementing frequency adaptability in metamaterial structures have been proposed recently. Most of them focus on affecting the resonant frequency of the particle. The particle is usually a SRR with inductance  $L$  and capacitance  $C$ . The particle's resonant angular frequency is given in the microwave frequency regime by [17]

$$\omega_0 = \frac{1}{\sqrt{LC}}. \quad (35)$$

The capacitance and inductance of an SRR is dependent on the material it is made of as well as its dimension and shape. For a SRR made of a PEC material,  $L$  and  $C$  can be approximated using [49]

$$L \approx \mu_0 \frac{\ell}{4} \ln \left( \frac{8l}{w+h} \right), \quad (36a)$$

$$C \approx \epsilon_0 \frac{wh}{\delta}, \quad (36b)$$

where  $h$  is the thickness of the SRR,  $l$  is the length of the SRR, and  $w$  and  $\delta$  are shown in Figure 22. Note the use of Equation (36b) assumes the capacitance of the gap can be approximated with the model for a parallel-plate capacitor. While the assumption may not be valid in all scenarios, Equation (36b) can be used for illustrative purposes.

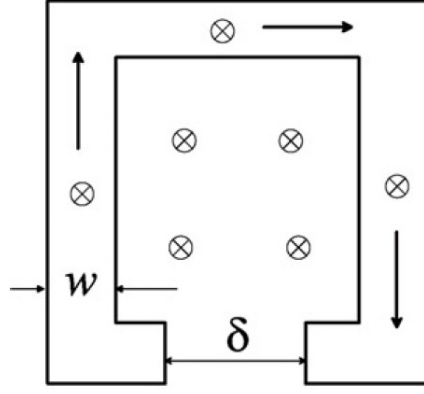


**Figure 22. Dimensions of a SRR particle.** The thickness of the particle (into the page) is denoted as  $h$ ; while the length of the SRR is denoted as  $l$  [49].

Current attempts to introduce frequency adaptability into SRR structures focus on manipulating the inductance or capacitance of the circuit to change the resonant frequency of the structure. Gollub et al. in [14] show that the effective inductance of the structure can be influenced by incorporating a magnetic layer in the material. Conversely, Gil et al. in [13] and Shadrivov et al. in [43] propose structures that make use of a varactor diode to control the capacitance of the structure. Shadrivov et al. in [42] propose similar structures that make use of changes in field intensity to enhance or suppress wave transmission. Han et al. in [16] propose the use of semiconductor materials for the SRR allowing control of the resonant frequency through

the application of an external magnetostatic field. A tunable metamaterial structure that utilizes a MEMS switch to change the capacitance of the SRR is proposed by Hand and Cummer in [17]. The following sections will look at these proposals in more detail.

### 2.5.1 Magnetic Circuits.

The structure proposed by Gollub et al. combines the dispersive properties of the metamaterial structure with the dispersive properties of a magnetic layer. The basic structure is shown in Figure 23. The additional magnetic layer introduces an approximately perpendicular magnetic field in the gap at resonance [14].

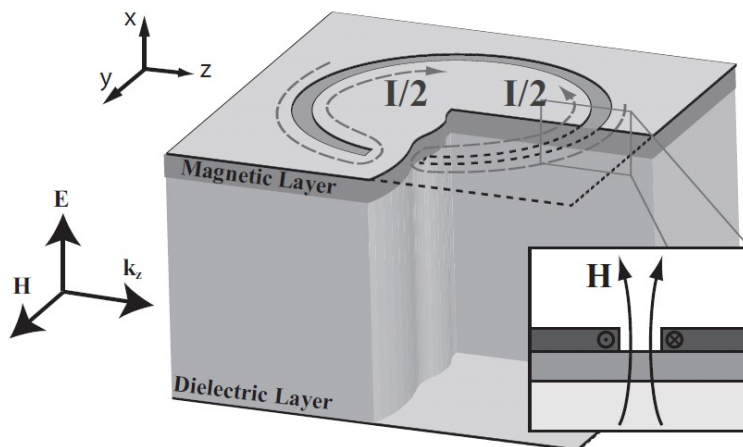


**Figure 23.** Unit cell structure that utilizes a magnetic layer. Inset: A magnetic field that is approximately perpendicular is produced in the gap of the magnetic material at resonance [14].

The magnetic field changes the equivalent inductance of the structure. The new inductance  $L$  is given by [14]

$$L = \mu_0 \left( \frac{\mu_r(\omega)}{\mu_r(\omega)(1 - q) + q} \right) g_{geom}, \quad (37)$$

where  $\mu_r$  is the relative permeability of the magnetic material and  $q$  is the volume fraction of the frequency dependent magnetic material. The new resonance frequency

$(\omega'_0)$  is found by substituting the new expression for inductance from Equation (37) into Equation (35) yielding [14]

$$\omega'_0 = \frac{1}{\sqrt{\frac{\mu_r(\omega'_0)}{\mu_r(\omega'_0)(1-q)+q}}} \omega_0. \quad (38)$$

Gollub et al. go on to show that by tuning the biasing field of the magnetic material, the resonance frequency of the metamaterial structure can be adjusted. They then went on to validate their findings through simulation using the Ansoft HFSS finite element solver. The results of the analysis for bias values 0 kilogauss (kG), 1 kG, 2 kG, and 3 kG are shown in Figure 24. The resonance bands are characterized by the drops in transmission. From the plots in Figure 24 it is clear to see that the resonance frequencies are indeed dependent on the bias values.

While there are non-metamaterial structures that make use of magnetic materials to make tunable microwave devices, the proposed structure has a larger range of material properties and can function in a larger resonance band. Furthermore, the combined effects of the metamaterial structure and magnetic layer would require less material than a similar device that did not implement a metamaterial structure [14].

### 2.5.2 Varactor-Loaded Circuits.

Gil et al. propose the use of a varactor-loaded SRR in the design of a tunable notch filter. Their proposal utilizes a square-shaped geometry to increase the coupling between the line and ring. Their design incorporates a varactor diode between the inner and outer rings as shown in Figure 25. The structure's overall effective capacitance is dominated by the varactor's capacitance. By using a tunable diode, the resonant frequency of the structure can be changed to block transmission at certain frequencies [13].

By adjusting the bias applied to the structure, the resonant points shift in fre-



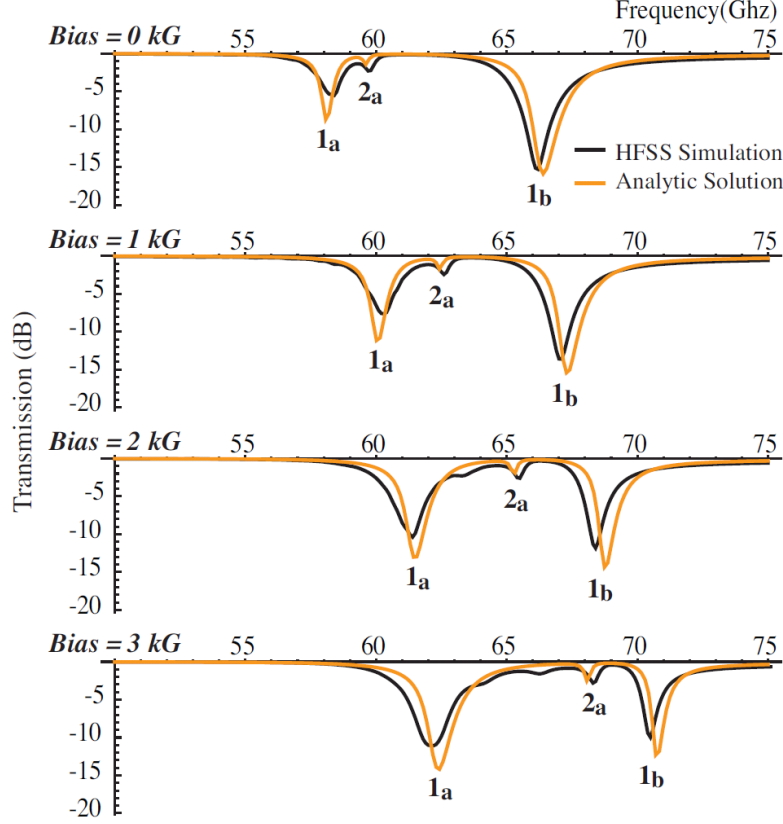
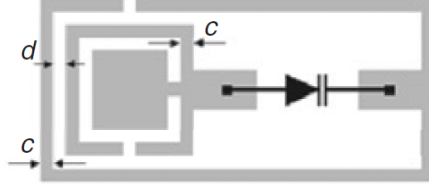


Figure 24. Results from the analysis of the SRR structure with magnetic layer. The transmission results are shown for four different bias values: 0 kilogauss (kG), 1 kG, 2 kG, and 3 kG. The resonant frequencies are the drops in transmission. Note that the location of the resonance frequencies are dependent on the bias values [14].

quency. Figure 26 shows the results of measurements of the structure's transmission coefficient under different bias conditions. The bias voltage changes the capacitance of the varactor diode circuit. This has a large impact on the overall effective capacitance of the circuit. The different locations of the resonant points in Figure 26 at each of the bias voltages is evidence of the ability to tune the proposed structure to different frequencies [13].

Shadrivov et al. also propose a structure that implements a varactor diode to control the capacitance of the circuit. However, their design differs in the placement of the diode. Whereas Gil et al. placed the varactor between the outer rings, Shadrivov et al. propose placing the varactor diode in series with the distributed capacitance



**Figure 25.** SRR structure proposed by Gil et al. A varactor diode is placed between the inner and outer rings [13].

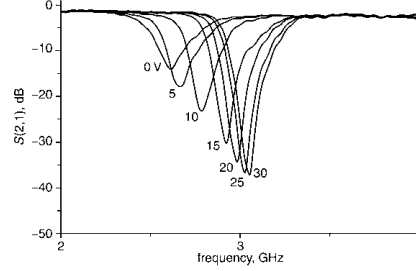


**Figure 26.** Measured transmission coefficients for the varactor-loaded SRR structure proposed by Gil et al. The different curves show the results at the different bias conditions used. Note that the resonant frequency depends on the bias voltage that controls the capacitance of the varactor diode circuit [13].

of the outer ring. This is achieved by adding an additional gap in the outer ring and placing the varactor across it. They show that this structure also allows for tunability of the transmission response by changing the bias voltages. For example, they show that with a negative bias voltage of 10 V, the resonant frequency is 2.9 GHz. With a positive bias of 1 V, the resonant frequency is 2.27 GHz [43].

Shadrivov et al. go on to show that the bias of the diode can be controlled by the incident electromagnetic field [43]. These results demonstrate the structure's ability to respond dynamically to an incident electromagnetic wave. In [42], Shadrivov et al. extend the study of this structure with experimental waveguide measurements. Their proposed design is applied to the metamaterial array shown in Figure 27.

The results from waveguide measurements of this varactor loaded structure are shown in Figure 28. The source power influences the bias of the diode that, in turn, changes the capacitance of the structure and ultimately, the resonance frequency of

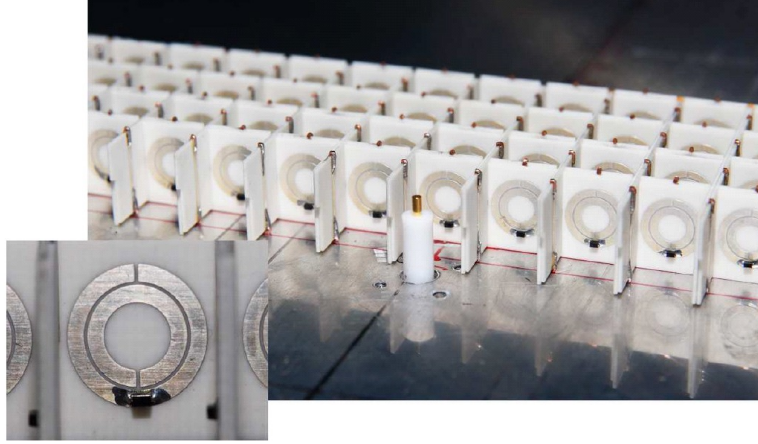


**Figure 27.** An array of SRR metamaterial structures that contain varactor diodes to allow for frequency adaptability. Inset: A closeup of an individual cell. The varactor diode is the small structure attached at the bottom of the outer ring [42].

the metamaterial. The result is a structure that can adapt based on the power carried by the incident electromagnetic field [42].

### 2.5.3 Semiconductor Split Ring Resonators with Magnetostatic Fields.

Han et al. also demonstrate frequency adaptability with a proposed design where the SRRs are made of a semiconductor material instead of metal. Their structure varies significantly in geometry from the previous designs. Concentric rings are replaced by the structure shown in Figure 29.

The use of semiconductor material in the SRR changes the relative permittivity of the structure. The new relative permittivity ( $\epsilon_r$ ) is given by [16]

$$\epsilon_r(\omega) = \epsilon_\infty - \frac{\omega_p^2}{\omega^2 + j\gamma\omega}, \quad (39)$$

where  $\epsilon_\infty$  is the high-frequency relative permittivity value,  $\omega_p$  is the plasma frequency, and  $\gamma$  is the damping constant.

Han et al. propose the introduction of an external magnetostatic field to control

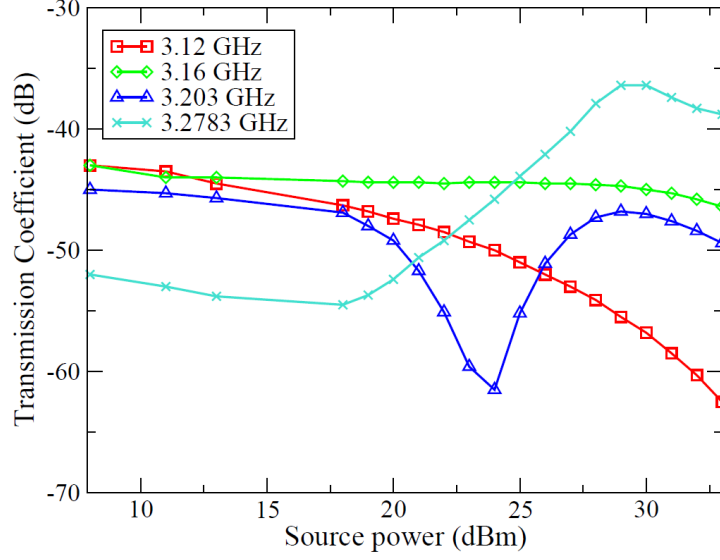


**Figure 28.** Waveguide measurement results for the design proposed by Shadrivov et al. The transmission coefficient as a function of source power is shown for four different frequencies [42].

the response of the structure. They show simulation results for various incident configurations. In the Faraday configuration, the magnetostatic field is aligned parallel to the wave vector of the incident field. In that case, the resonant frequency decreases as the amplitude of the magnetostatic field increases [16]. In the Voigt configuration, the magnetostatic field is aligned perpendicular to wave vector of incident wave. Two cases were analyzed in the Voigt configuration:

- when the magnetostatic field is perpendicular to the electric field the resonant frequency decreases with increases to the intensity of the magnetostatic field (similar to the Faraday configuration); and
- when the magnetostatic field is parallel to the electric field, the intensity of the magnetostatic field has no effect on the resonance of the structure [16].

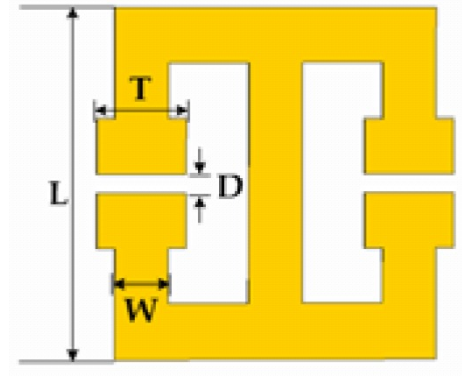


**Figure 29.** Geometry of a tunable metamaterial structure that contains SRRs made of semiconductor material [16].

#### 2.5.4 SRRs with MEMS Switches.

Hand and Cummer propose a metamaterial element with frequency adaptability by the inclusion of a MEMS switch in either a series or parallel configuration. Equivalent circuits for the series configuration are shown in Figure 30. When the switch is open, there is an additional capacitance ( $C_s$ ) and resistance ( $R_s$ ) due to the MEMS switch itself. When the switch is closed,  $C_s$  is shorted out. In this configuration, the MEMS switch allows the particle to resonate at two different resonant frequencies [17].

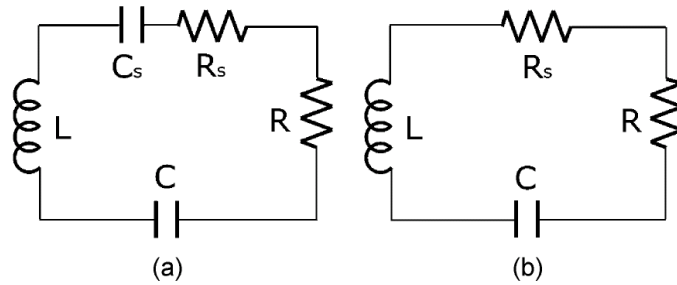


**Figure 30.** Equivalent circuits for a SRR element with a MEMS switch in the series configuration. (a) The capacitance ( $C_s$ ) and resistance ( $R_s$ ) of the switch are in series with the capacitance of the SRR ( $C$ ) when the switch is open. (b) When the switch is closed,  $C_s$  is removed from the circuit, but  $R_s$  remains [17].

The parallel configuration has the equivalent circuit depicted in Figure 31. There is an additional capacitance ( $C_s$ ) and resistance ( $R_s$ ) due to the switch when it is

open, but now they are parallel with the capacitance of the SRR ( $C$ ). When the switch is closed,  $C_s$  again disappears. In this configuration, the open-state yields resonance at a certain frequency, while the closed-state has no resonance at all [17].

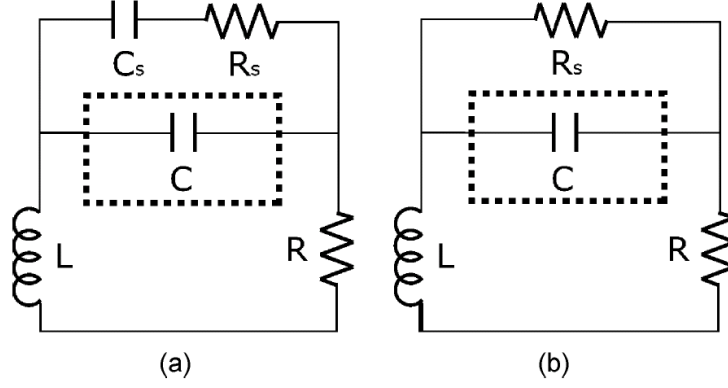


**Figure 31. Equivalent circuits for a SRR element with a MEMS switch in the parallel configuration. (a) The capacitance ( $C_s$ ) and resistance ( $R_s$ ) of the switch are in parallel with the capacitance of the SRR ( $C$ ) when the switch is open. (b) When the switch is closed,  $C_s$  is removed from the circuit, but  $R_s$  remains [17].**

Hand and Cummer measured both configurations in a waveguide. The results of the SRR with the series switch are shown in Figure 32(c). As expected, the resonant frequency shifts when the MEMS switch changes states. In the closed state, the resonant frequency is approximately 2.04 GHz; whereas the resonant frequency of the open state is over 2.9 GHz [17]. The results of the parallel configuration are shown in Figure 32(d). In the open state, the resonant frequency is 2.26 GHz. However, as mentioned above, the closed state shows no resonant behavior [17].

The parallel configuration also demonstrates the difficulty of scaling the frequency response outside of a small band. As the size of the ring decreases, the capacitance decreases as well. Below a certain size, the capacitance of the gap approaches the capacitance of the switch. Therefore, to make use of this design at higher frequencies, the switch capacitance needs to be reduced [17].

### 2.5.5 Adaptive Metamaterial Literature Summary.

The research efforts on adaptive metamaterials presented in this chapter show different ways to manipulate the resonant frequency of the metamaterial structure. However, these efforts differ from the approach taken with this research vector. The metamaterial design in [14] relies on the introduction of a magnetic material to adjust the resonant frequency. In [13], the authors propose a design that employs a varactor capacitor to adjust the resonant frequency. However, the varactor diode is quite large. The authors of [42] propose a similar design with a varactor diode. Their diode, however, is controlled by the incident electric field. The varactor diode adjusts automatically to the incident field. The metamaterial design in [16] is also dependent on the incident electromagnetic fields. Like the design proposed in this thesis, the structures in [17] use a MEMS device to control the resonance of a SRR particle, but their MEMS device is a switch and not a variable capacitor.

The metamaterial design proposed in this thesis uses a MEMS variable capacitor that has six different states. It has a small footprint that is fabricated as part of the SRR elements and is not dependent on the incident electromagnetic field.

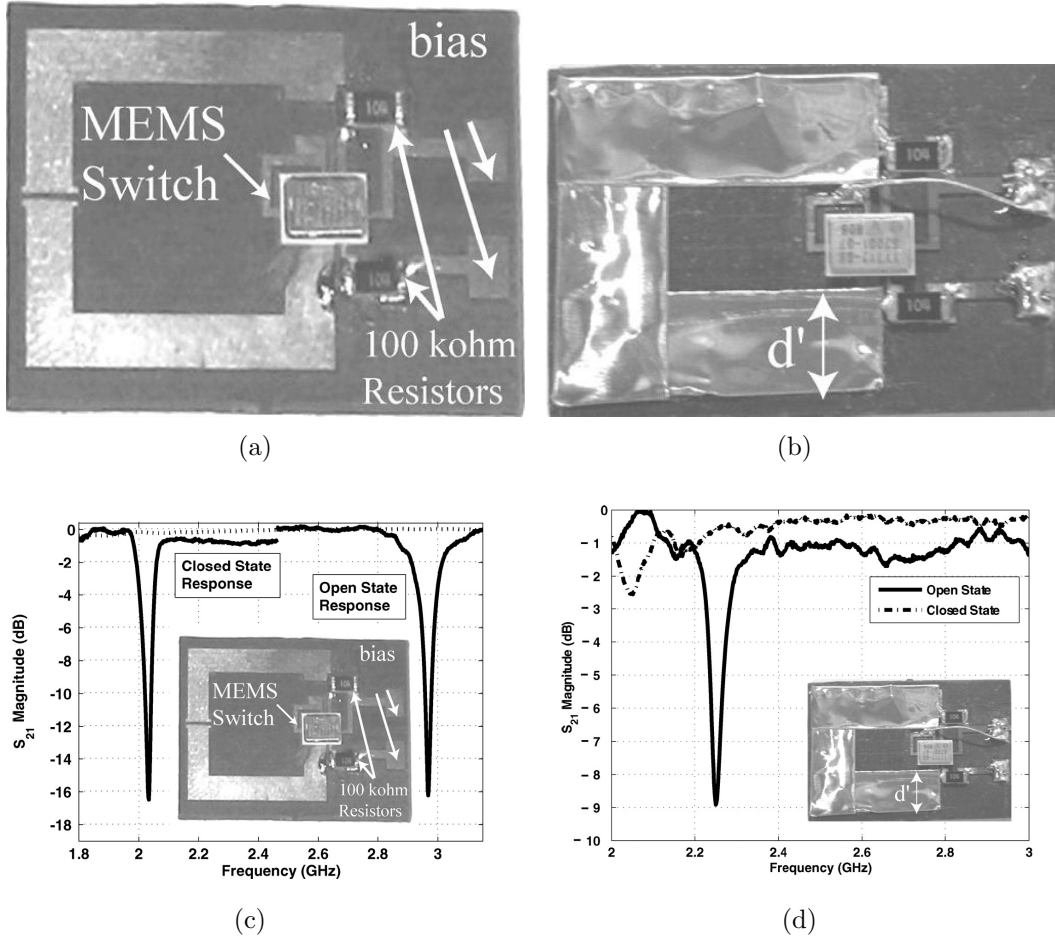


Figure 32. Results from measurements of the metamaterial structures implemented by Hand and Cummer. (a) Photograph of the series configuration circuit used. (b) Photograph of the parallel configuration circuit used. (c) For the series configuration, the open state shows the expected resonant behavior at over 2.9 GHz. The closed state lowers the resonant frequency down to approximately 2.04 GHz. (d) For the parallel configuration, the open state (solid line) shows the expected resonant behavior at approximately 2.26 GHz. The closed state (dash-dot line) shows no resonant behavior [17].



## III. Calculations and Computational Models

### 3.1 Chapter Overview

The purpose of this chapter is to describe efforts to model metamaterial structures using CST MWS®. As described in Section 2.3, CST MWS® employs the FIT. The models presented here are for the purposes of

- determining effects of model size on computational time,
- recreating results in published articles,
- characterizing a metamaterial wedge, and
- calculating the bandwidth of the AFIT adaptive metamaterial design as well as it's expected behavior in a waveguide.

The models presented in this chapter are an important piece of this research effort. The use of these models should provide insight into the physical phenomena that give metamaterial structures their unique properties. However, in order to increase confidence in the modeling process, basic benchmark comparisons are presented. The results of published efforts are recreating using the modeling process of this thesis. The results of this modeling process agree with the published results.

The electric field results from the models of the metamaterial wedge show the reflection, transmission, and attenuation of the incident fields on the structure. In turn, these phenomena aid in the interpretation of farfield results. The farfield results from the models presented in this section predict the measurement results of Chapter IV.

The models of the adaptive metamaterial structures presented in this chapter are a solid foundation on which to base future designs. The results of this modeling effort

show that introducing an additional variable capacitor at the gaps of the SRR particles is an effective method of changing the resonant frequency of the metamaterial device. Furthermore, the scale of the metamaterial structure is a key determinant of the resonant frequency. In this chapter, scaled versions of the AFIT adaptive structure are presented that accommodate a larger stripline. The models also accurately predict the measurement results, showing that the computing techniques used in this thesis can greatly aid the systems engineering process by reducing the cost and length of the design cycle.

### 3.2 Calculation Time Studies

The trade off between model size and the time required to perform the model computations is of major concern. Larger models require larger meshes. This in turn increases the amount of calculations the model has to perform. Tools like periodic boundary conditions can help reduce the size of the computational domain. However, periodic boundary conditions can also place constraints on what can be modeled. For example, edge effects and grazing incidence can not be modeled with periodic boundary conditions because the source would be located in the infinite array. Information on the different kinds of boundary conditions is located in Section 2.3.2.

In order to get an idea of the trade offs between computation time and model size, different-sized structures were modeled with CST MWS®. The structure chosen for the basis of the model is the frequency selective ring resonator from the CST MWS® frequency selective surface tutorial. Figure 33(a) shows the single cell structure. To create the different-sized models, the ring resonator structure was mirrored a number of times in each direction to create a square matrix of ring resonators. Figure 33(b) shows a  $4 \times 4$  array.

The frequency domain solver was used for these tests. Though the field values

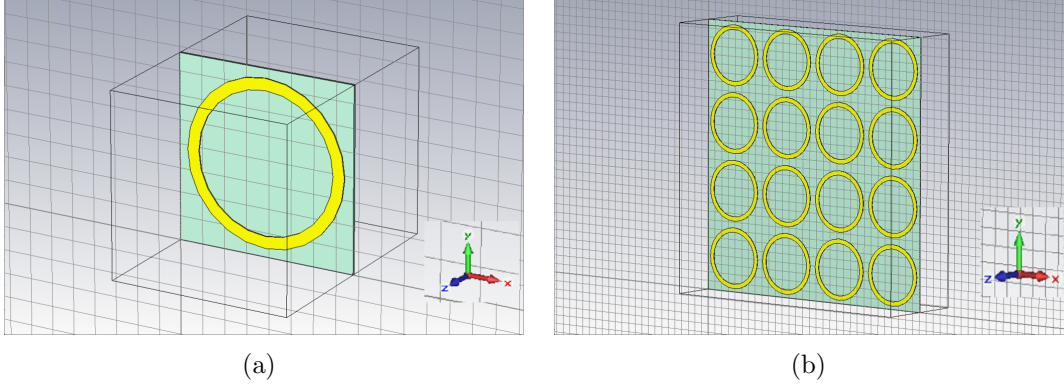


**Figure 33.** Ring resonator models used as time studies. (a) The single cell ring resonator structure from the CST MWS® tutorial was the basis for the time study. (b) A  $4 \times 4$  ring resonator structure.

are not of particular concern for this structure,  $\mathbf{H}$  and RCS monitors were created to simulate increased computational requirements. The solver times were retrieved from the log files created by the frequency domain solver. The results are shown in Table 2.

**Table 2.** Computational time for various ring resonator model sizes.

Elements Per Side	Boundary Conditions	Incident Angle	Computation Time
1	Unit cell	Normal	174 s
1	Open	Grazing	112 s
2	Open	Grazing	185 s
3	Open	Grazing	316 s
4	Open	Grazing	749 s
6	Open	Grazing	2140 s

All of the computations for this thesis were completed using the workstations in the AFIT LOREnet. The computers are Dell Precision 690™ Workstations with Quad 3.00 GHz Intel Xeon® processors and 32 GB of RAM. All workstations run Microsoft Windows® XP Professional x64. Note that this study was completed before the upgrade to 32 GB of RAM (the workstations had 20 GB of RAM when it was run). For the rest of the models presented in this thesis, the computers had 32 GB of RAM.

The results of the time study show that large computations can be carried in a relatively timely manner. Modeling of large arrays of structures can be accomplished with CST MWS®. For comparison purposes, the calculation times of the more advanced models used in this thesis are shown in Table 17 of Appendix A. Despite running some very large simulations, the calculation times were all reasonable. For example, the largest model has just over 1.5 million mesh cells, but CST MWS® calculated the solutions for four different runs in under two days.

### 3.3 Model Validation and Comparisons

In order to increase confidence and improve modeling techniques, a couple of models were recreated from published results to serve as benchmarks for the modeling process. This section describes the efforts and results. Two published models were recreated. The first model was from the symmetric structure described by Smith et al. in [47]. The second model was a structure that was described, fabricated, and tested by Hand and Cummer in [17]. The results from CST MWS® of both models match the published results. However, there are slight differences most likely caused by different modeling parameters and dimensional tolerances. These differences are discussed in the following sections.

#### 3.3.1 Modeling 2005 Smith et al. structure.

The structure modeled by Smith et al. in [47] (see Figure 12 in Section 2.3.4.1) was recreated in CST MWS® and is shown in Figure 34(a). To match the model presented in [47], periodic boundary conditions are used in the  $x$ - and  $y$ -directions. The electromagnetic wave is incident from the  $z$ -direction. Figure 34(b) shows the boundary conditions. The excitation signal is the default Gaussian pulse for the frequency solver. The pulse is centered is about 0.178 ns in duration with the peak at

0.887 ns. The peak of the pulse has a magnitude of 1 and it crosses 0.5 magnitude at about 0.069 and 0.109 ns. The frequency solver is used to perform a frequency sweep from 0 to 20 GHz. The incident mode is transverse electromagnetic (TEM) with  $\mathbf{E}$  vertically directed. The computational mesh for this model is shown in Figure 106(a) of Appendix A.

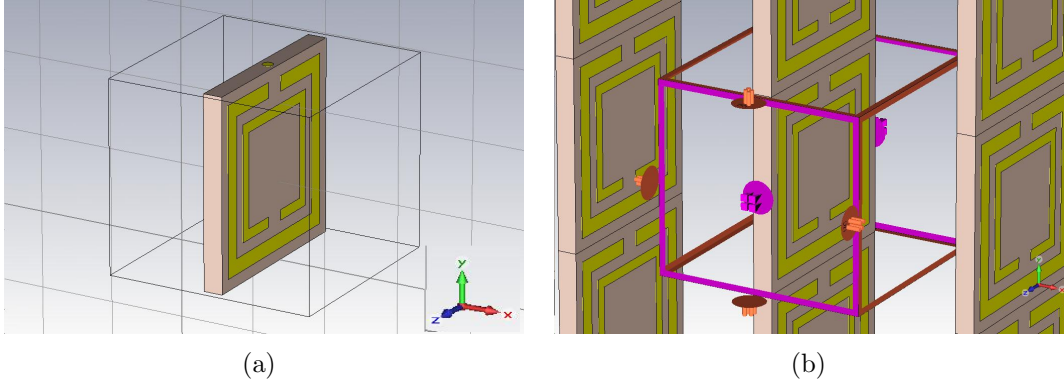


**Figure 34.** CST MWS® model of the structure presented in [47]. (a) The basic structure of the SRR consists of a wire and two concentric split rings. (b) Periodic boundary conditions are used in the directions transverse to propagation to simulate an infinite array.

The results from the simulation in CST MWS® are shown in Figure 35. They are in good agreement with the published results shown in the insets of Figure 35 (also see Figure 13 in Chapter II). The index of refraction, impedance, relative permittivity, and relative permeability were extracted using the method described in Section 2.3.5 with the MATLAB™ described in Appendix C. However, care must be exercised in choosing the time convention. Smith et al. use a  $e^{j\omega t}$  time convention whereas CST MWS® uses the  $e^{-j\omega t}$  convention. Once the proper adjustments are made, the results from the CST MWS® model match the results published in [47].

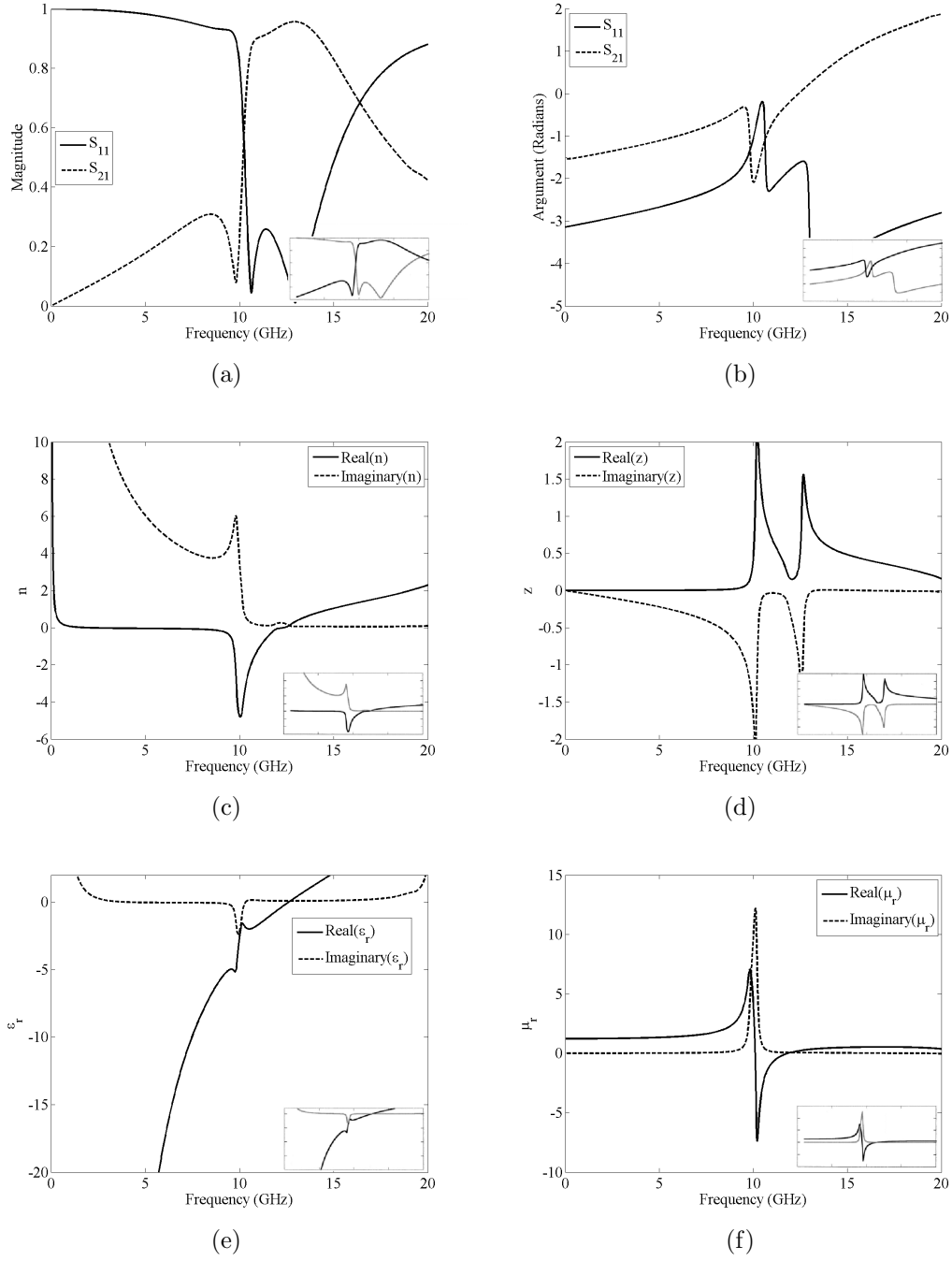


**Figure 35.** Results from the simulation of the structure in [47]. The insets show the results published in [47] (see Figure 13). (a) The magnitude of the  $S$ -parameters match the values found by Smith et al. (b) The phases of the  $S$ -parameters match as well. The index (c), impedance (d), permittivity (e), and permeability (f) were extracted using the method described in section 2.3.5. They match the published results.

### 3.3.2 Modeling 2007 Hand and Cummer structure.

The structures presented by Hand and Cummer in [17] are designed to provide frequency adaptability. The theory behind this implementation is explained in Section 2.5.4. A MEMS switch is placed in different locations in order to modify the capacitance of the SRR. The angular resonant frequency for this structure is given by Equation (35)

In the series configuration, a new gap in the SRR is created on the opposite side from the original gap. A MEMS switch is placed over the gap. When the switch is closed, the gap is electrically shorted. This has the effect of removing the additional gap. When the switch is open, a series capacitance is generated at the additional gap. Recall that the equivalent capacitance ( $C_{eq}$ ) of two series capacitors is calculated using [18, 133]

$$C_{eq} = \frac{C_{VC}C}{C_{VC} + C}, \quad (40)$$

where, in this case,  $C_{VC}$  represents the capacitance of the variable capacitor. Dividing the top and bottom of the right-side of Equation (40) by  $C_{VC}$  yields

$$C_{eq} = \frac{C}{1 + C/C_{VC}}. \quad (41)$$

When the capacitance of the variable capacitor increases, the denominator of right side of Equation (41) decreases. This means that the equivalent capacitance increases. The capacitance of the SRR is decreased when the switch is open. Therefore, by Equation 35 the resonant frequency increases. The series configuration switch allows the metamaterial structure to switch between two different resonant frequencies [17].

Hand and Cummer fabricated the structure and measured it in a waveguide. They first started with the basic SRR structure shown in the inset of Figure 36. They

designed the structure to have a resonant point at 2.2 GHz. This corresponds to the design parameters shown in Table 3. The substrate thickness is 1 mm, and it is made of Rogers Duriod material. Its properties are also shown in Table 3 [17].

**Table 3. SRR design parameters for structure proposed in [17].**

Parameter	Symbol	Value
Side length	$a$	16 mm
Trace width	$d$	2.5 mm
Gap width	$g$	0.3 mm
Substrate relative permittivity	$\epsilon_r$	2.2
Substrate loss tangent	$\tan \delta$	0.0009

Figure 36 also shows the transmission results. The dip in  $S_{21}$  shown in Figure 36 confirms the resonance point occurs at 2.2 GHz [17].

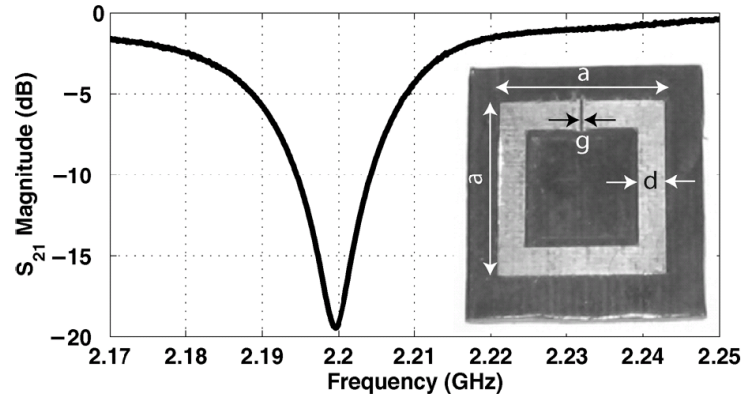


**Figure 36. Results from measurements by Hand et. al. of the SRR circuit without the MEMS switch. The resonant frequency is approximately 2.2 GHz. Inset: Photograph of SRR circuit used [17].**

The inset of Figure 32(c) in Section 2.5.4 shows a picture of the SRR circuit with the series MEMS switch. Aside from the additional gap and MEMS switch, the structure is identical to the SRR without the switch. Figure 32(c) shows the transmission results with the switch in both the open- and closed-states. As expected, the 2.9 GHz open-state resonance frequency is higher than the resonance frequency of the SRR with no switch. The closed-state resonance did drop slightly compared



to the resonance frequency of the SRR without a switch, despite having the same equivalent circuit model. This is due to parasitic capacitances introduced by the MEMS-loaded circuit [17]. As noted in Section 2.5.4, Hand and Cummer also present a parallel switch configuration where the MEMS switch is placed over the original gap allowing the metamaterial structure to turn on and off. That circuit was not modeled in CST MWS®.

The structure presented in [17] was modeled in CST MWS®. The structure is shown in Figure 37. The additional gap is shown at the top of the drawing. The boundary conditions in the  $y$ -directions (top and bottom planes) are PEC. Open boundary conditions are used in the  $x$ -direction. The waveguide ports are  $z$ -oriented as shown. The blue device is the lumped network element used to model the MEMS switch. The structure was modeled with a high frequency tetrahedral mesh. Figure 37 shows the structure of the series configuration model, and Figure 106(b) in Appendix A shows the tetrahedral mesh. The configuration without the switch is similar.

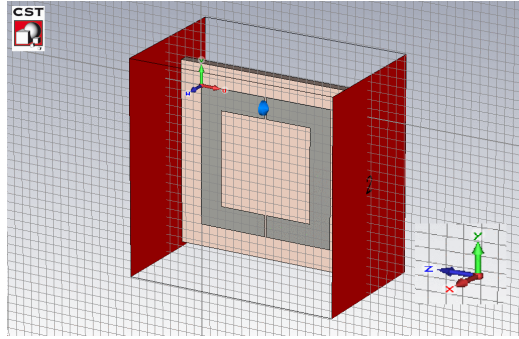


**Figure 37.** CST MWS® model of the structure presented in [17]. The basic structure of the SRR with the switch consists of a split ring resonator with gaps on two ends. The gap with the lumped network element (top) represents the MEMS switch. The SRR model without the MEMS switch is similar but is modeled with no extra gap or lumped network element.

The frequency domain solver was used to perform a sweep from 0 to 5 GHz. The lowest order mode that will propagate given the boundary conditions is chosen as the excitation. This corresponds to TEM with  $\mathbf{E}$  vertically polarized.

The results from the SRR without the switch as well as the SRR with the switch are shown in Figure 38, and the resonant frequencies are shown in Table 4. The overall shapes of the curves match those shown in Figures 36 and 32(c). The resonant frequencies differ slightly. Some of this may be due to differences in the model and their measurement setup. The difference in the resonant frequency of the open-switch configuration is partly due to the use of the lumped network element versus a model of the actual switch.

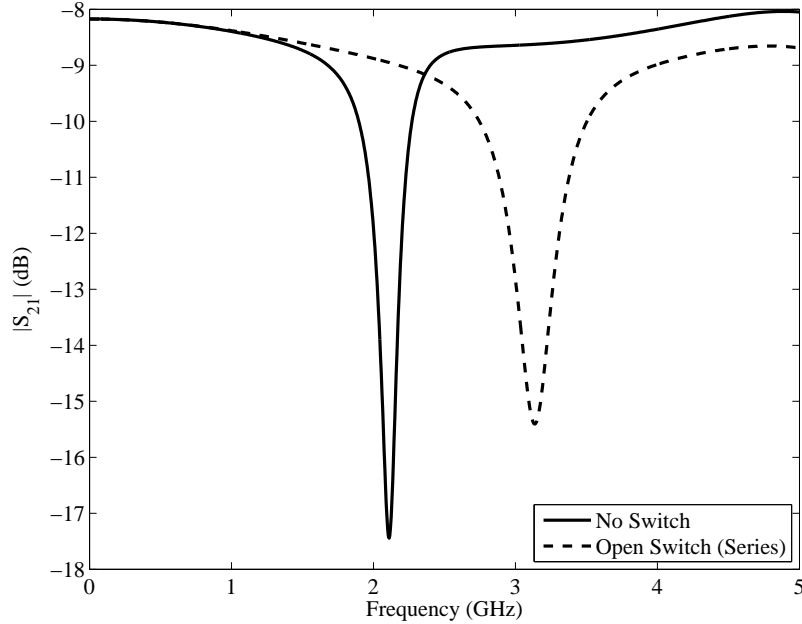


**Figure 38.** Transmission results (magnitude of  $S_{21}$  in dB) from the CST MWS® simulation of the structure in [17]. The results are similar to those published in the paper (See Figures 36 and 32(c)).

The results shown in these sections help to validate the approach to modeling metamaterial structures with CST MWS®. Slight differences in the results can be at

**Table 4.** Resonant frequencies ( $f_0$ ) published in [17] versus those found with CST MWS®.

Configuration	Published $f_0$	$f_0$ Found with CST	Error
No switch	2.2 GHz	2.1 GHz	4.5%
Series switch open	2.9 GHz	3.1 GHz	6.9%

least partially explained by differences in the setup of our model versus their model or experiment. But it is important to note that these results demonstrate the same behavior as those in the published works.

### 3.4 Metamaterial Wedge Models

A metamaterial wedge was obtained by AFIT for analysis. The metamaterial unit cell structure contains three basic particles: two concentric SRRs and a wire trace. The dimensions of the particles have been adjusted to create a resonance point near the X- and Ku-bands. The metamaterial cells were fabricated into the wedge shown in Figure 4 of Chapter I. The dimensions of the wedge's unit cell are shown in Figure 39.

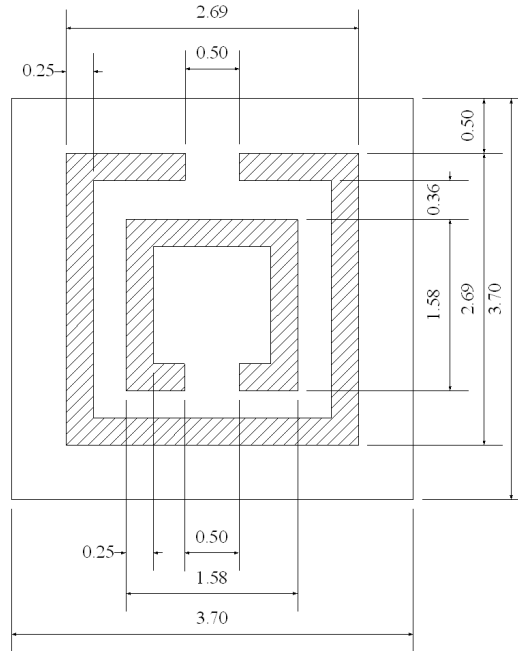


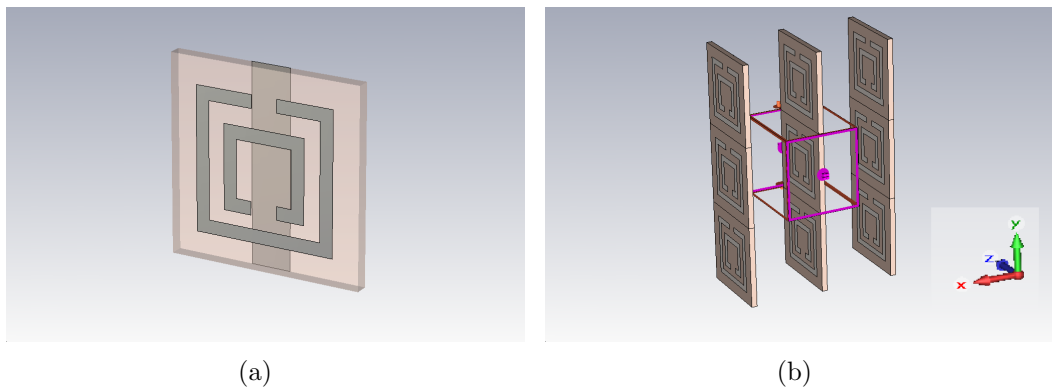
**Figure 39.** The dimensions of the metamaterial wedge's unit cell. All dimensions are in mm. Not shown is the 0.76 mm wide flat wire trace that is on the backside of the dielectric board containing the SRRs.

The proposed measurement technique for this wedge involves bistatic RCS measurements. More details on the measurement process can be found in Chapter IV. In

order to predict the measurements and understand the resulting phenomena, several theoretical and computational models are developed and analyzed in the following sections.

### 3.4.1 Unit Cell Model.

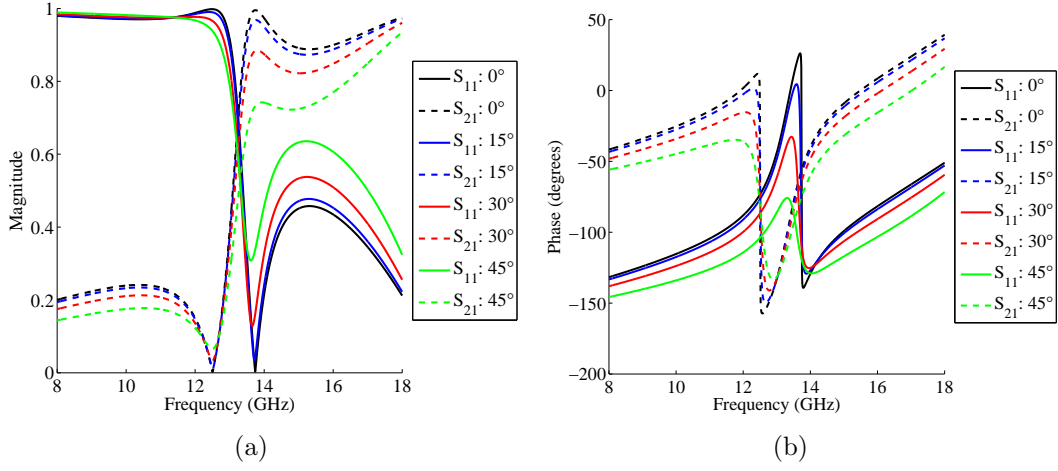
The unit cell model of the metamaterial wedge is calculated using CST MWS®. The setup of the model is shown in Figure 40. The metal for the SRR particles and wire traces are modeled as infinitely-thin PEC material. The dielectric board is a Taconic TLY-5 circuit board with a thickness of 0.25 mm, dielectric constant of 2.2, and loss tangent of 0.001. The media surrounding the circuit board is modeled as free space. In the actual wedge, there is an Emerson Cumming Eccostock PP-2 dielectric media between the boards. It has a dielectric constant of 1.03 and loss tangent of 0.0001. Modeling it as free space should provide enough model accuracy. Mesh statistics for the  $0^\circ$  incident angle are shown in Table 15 and the mesh is shown in Figure 107 of Appendix A. The other incident angles produce similar meshes.



**Figure 40.** CST MWS® model of the metamaterial unit cell. (a) The unit cell is modeled according to the dimensions shown in Figure 39. The wire trace on the backside of the dielectric board is visible. (b) Periodic boundary conditions are used in the  $x$ - and  $y$ -directions. The  $z$ -directed boundary conditions are the Floquet ports.

Figure 41 shows the  $S$ -parameter results from the simulation at incident angles of  $0^\circ$ ,  $15^\circ$ ,  $30^\circ$ , and  $45^\circ$ . The solid lines represent  $S_{11}$  while the dashed lines represent  $S_{21}$ .

The data suggest that the incident angle impacts the magnitude of the  $S$ -parameters, but not the location of the resonance.



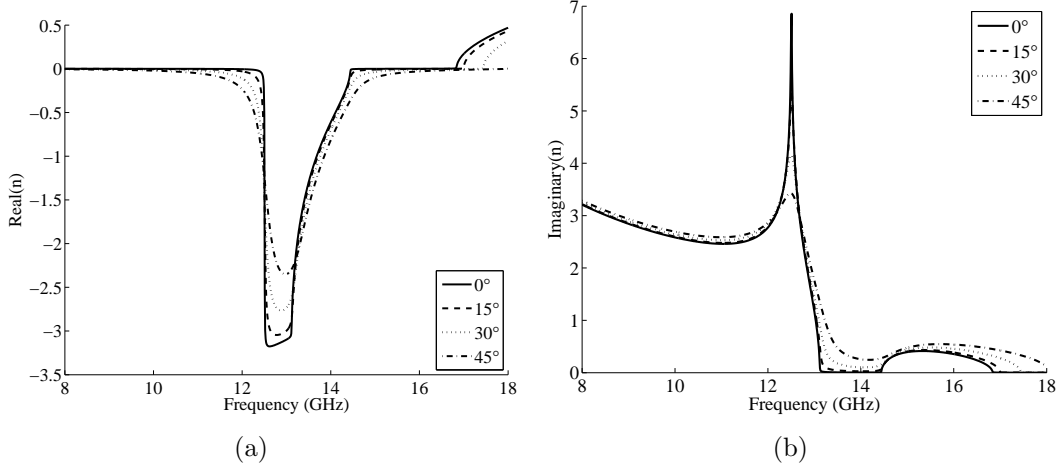
**Figure 41.**  $S$ -parameter results from the metamaterial wedge unit cell model for various angles of incidence. The magnitude (a) and phase (b) of  $S_{11}$  and  $S_{21}$ . The incident angle impacts the magnitudes of the  $S$ -parameters, but has little impact on the location of the resonant band.

Figure 42 shows the  $n$  values extracted using the theory described in Section 2.3.5 and the MATLAB<sup>TM</sup> code described in Appendix C. The magnitude of  $n$  and the width of the resonance band shows a dependence on the incident angle (the impact of the incident angle on the width of the resonance band is slight). However, the location of the resonance band appears unchanged at the different incident angles. It is important to note the local maximum in the imaginary component of  $n$  near the 13 GHz resonant frequency. This peak for the imaginary part of  $n$  indicates that the metamaterial structure will attenuate the signal at resonance.

### 3.4.2 Predictions Using Effective Medium Theory.

#### 3.4.2.1 Assuming No Losses in the Wedge.

Figure 43 shows the geometry of the metamaterial wedge and metal plate relative to the electromagnetic fields incident on the wedge, fields transmitted through the



**Figure 42.** The real (a) and imaginary (b) components of  $n$  for the metamaterial wedge unit cell. The variation of the incident angle has an impact on the depth resonant effect. It also has a slight impact on the width of the resonant band. The peak in the imaginary part of  $n$  indicates that the metamaterial will cause attenuation at resonance.

wedge, fields reflected off of the metal plate, and fields transmitted from the wedge back into free space. The angle of the fields transmitted through the first boundary of free space and the wedge ( $\varphi_{t1}$ ) can be calculated using Equation (6) where  $n_2$  is the refractive index of the wedge ( $n_w$ ),  $n_1$  is the refractive index of free space ( $n_a = 1$ ). The angle of incidence is denoted as  $\varphi_{i1}$ .

The angle relative to the plate normal of the fields incident on the boundary between the metamaterial wedge and the metal plate ( $\varphi_{i2}$ ) can be found using the geometry of Figure 43(b). Since the reflected angle is equal to the incident angle, the angle of reflection from this boundary ( $\varphi_{r2}$ ) is dependent on  $\varphi_{t1}$  and the angle formed by the wedge ( $\alpha$ )

$$\varphi_{r2} = \varphi_{i2} = \varphi_{t1} - \alpha. \quad (42)$$

Using the geometry shown in Figure 43(c) and Equation (42) and noting that  $\varphi_{i1} = \alpha + \beta$ , where  $\beta$  is the rotational angle of the wedge and plate, the expression for the angle of incidence on the boundary between the wedge and free space ( $\varphi_{i3}$ ) is

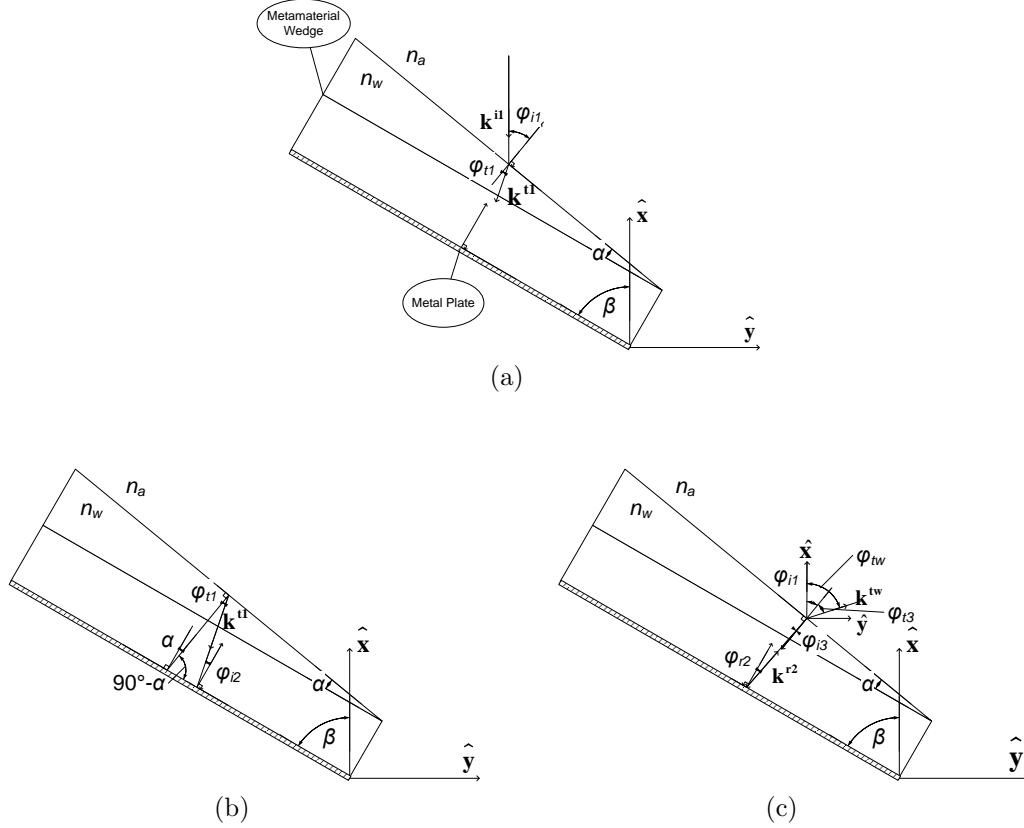


Figure 43. The geometry for the case of the (a) incident fields at the boundary between free space and the wedge, (b) fields incident on the boundary between the wedge and metal plate, and (c) the reflected fields incident on the boundary between the wedge and free space.

$$\begin{aligned}
 \varphi_{i3} &= \varphi_{r2} - \alpha = \varphi_{t1} - 2\alpha \\
 &= \text{sgn}(n_w) \arcsin \left[ \frac{n_a}{|n_w|} \sin(\alpha + \beta) \right] - 2\alpha.
 \end{aligned} \tag{43}$$

The transmission angle for this interface ( $\varphi_{t3}$ ) is calculated using Snell's law again as

$$\varphi_{t3} = \text{sgn}(n_w) \arcsin \left[ \frac{|n_w|}{n_a} \sin(\varphi_{i3}) \right], \tag{44}$$

To calculate the angle of of transmission from the wedge into free space relative to the  $x$ -axis,  $\varphi_{i1}$  is added to  $\varphi_{t3}$ . The angle of the fields from the wedge ( $\varphi_{tw}$ ) becomes

$$\varphi_{tw} = \alpha + \beta + \text{sgn}(n_w) \arcsin \left[ \frac{|n_w|}{n_a} \sin(\varphi_{i3}) \right], \quad (45)$$

where  $\varphi_{i3}$  is calculated using Equation (43).

For the initial RCS measurements, the metal plate on the backside of the wedge will be placed at an angle of  $\beta = 45^\circ$  and the angle of the wedge is approximately  $\alpha = 10.59^\circ$ . The case of  $n_w = 1$  is used to check the validity of Equation (45). At this refractive index, Equation (45) yields  $\varphi_{tw} = 90^\circ$ . This is expected since at  $n_w = 1$ , the wedge will have no effect on the incident fields and the fields will reflect off of the metal plate at an angle of  $2\beta$ .

Figure 44 shows  $\varphi_{tw}$  for the metamaterial wedge at incidence angles of  $0^\circ$ ,  $15^\circ$ ,  $30^\circ$ , and  $45^\circ$ . Equation (45) is used to calculate  $\varphi_{tw}$ . Complex values for  $\varphi_{tw}$  indicate total internal reflection. Since the transmitted mode is evanescent when total internal reflection occurs, those results have been removed from Figure 44.

#### 3.4.2.2 Wedge Losses and Nonuniform Plane Wave Propagation.

Calculations using Equations (43) and (45) are usually performed using the real part of  $n$  only. This assumes no losses in the media. However, for media with losses, the index of refraction is complex ( $\tilde{n}$ ) and takes the form [4, 737]

$$\tilde{n} = n(1 + j\kappa), \quad (46)$$

where  $\kappa$  is the attenuation index. Using  $\tilde{n}$  in Snell's law results in a complex transmission angle that has no physical meaning. To adjust for the losses in the medium, a nonuniform plane wave model must be used [4, 740].

A method for establishing a nonuniform plane wave model is described in [37]. At the interface between the two media, the incident and transmitted fields are decom-



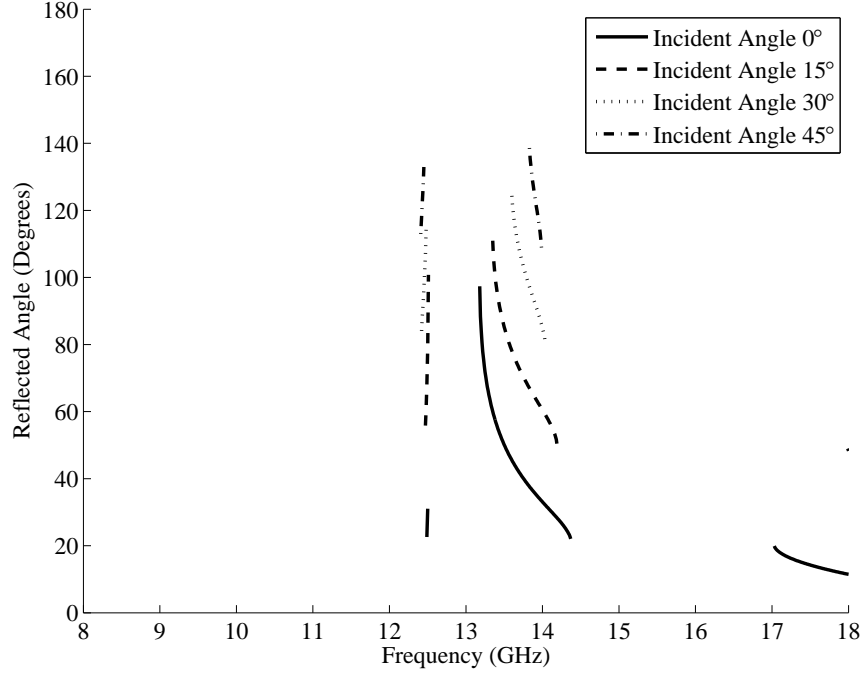


**Figure 44.** Reflection from the metamaterial wedge and metal plate assuming no losses. This only shows the results for the electromagnetic waves transmitted into the wave (there will be energy that arrives at different angles due to reflection off of the face of the wedge). The angles of reflection where the transmitted mode is evanescent have been removed.

posed into attenuation and propagation vectors. Because the planes are nonuniform, the attenuation and propagation constants need to be adjusted. The angles of the attenuation and propagation vectors can then be determined by [37]

$$\psi_2 = \arcsin \left( \frac{\alpha_{01}}{\alpha_2} \sin \psi_1 \right), \quad (47a)$$

$$\zeta_2 = \arcsin \left( \frac{\beta_{01}}{\beta_2} \sin \zeta_1 \right), \quad (47b)$$

where  $\psi_1$  and  $\zeta_1$  are the angles of the incident attenuation and propagation vectors,  $\psi_2$  and  $\zeta_2$  are the angles of the transmitted attenuation and propagation vectors,  $\alpha_{01}$  and  $\beta_{01}$  are the incident intrinsic attenuation and propagation constants, and  $\alpha_2$  and  $\beta_2$  are the transmitted adjusted attenuation and propagation constants. All angles

in Equation (47) are relative to the normals on the respective sides of the interface. The transmitted field propagates in the direction of  $\beta_2$ , and the refraction angle is given by  $\zeta_2$  [51].

To use Equation (47),  $\alpha_2$  and  $\beta_2$  must be determined. These can be calculated from [37]

$$\alpha_1 = \alpha_{01} \sin \psi_1, \quad (48a)$$

$$\beta_1 = \beta_{01} \sin \zeta_1, \quad (48b)$$

$$\gamma_1 = \alpha_1 + j\beta_1, \quad (48c)$$

$$\alpha_2 = \sqrt{\frac{1}{2} [|\gamma_1|^2 + \Re\{\gamma_{02}^2\} + |\gamma_1^2 - \gamma_{02}^2|]}, \quad (48d)$$

$$\beta_2 = \sqrt{\frac{1}{2} [|\gamma_1|^2 - \Re\{\gamma_{02}^2\} + |\gamma_1^2 - \gamma_{02}^2|]}. \quad (48e)$$

The basic geometry of the setup remains the same as described in Section 3.4.2.1. At the first interface the incident fields are propagating in free space and are uniform. Thus  $\psi_1$  and  $\zeta_1$  at this interface are both equal to  $\varphi_{i1}$ . The transmission angles  $\psi_2$  and  $\zeta_2$  are then calculated using Equations (47) and (48). As shown in the development of Equation (43), the metal plate allows the incident angles at the second interface between the wedge and free space to be calculated by subtracting  $2\alpha$  from the transmitted angles from the first interface. The final transmission angles are then again calculated using Equations (47) and (48) and adding  $\varphi_{i1}$  to make the resulting angles relative to the incident field.

Figure 45 shows the angle of the electromagnetic wave transmitted through the wedge and reflected off of the plate at incident angles of  $0^\circ$ ,  $15^\circ$ ,  $30^\circ$ , and  $45^\circ$ . The angles are relative to the incident field.

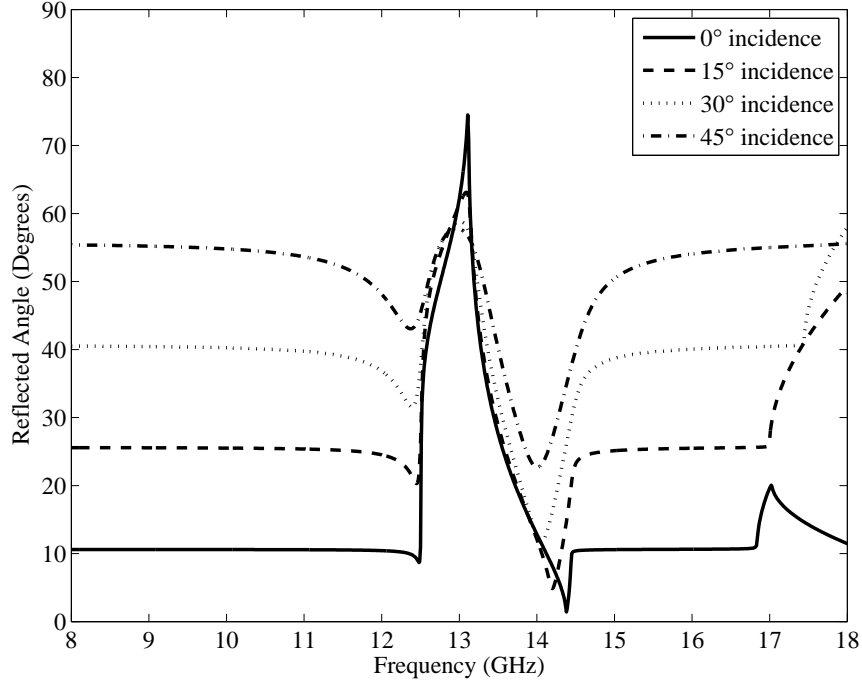


**Figure 45.** The angles transmitted through the metamaterial wedge and reflected off of the metal plate taking into account the losses in the metamaterial wedge.

### 3.4.3 Predictions Using Surface Wave Scattering Theory.

As discussed in Section 2.2.3, scattering from the metamaterial wedge can be predicted using FSS theory. The scattered waves (forward and reverse) can be expressed as a series of Floquet waves in the directions given by  $m_1, m_2 = 0, 1, 2, \dots$  in Equation (13). The principle forward scattering direction where  $m_1 = m_2 = 0$  is unaffected by the metamaterial wedge and will appear at twice the rotation angle of the plate. The principle reflected angle will also be independent of frequency and will appear at twice the angle of incidence. Table 5 shows the principle forward (transmission into the wedge) and back (reflection from the face of the wedge) return angles.

The interelemental spacing  $D_x$  and  $D_z$  for the metamaterial wedge are 3.7 mm. Setting  $m_1$  and/or  $m_2$  greater than zero in Equation (13), the transmitted/reflected angles become complex at all frequencies. This indicates that for Floquet modes  $m_1 > 0$  or  $m_2 > 0$ , the grating lobes are “trapped” and do not radiate. Thus,

**Table 5. Metamaterial wedge principle scattering angles using FSS theory.**

$\beta$ (degrees)	Forward Angle (degrees)	Back Angle (degrees)
0	0	21.2
15	30	51.2
30	60	81.2
45	90	111.2

additional radiation from the wedge for these conditions must be due to residual currents. While it is difficult to predict exactly where the radiation from these residual currents will appear, the amplitude of the radiation at those points should be about 14 to 20 dB down from the mainbeam.

#### 3.4.4 Simple Wedge Model.

An early attempt to model the metamaterial wedge in CST MWS® is shown in Figure 46. The model has been simplified to include only three steps and be only one unit cell deep at the shortest step (the full structure is eleven steps wide and six unit cells deep at the shortest step). The model is one unit cell tall. This, combined with periodic boundary conditions in the vertical direction ( $z$ ) create a two-dimensional model of the wedge. The excitation source for this model is a plane wave incident from  $45^\circ$  with the electric field  $p$ -polarized (that is, horizontally-polarized) as shown in Figure 46(b). It turns out that this is the incorrect polarization to see the negative refraction effects with this unit cell geometry. The electric field is changed to  $t$ -polarized in later models.

The boundary conditions for the model are summarized in Table 6. The boundary conditions in the  $\pm z$  direction are set to periodic. This approximates the wedge as infinitely-tall. The boundary condition in the  $-x$  direction is set to PEC to model the metal plate behind the wedge. One of the key values to be calculated from this model is RCS. Accordingly, the boundary conditions in the  $\pm y$  and  $+x$  directions are set to open with additional space included to facilitate the calculation of farfield

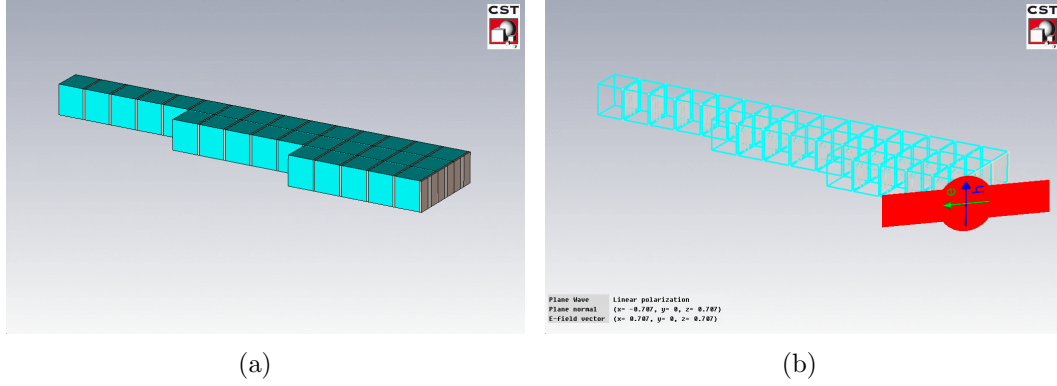


**Figure 46.** CST MWS® model of a simplified version of the metamaterial wedge. (a) The structure consists of three steps with the shortest step being one unit cell deep and each step adding one unit cell in depth. The model is one unit cell tall. (b) The excitation source for this model is a plane wave incident from  $45^\circ$  with the electric field  $p$ -polarized.

values.

**Table 6.** Simple metamaterial wedge model boundary conditions.

Boundary Normal	Condition
$-x$	PEC
$+x$	Open (add space)
$\pm y$	Open (add space)
$\pm z$	Periodic

This model uses the frequency solver with tetrahedral mesh. The mesh statistics for this model are shown in Table 15 and the mesh is shown in Figure 108(a) in Appendix A.

Broadband farfield RCS monitors are not compatible with the frequency solver in CST MWS®. Therefore, multiple single-sample farfield RCS monitors are used, and the frequency sampling is performed at every 500 MHz between 6 and 18 GHz resulting in 25 frequency samples. To achieve a higher resolution in frequency-space, interpolation is used at every 100 MHz. The results from the 25 frequency samples are imported into MATLAB™ and analyzed using the AFIT RCS Processing Code©. After the 25 frequency samples are interpolated at every 100 MHz between 6 and 18

GHz, the global RCS pattern is created and shown in Figure 47. The plot shows a shift of the specular return near the 13 GHz resonance point. The angles in Figure 47 have been transformed to reference the incident wave vector as the  $x$ -axis (i.e., the angles are from the incident wave vector and not the  $x$ -axis shown in Figure 46). This is the convention used in the AFIT RCS range and allows for direct comparison between the model and measurement results.

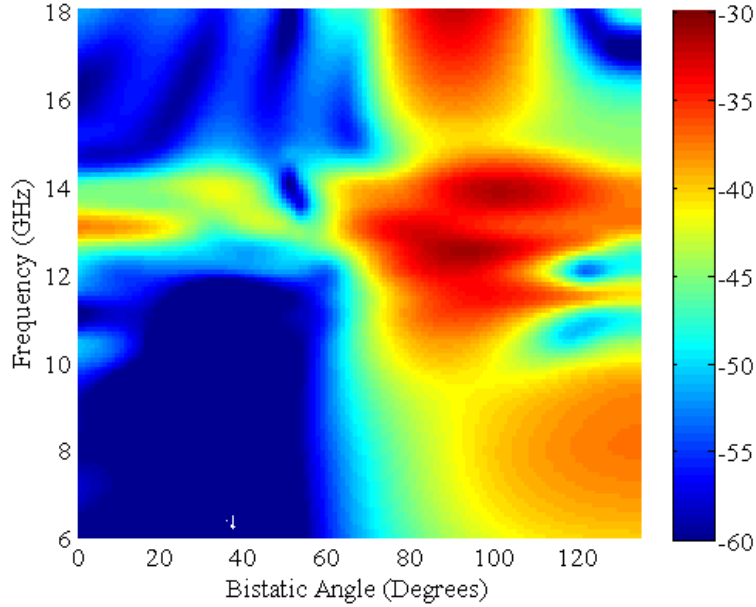


**Figure 47.** The global bistatic RCS pattern of the simple metamaterial wedge model. The receiver angles are shown on the  $x$ -axis. Resonant behavior is evident near 13 GHz. Note that in this figure the angles have been adjusted so that  $0^\circ$  in  $\phi$  represents the angle of incidence.

### 3.4.5 Mid-Size Wedge Model.

Since the full width and depth model of the wedge is too large for the frequency solver, a mid-sized model was created and is shown in Figure 48. This model is seven steps wide, and the depth of the model is reduced by 5 unit cells. The boundary conditions for this model are the same as those shown in Table 7. These conditions are similar to the boundary conditions for the simple metamaterial wedge model

except the PEC ground plane at the  $-x$  boundary has been replaced. Instead, an infinitely-thin PEC plate is put into the model and the  $-x$  boundary has been changed to open. The incident field polarization is also changed to  $t$ -polarized. This model is run at incident angles of  $0^\circ$ ,  $15^\circ$ ,  $30^\circ$ , and  $45^\circ$ . The mesh statistics are shown in Table 15 of Appendix A. The meshes are shown in Figure 108 of Appendix A.

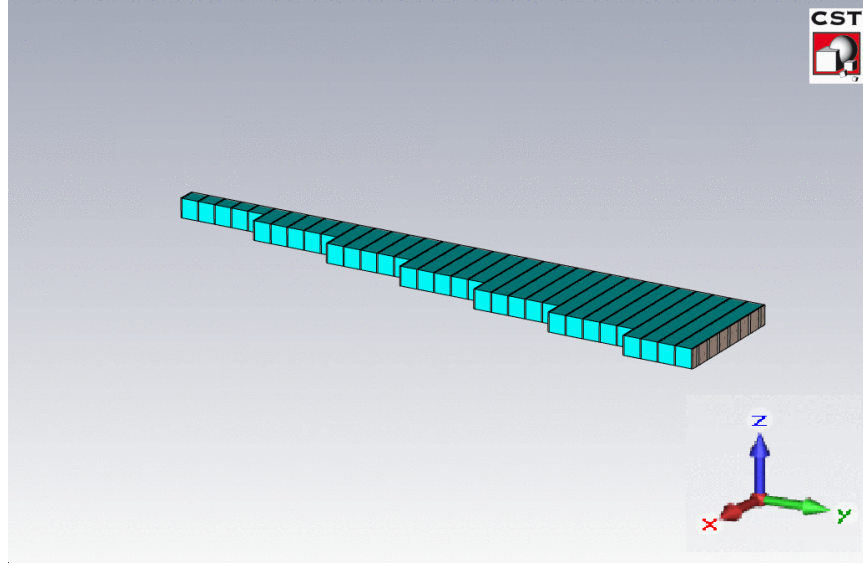


**Figure 48.** CST MWS® model for mid-size version of the metamaterial wedge. The structure model is a single unit cell in height. The model includes seven steps where the smallest step is one unit cell deep.

**Table 7.** Mid-size metamaterial wedge model boundary conditions.

Boundary Normal	Condition
$\pm x$	Open (add space)
$\pm y$	Open (add space)
$\pm z$	Periodic

Figure 49 shows the  $t$ -polarized electric field amplitude projected on a 2-D plane that is located in the vertical center of the structure for this model at  $0^\circ$  incidence. The electric field amplitude at 10 GHz shows very little penetration into the metamaterial wedge. The majority of the energy is reflected off of the face of the wedge. The energy is directed outwards at the specular angle of the wedge face. Contrast that

with the electric field amplitude at 14 GHz, where a larger portion of the incident energy is able to penetrate the wedge. The amplitude of the outgoing wave at the specular angle is much less. The energy that penetrates the wedge also appears to make the SRRs resonate, as evidenced by the electric fields that seemingly radiate from the SRRs.

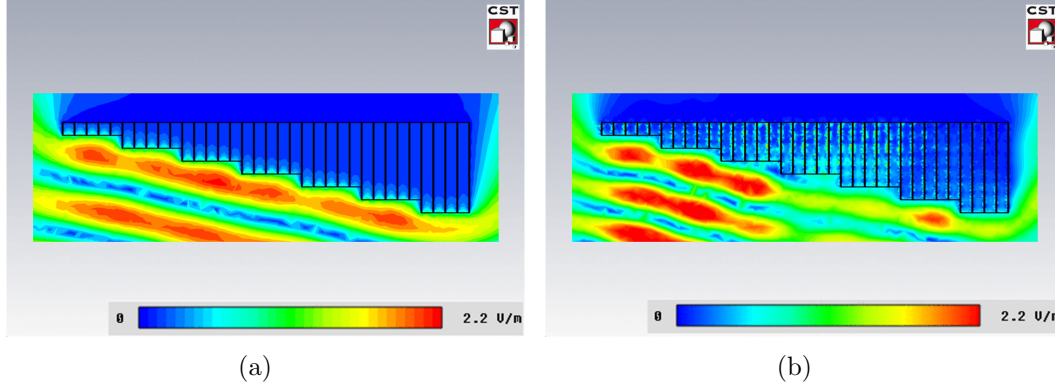


**Figure 49.** The  $t$ -polarized electric field amplitude from the mid-sized 2-D metamaterial wedge model at  $0^\circ$  incidence. The field results are shown at a 2-D plane located in the vertical center of the structure. (a) The electric field amplitude at 10 GHz shows most of the energy being reflected at the wedge face. (b) The electric field amplitude at 14 GHz shows much more penetration.

Figure 50 shows the global bistatic RCS pattern from the simulation. The distortion of the scatterer between 13 and 14 GHz indicates resonant behavior. Throughout most of the frequency band shown, the strongest return is at the specular angle for the wedge face. Inside the resonance band the scatterers shift only slightly in angle, but the brightest scatterer remains at the specular angle for the wedge. Judging by the refractive index for this metamaterial's unit cell (see Figure 42), the energy that penetrates the wedge will be significantly attenuated by the losses in the wedge. However, negative refraction should be more evident in this model than the measurements because the wedge in this model is thinner. The electromagnetic fields will travel through less of the effective medium and be attenuated less.

The RCS patterns in Figure 50 show interesting behavior beyond 17 GHz. At



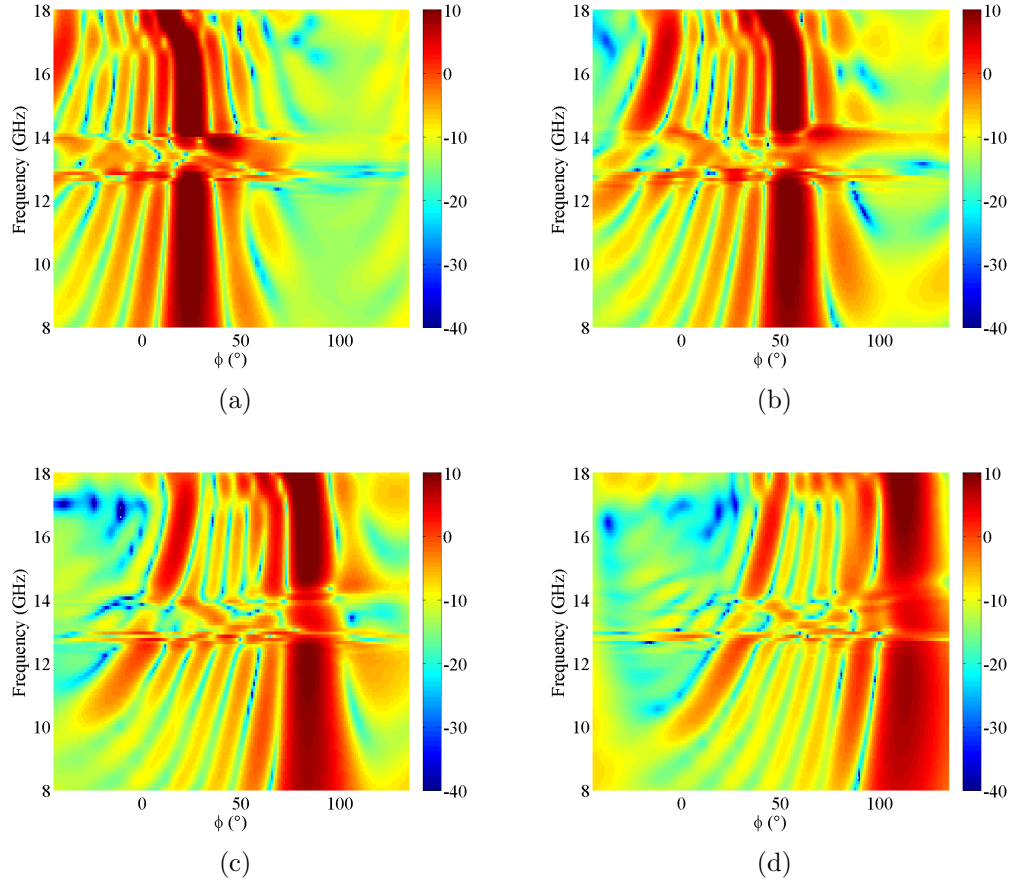


**Figure 50.** The global bistatic RCS pattern of the mid-sized 2-D metamaterial wedge model for incident angles of  $0^\circ$  (a),  $15^\circ$  (b),  $30^\circ$  (c), and  $45^\circ$  (d). The color axis shows the RCS in dBsm. Resonant behavior is evident at all incident angles between 13 and 14 GHz.

those frequencies, the main return from the wedge appears to follow a pattern that is consistent with the trends shown in Figure 45. The refractive index for this metamaterial's unit cell (see Figure 42) shows a positive refraction band at these frequencies, and the trend in the refractive index seems to follow the trend in the specular return angle.

Figure 51 shows the angle of the maximum return as a function of frequency for each of the incident angles. Below the resonance band, the strongest return appears at the specular angle for the front face of the wedge. Referring back to the plots of the  $S$ -parameters from the unit cell model for this structure (see Figure 41), specular

reflection off of the wedge is expected to be the main behavior since the magnitude of  $S_{11}$  is very near one at these frequencies. At the higher frequencies, the main angle follows a curve that seems to correspond with the trend in  $n$  as noted above. Inside the resonance band, the angle of the main scatterer seems to shift towards the negative refraction area. However, it should be noted that the patterns shown in Figure 51 do not match either set of angles from transmission through the wedge and off of the plate given in Figures 44 and 45.

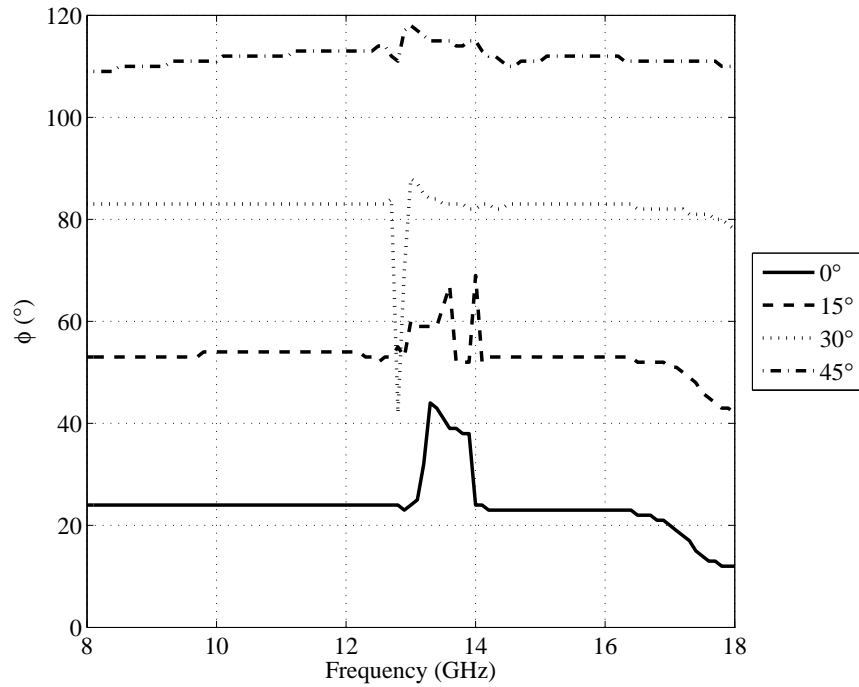
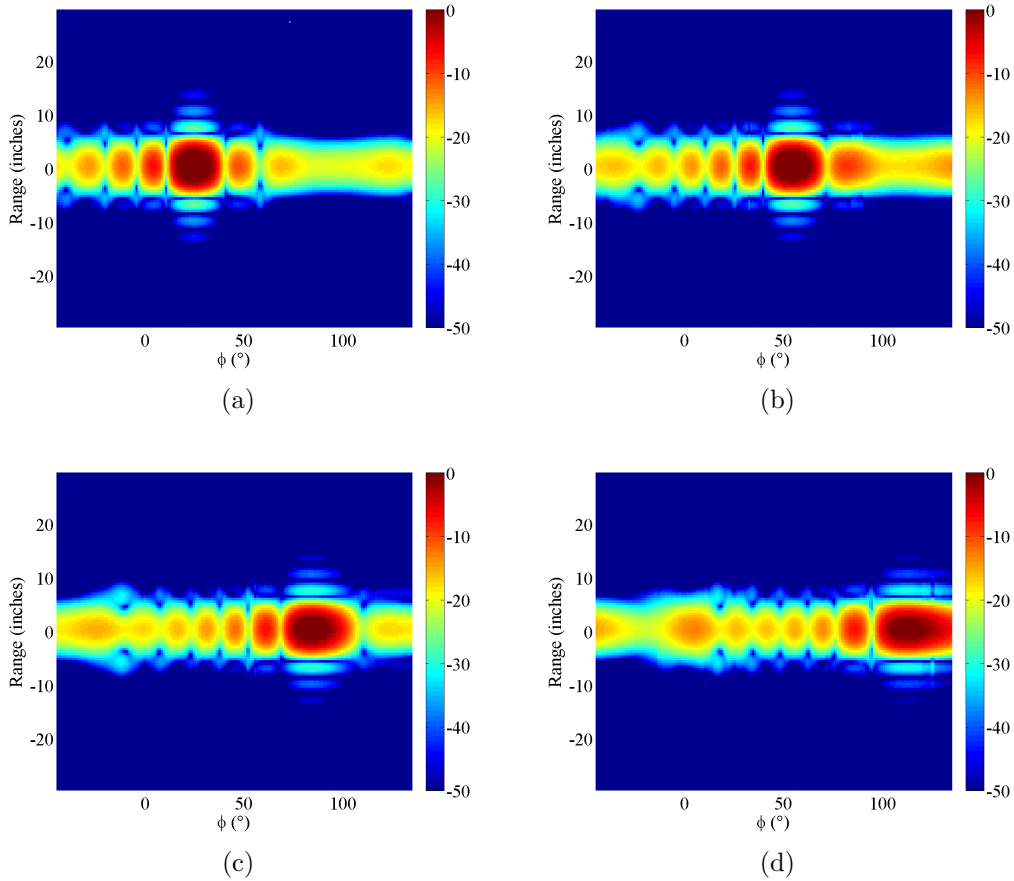


**Figure 51.** The maximum return angles as a function of frequency from the mid-sized 2-D metamaterial wedge model for each of the incident angles.

Range images for the metamaterial wedge are derived from the RCS data according to the theory presented in Section 2.3.3.3. Because the metamaterial structure is resonant, the data are analyzed using 2 GHz windows. However, this will result in a decrease in range resolution. According to Equation (28), the range resolution for a 2 GHz window is 7.5 cm.

Figure 52 shows the global range plots for each of the incident angles at 10 GHz.

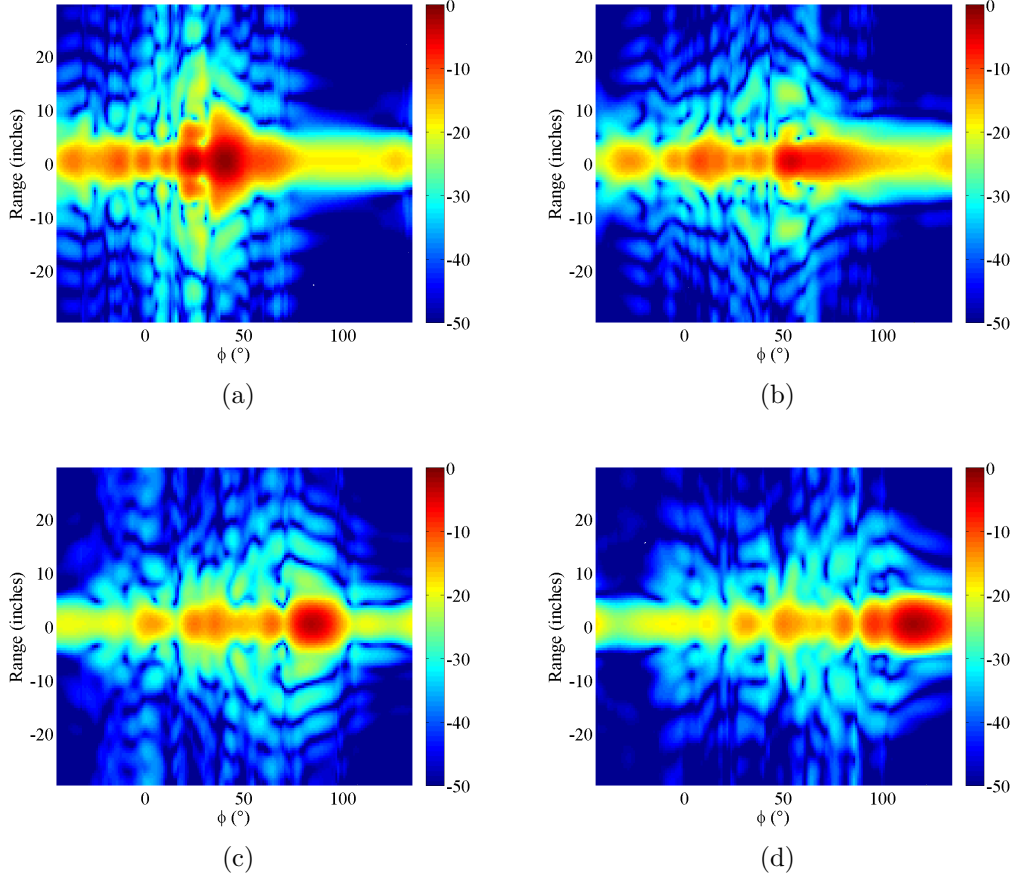
At each incident angle, the main scatterer appears at the specular angle for the metamaterial wedge. This is expected from the RCS data. The range plot shows that all the strong scatterers appear to be centered very near 0 inches downrange. Because the range resolution is so large, it is difficult to distinguish from scattering at the wedge face versus scattering at the metal plate. However, because of the angle of the returns it appears they are the return from the wedge face.



**Figure 52.** The global range patterns of the mid-sized 2-D metamaterial wedge model at 10 GHz for incident angles of  $0^\circ$  (a),  $15^\circ$  (b),  $30^\circ$  (c), and  $45^\circ$  (d). The color axis shows the RCS in dBsm. The strongest scatterer for each of the incident angles is near 0 inches downrange.

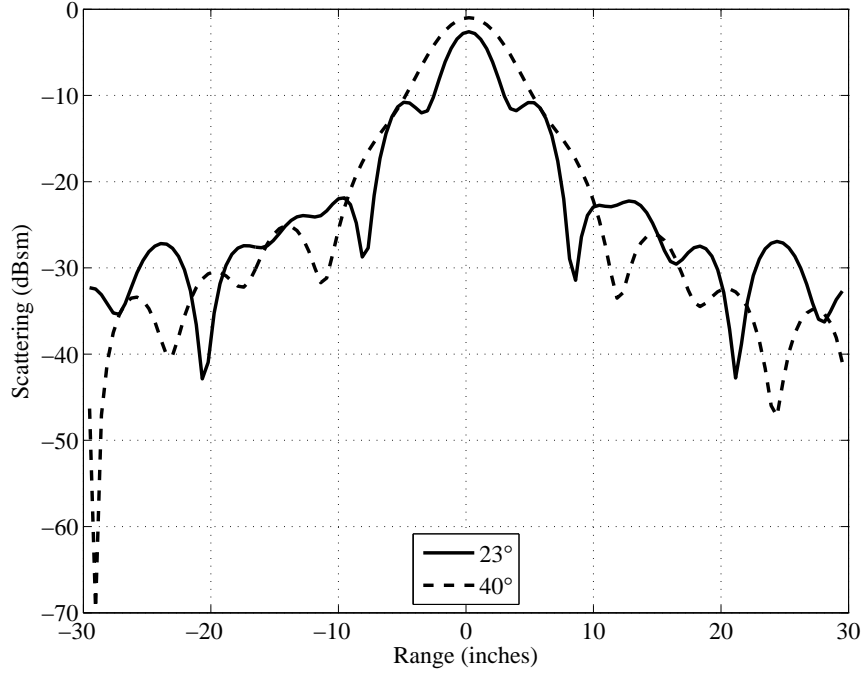
Figure 53 shows the global range patterns inside the resonance band. For these patterns, 13.5 GHz is chosen as the center of the frequency window since it is close to the center of the resonance band. For  $0^\circ$  incidence, the main scatterer has split into

two lobes that appear at  $23^\circ$  and  $40^\circ$ . The lobe at  $40^\circ$  is stronger in magnitude by about 1.5 dBsm. Both of these appear to be centered at 0 inches downrange. This seems to indicate that the scattering phenomena creating these lobes are located near each other. For the other incident angles, the main scatterers appear as single lobes. All of the strong scatterers appear at about 0 inches downrange.



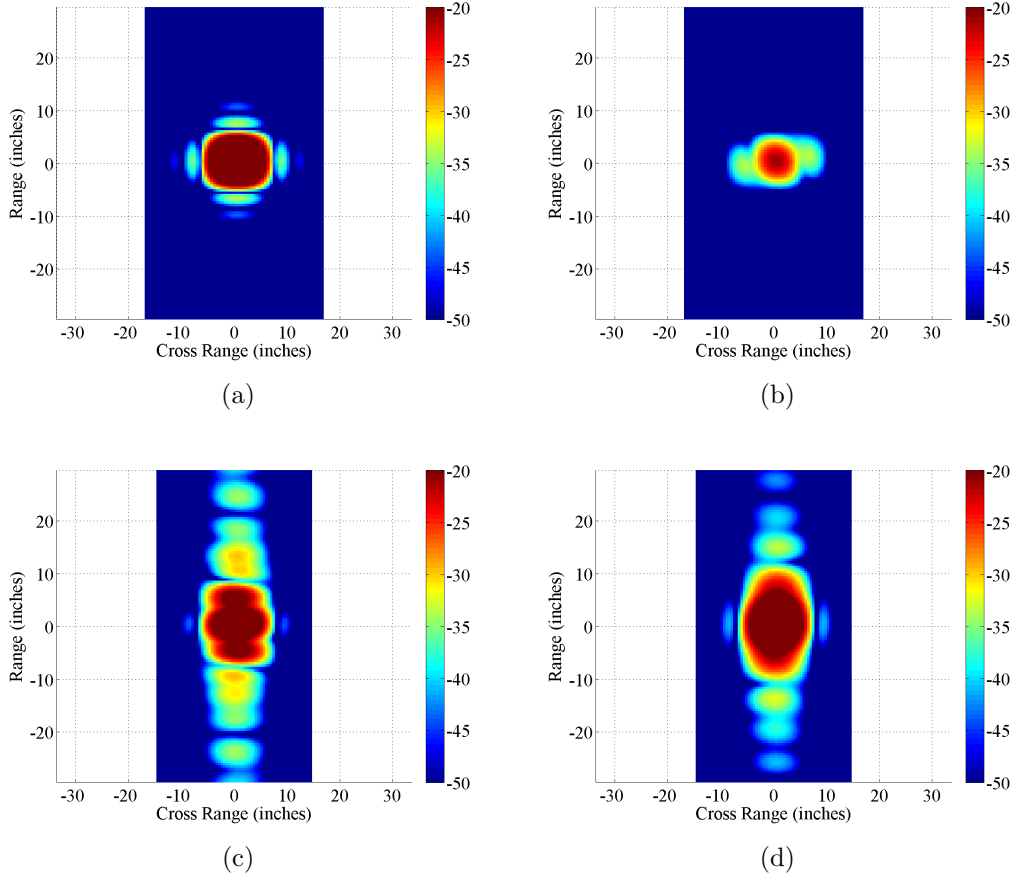
**Figure 53.** The global range patterns of the mid-sized 2-D metamaterial wedge model at 13.5 GHz for incident angles of  $0^\circ$  (a),  $15^\circ$  (b),  $30^\circ$  (c), and  $45^\circ$  (d). The color axis shows the RCS in dBsm. The strongest scatterer for each of the incident angles is near 0 inches downrange.

Figure 54 shows the range plots for the  $23^\circ$  and  $40^\circ$  scatterers at  $0^\circ$  incidence and 13.5 GHz. As noted above, the scatterer at  $40^\circ$  is stronger than the scatterer at  $23^\circ$ . Furthermore, both appear to be centered at 0 inches. This indicates that the scatterers originate from nearby features.



**Figure 54.** Range plots for the mid-sized 2-D metamaterial wedge at  $23^\circ$  and  $40^\circ$ . A 2 GHz frequency window centered at 13.5 GHz is used. The scatterer for both angles seems to be centered near 0 inches downrange.

Figure 55 shows ISAR images for the mid-sized metamaterial wedge model at  $0^\circ$  incidence. The images are created according to the procedure described in Section 2.3.3.4. At 10 GHz, the stronger scatterer is seen at the center of the range near  $23^\circ$ . The scatterer at  $40^\circ$  is not nearly as strong at 10 GHz as the scatterer at  $23^\circ$ . When the metamaterial wedge resonates at 13.5 GHz, the scatterer at  $40^\circ$  becomes much stronger, while the scatterer at  $23^\circ$  becomes weaker. This indicates that the scatterer at  $23^\circ$  is the specular reflection off of the wedge face and the scatterer at  $40^\circ$  is related to the resonance. Because the range cells are relatively large (7.5 cm), it is difficult to determine the exact location of the scattering centers, but they appear to be located very near the center of the range in all of the images. This leads to the conclusion that the  $40^\circ$  scattering mechanism is located near the  $23^\circ$  mechanism.



**Figure 55.** ISAR imagery for the mid-sized 2-D metamaterial wedge model at  $0^\circ$  incidence. (a) At 10 GHz, the ISAR image centered at a receiver angle of  $23^\circ$  shows a very strong return. (b) At 10 GHz and  $40^\circ$  in receiver angle, the return is small. (c) At 13.5 GHz and  $23^\circ$  in receiver angle, the main scatterer is weaker than at 10 GHz. (d) For 13.5 GHz and  $23^\circ$  in receiver angle, the main scatterer is much stronger than at 10 GHz.

This simulation is also performed with the PEC plate removed. The computational mesh statistics for these models are given in Table 15 of Appendix A, and the meshes are shown in Figure 108 of Appendix A.

Figure 56 shows the amplitude of the electric field for the mid-sized metamaterial wedge model with the PEC plate removed at  $0^\circ$  incidence. Like before, the electric field amplitude shown is for the  $t$ -polarized component projected on a 2-D plane at the vertical center of the structure. The results are very similar to the results from the model with the PEC plate. At 10 GHz, most of the energy is reflected at the wedge face. The reflected field is at the specular angle for the wedge face. At 14 GHz, the incident electric field travels all the way through the metamaterial wedge, exciting the SRR particles along the way. An electromagnetic field is radiated outward from the backside of the wedge.

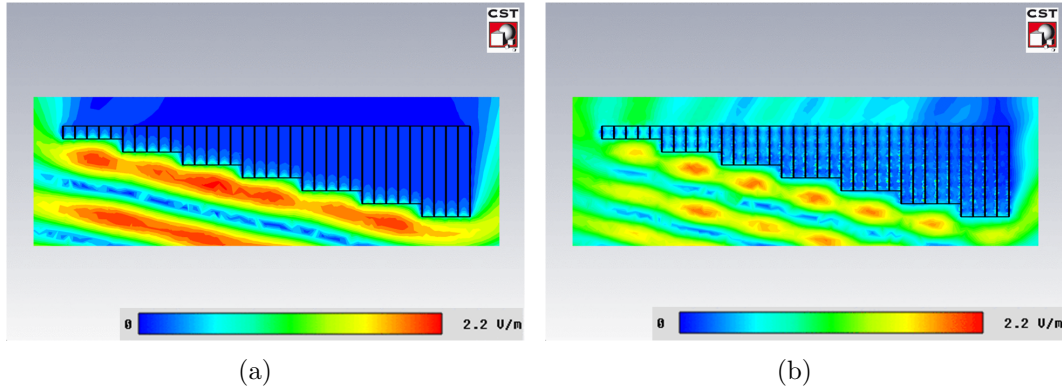


**Figure 56.** The  $t$ -polarized electric field amplitude from the mid-sized 2-D metamaterial wedge model without the PEC plate at  $0^\circ$  incidence. (a) Like the model with the PEC plate, most of the the electric field at 10 GHz is reflected at the wedge face. (b) The electric field amplitude at 14 GHz shows the incident field traveling all the way trough the metamaterial wedge.

The global RCS results are shown in Figure 57. Each of the patterns display interesting behavior near the resonance band of 13-14 GHz. Since there is no PEC plate behind the wedge in this model, none of the scattering lobes in this pattern can be due to negative refraction. That is, these patterns show only the energy reflected

off the front wedge face or radiated from surface waves.

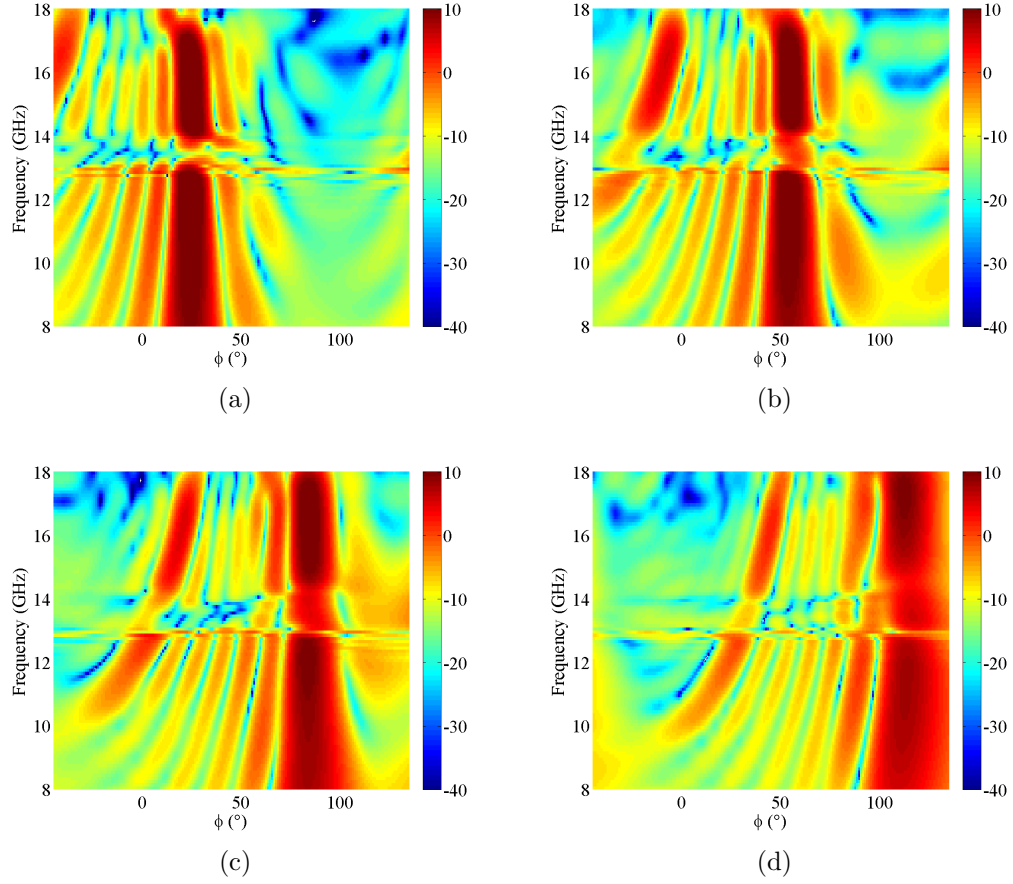


**Figure 57.** The global bistatic RCS pattern of the mid-sized 2-D metamaterial wedge model without the PEC plate for incident angles of  $0^\circ$  (a),  $15^\circ$  (b),  $30^\circ$  (c), and  $45^\circ$  (d). Resonant behavior is evident at all incident angles between 13 and 14 GHz.

The results in Figure 57 show that the returns in the resonance band are reduced in magnitude. This indicates that some energy is transmitted into the wedge. That energy is attenuated by the losses in the wedge.



### 3.4.6 Full 2-D Wedge Model.

A model of an entire slice of the metamaterial wedge with the frequency solver was created. The model includes the full width and depth of the wedge. The boundary conditions for this model are the same as those shown in Table 7. The incident electric field is  $t$ -polarized, and the model is run at incident angles of  $0^\circ$ ,  $15^\circ$ ,  $30^\circ$ , and  $45^\circ$ . The first attempt to solve this model employed the frequency solver, but the computer ran out of memory during the seventh step of the adaptive meshing algorithm. This model contained over 2.86 million mesh cells when the solution process was aborted.

Despite the difficulties with the frequency-domain solver and tetrahedral mesh, the transient solver with hexahedral mesh provides a solution in a reasonable amount of time. This model is shown in Figure 58. A summary for the hexahedral mesh is shown in Table 14 in Appendix A. Note that the same mesh is used for the four incident angles.

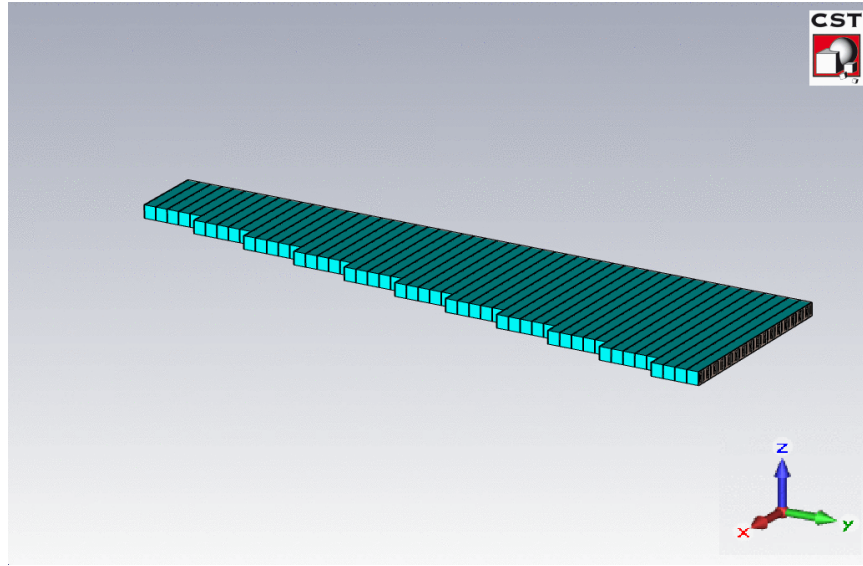
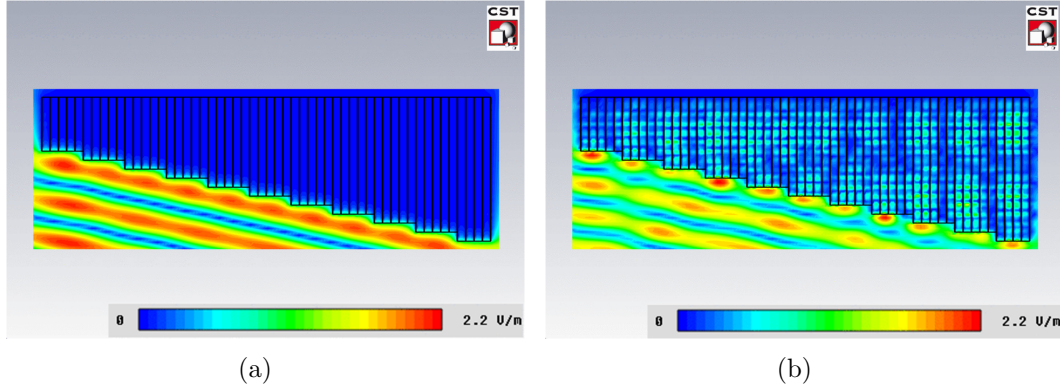


Figure 58. CST MWS® model for the full width and depth of the metamaterial wedge.

Figure 59 shows the  $t$ -polarized electric field amplitude for the full 2-D metamaterial wedge model at  $0^\circ$  incidence. Like the previous model, the fields at 10 GHz are

mostly reflected—little energy is transmitted into the wedge. However, at 12 GHz the incident electric field is able to penetrate the wedge and excite the SRR particles. It is interesting to note that the resonance for this model occurs at a lower frequency band. This could be due to some inaccuracies in the FFT used to convert the results from the time-domain to the frequency-domain.



**Figure 59.** The  $t$ -polarized electric field amplitude from the full 2-D metamaterial wedge model at  $0^\circ$  incidence. (a) Like before, most of the the electric field at 10 GHz is reflected at the wedge face. (b) At 12 GHz the metamaterial structure resonates, and the electric field travels through the metamaterial wedge to the PEC plate.

Figure 60 shows the global RCS patterns for incident angles of  $0^\circ$ ,  $15^\circ$ ,  $30^\circ$ , and  $45^\circ$ . The patterns are for the  $tt$ -polarization. Each of the different incident angles shows a resonant behavior near 12-13 GHz. This appears to be a slightly lower resonance band than that of the unit cell model (see Figure 42).

Figure 61 shows global range patterns of the full 2-D metamaterial wedge model. These global range patterns are created using 2 GHz windows around a center frequency of 10 GHz. Thus, these data should show little resonance effects. For all of the incident angles, the strongest scatterer appears at the wedge face's specular angle and at 0 inches downrange.

Global range patterns of the full 2-D metamaterial wedge model centered at the resonant frequency of 12.5 GHz are shown in Figure 62. Like the previous range data, these are computed using 2 GHz windows. And, like before, the main scatterers

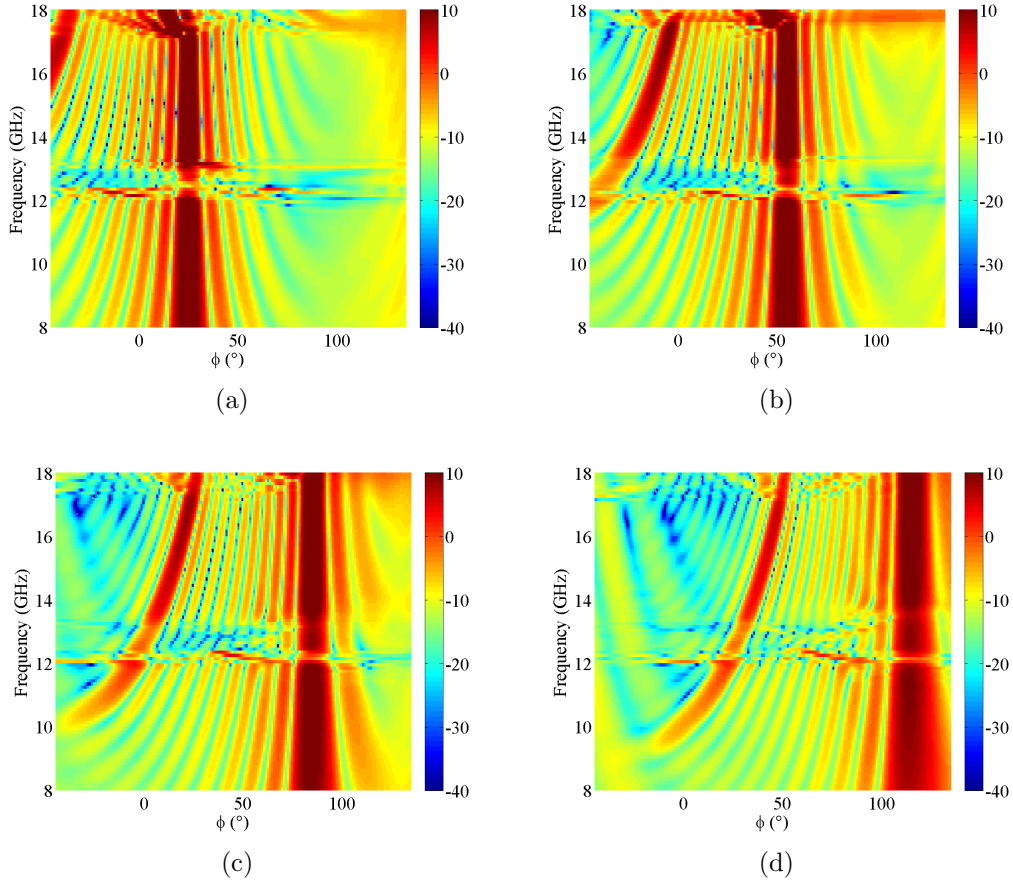


**Figure 60.** The global bistatic RCS pattern of the full 2-D metamaterial wedge model for incident angles of  $0^\circ$  (a),  $15^\circ$  (b),  $30^\circ$  (c), and  $45^\circ$  (d). Resonant behavior is evident at all incident angles near 12-13 GHz.

appear at the specular angle for the wedge face. What is more apparent, however, are lobes that appear at different ranges. These lobing effects are most likely an indicator that resonance is occurring in the wedge. As is noted with the mid-size wedge model, the strength of the scatterers is also diminished at 12.5 GHz. This is due to the attenuation caused by the wedge at resonance.

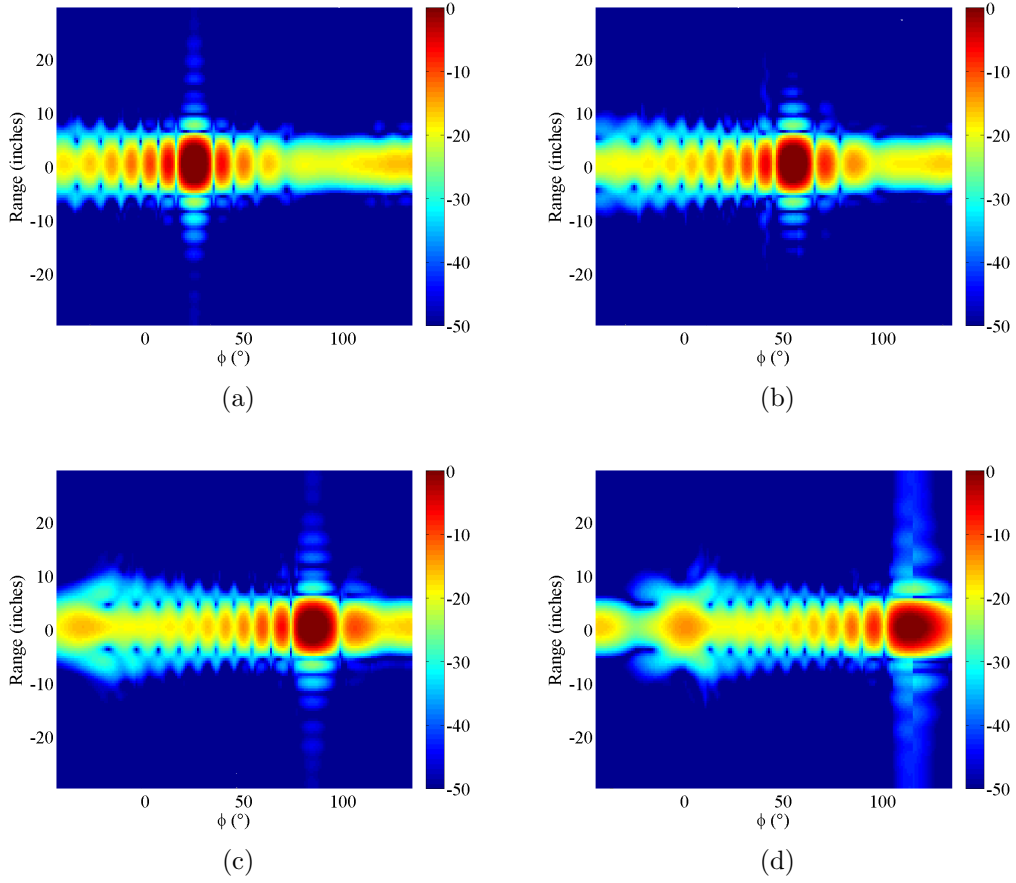
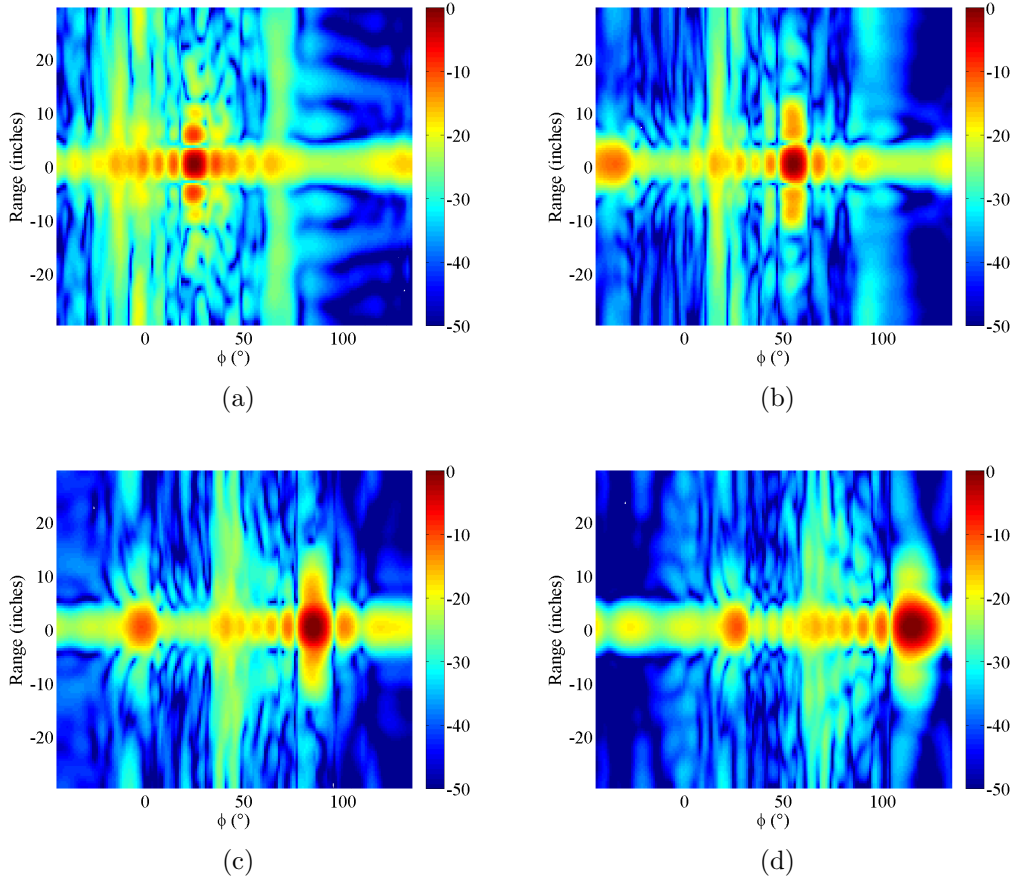


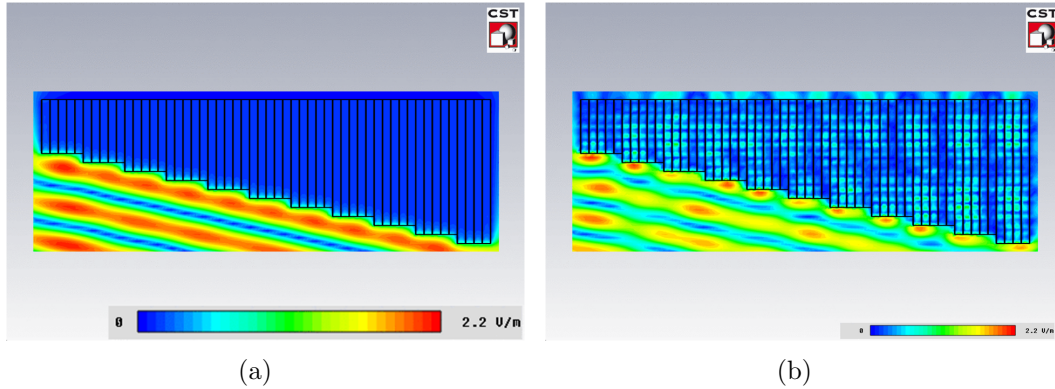
Figure 61. Global range patterns of the full 2-D metamaterial wedge model at 10 GHz for incident angles of 0° (a), 15° (b), 30° (c), and 45° (d). For all of the incident angles, the strongest scatterer appears at 0 inches downrange and at the specular angle of the wedge face.



**Figure 62.** Global range patterns of the full 2-D metamaterial wedge model at 12.5 GHz for incident angles of  $0^\circ$  (a),  $15^\circ$  (b),  $30^\circ$  (c), and  $45^\circ$  (d). Like before, the main scatterers appear at the specular angle of the wedge face. The lobing effects seen in the range dimension are most likely due to resonance effects.

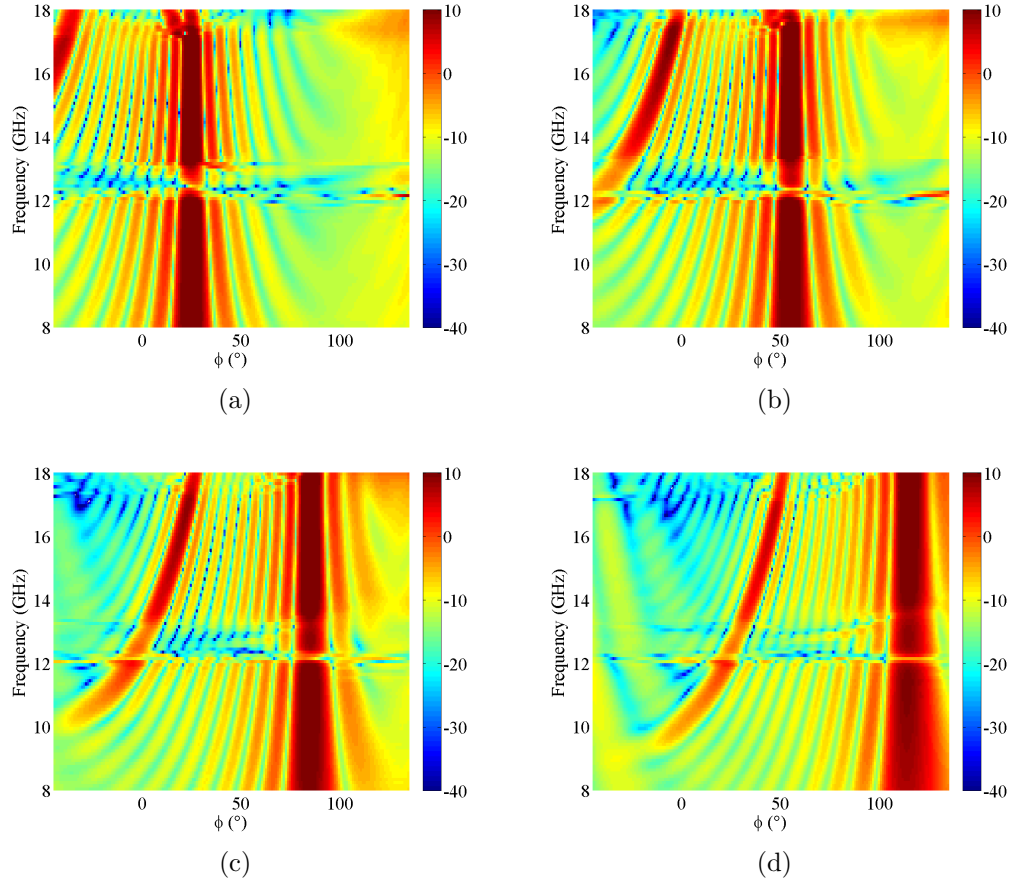
This model is also simulated without the PEC plate behind the metamaterial wedge. Figure 108 shows the mesh and Table 15 shows the mesh statistics for this model (both are found in Appendix A).

Figure 63 shows the  $t$ -polarized electric field amplitude for the full 2-D metamaterial wedge model with the PEC plate removed. The results are similar to the previous model. Most of the energy at 10 GHz is reflected at the wedge face. At the resonant frequency of 12 GHz, the electric fields are able to penetrate the wedge. A radiation pattern can be seen behind the wedge.



**Figure 63.** The  $t$ -polarized electric field amplitude from the full 2-D metamaterial wedge model without the PEC plate at  $0^\circ$  incidence. (a) The majority of the incident energy at 10 GHz is reflected at the wedge face. (b) At 12 GHz the metamaterial structure resonates, and the electric field travels through the metamaterial wedge. A radiation pattern can be seen behind the wedge.

The global RCS patterns from the simulation are shown in Figure 64. The patterns appear similar to the patterns from the simulation with the PEC plate. The strongest returns are seen at the specular angles for the metamaterial wedge face. The behavior in the resonance band is the same as the returns for the model with the wedge. Since the plate is not in this model, none of the energy transmitted into the wedge is reflected back towards the receiver. This could indicate that the energy transmitted into wedge at resonance is absorbed by the losses, or the returns at resonance are due to surface waves and not refraction.



**Figure 64.** The global bistatic RCS pattern of the full 2-D metamaterial wedge without plate model for incident angles of  $0^\circ$  (a),  $15^\circ$  (b),  $30^\circ$  (c), and  $45^\circ$  (d). Resonant behavior is evident at all incident angles near 12-13 GHz.

### 3.4.7 Metamaterial Wedge Model Conclusions.

The metamaterial wedge model results display the expected behavior. The response from the unit cell model matches the results published for this type of DNG metamaterial. The unit cell model predicts a resonance band between about 12.5 GHz and 14.5 GHz. Below this resonance band, the magnitude of  $S_{11}$  is close to one, indicating that the material is opaque at those frequencies. The extracted index of refraction predicts a negative effective index of refraction in the resonance band. However, this index of refraction is marked with a large imaginary component. This should result in large amount of attenuation in the wedge at resonance.

The effective medium theory predictions show that if the losses are not taken into account, most of the incident angles are beyond the critical angles for the extracted index of refraction. When the losses are taken into account, the refraction angle results look much different. None of the effective medium predictions shown in this thesis attempt to predict the magnitudes of the fields that are transmitted through the wedge. Outside of the resonance band (especially below the resonance band), reflection off of the face of the wedge is expected to be the dominant response. This reduces the importance of the transmission angle results below the resonance band shown in Figures 44 and 45. Inside the resonance band, losses in the wedge will attenuate any fields that are transmitted into the wedge. The attenuation makes it difficult to see any sort of refraction in the wedge.

Predictions of the principle scattering directions with FSS theory are easy to make, but they are not dependent on the frequency of the incident electromagnetic fields. The response from this metamaterial wedge is expected to be frequency-dependent, so predictions using higher-order Floquet modes are necessary. However, the resulting angles for higher-order scattering directions are complex, indicating that the frequency-dependent radiation will be due to residual currents. These residual cur-



rents are difficult to predict without the use of complex computer models.

Three different computer models for the metamaterial wedge sample are presented in this thesis. The first model, a simple model that includes only three of the eleven steps in width, shows some interesting behavior, but the simulation is run with the opposite polarization than what causes the unique behavior in this type of DNG metamaterial. Furthermore, the simple model is run at 500 MHz frequency samples, and the results are interpolated at a 100 MHz rate. This interpolation reduces the resolution of the global RCS plots and blurs out many of the features.

The second model is a seven-step model that only includes one unit cell in depth at the smallest step. The real wedge is six unit cells deep at the smallest step. This model seems to be the largest wedge model that the frequency solver can handle on AFIT's computers. Larger models ran into memory and convergence issues. Unlike the smaller model, this model is run with the correct incident polarization. Moreover, this model is run at a 100 MHz sample rate near the resonance band. Because this model does not include the full depth of the wedge, the attenuation of the incident fields is not as great and more scattering is seen inside the resonance band. Plots of the electric fields show that little penetration into the wedge occurs below the resonance band as predicted by the  $S$ -parameters. Inside the resonance band, it appears that the fields do penetrate the wedge. Global RCS patterns, range data, and ISAR images from this model show that specular reflection off of the face of the wedge dominates transmission through the wedge. Thus, the results of this model do not seem to match the results of the effective medium predictions since they did not analyze the relative strength of the transmitted fields.

The third model encompasses an entire 2-D slice of the metamaterial wedge. This model is run using the transient solver and the results show much of the same phenomena that the mid-sized model shows. Because this model includes the full width

of the wedge, the transmitted fields in the resonance band are more attenuated, so resonance effects are harder to observe. It is interesting to note, however, that the transient and frequency solvers do not predict exactly the same resonance bands. The resonance band predicted by the transient solver is about 0.5 GHz lower than the resonance band predicted by the frequency solver.

The computational models presented in this chapter predict similar results. In Chapter IV, the computational results are compared to actual measurements. It is shown that the computational results display much of the same phenomena seen in the measurements. One of the benefits of using a full-wave solver is the ability to see the electromagnetic field results, which help explain the RCS observations. This is one of the key reasons that full-wave electromagnetic solvers, and the FIT in particular, are so useful for characterizing field behavior in metamaterial structures.

### 3.5 Basic AFIT Adaptive Metamaterial Models

AFIT-designed adaptive metamaterial structures are modeled using CST MWS®. Four different models are presented: a single structure with periodic boundary conditions, a single structure where the boundary conditions are modified to remove the periodicity, four coplanar cell structures with non-periodic boundaries, and four coplanar cell structures where the unit cells have different geometries. For these models, the MEMS capacitor is modeled using a lumped network element. Modeling the actual MEMS capacitor would be difficult due to how small it is compared to the rest of the structure. The lumped network element demonstrates the basic concept of operation and shows the movement of the resonant frequency relative to the change in capacitance. The models and results are described in this section.

### 3.5.1 One Cell Periodic Model.

The basic metamaterial structure of interest in this paper is shown in Figure 65. It consists of four particles:

- an inner SRR,
- an outer SRR concentric with the inner SRR and arranged such that its gap is on the opposite side from the gap of the inner SRR, and
- two wire traces.

The SRR particles provide a negative permeability at resonance; while the traces provide a negative permittivity at resonance. In the gaps of the SRR particles is a variable capacitor. This is fabricated with a MEMS device and is described in detail in [39]. A few modifications to the dimensions are made in this structure to improve the robustness of the design. The SRR particles and traces are modeled as infinitely-thin PEC surfaces. Attempts to model the SRR particles and traces using a lossy metal with an actual thickness were not successful because the thicknesses of the actual surfaces that are fabricated will be too small relative to the other dimensions of the structure. The resultant mesh was too complicated for fast and accurate modeling. Using the infinitely-thin PEC surfaces provides a clean mesh (see Figure 109(a) in Appendix A).

The substrate is modeled as a dielectric with  $\epsilon_r = 9.4$ . Original fabrications of this device used Sapphire as the dielectric. While the relative permittivity of the model is set close to Sapphire, it should be noted that Sapphire is actually anisotropic. For the model, an isotropic dielectric is assumed. Furthermore, the dielectric is modeled as lossless (Sapphire is nearly lossless, but does have a very small loss tangent).

For this implementation, periodic boundary conditions are assumed in the  $xy$ -plane. This creates the infinite surface portrayed in Figure 65(b). While this may not

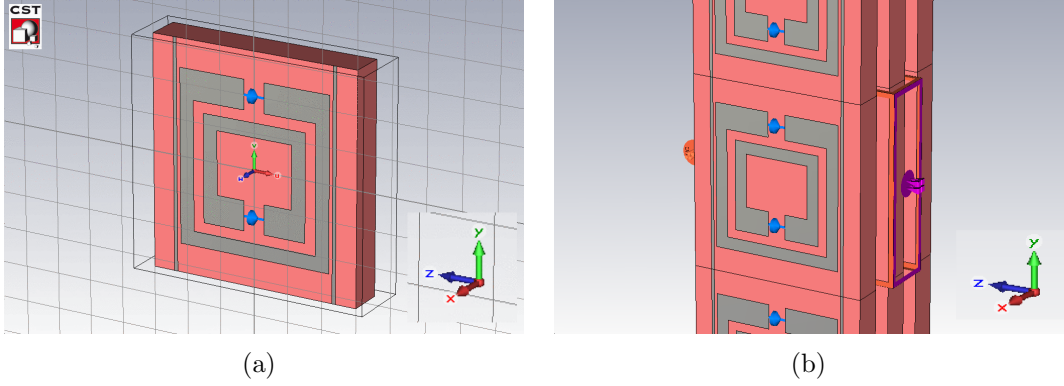


**Figure 65.** CST MWS® model of a single cell variable capacitance SRR metamaterial structure with periodic boundary conditions. (a) The basic structure consists of two concentric SRR particles with variable capacitors over their gaps. There are also two wire traces that run along the sides of the outer SRR. (b) Periodic boundary conditions are used in the  $xy$ -plane.

be the most representative case for modeling a structure in a waveguide, it provides a starting point and allows models of very large structures without increasing the simulation domain. The  $z$ -boundaries are the Floquet ports. These will be the source and measurement areas for the  $S$ -parameter analysis. The  $z$ -plane on the left side of Figure 65(b) corresponds to port 1, while the  $z$ -plane on the right side corresponds to port 2. The reference plane for port 1 is adjusted to be flush with the left face of the surface. Similarly, the reference plane for port 2 is adjusted to be flush with the right face of the surface. The device is swept over a frequency range of 6 to 20 GHz.

The results of the  $S$ -parameter analysis for the model are shown in Figure 66. The magnitudes of  $S_{11}$  and  $S_{21}$  cross near 6 GHz and again at 15 GHz. These are the resonant frequencies. There also appears to be some resonant behavior near 12 GHz, though it is not as strong. It is interesting to note that in the previous DNG structures modeled,  $S_{21}$  remained near one after the resonant frequency. Here,  $S_{21}$  dips back down to near zero after each resonant frequency.

Using the parameter extraction code described in Appendix C,  $n$  and  $z$  were extracted from the  $S$ -parameters. The results of the extraction are shown in Figure

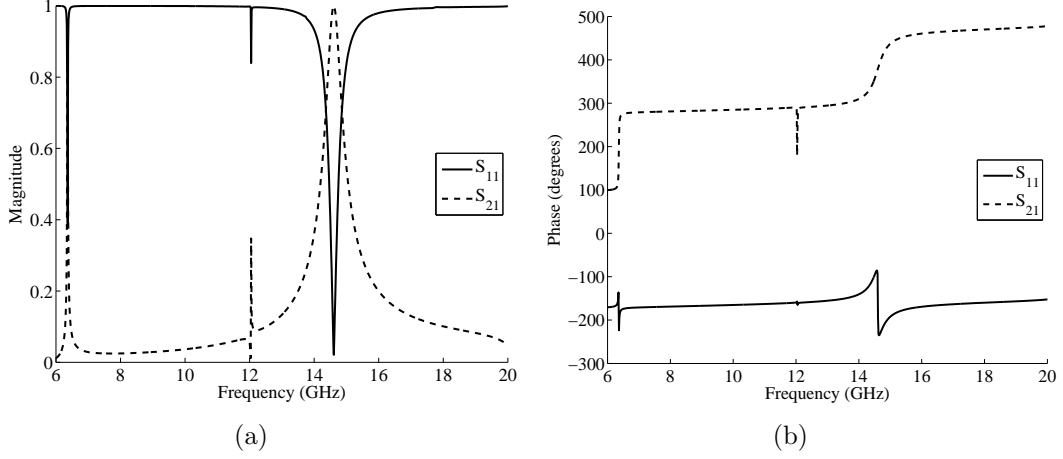


**Figure 66.**  $S$ -parameter results from the single cell periodic model. (a) The magnitudes of  $S_{11}$  and  $S_{21}$  show resonance points near 6 and 15 GHz. (b) The phases of  $S_{11}$  and  $S_{21}$ .

67. The results confirm negative refractive index occurs near 6 GHz, 12 GHz, and 17 GHz. It is possible that the 17 GHz negative refraction band is actually just an extraction problem. At the earlier mentioned resonance point of 15 GHz, the refractive index does increase.

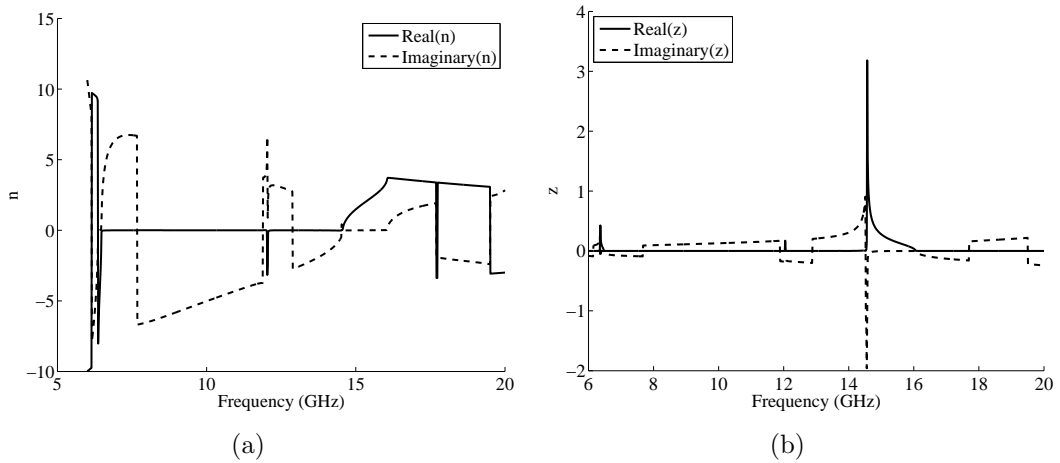


**Figure 67.** The extracted index of refraction (a) and impedance (b) for the single cell periodic structure. The index of refraction and impedance were extracted using the method described in Section 2.3.5.

The relative permittivity and permeability are calculated using the extracted values of  $n$  and  $z$ . Figure 68(a) shows  $\epsilon_r$ . Large negative permittivity values are gener-

ated near the low end of the frequency band. Near 14 GHz, the relative permittivity becomes positive. The permittivity continues to climb until it reaches a maximum near 17 GHz, where it rapidly turns negative. Figure 68(b) shows  $\mu_r$ . At the 6 GHz resonance point, the relative permeability is negative.

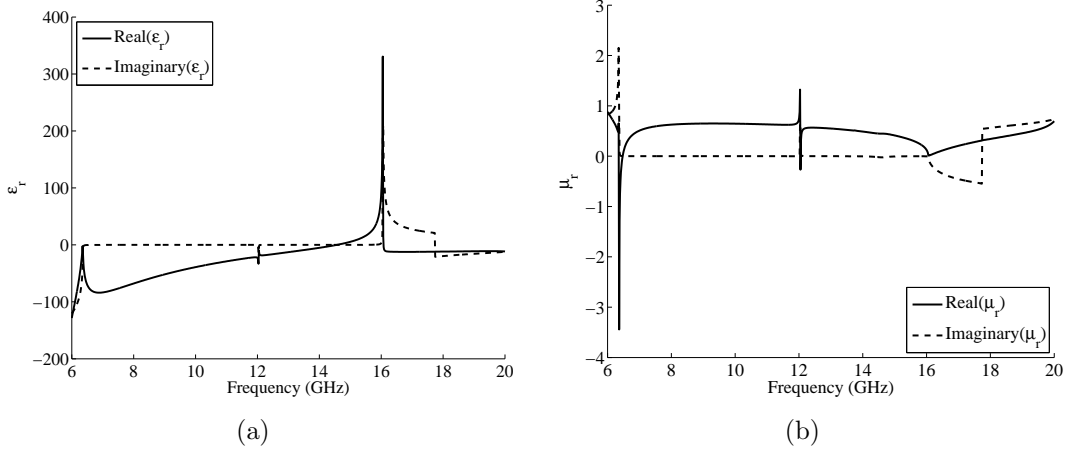


**Figure 68.** The extracted relative permittivity (a) and permeability (b) calculated from  $n$  and  $z$  of the single cell periodic structure.

### 3.5.2 One Cell Non-Periodic Model.

The next step in modeling the AFIT structure is the removal of the periodic boundary conditions which removes the coupling between the SRR particles of different layers. Otherwise, the structure of this section is the same as the previous. Here, the boundary conditions in the  $x$ -direction are set to open; while the boundary conditions in the  $y$ -direction are set to PEC. In this and the following models, the Floquet ports are replaced by waveguide ports. Like before, the reference planes of the ports are set flush with the faces of the structure. The amount of space inserted into the model between the surface and the  $y$ -directed boundary conditions is of critical importance. If not enough space is allowed, the ports will not capture all of the energy at the resonance points. If too much space is inserted, additional modes will be generated in the ports [54]. After experimentation it is found that the best results

are found when the width of the computational domain is set equal to the width of the large SRR. The boundary conditions and spacing are summarized in Table 8.

**Table 8. Non-periodic adaptive AFIT metamaterial model boundary conditions and spacing.**

Boundary Normal	Condition	Spacing from Edge ( $\mu\text{m}$ )
$\pm x$	Open	957.5
$\pm y$	PEC	0
$+z$	Open (waveguide port 1)	200
$-z$	Open (waveguide port 2)	200

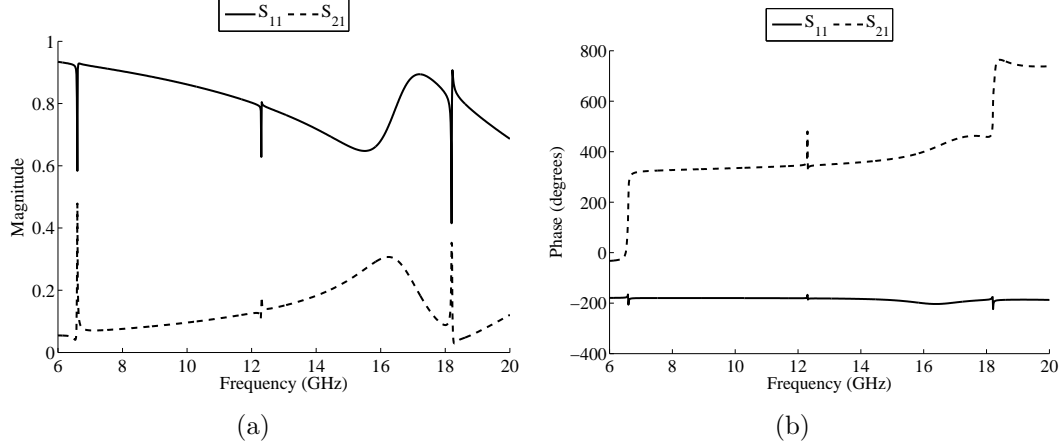
As in the other simulations, the frequency domain solver is used. For this structure, the lowest-order mode is TEM with  $\mathbf{E}$  vertically polarized. Experiments were conducted with the transient solver, but the resonance of the structure will not allow the transient solver to reach steady-state in a reasonable amount of pulses (steady-state was not achieved even when the maximum number of pulses was increased to 200). The computational mesh is shown in Figure 109 of Appendix A.

Figure 69 shows the results of the  $S$ -parameter analysis. Here, strong resonant points are at 6 GHz and 18 GHz. There also appears to be some resonant behavior near 12 GHz. Like before, the magnitude of  $S_{21}$  falls back to near zero after each resonant point.

The purpose of this and the remaining models is to locate the resonant frequencies and see how they move as the extra capacitor is adjusted. Because of this and the fact that these are not models of bulk media, extractions for  $n$ ,  $z$ ,  $\epsilon_r$ , and  $\mu_r$  are omitted.

### 3.5.3 Four Cell, Single Geometry Non-Periodic Model.

While the previous structure is closer to representing a waveguide measurement, the structure to be measured in AFIT's stripline will be several layers thick. Adding additional layers increases the computational domain and, therefore, the amount of simulation time. Thus, a trade off between computational time and simulation



**Figure 69.**  $S$ -parameter results from the single cell non-periodic model. (a) The magnitude of  $S_{11}$  and  $S_{21}$  show resonance points near 6, 12, and 18 GHz. (b) The phase of  $S_{11}$  and  $S_{21}$ .

accuracy exists. In the model presented in this section, a four-cell structure is chosen. This structure was created by mirroring the previous structure three times. Thus, the dimensions of the particles are identical.

The same boundary conditions and spacing from the previous model are used here (see Table 8). This makes the model resemble a parallel plate waveguide. The computational mesh is shown in Figure 109 of Appendix A.

Figure 70 shows the results of the  $S$ -parameter analysis. Here, two different capacitance values are used for the variable capacitors (0.0001 pF and 0.01 pF). The additional capacitance in this structure is in series with the capacitance between the SRR particles. The equivalent capacitance, given by Equation (41), increases with the additional capacitance. The resonant frequency, related to the capacitance by Equation (35), decreases as the additional capacitance increases.

A zoomed-in view near 6.5 GHz of the magnitude of  $S_{11}$  is shown in Figure 71. The dips in the magnitude of  $S_{11}$  correspond to the resonant frequencies of the structure with the additional capacitance. As expected, Figure 71 shows that the resonance frequencies decrease when the additional capacitance increases, though the effects



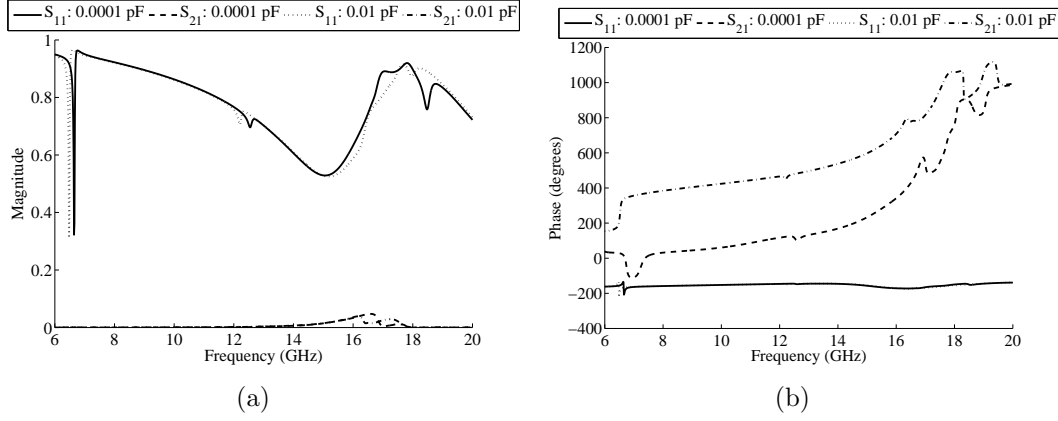


**Figure 70.**  $S$ -parameter results from the the four cell non-periodic model. (a) The magnitudes of  $S_{11}$  and  $S_{21}$  with additional capacitances of 0.0001 pF and 0.01 pF introduced. The resonant frequency decreases when the additional capacitance increases. (b) The phases of  $S_{11}$  and  $S_{21}$ .

are not that strong. The change in resonant frequency between the two capacitance values is 0.168 GHz. This is a difference of approximately 2.5%.

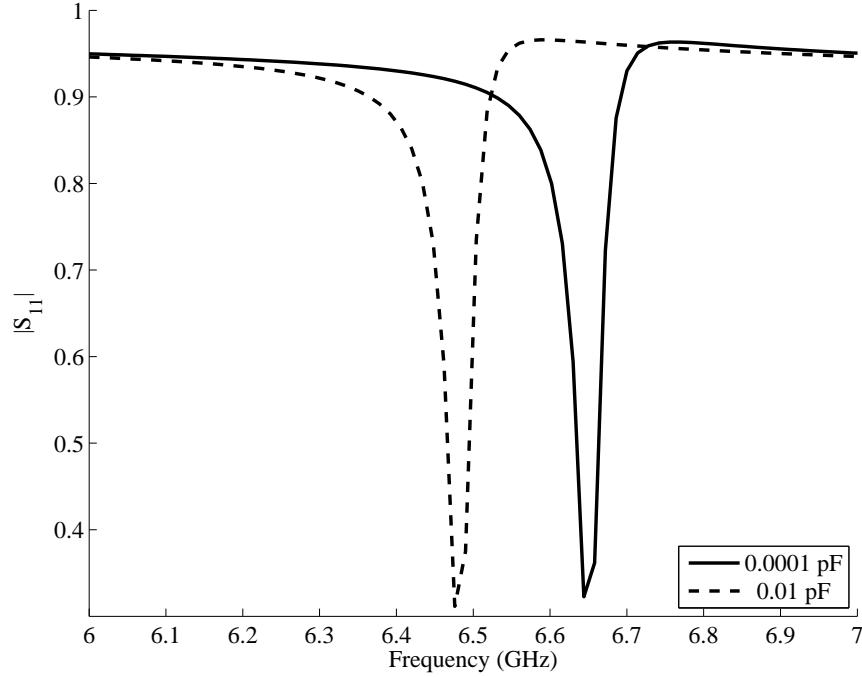


**Figure 71.** The dips in the magnitudes of  $S_{11}$  show the effect changing the additional capacitance value has on the resonant frequency. With an additional capacitance value of 0.0001 pF, the resonant frequency is slightly above 6.6 GHz. With an additional capacitance of 0.01 pF, the resonant frequency is just below 6.5 GHz.

### 3.5.4 Four Cell, Double Geometry Non-Periodic Model.

Another proposed structure attempts to increase the bandwidth of the resonance points by implementing multiple geometries. One way to do this is to create two different sizes of SRR pairs and arrange them in a periodic structure. Figure 72 shows the model of such a structure. The SRR pairs in the first and third cells are the same size as the SRR pairs in the previous models. The smaller SRR pairs in the second and fourth cells are 45% the size of the SRR pairs in the first and third cells. The smaller SRR pairs are turned at different angles.

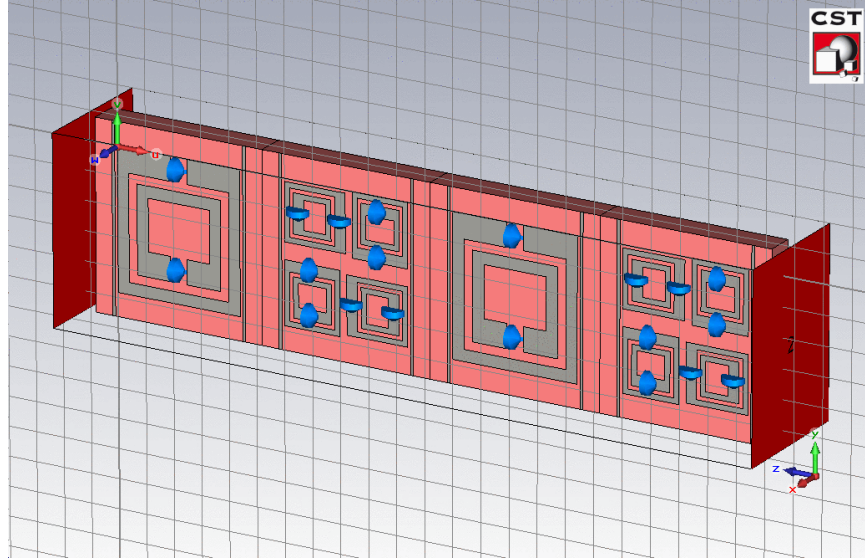


**Figure 72.** CST MWS® model of a double geometry, four cell, non-periodic metamaterial device. The SRR particles in the second and fourth cells are scaled versions of the SRR particles in the first and third cells.

The boundary conditions and spacing are identical to those of models described previously and are shown in Table 8. The computational mesh for this model is shown in Figure 109(d) of Appendix A. The frequency domain solver was again used in this analysis. An incident TEM mode is chosen. Here,  $\mathbf{E}$  is vertically polarized.

Figure 73 shows the results of the  $S$ -parameter analysis for additional capacitance values of 0.0001 pF and 0.01 pF. The same additional capacitance values are used for all of the variable capacitances. As seen in the previous section, the resonance

frequency decreases as the additional capacitance increases.

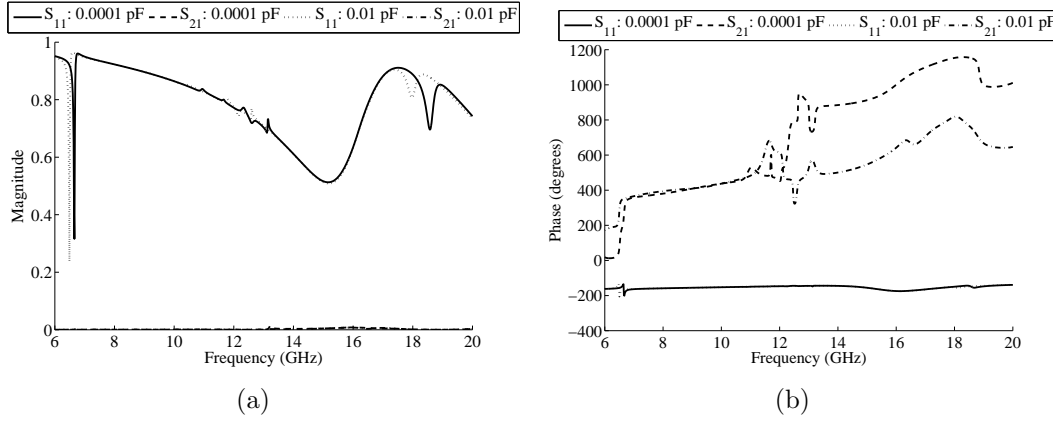


**Figure 73.**  $S$ -parameter results from the four cell non-periodic model with two different geometries. (a) The magnitudes of  $S_{11}$  and  $S_{21}$  with additional capacitances of 0.0001 pF and 0.01 pF introduced. (b) The phases of  $S_{11}$  and  $S_{21}$ .

In theory, the variation in the size of the SRR pairs in this structure is supposed to enlarge the resonance bands. The different sizes lead to different resonant frequencies. This should increase the amount of frequencies for which the structure resonates. However, the results in this section do not appear to have larger resonance bands than what was found in the previous sections.

### 3.6 Advanced AFIT Adaptive Metamaterial Structure Models

The AFIT adaptive metamaterial structures presented in the previous sections are designed with the intention that they would be tested using a stripline waveguide designed for operation up to 20 GHz. However, the center conductor of the 20 GHz stripline is not very rigid making it difficult to get repeatable measurements using that stripline. To get more consistent measurements, a larger waveguide is used. Figure 74 shows the larger stripline. The center conductor of this stripline is much more rigid.

The drawback of the larger stripline is that the higher-order modes have lower cut-off frequencies than in the smaller waveguide. These higher-order modes complicate



**Figure 74. AFIT's large stripline.**

the process of parameter extraction. If the faces of the center and outer conductors are normal to the  $y$ -axis, the wavenumber along the  $y$ -axis ( $k_y$ ) determines the cutoff values for the higher-order modes. To see this, note that the propagation constant inside the stripline ( $\beta_{sl}$ ) is [36, 135]

$$\beta_{sl} = \sqrt{k^2 - k_c^2}, \quad (49)$$

where the cutoff wavenumber ( $k_c$ ) is determined by the wavenumbers along the bound directions. If  $k$  is less than  $k_c$ ,  $\beta_{sl}$  becomes imaginary and propagation can not take place. Since propagation in the  $y$ -direction is bound by the outer conductors of the stripline,  $k_c = k_y$ , and  $k_y$  for the  $m$ -th mode is given by [50]

$$k_y = \frac{m\pi}{b}, \quad (50)$$

where  $b$  is the distance between the outer conductors of the stripline. The wavenumber is related to frequency by  $k = 2\pi f/c$ . Thus, the cutoff frequency ( $f_c$ ) for the  $m$ -th

mode is

$$f_c = \frac{mc}{2b}. \quad (51)$$

For the large stripline,  $b$  is 34.7 mm; thus, the cutoff frequency of the first higher-mode is 4.32 GHz. Therefore, parameter measurements in the large waveguide are best accomplished below 4 GHz where only a single mode is present.

### 3.6.1 Empty Stripline Model.

To verify the operation of the stripline and gain some insight into its frequency modes, a cross-sectional model of the stripline is constructed using CST MWS®. Figure 75 shows the model. The cross-sectional dimensions of the structure are true to the actual stripline. The shorting pins have been included in the model. All metal pieces are modeled as PEC. All boundaries are set to open. The length of the center conductor in the  $z$ -direction is three times the length of a metamaterial strip that is four times larger than the original strip. To reduce the computational requirements for this model, a magnetic symmetry condition has been placed on the  $xz$ -plane at  $y = 0$  (corresponds to the center of the center conductor). Therefore, CST MWS® assumes that the fields of the top half of the model are identical to the fields in the bottom half of the model. Similarly, another magnetic symmetry plane is placed in the  $yz$ -plane at  $x = 0$ . There is no symmetry in the  $xy$ -plane. The mesh statistics are shown in Table 16 and the computational mesh for this model is shown in Figure 110 of Appendix A.

The results of the simulation of the CST MWS® model are shown in Figure 76. Figure 76(a) shows  $\mathbf{E}$  and  $\mathbf{H}$  at the center cross-sectional plane of the stripline. As expected,  $\mathbf{E}$  radiates in and out of the center conductor, and  $\mathbf{H}$  circles around the center conductor. The magnitudes of  $S_{11}$  and  $S_{21}$  from the model are shown in Figure

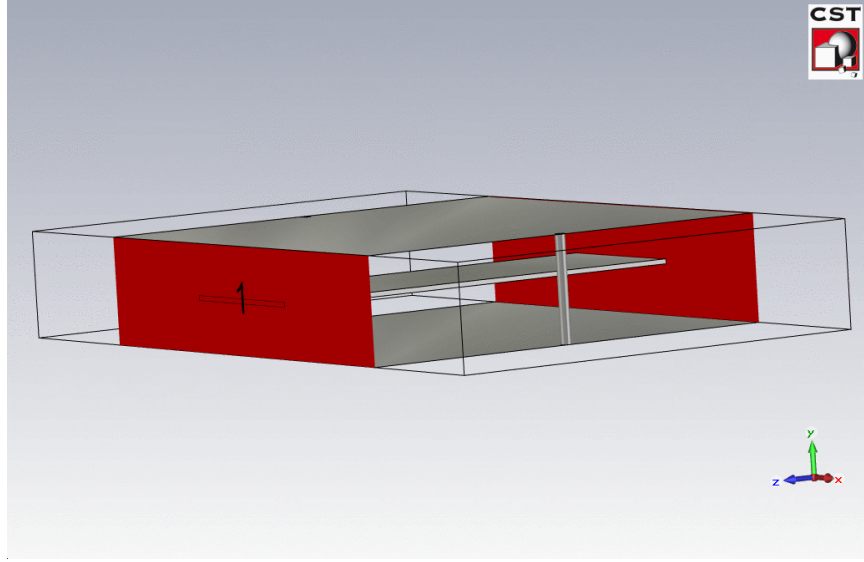


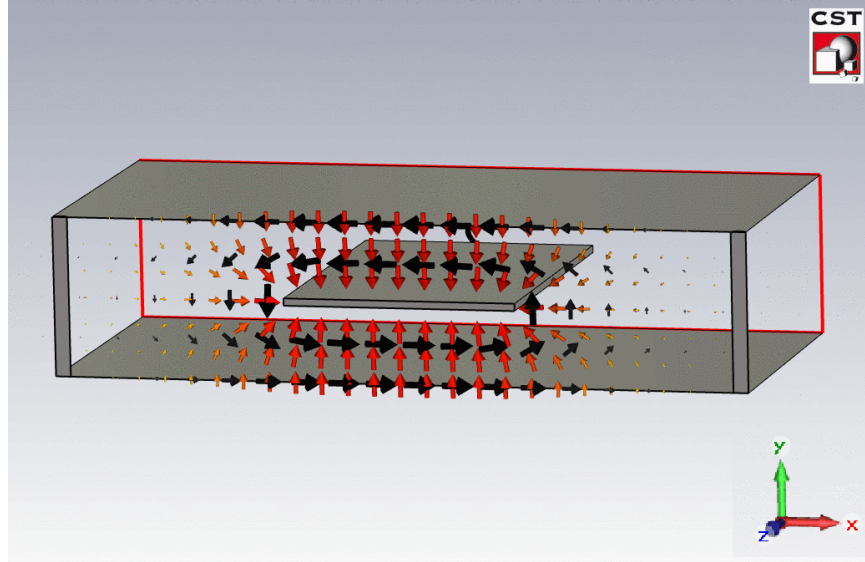
**Figure 75. Model of the empty large stripline. The cross-sectional dimensions of the stripline structure match the physical dimensions of the actual stripline.**

76(b). For an ideal empty stripline,  $S_{11}$  should be close to zero and  $S_{21}$  should be close to one for the frequency span where a single mode is propagating through the stripline. The model results for  $S_{11}$  and  $S_{21}$  match the expected behavior.

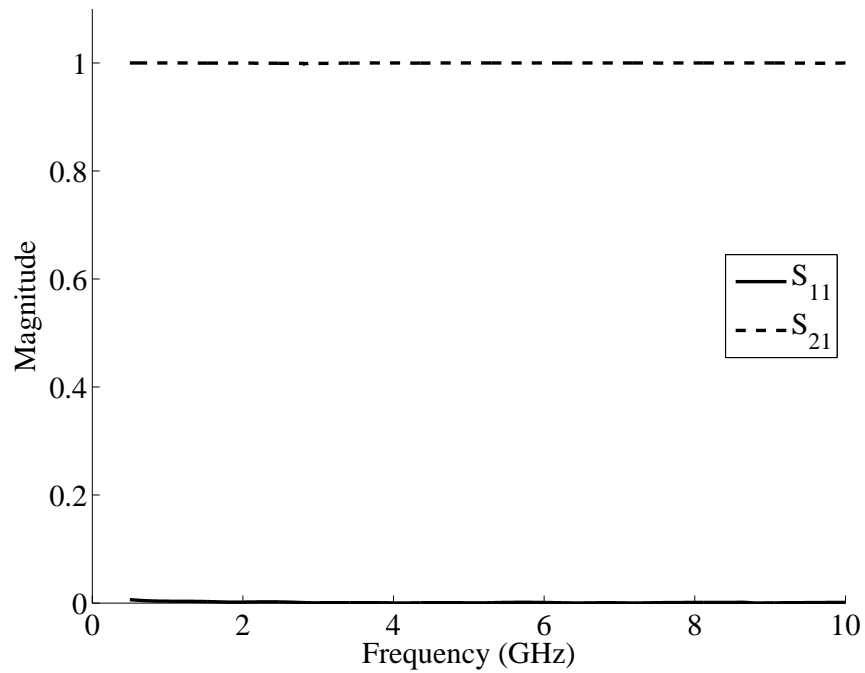
The simulation also reveals that the cutoff frequency for the second mode is about 4.06 GHz. This is close to the 4.32 GHz cutoff frequency calculated above. This confirms that results above 4 GHz should be disregarded.

### 3.6.2 Original-Size AFIT Adaptive Metamaterial Models.

The model of the AFIT adaptive metamaterial structure is placed into the empty stripline model described in the previous section. Figure 77 shows the model. The boundary conditions and symmetry planes for this model are identical to the empty stripline model except that the magnetic symmetry is removed from the  $yz$ -plane. With the control wire traces arranged perpendicular to the stripline's center conductor as shown in Figure 77, a metamaterial slab that is 5 unit cells tall is the largest structure that can fit in the waveguide. To ease some of the computational require-



(a)



(b)

Figure 76. Results from the empty large stripline model. (a)  $E$  (red-orange) and  $H$  (black-gray) at the center cross-sectional plane of the stripline. As expected,  $E$  radiates in and out of the center conductor while  $H$  circles around the center conductor. (b) Magnitudes of  $S_{11}$  and  $S_{21}$  from the empty large waveguide stripline. Ideally,  $S_{21}$  should be one and  $S_{11}$  should be zero. The results match the expected behavior.

ments, the slab is just four unit cells in the  $z$ -direction. The center conductor is scaled in length to be three times longer than the metamaterial slab. Table 16 of Appendix A summarizes the mesh statistics for this model. Figure 111(a) of Appendix A shows the computational mesh.

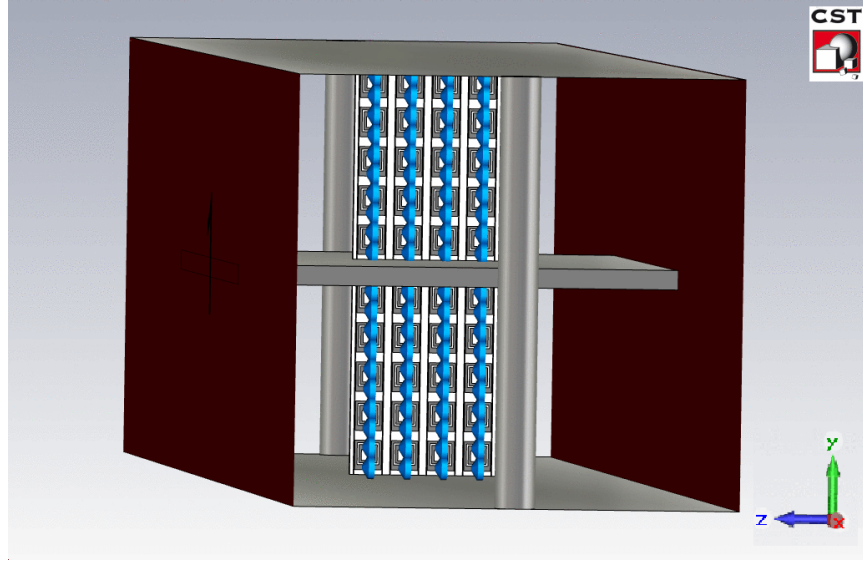


**Figure 77.** Advanced CST MWS® model of the AFIT adaptive metamaterial structure.

All of the previous models use generic values for the lumped element capacitance. For this model, actual capacitance values from the MEMS capacitor are used. In [39], DC measurements of the MEMS capacitor in its various operational states are performed. Measurement of the MEMS capacitor in microwave regime are desired since the capacitance may be different. However, the traces on the MEMS sample are not spaced properly for measurement with high-frequency probes. For this thesis, the measurements in [39, 88] are used. There are minor structural differences between the MEMS device in [39] and this thesis. These differences could lead to small variations in the capacitance between the two designs, but for the purposes of this research the values in [39, 88] should be sufficient.

It should be noted that in [39] the MEMS samples had problems with the beams not flexing properly when they were activated. That problem should be mitigated



in the next design iteration. To get the capacitance of the MEMS device in its intended operational state, probes were used to push down the beams. Capacitance measurements were done as the different beams were activated. No measurements of the 325  $\mu\text{m}$  beam are included in [39]. For this thesis, the capacitance for that beam is assumed to be equal to the average of the capacitance of the other beams. The capacitance values used in these models are shown in Table 9.

**Table 9. Measured capacitances for MEMS device.**

State	Activated Beams	Capacitance (pF)
1	None	0.12
2	300 $\mu\text{m}$	0.77
3	300 and 325 <sup>1</sup> $\mu\text{m}$	1.36
4	300, 325 <sup>1</sup> , and 350 $\mu\text{m}$	1.90
5	300, 325 <sup>1</sup> , 350, and 375 $\mu\text{m}$	2.52
6	300, 325 <sup>1</sup> , 350, 375, and 400 $\mu\text{m}$	3.06

<sup>1</sup> The 325  $\mu\text{m}$  beam capacitance is estimated with the average of the other beam capacitances. The other beam capacitances are measured in [39, 88].

Figure 78 shows the  $S$ -parameter results from this model for each of the capacitance values shown in Table 9. There is a lot of erratic behavior in the data, possibly indicating the presence of multiple modes. There appears to be a resonance point near 2.25 GHz, but there is too much erratic behavior to clearly determine the resonance points.

The model is modified to add two more metamaterial strips parallel to the two already in the model (two strips above the center conductor and two strips below the center conductor) to determine the effects of non-coplanar coupling. The strips are spaced such that they are separated by a distance equal to the width of one unit cell. The computational mesh for this model is shown in Figure 111(b) and the statistics are shown in Table 16 of Appendix A. The  $S$ -parameter results from this model are very similar to the results from the previous model shown in Figure 78. The

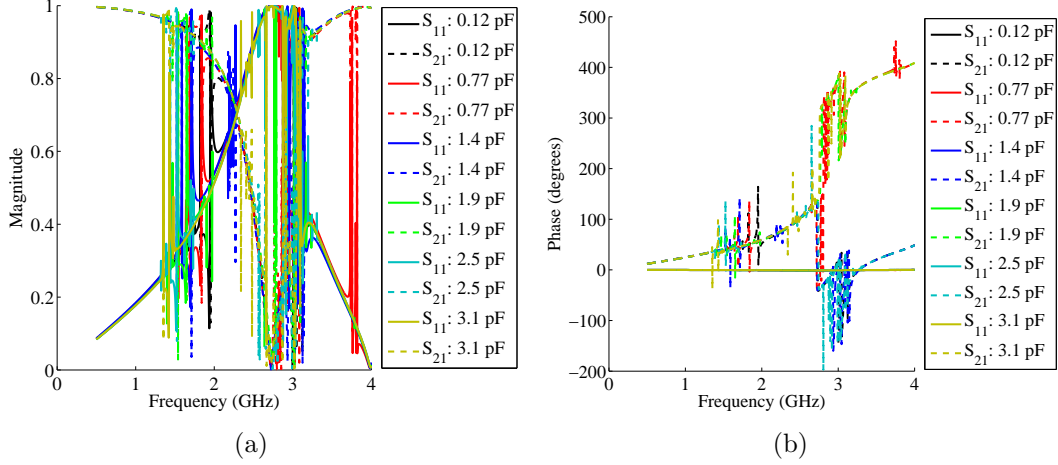


**Figure 78.**  $S$ -parameter results from the advanced model of the original scale AFIT metamaterial structure. The magnitudes (a) and phases (b) of  $S_{11}$  and  $S_{21}$ .

apparent resonance is shifted to about 1.8 GHz. However, like the previous results, the results for this model display too much erratic behavior to accurately determine the resonance points.

### 3.6.3 Larger-Scale AFIT Metamaterial Models.

Because the larger stripline operates in a lower frequency band, the metamaterial structure can be redesigned to match the new frequency band. This means increasing the size of the structure. Unlike a rectangular waveguide, the TEM mode of the stripline has no lower frequency cutoff. So, only the physical size of the stripline restricts how large the structure can be. Scaling the metamaterial structure between four to five times larger than the original design will nearly fill the height of the stripline with a single unit cell.

The relationship between the scale of the metamaterial structure and its resonant frequency can be seen with Equation (10) since the effective  $\mu$  has a larger impact on the negative refraction band than the effective  $\epsilon$ . However, it should be noted that this relationship is only approximately true for this structure since the SRR particles are not round. Scaling both  $d$  and  $r_{SRR}$  by the scaling factor and changing

the substrate to quartz produces the resonant frequency shown in Figure 79. This predicts that a structure that is five times larger than the current design will resonate near 2 GHz. Furthermore, it appears anything scaled at least 2.5 times larger than the current design will have a resonant frequency in the frequency band that is TEM for the stripline.

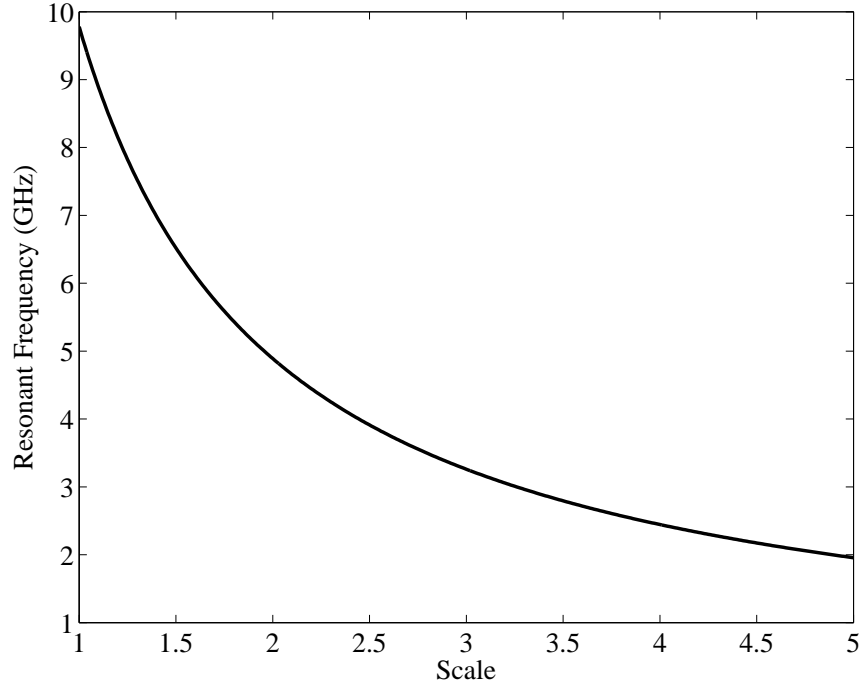


**Figure 79. Resonant frequency as a function of scale for a DNG metamaterial structure. Note that this relationship is only approximate since the SRR particles are not round in the AFIT structure. A scale factor of 5 is the maximum size that will fit in the large stripline.**

### 3.6.3.1 Large Scale Unit Cell Model.

To quickly confirm the results shown in Figure 79, a freespace periodic model is created in CST MWS®. This model is like the periodic model of Section 3.5.1 except that the lumped elements representing the MEMS capacitors have been removed and the size of the structure has been multiplied by a scaling factor. Unit cell boundary conditions are used in the  $\pm x$  and  $\pm y$  directions to simulate an infinite array. The

boundary conditions in the  $\pm z$  directions are the Floquet ports.

This simulation focuses on scaling factors between 4.0 and 5.0. Structures of this size are large enough to be quickly constructed using the laser etcher. The circuit boards for the laser etcher have an FR4 substrate, and that is the substrate used for this model. The magnitudes of  $S_{21}$  for the different scaling factors are shown in Figure 80. The sudden jump in the magnitude of  $S_{21}$  between 2 and 3 GHz occurs at the resonant frequency. Thus, the resonant frequency for the 4.0 scale model is just below 3.0 GHz. Likewise, the resonant frequency for the 5.0 scale is just below 2.5 GHz. The other resonant frequencies fall between those two extremes.

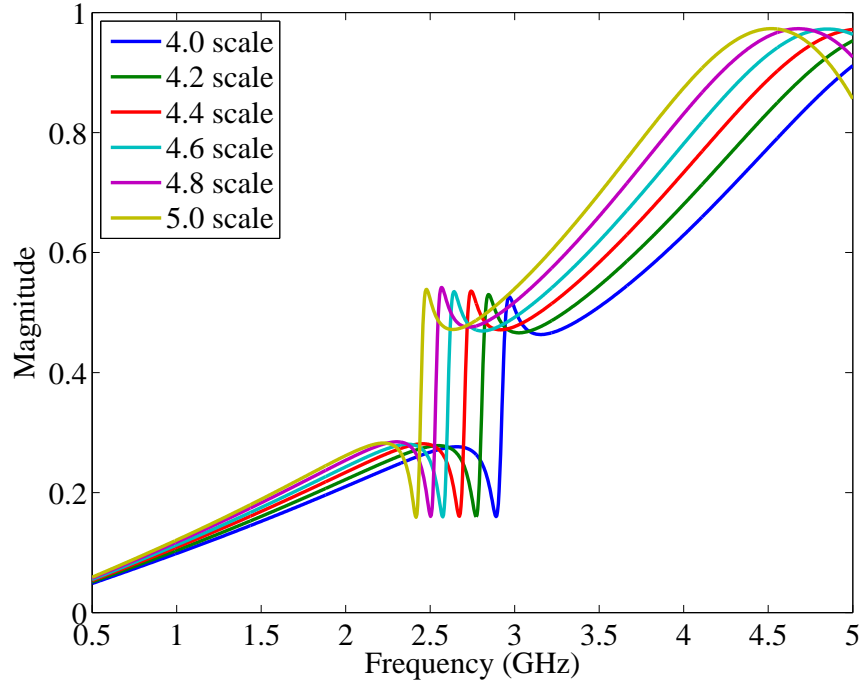


**Figure 80.** Magnitude of  $S_{21}$  at different scaling factors for the larger scale AFIT models with FR4 substrate. The 4.0 scale model produces a resonant frequency just below 3 GHz. The 5.0 scale model produces a resonant frequency just below 2.5 GHz.

### 3.6.3.2 Large-Scale Non-Adaptive Models.

The next step is to place the scaled structures into the true stripline model. The structure for this model at a scale factor of 4.0 is shown in Figure 81. The bound-

ary conditions and symmetry plane for this model are the same as the original-size stripline model. The model is run with scale factors of 4.0 and 4.9. The computational mesh statistics are shown in Table 16 of Appendix A. Figure 112 of Appendix A shows the meshes for this model.

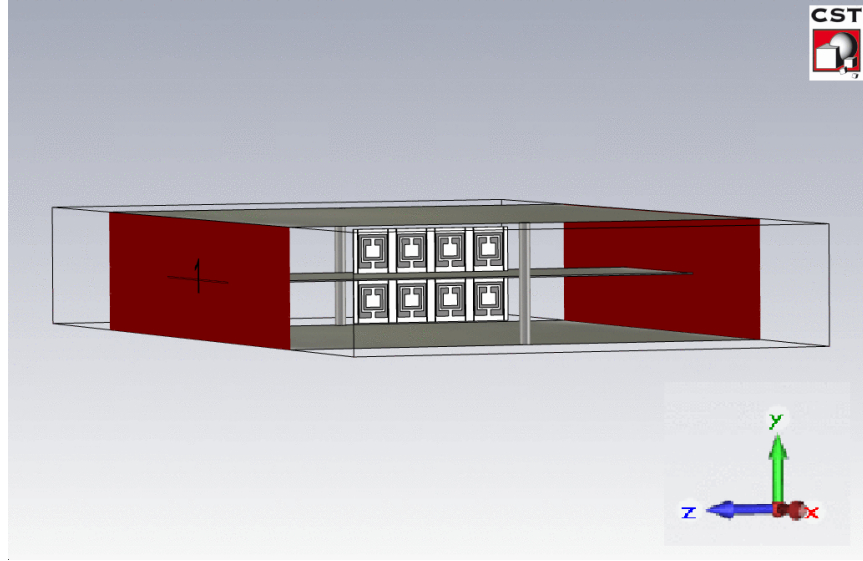


**Figure 81. Advanced CST MWS® model of the AFIT metamaterial structure scaled 4 times larger than the original design.**

The results from the simulation are shown in Figure 82 for scale factors of 4.0 and 4.9. This model has the FR4 substrate. For a scaling factor of 4.0, the  $S$ -parameter results show resonant behavior near 2.5 GHz. As expected, similar resonant behavior occurs at a scaling factor of 4.9, but at lower frequencies. The results also seem to indicate that the metamaterial structures introduce a higher order mode below 4 GHz. This is clearly seen in the electric field. The component of  $\mathbf{E}$  normal to a plane halfway between the center and bottom conductors at 2 GHz for the 4.0 scale factor is shown in Figure 82(c). The fields appear to propagate in the dominant TEM mode for this stripline. Figure 82(c) shows the same component of  $\mathbf{E}$  at 4 GHz. The metamaterial sample perturbs the fields enough that a second mode is introduced.

The model is modified to add two more metamaterial strips parallel to the two

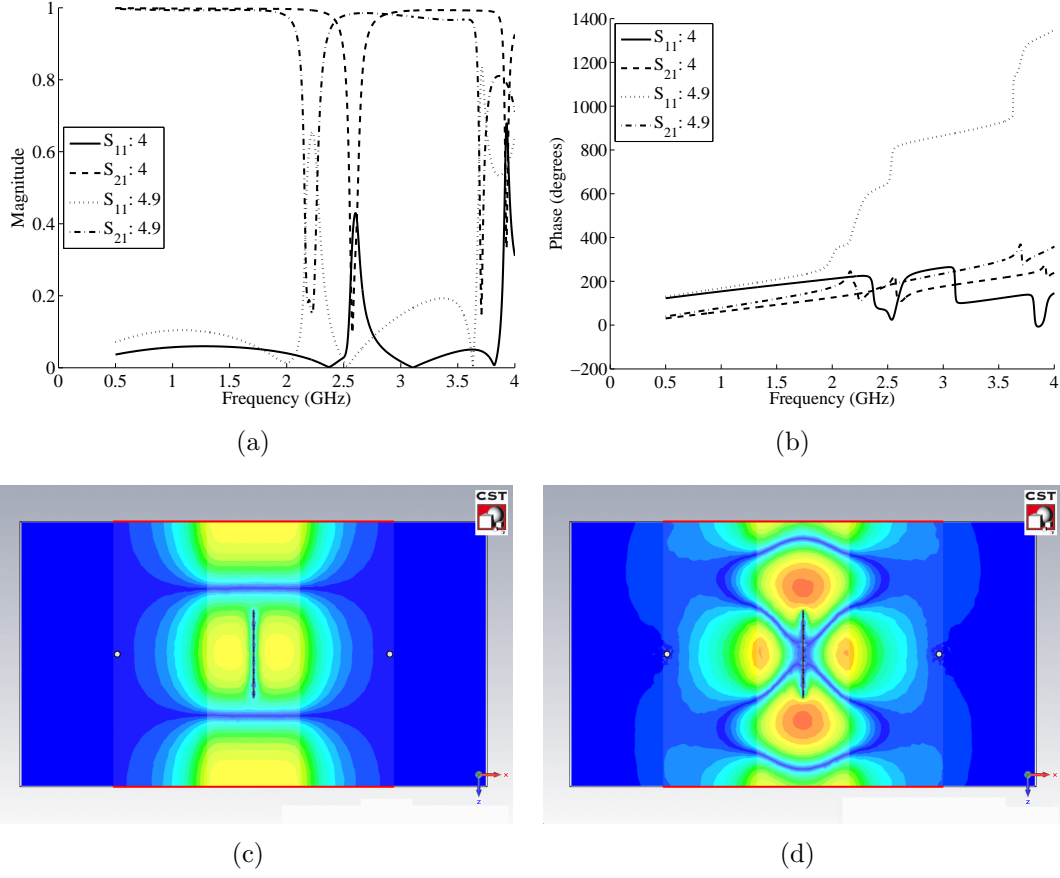


**Figure 82.** Advanced AFIT large scale metamaterial simulation results. (a) The magnitude of  $S_{11}$  and  $S_{21}$  at the 4.0 and 4.9 scale factors. (b) The phase of  $S_{11}$  and  $S_{21}$  at the 4.0 and 4.9 scale factors. (c) The component of  $E$  normal to a plane half-way between the center conductor and bottom plate at 2 GHz for the 4.0 scale factor shows the dominant mode for this stripline. (d) The same component of  $E$  at 4 GHz shows that the metamaterial structure perturbs the fields enough to introduce a second mode.

already in the model (two strips above the center conductor and two strips below the center conductor) to determine the effects of non-coplanar coupling. The strips are spaced such that they are separated by a distance equal to the width of one unit cell. Scale factors of 4.0 and 4.9 are used in the model. Again, the substrate is FR4. The computational mesh for this model is shown in Figure 112 and the statistics are shown in Table 16 of Appendix A.

The  $S$ -parameter results are shown in Figure 83. The results are similar to the two-strip model shown in Figure 82. The resonance frequencies are the same here as

in the previous model. The key differences occur in the resonance band. Inside the resonance band, the four-strip model shows a larger resonance effect: the dip in  $S_{21}$  is lower and the corresponding peak in  $S_{11}$  is greater in magnitude. The bulk behavior of the structure is more evident in this model because another dimension is added to the periodicity.

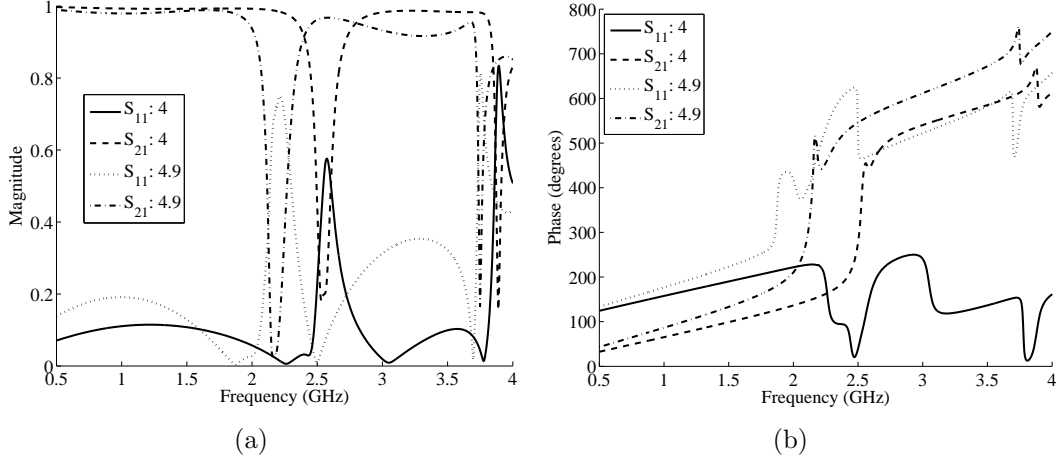


**Figure 83. Advanced AFIT large-scale non-adaptive metamaterial four-strip model  $S$ -parameter results. The results appear very similar to the two-strip model. The magnitudes (a) and phases (b) of  $S_{11}$  and  $S_{21}$  for the 4.0 and 4.9 scale factors.**

### 3.6.3.3 Large-Scale Adaptive Models.

Models of the AFIT adaptive metamaterial design at the 4.0 and 4.9 scale factors in the stripline were created in CST MWS®. Like the structures that will be built, the models have a quartz substrate. Like the previous adaptive metamaterial models, these models use lumped network elements to model the MEMS capacitors. The capacitors for these models are assumed to be the same as the capacitances in the smaller-scale models and are shown in Table 9. The first set of models have two strips total—one above the center conductor and one below. The computational meshes for these models are shown in Figures 113(a) and 113(b) in Appendix A. Table 16 in Appendix A shows the mesh statistics.

The results of the simulation clearly show the change in resonant frequency at each capacitance value. Figure 84 shows the magnitude of  $S_{21}$  for the 4.0 and 4.9 scale factors. The dips in  $S_{21}$  show the resonant frequencies. The resonant frequencies for the 4.0 scale structure are approximately 2.17, 1.26, 0.995, 0.833, 0.752, and 0.680 GHz for additional capacitances of 0.12, 0.77, 1.36, 1.90, 2.52, and 3.06 pF, respectively. Likewise, the resonant frequencies for the 4.9 scale structure are approximately 1.93, 1.12, 0.883, 0.761, 0.667, and 0.608 GHz for additional capacitances of 0.12, 0.77, 1.36, 1.90, 2.52, and 3.06 pF, respectively.

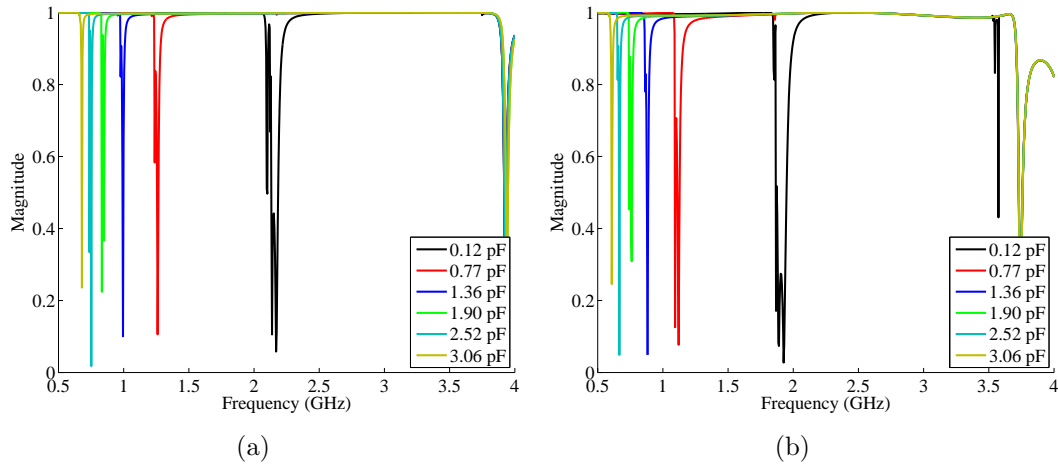


**Figure 84. Results for the large-scale AFIT adaptive metamaterial model. (a) The dips in the magnitudes of  $S_{21}$  show the resonant frequencies at each capacitance for the 4.0 scale model. (b) The magnitudes of  $S_{21}$  show that the resonant frequencies for the 4.9 scale model are lower.**

Like before, two strips are added to each model to create a total of four strips (two above and two below the center conductor). The mesh statistics for these models are shown in Table 16 and the computational meshes are shown in Figure 113(c) and 113(d) in Appendix A.

The results of these models are very similar to the results of the two-strip models. Figure 85 shows the magnitudes of  $S_{21}$  for the 4.0 and 4.9 scale structures. The resonant frequencies are very close to the two-strip models. The resonant frequencies for



the 4.0 scale structure are 2.15, 1.24, 0.977, 0.838, 0.739, and 0.671 GHz for additional capacitances of 0.12, 0.77, 1.36, 1.90, 2.52, and 3.06 pF, respectively. Similarly, the resonant frequencies for the 4.9 scale structure are 1.89, 1.11, 0.874, 0.752, 0.658, and 0.604 GHz for additional capacitances of 0.12, 0.77, 1.36, 1.90, 2.52, and 3.06 pF, respectively.

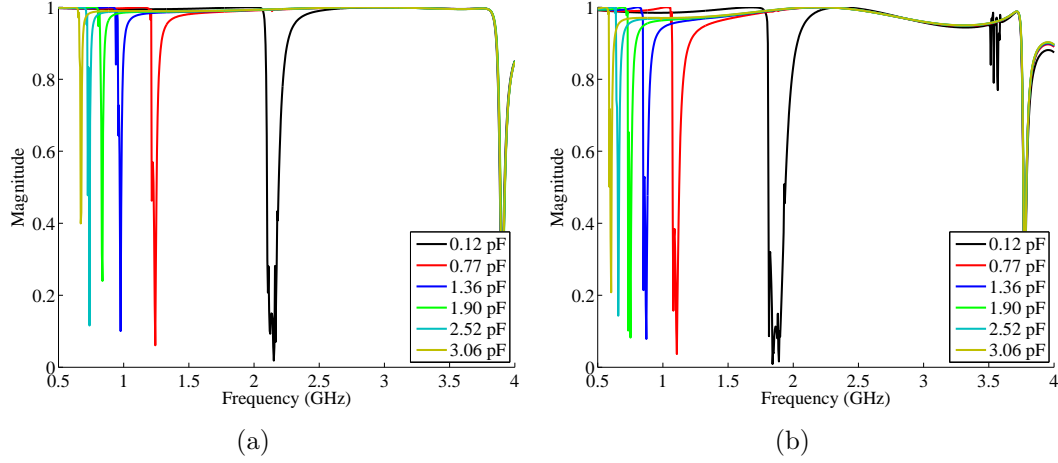


**Figure 85. Results for the large-scale AFIT adaptive metamaterial four-strip model. (a) The dips in the magnitudes of  $S_{21}$  show the resonant frequencies at each capacitance for the 4.0 scale model. (b) The magnitudes of  $S_{21}$  for the 4.9 scale model show that the resonant frequencies are lower.**

The results of the four-strip models match the two-strip model results closely. Table 10 shows the resonant frequencies and the percentage difference between the results of the four-strip and the two-strip models. The maximum difference is slightly over 2%. Differences between the two models could also be due to human error in selecting exactly where the resonance occurs.

### 3.6.4 Advanced AFIT Metamaterial Model Conclusions.

The advanced stripline models provide a powerful tool to explore electromagnetic field behavior in metamaterials. The empty stripline model accurately predicts the propagating modes, including the cutoff frequencies. The  $S$ -parameters from the

**Table 10. Resonant frequencies for large-scale adaptive metamaterial models**

Scale	Capacitance (pF)	Two-Strip Model	Four-Strip Model	Difference (%)
		$f_0$ (GHz)	$f_0$ (GHz)	
4.0	0.12	2.17	2.15	0.92
	0.77	1.26	1.24	1.59
	1.36	0.995	0.977	1.81
	1.90	0.833	0.838	0.60
	2.52	0.752	0.739	1.73
	3.06	0.680	0.671	1.32
4.9	0.12	1.93	1.89	2.07
	0.77	1.12	1.11	0.89
	1.36	0.883	0.874	1.02
	1.90	0.761	0.752	1.18
	2.52	0.667	0.658	1.35
	3.06	0.608	0.604	0.66

empty stripline model show that the operation of the stripline between 0 and 4 GHz is very close to ideal. The model results also confirm that results for the large stripline above 4 GHz should be disregarded

The results from the model of the original-size AFIT adaptive metamaterial structure show a lot of erratic behavior. Furthermore, when two additional strips are added to the model, the resonant frequency shows a significant change. This behavior is not seen in other models. This could indicate that the resonant behavior seen in the  $S$ -parameters is not the true resonance. Rather, the behavior seen below 4 GHz may be due to higher order modes caused by the metamaterial structure disturbing the electromagnetic fields. Moreover, resonance of the SRR particles in the original-scale is not expected below 4 GHz. Changing the variable capacitor in accordance with the measured values of the MEMS capacitor does not appear to have a significant impact on the resonant frequency.

To see the resonant behavior of metamaterial structure in the large stripline, a larger metamaterial structure is necessary. In this chapter it is shown that structures that are four to five times larger than the original structure move the resonant be-

havior below 4 GHz. The largest structure that will fit in the stripline is between 4.9 and 5 times larger than the original structure, so the analysis here focused on scale factors of 4.0 and 4.9. Models of passive metamaterial structures show that the resonant frequencies are below 4 GHz. The resonant frequency for the 4.0 scale structure is just above 2.5 GHz, while the resonant frequency for the 4.9 scale structure is near 2.25 GHz. It should be noted that the metamaterial structures also cause a small reduction in the cutoff frequency for the higher-order modes. The disturbance of the fields cause the higher order modes that most likely would die out before they can propagate to the second port in the full-size stripline. In the shorter-length model of the stripline, the higher order modes can reach the second port. However, these higher-order modes do not obstruct the resonant behavior.

The four-strip models of the 4.0 and 4.9 scale passive metamaterial structures show very similar behavior as the two-strip models. The resonant frequencies are very close to the same. The largest difference is in the heights and depths of the peaks and valleys of  $S_{11}$  and  $S_{21}$  at resonance. The coupling between the non-coplanar slabs increases the resonance behavior. Thus, at resonance  $S_{11}$  has a higher peak and  $S_{21}$  has a deeper valley.

The results of the large-scale adaptive metamaterial structure are very interesting. The resonant behavior of the structure is clearly evident below 4 GHz. Furthermore, the resonant frequency appears to be highly influenced by the parallel capacitor. Figure 86 shows the resonant frequency of the 4.0 and 4.9 scale models at the measured values of the MEMS capacitor. The resonant frequency is inversely proportional to the capacitance. The capacitance between the two SRR particles is in series with the MEMS capacitor, and their equivalent capacitance is given by Equation (41). Note that here  $C$  refers to the capacitance between the two SRR particles. As a consequence of Equation (41), the equivalent capacitance increases with the MEMS

capacitor. Furthermore, Equation (35) shows that the resonant frequency is inversely proportional to the equivalent capacitance. Thus, the trends in the resonant frequencies shown in Figure 86 are expected.

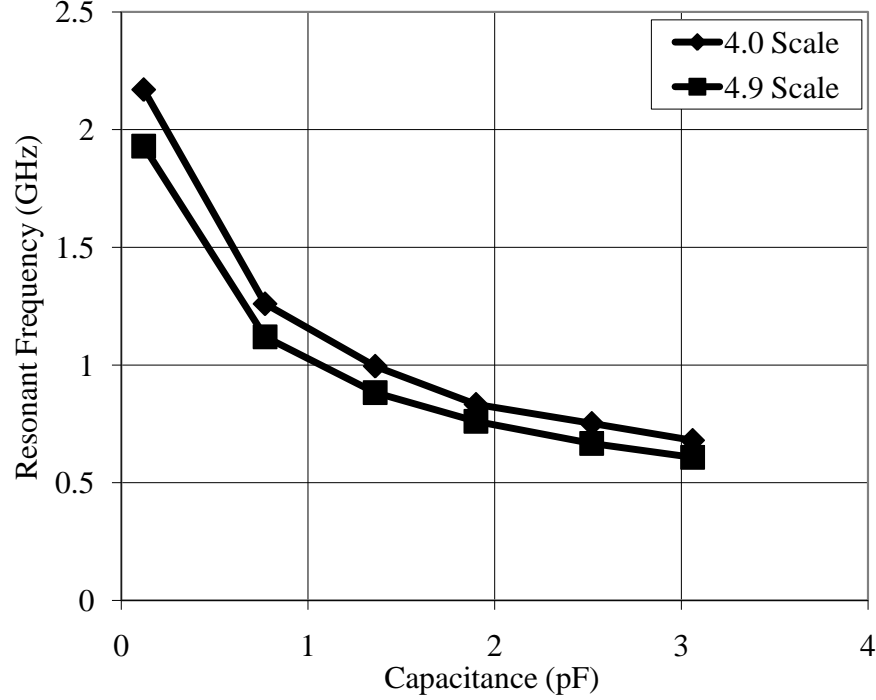


**Figure 86. Resonant frequencies for the large scale AFIT adaptive metamaterial designs as a function of MEMS capacitance.**

Analyzing Equation (40) reveals that if  $C$  is small, the denominator is close to  $C_{VC}$ . That will approximately cancel out the  $C_{VC}$  term in the numerator. In that scenario, changes in the variable capacitor will have minimal effect on the equivalent capacitance. The capacitance per unit length between the two SRR particles ( $C_l$ ) is given by [32]

$$C_l = \frac{\epsilon_0}{\pi} \ln \frac{2w}{d}. \quad (52)$$

Multiplying  $C_l$  by the length of the SRR particles (roughly  $2\pi r_{SRR}$ ) yields  $C = 2r_{SRR}\epsilon_0 \ln(2c/d)$ . Therefore, multiplying the size of the structure by a scaling factor directly increases the capacitance between the SRR particles. This explains why

the MEMS capacitances cause larger changes in the resonant frequency of the larger designs and not the smaller designs. The capacitance between the SRR particles in the smaller design is small and dominates Equation (40). The capacitance of the larger design is bigger, allowing the variable capacitor to have more influence on the equivalent capacitance.

The stripline model results show that the effectiveness of the variable MEMS capacitor design is very dependent on the size of the structure. In addition to being easier to measure in the large stripline, the larger-scale metamaterial structures also have a larger dynamic frequency range with the current MEMS capacitor design.

## IV. Experimental Measurements

### 4.1 Chapter Overview

This chapter presents data obtained through experimental measurements. Two main measurement efforts are presented: RCS measurements of the metamaterial wedge and stripline measurements of AFIT's adaptive metamaterial design. The setup, measurement procedures, and results are described.

### 4.2 RCS Measurement Procedures and Theory

For this effort, bistatic RCS measurements of a metal plate and the metamaterial wedge are taken and compared. In these measurements, the transmitter remains fixed at an angle of  $0^\circ$  in azimuth. The receiver angle in azimuth ( $\phi$ ) is swept through various angles. Elevation ( $\theta$ ) remains at the waterline ( $\theta = 90^\circ$ ). Different pylon angles are used to create different angles of incidence.

To remove the effects of the background and normalize the response of the radar system it is necessary to calibrate the range measurements against a known standard. For this comparison, measurements of the calibration device background ( $\sigma_{cb}$ ), calibration device ( $\sigma_c$ ), target background ( $\sigma_{tb}$ ), and target ( $\sigma_t$ ) are collected. The calibrated bistatic RCS ( $\sigma_{tc}$ ) of the target is given by [5]

$$\sigma_{tc} = \frac{\sigma_t - \sigma_{tb}}{\sigma_c - \sigma_{cb}} \sigma_{ce}, \quad (53)$$

where  $\sigma_{ce}$  is the exact (calculated) bistatic RCS of the calibration device.

Upon gathering the appropriate data (target, calibration standard, and background measurements) the AFIT Processing Code Suite© is used to perform the calibration outlined in Equation (53).

### 4.3 Initial Metamaterial Wedge RCS Measurements

Initial bistatic RCS measurements of the metamaterial wedge were taken on 15 Aug 09. For these measurements, the receiver angle in azimuth ( $\phi$ ) is located at  $45^\circ$  for the calibration measurements and is swept from  $0^\circ$  to  $145^\circ$  at  $1^\circ$  increments for the target measurements. The targets are rotated  $-45^\circ$  on the pylon. Thus, the angle of incidence remains  $45^\circ$  throughout the test. In order to ensure accuracy throughout the RCS measurements, calibration is performed before and after the bistatic measurements. The test matrix is shown in Table 18 in Appendix B. Figure 87 shows the setup for the metamaterial wedge measurement.

#### 4.3.1 Calibration Verification.

The measurement of RCS in the range necessarily carries with it an uncertainty that can be due to many sources, e.g., thermal noise in the radar equipment, misalignment of the target with the antenna, interactions with the target support structure, RF interference and drift. In order to help quantify the impact of those errors on the RCS measurements, the system's response to an established calibration standard with a known RCS pattern is analyzed through Equation (53). Because the radar system and range parameters can change with respect to time (commonly referred to as drift), the system is calibrated before and after the target measurements.

The calibration devices for these measurements are the 375 and 450 short, squat cylinders. The 450 cylinder calibration standard is used to calibrate the target measurements. In order to determine the accuracy of the calibration process, the 375 cylinder calibration standard measurement is calibrated with the 450 cylinder calibration standard using Equation (53) in the AFIT Processing Code Suite©.

The 375 and 450 calibration cylinders are too small for accurate calibration in the 3 to 6 GHz range, so the calibration errors for those measurements are large. The data



**Figure 87. Setup for the initial bistatic RCS measurements.** (a) The view as seen by the transmit antenna. The bistatic antenna is seen at about  $135^\circ$ . The angle convention for the bistatic arm is that a positive rotation angle is clockwise. (b) Top view of the metamaterial wedge attached to the metal plate. The metamaterial wedge is attached to a  $12 \times 12$  inch metal plate rotated  $-45^\circ$  on the pylon. The angle convention for the pylon is that a positive rotation angle is counterclockwise.

from the first calibration at the 3 to 6 GHz range are unusable due to an incorrect equipment setting during measurement. The results of the second calibration are shown in Figure 114 in Appendix B. Note that in the 3 to 6 GHz frequency range, only the  $tt$ -polarization was measured.

The calibrated 375 cylinder measurements in the  $tt$ -polarization are compared to the exact values for the 375 cylinder calculated using the Mercury method of moments (MOM)<sup>TM</sup> algorithm in Figure 88. To quantify the error in the measurement (i.e. the difference between the calibrated measurement and exact values for the 375 cylinder), the mean and standard deviation of the first calibration measurement are calculated to be 4.3 dB and 1.98 dB respectively for the  $pp$ -polarization and 4.02 dB and 1.74 dB respectively for the  $tt$ -polarization. The error in the calibration measurement for the  $tt$ -polarization is plotted in the histogram of Figure 88(b). The histogram is made by grouping the error into 20 evenly-spaced bins. The dashed line shows a theoretical normal distribution based on the mean and standard deviation calculated for these data. By comparing the histogram to the theoretical normal distribution, it



appears the data are normally distributed. The large error values could be caused by many things. The data for the second calibration show much lower error values. This could point to insufficient equipment warm up time as the cause of the large error in the first calibration. It should be noted that the radar equipment was turned on at 816 on 15 Aug 09 and the first calibration measurement was taken at 851. However, the data from the first calibration were not analyzed until a couple of hours later. Figure 88 also shows the measured RCS of the 375 cylinder calibrated with the 450 cylinder measurement in the second calibration measurement in the  $tt$ -polarization. The larger error values in the region between 6 and 8 GHz is most likely due to antenna effects. The cutoff frequency for the transmit antenna is 6 GHz. Figure 88(d) shows the histogram of the calibration error from the second calibration measurement in the  $tt$ -polarization. The means and standard deviations are calculated to be -0.089 dB and 0.373 dB respectively for the  $pp$ -polarization and -0.112 dB and 0.344 dB respectively for the  $tt$ -polarization. Visual inspection reveals that the data appear normally distributed. The  $pp$ -polarization shows a similar distribution (see Figure 115 in Appendix B).

For a normally distributed random variable, the 95% confidence interval (CI) is contained within plus and minus two standard deviations of the mean [57, 639]. Table 11 shows the mean, standard deviation, and 95% CI upper and lower limits in dB for the calibration measurements.

**Table 11. Initial metamaterial wedge measurement calibration statistics in dB**

	First Calibration		Second Calibration		
Frequency Band	6-18 GHz		6-18 GHz	3-6 GHz	
Polarization	$pp$	$tt$	$pp$	$tt$	$tt$
Mean Error	4.3	4.02	-0.0819	-0.112	0.0945
Std. Dev.	1.98	1.74	0.373	0.344	2.78
CI Lower Lim.	0.340	0.540	-0.835	-0.800	-5.47
CI Upper Lim.	8.26	7.50	0.657	0.576	5.65

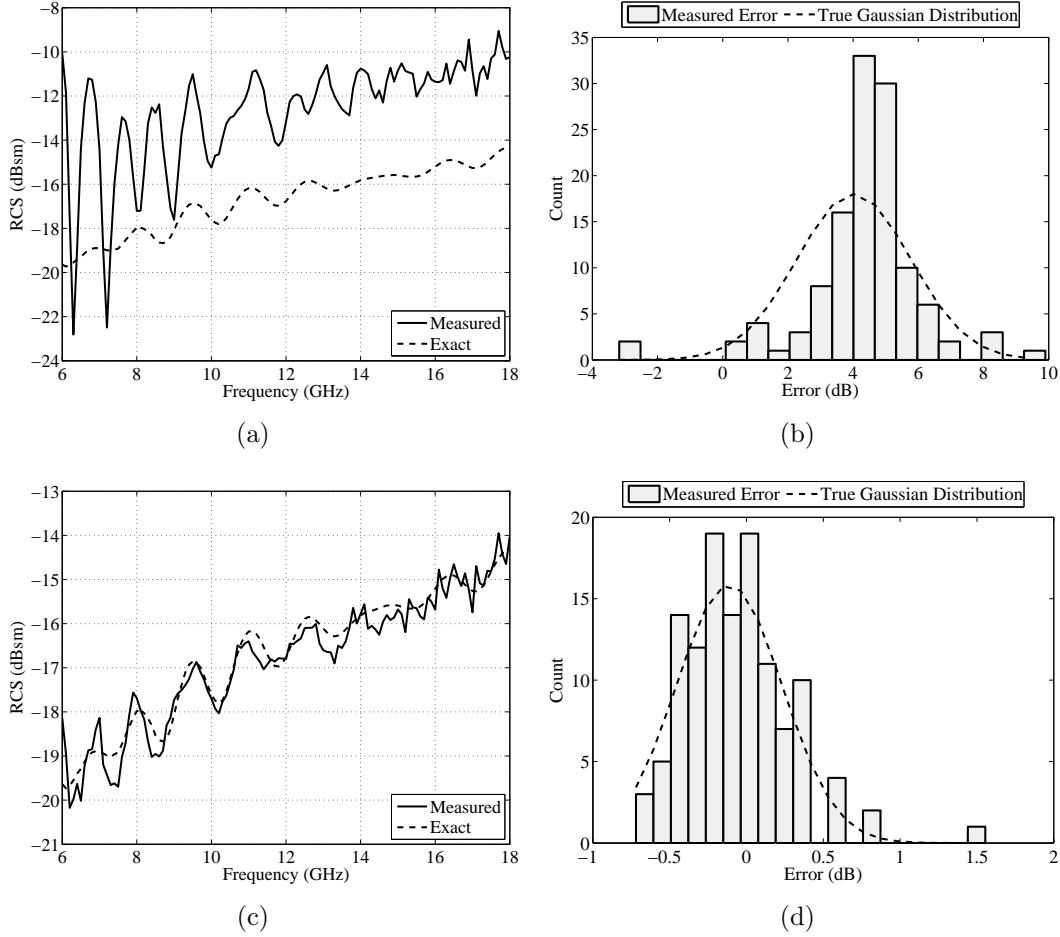


**Figure 88.** Calibration verification for the initial RCS measurements over the 6 to 18 GHz frequency range in the  $tt$ -polarization. The 375 calibration standard is calibrated against the 450 cylinder calibration standard measured at  $\phi = 45^\circ$ ,  $\theta = 90^\circ$ . (a) The first set of calibrated measurements of the 375 cylinder are plotted with the exact values for the 375 cylinder. (b) Histogram of the first calibration measurement error (measured - exact). The dashed line shows a Gaussian distribution using the mean and standard deviation calculated from the data. The data appear normally distributed. (c) The second set of calibrated measurements of the 375 cylinder are plotted with the exact values for the 375 cylinder. (d) Histogram of the second calibration measurement error. The error is less in this calibration than in the first calibration.

It appears that equipment warm up time and/or range drift played a significant factor in the measurements. However, range availability issues did not allow for taking further measurements at that time. Therefore, the second calibration is used to calibrate the other measurements.

### 4.3.2 Measurement Results.

#### 4.3.2.1 RCS Measurements.

Figure 89 shows the global RCS patterns for the metal plate and metamaterial wedge in the  $tt$ -polarization at 6 to 18 GHz. The metal plate demonstrates the expected behavior in that there is a large specular return near  $90^\circ$ . The global RCS plot for the metamaterial wedge shows a bright return near  $90^\circ$  for most of the frequency band. This is most likely due to the portions of the metal plate that extend beyond the metamaterial wedge. The wider lobes, however, are near  $110^\circ$ . This return is present throughout most of the frequency band. This seems to correspond to the specular return off of the face of the wedge. It should be noted that the return near  $90^\circ$  is slightly higher in magnitude. There is a very small resonance band near 13.3 GHz. Here, the specular return from the wedge face is reduced in magnitude, but no new lobes appear. This could indicate that most of the incident energy is absorbed by the losses in the wedge. The  $pp$ -polarized global RCS pattern is shown in Figure 116 of Appendix B).

It is interesting to note the additional returns near  $0^\circ$  in the patterns for the metamaterial wedge. The wedge and the portion of the metal plate that extends beyond the wedge towards the transmit antenna form a corner reflector. This is most likely the cause of the return at the smaller angles.

The RCS patterns for the metal plate and metamaterial wedge at 10 GHz and 13.3 GHz in the  $tt$ -polarization are shown in Figure 90. At 10 GHz, the metamaterial

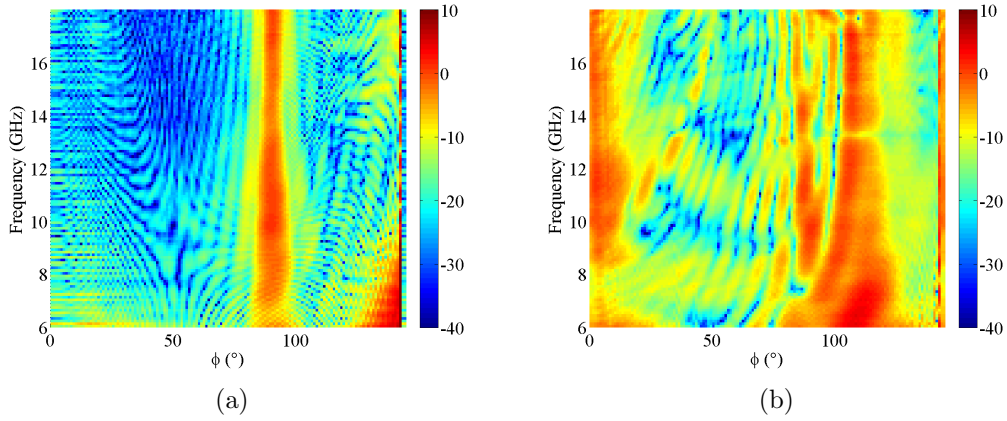


**Figure 89.** Measured global RCS patterns for the horizontal polarization. The angles on the  $x$ -axis are the angle of the receive antenna. (a) The global RCS pattern for the metal plate. The large specular return occurs at  $90^\circ$  as expected. (b) The global RCS pattern for the metamaterial wedge. The pattern shows some return near  $90^\circ$ , but the main return is near  $110^\circ$ . There is a small resonance band near 13.3 GHz.

structure does not resonate. The mainlobe for the metamaterial wedge is aligned with the metal plate at  $90^\circ$ . The large sidelobe appears at  $103^\circ$ . The 13.3 GHz pattern shows the behavior at resonance. The return near  $90^\circ$  for the metamaterial wedge is actually at  $86^\circ$ . This is slightly to the left of the  $90^\circ$  specular return for the metamaterial wedge. The larger sidelobe near  $110^\circ$  actually reaches a peak near  $106^\circ$ . This is a shift of  $3^\circ$ .

Figure 91 shows the  $tt$ -polarized RCS frequency sweep at receiver angles of  $90^\circ$  and  $103^\circ$ . Both return angles show nulls at the resonance near 13 GHz. That is the only frequency band where both returns show nulls. This indicates that the energy in that band is either absorbed or redirected by the wedge. The lack of sidelobes in the global RCS plot for the metamaterial wedge in the resonant band (see Figure 89(b)) points toward the idea that the energy is absorbed.

The global RCS patterns for the 3 to 6 GHz  $tt$ -polarization are shown in Figure 92. The metal plate shows a large specular return near  $90^\circ$ . The mainlobe for the metal plate is substantially wider than it is in the 6 to 18 GHz frequency band. The

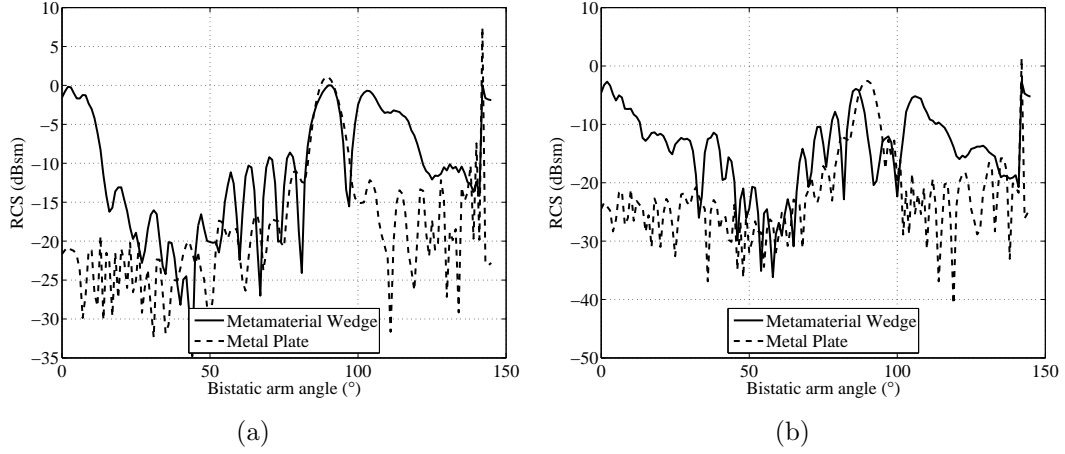


Figure 90. The measured RCS pattern for the metamaterial wedge and metal plate in the  $tt$ -polarization. (a) The pattern at 10 GHz (outside the resonance band). The brightest return is aligned with the specular return for the metal plate. (b) The pattern at 13.3 GHz (inside the resonance band). A large sidelobe appears at  $103^\circ$ .

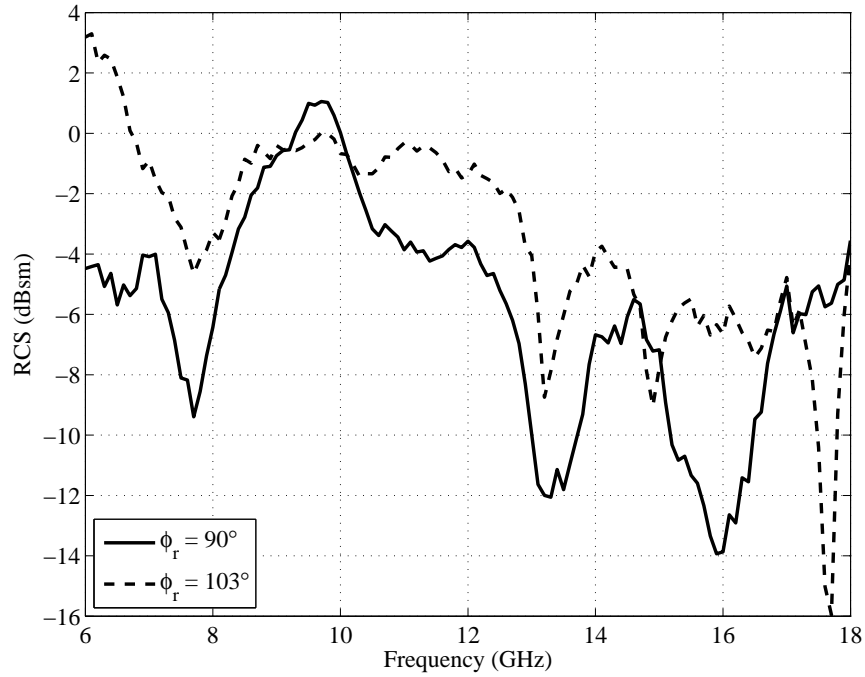
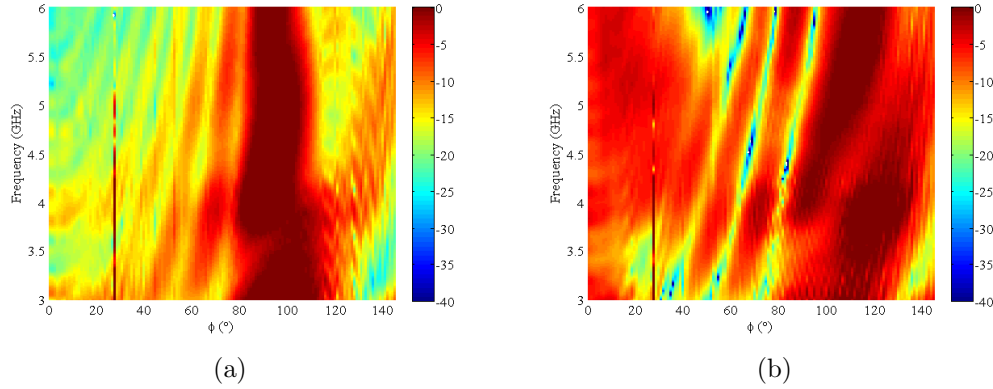


Figure 91. RCS frequency sweeps for the metamaterial wedge at return angles of  $90^\circ$  and  $103^\circ$ . Both returns show nulls near the resonant frequency of 13 GHz.

null-to-null width of the mainlobe in degrees ( $\theta_{ml}$ ) can be approximated with [21, 562]

$$\theta_{ml} = 57 \frac{\lambda}{L_p}, \quad (54)$$

where  $L_p$  is the length of the plate. Equation (54) implies that the width of the mainlobe is directly proportional to the wavelength. For example, at 6 GHz the width of the mainlobe for the 12 inch plate should be approximately  $9.34^\circ$ ; at 3 GHz the width of the mainlobe should be  $18.7^\circ$ .



**Figure 92.** Measured global RCS patterns for the 3 to 6 GHz frequency band in the  $tt$ -polarization. (a) The pattern for the metal plate shows the specular return at about  $90^\circ$ , but the mainbeam is wider than at the 6 to 18 GHz frequency band because the plate is electrically larger. (b) The metamaterial wedge shows some large returns between  $80^\circ$  and  $90^\circ$ . There appears to be some frequency dependence in the return.

The global RCS pattern of the metamaterial wedge in the  $tt$ -polarization at 3 to 6 GHz is shown in Figure 92(b). There appears to be some frequency dependency despite no obvious resonance being visible in that frequency range in Figure 42. The large return above  $80^\circ$  seems to be shifted towards the location of the specular return from the wedge face, but the mainlobes are so wide it is difficult to resolve the scattering mechanisms from this diagram.

#### 4.3.2.2 Range Information.

The range information for the metamaterial wedge is determined according to the theories presented in Section 2.3.3.3. Since the metamaterial wedge is resonant, it does not make sense to use the entire 6 to 18 GHz frequency range in the calculation of the range data. Rather, 2 GHz frequency windows are used at different points in

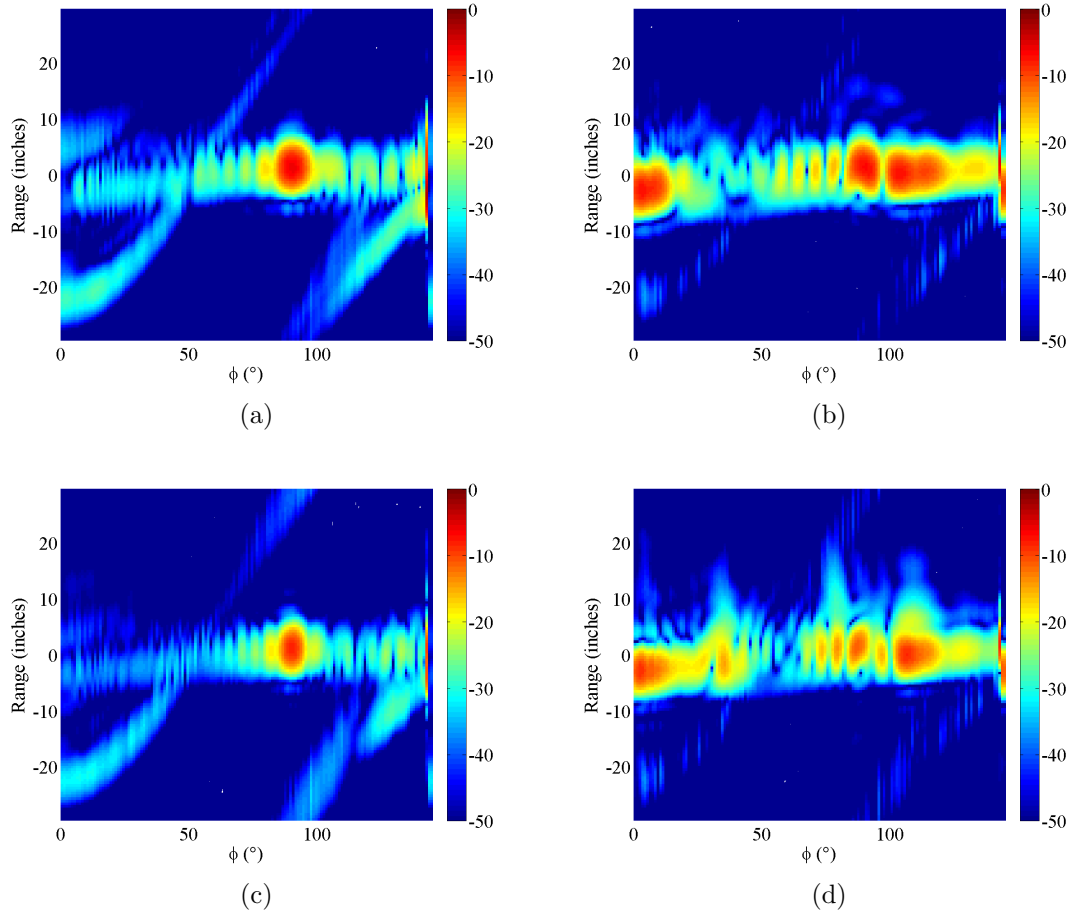
the total frequency range to show how the range data changes as the metamaterial wedge resonates. As noted in Section 3.4.5, the use of 2 GHz range windows limits the range resolution to 7.5 cm.

Figure 93 shows the global range patterns for the metal plate and metamaterial wedge at different center frequencies in the 6-18 GHz frequency range. Note that the periodic curves in the pattern are most likely due to interactions with the RCS range. The scatterer for the metal plate remains relatively unchanged throughout the frequency range. The locations of the scatterers for the metamaterial wedge do not appear to change in their angular location, but they do appear attenuated at the resonant frequency of 13 GHz. This, again, points to losses in the metamaterial wedge absorbing the incident energy.

#### **4.3.2.3 ISAR Imagery.**

ISAR images for the metamaterial wedge are generated using the procedure explained in Section 2.3.3.4. Since the metamaterial wedge has a resonant band inside the 6 to 18 GHz range, the frequency bandwidth used for the ISAR imagery will need to be limited to show the impact of the resonance. Unfortunately, this will have the effect of reducing the range resolution. So, care must be exercised in making the trade off between bandwidth choice and range resolution. Using the same 2 GHz window from above, the cross and down range resolutions are 7.5 cm. Looking at the two frequency windows centered at 13 GHz and 17 GHz, the angular extents for those bands become  $8.850^\circ$  and  $6.750^\circ$  respectively.

Figure 94 shows the ISAR imagery for the metal plate and metamaterial wedge calculated using a 2 GHz band centered around 13 GHz (in resonance band). All of the images are calculated using the *tt*-polarization data. Sidelobe suppression of the FFT is accomplished using a Hann window. At angles near  $90^\circ$ , the image of



**Figure 93.** Global range patterns derived from 2 GHz windows of the  $tt$ -polarized measurements in the 6 to 18 GHz frequency band. (a) With the center frequency at the resonance frequency of 10 GHz, the global range plot of the metal plate appears at  $90^\circ$ . (b) For the metamaterial wedge, the return at  $0^\circ$  is still evident, but sidelobes appear near  $0^\circ$  and just over  $100^\circ$ . (c) The pattern for the plate at 13 GHz is similar to the pattern for the plate at 10 GHz. (d) At 13 GHz, the same lobes appear for the metamaterial wedge, but they are attenuated.

the plate displays the strong return at the center of the range corresponding to the specular return. The metamaterial wedge also shows a strong return at the center of the range near  $90^\circ$ . This probably corresponds to the return from the portion of the metal plate that extends above the wedge. Near  $110^\circ$ , the metal plate image still shows the main return near the center of the range, but the magnitude is greatly reduced. Near  $110^\circ$ , the metamaterial wedge shows a strong return at the center of the range. This return is due to specular reflection off of the face of the wedge. Note



that the return at the center spreads downrange. This is an indicator of resonance.

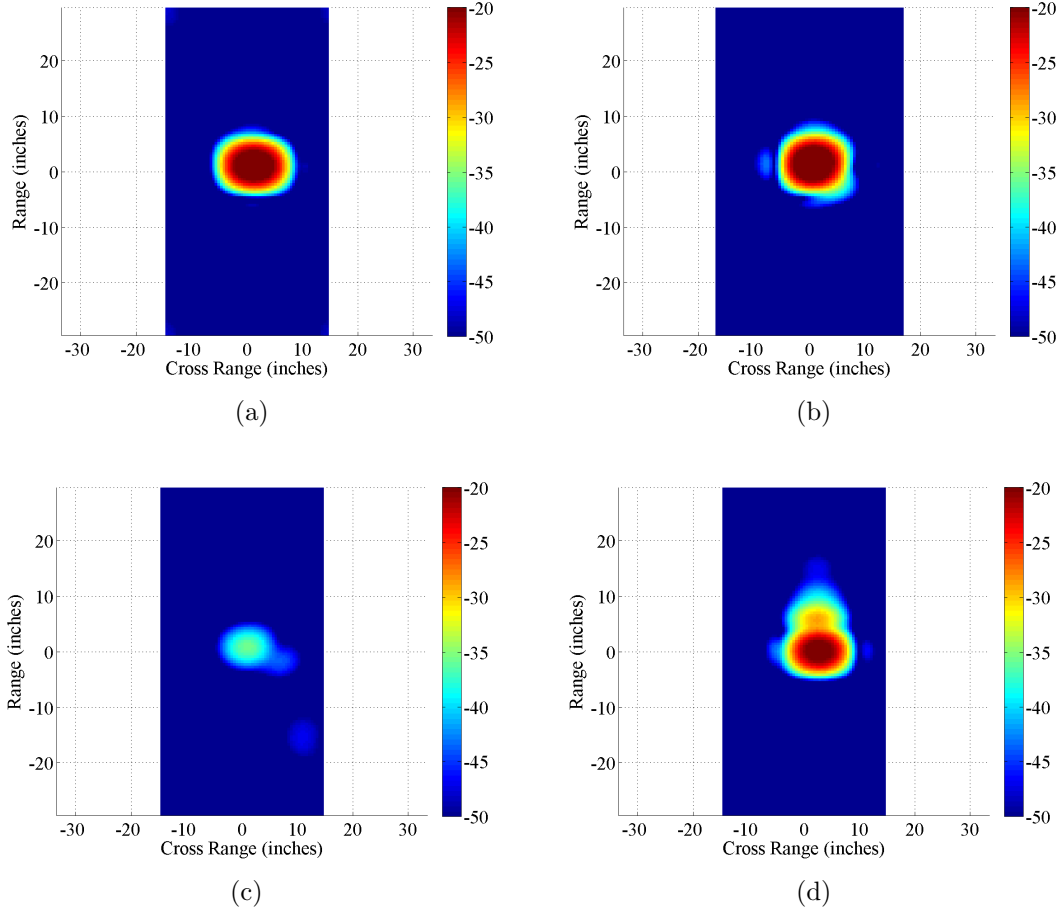


**Figure 94.** ISAR imagery taken with a bandwidth of 2 GHz centered at 13 GHz calculated with the *tt*-polarization data. (a) The ISAR image of the metal plate taken at  $90^\circ$  shows a strong scatterer at the range center. (b) The image of the metamaterial wedge at  $90^\circ$  also shows a strong scatterer at the center point. (c) At  $110^\circ$ , the scatterer for the metal plate remains at the center but is greatly reduced in magnitude. (d) For the metamaterial wedge at  $110^\circ$  a strong scatterer remains at the center point. This is due to reflection off of the wedge face.

Figure 95 shows the ISAR imagery for the metamaterial wedge calculated using a 2 GHz band centered around 10 GHz (out of resonance band). The ISAR imagery for the metal plate at 10 GHz is very similar to the imagery at 13 GHz. At angles near  $90^\circ$ , the metamaterial wedge shows a strong return at the center of the range near  $90^\circ$ . This probably corresponds to the return from the portion of the metal plate that extends above the wedge. Near  $110^\circ$ , the metamaterial wedge shows the main

return near the center of the range. This corresponds to the specular reflection off of the face of the metamaterial wedge.

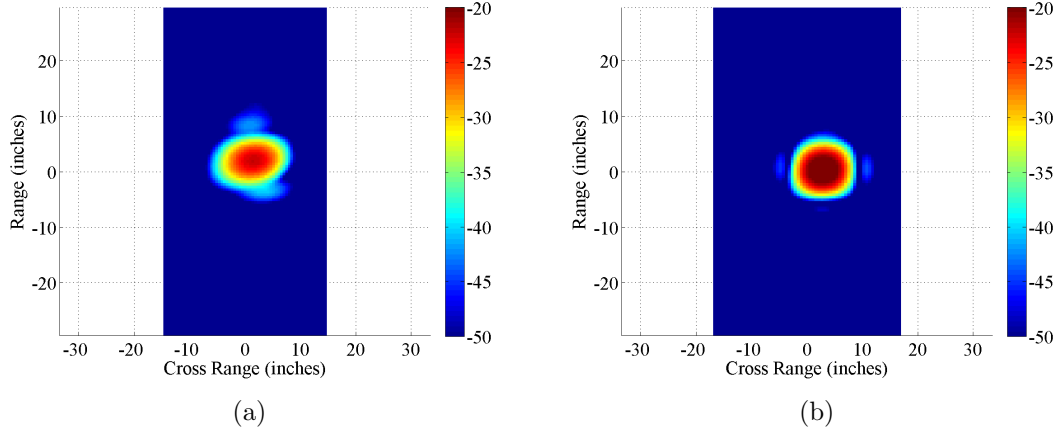


**Figure 95. ISAR imagery of the metamaterial wedge taken with a bandwidth of 2 GHz centered at 10 GHz calculated with the *tt*-polarization data from the initial RCS measurements. (a) The image at  $90^\circ$  also shows a strong scatterer at the center point. (b) At  $110^\circ$ , the main scatterer remains at the center point. This is due to reflection off of the wedge face.**

Comparing the images of the metamaterial wedge in Figures 94(d) and 95(b), there is a difference in the magnitudes of the scatterers at the range center. The main scatterer at 10 GHz is about 1dB higher than the main scatterer at 13 GHz. This indicates that attenuation is occurring inside the resonance band.

### 4.3.3 Conclusions from the Initial Measurements.

There are several issues that occurred with the initial measurements. Difficulties include bad data in the first calibration, the loss of the first calibration at the low frequencies, the variance in the second low frequency calibration, interactions between the bistatic arm and the RCS range, and the difficulty in resolving angular differences between reflection off of the face of the wedge and transmission through the wedge. Nonetheless, the results do show several interesting phenomena. The resonance band of the metamaterial wedge is clearly visible in the RCS pattern near 13 GHz.

## 4.4 Final Metamaterial Wedge RCS Measurements

Another set of bistatic RCS measurements of the metamaterial wedge were taken on 10 and 11 Nov 09. Table 19 in Appendix B shows the test matrix. Unlike in the initial measurements, the receiver angle is swept for the calibration measurements. Furthermore, the pylon is rotated to produce incident angles of  $0^\circ$ ,  $15^\circ$ ,  $30^\circ$ , and  $45^\circ$  on the metal plate. For these measurements a metal plate was cut to the same size as the back of the metamaterial wedge. Thus, the edges of the plate do not extend beyond the metamaterial wedge. Figure 96 shows some of the setup photographs for these measurements

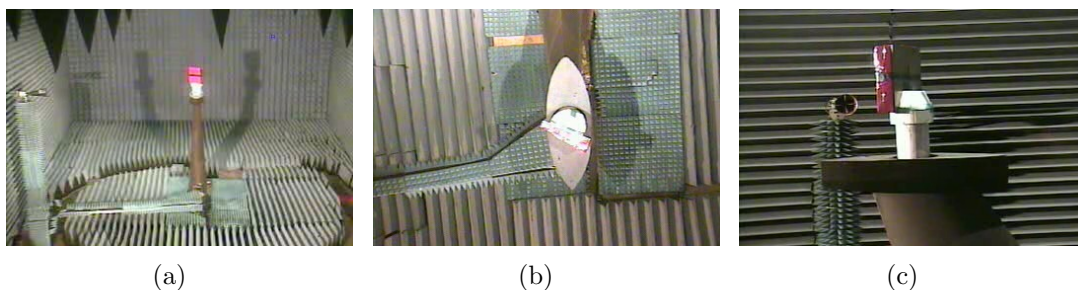


**Figure 96.** Setup for the final bistatic RCS measurements. (a) The view as seen by the transmit antenna. The target for this measurement is the metamaterial wedge with a metal plate backing. The pylon is rotated at an angle of  $-30^\circ$ . Also shown are the top (b) and side (c) views of the same measurement.

### 4.4.1 Calibration Verification.

Table 12 shows the mean, standard deviation, and 95% CI upper and lower limits in dB for the calibration measurements. The receiver antenna sweeps from  $-45^\circ$  to  $135^\circ$  for all measurements; the calibration data shown are the results extracted at  $45^\circ$ . Histograms for the *pp*- and *tt*-polarized calibration data are shown in Figures 117 and 118 in Appendix B.

Unfortunately, the calibration verification shows large standard deviations in the *tt*-polarized measurements for the second day. Figure 97 shows the *tt*-polarized cal-

**Table 12. Final metamaterial wedge measurement calibration statistics in dB**

	Day 1				Day 2			
Calibration	First		Second		First		Second	
Polarization	$pp$	$tt$	$pp$	$tt$	$pp$	$tt$	$pp$	$tt$
Mean Error	0.438	0.572	-0.120	-0.127	0.334	0.160	-0.0325	-0.0844
Std. Dev.	2.47	0.221	0.591	0.516	1.31	0.908	0.494	0.980
CI Lower Lim.	-4.50	0.13	-1.30	-1.16	-2.28	-1.66	-1.02	-2.04
CI Upper Lim.	5.38	1.01	1.06	0.905	2.96	1.98	0.956	1.88

ibrated and exact data for both measurements on both days (the  $pp$ -polarized data are shown in Figure 119 in Appendix B). Post-processing attempts were unable to remove the large deviations. The day two calibration set is used for calibrating the measurements since the mean errors for the second day are lower.

#### 4.4.2 Measurement Results.

##### 4.4.2.1 RCS Measurements.

Figure 98 shows the global RCS patterns in the  $tt$ -polarization for the metamaterial wedge with the metal plate (the  $pp$ -polarization plots are shown in Figure 120 of Appendix B). At the  $0^\circ$  incident angle, there appears to be some resonant behavior just below 14 GHz. The strong return at  $24^\circ$  disappears and a small sidelobe appears near  $30^\circ$ ; though, this sidelobe could be a continuation of a sidelobe from outside of the resonance band. When the incident angle is changed to  $15^\circ$ , the main return at  $53^\circ$  remains, but appears to be diminished. At  $30^\circ$  incidence, the resonance band appears near 14 GHz, and the behavior is similar to the other incident angles. Similar resonance effects are present in the  $45^\circ$  incident angle measurement. It is interesting to note that at about 16-18 GHz, the main return follows a pattern similar to the pattern from the lossy effective medium theory shown in Figure 45 of Section 3.4.2.2.

RCS patterns for the metamaterial wedge at 10 GHz (outside the resonance band) and 14 GHz (inside the resonance band) are shown in Figure 123 of Appendix B. The

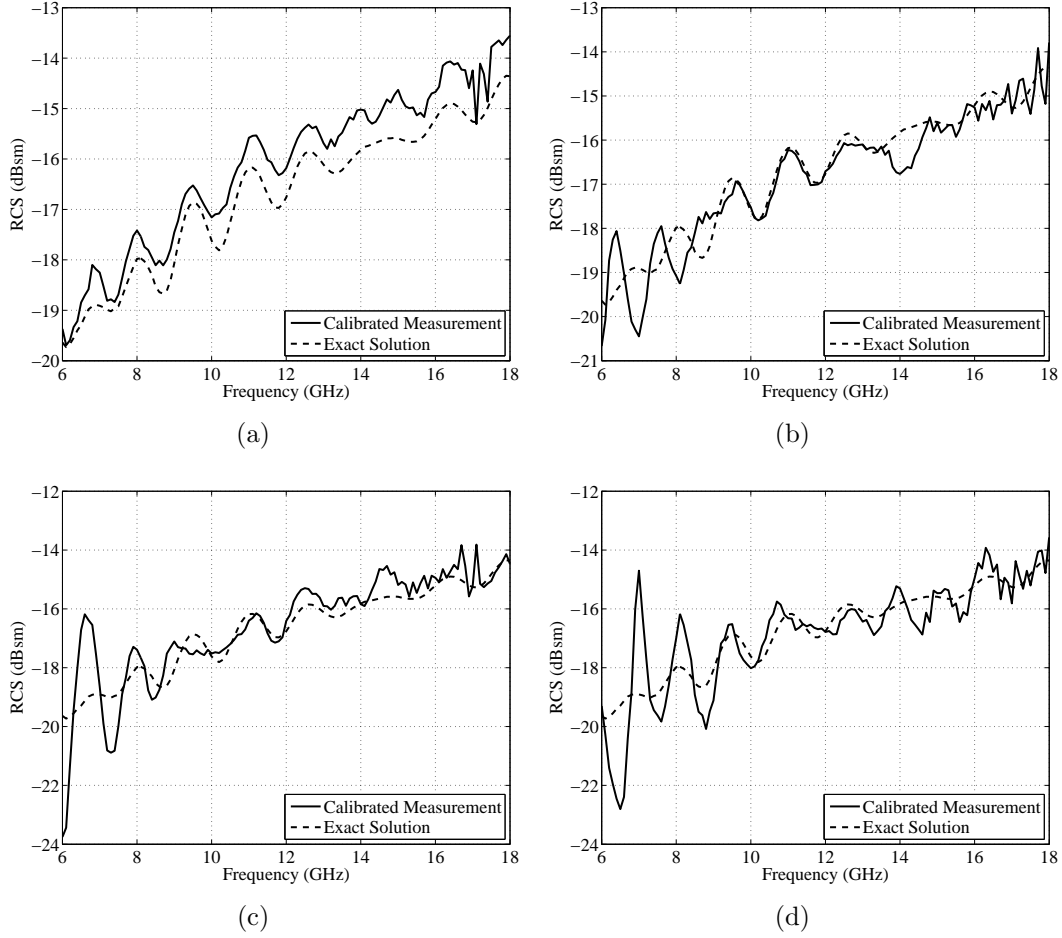


**Figure 97. Calibration comparison of the  $tt$ -polarized data for the final metamaterial wedge RCS measurements. (a) The first calibration on the first day shows a large variation in the calibrated data, but the average is approximately the same. (b) The second calibration on the first day agrees fairly well with the exact data. (c) Like the first day, the second day has a large disagreement between the calibrated and exact data of the first measurement. (d) The second measurement on the second day also shows improvement in the variation of the data.**

patterns show that the locations of the sidelobes and mainlobe remain the same in and out of the resonance band. The measurements at 14 GHz appear to be attenuated. As explained previously, inside the resonance band, part of the energy is transmitted into the wedge. However, that energy is attenuated by the losses in the wedge. Any negative refraction that occurs is not apparent from the data.

The measured global RCS patterns in the  $tt$ -polarization for the metamaterial

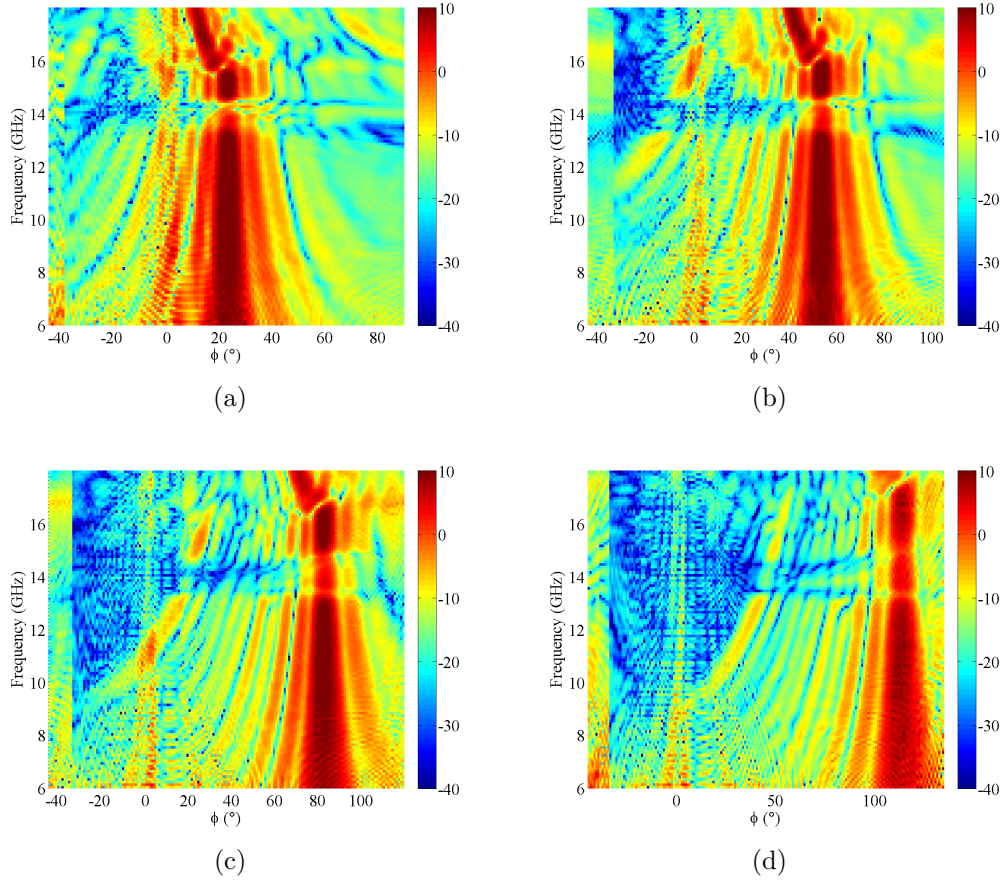


**Figure 98.** Global RCS patterns from the final metamaterial wedge measurements in the  $tt$ -polarization. (a) The global RCS pattern for an incident angle of  $0^\circ$  shows some resonant behavior around 14 GHz. (b) The global RCS pattern for an incident angle of  $15^\circ$  also shows some resonant behavior just near 14 GHz. (c) The global RCS pattern for an incident angle of  $30^\circ$ . (d) The global RCS pattern for an incident angle of  $45^\circ$ .

wedge with no metal plate behind it are shown in Figure 99. The results appear to be similar to the results from the wedge with the plate (see Figure 98). This seems to indicate there is little penetration into the wedge. At frequencies beyond 16 GHz, there appears to be more transmission into the wedge, as evidenced by the disappearance of the mainlobe at those frequencies. The global RCS patterns for the  $pp$ -polarization are shown in Figure 120 of Appendix B.

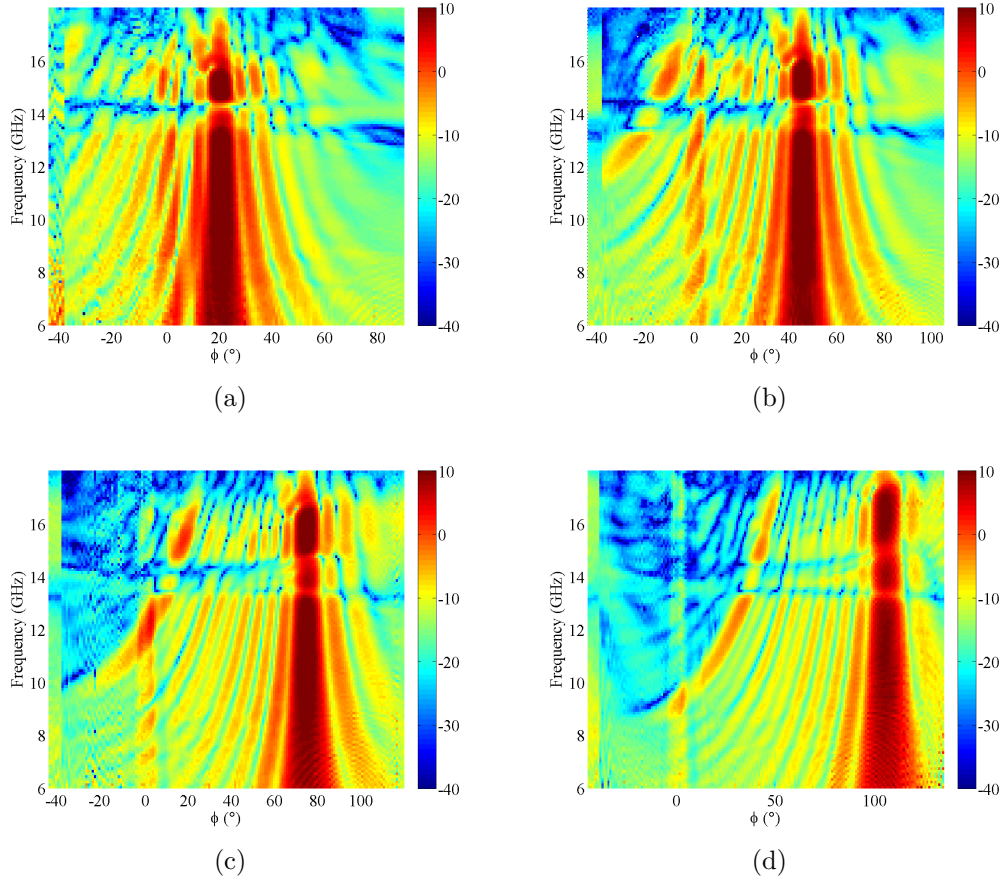


**Figure 99.** Global RCS patterns from the final metamaterial wedge measurements without the metal plate in the  $tt$ -polarization at incident angles of  $0^\circ$  (a),  $15^\circ$  (b),  $30^\circ$  (c), and  $45^\circ$  (d).

#### 4.4.2.2 Range Information.

Global range patterns for the final RCS measurements are generated using the process described in Section 4.3.2.2. The same 2 GHz windows centered at 10 GHz and 14 GHz are used. Again, at 10 GHz the metamaterial wedge does not resonate. Figure 100 shows the global range plots for the  $0^\circ$  incident angle. There is very little difference between the two patterns. This is expected since the RCS pattern shows little difference between the two frequency bands. The signal near 14 GHz does appear to be smaller than the signal near 10 GHz. Again, this indicates penetration into the wedge. Also, the range pattern for 14 GHz appears to spread further downrange than

at 10 GHz. This usually indicates time-resonant behavior. The global range patterns for the  $15^\circ$ ,  $13^\circ$ , and  $45^\circ$  incident angles are shown in Figure 124 of Appendix B. The results at these angles are similar.

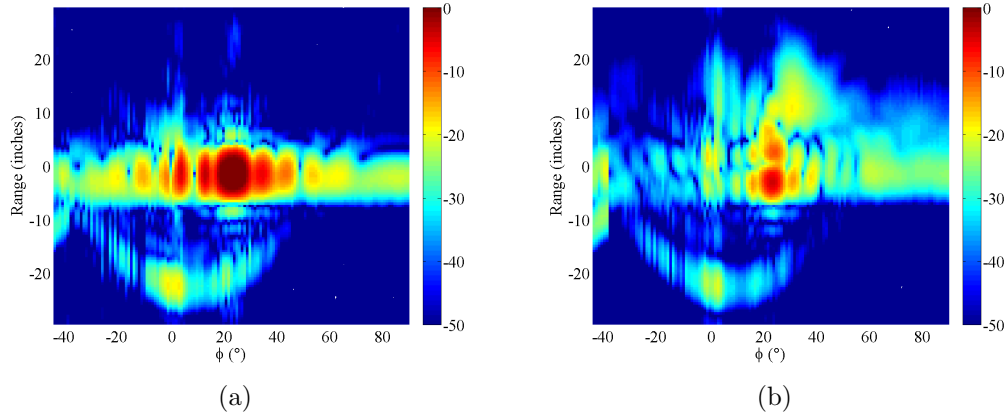


**Figure 100.** Global range patterns from the final metamaterial wedge measurements for an incident angle of  $0^\circ$ . The patterns for a 10 GHz center frequency (a) and 14 GHz center frequency (b) show very little difference in the location of the scatterers. The scatterers do appear smaller at 14 GHz than at 10 GHz. This indicates penetration into the wedge.

#### 4.4.2.3 ISAR Imagery.

The ISAR imagery for these measurements was analyzed. However, they were not found to have that much new information in them. Therefore, the ISAR analysis is omitted here. The ISAR imagery from the measurement of the metamaterial wedge with metal plate at incident angles of  $0^\circ$ ,  $15^\circ$ ,  $30^\circ$ , and  $45^\circ$  are shown in Figures 125, 126, 127, and 128 of Appendix B, respectively.

#### 4.4.3 Comparison of Measurement and Model Results.

The RCS measurements of the metamaterial wedge appear to be very similar to the model results. The models and measurements show that the dominant scattering mechanism is the specular reflection off of the wedge face. At the higher frequencies,



the model predicts more transmission through the wedge in that the global RCS shows the main return follows the profile of the index of refraction extracted from the unit cell model. Like the models, the measurements show that the magnitude of the return is reduced in the resonance band. The results of the unit cell model predict this behavior is due to transmission inside the wedge. The unit cell model also predicts losses in the wedge at resonance. The lack of additional lobes in the resonance band of the model and measurement results seem to back this up since any transmitted fields should be attenuated.

The range and ISAR analysis of the measurement and model data confirm the scattering mechanisms and, aside from some measurement errors and noise, match very well. The strongest scatterers according to the model and measurement results have the same downrange and cross range locations.

A key difference between the measurements and the models is the location of the resonance bands. The approximate resonance bands are shown in Table 13. The resonance of the bands from the models that use the frequency solver better match the measured frequency band. The transient solver shows the resonance band to be about 1 GHz lower than the measured band. The band edges in the unit cell model are easier to determine, which may be why it is closer to the measured band than the mid-size model's band.

The global RCS, range, and ISAR plots for the models and the measurements have

**Table 13. Metamaterial wedge resonance bands**

Data Set	Resonance Band	
	Starting Frequency (GHz)	Ending Frequency (GHz)
Unit cell <sup>1</sup>	12.5	14.5
Mid-size <sup>1</sup>	13	14
Full-size <sup>2</sup>	12	13
Measurement	12.8	14.5

<sup>1</sup> Model uses frequency solver.

<sup>2</sup> Model uses transient solver.

the same color scale. Thus, the return magnitudes match well, at least qualitatively. The scattering magnitudes from the mid-size model are difficult to compare since the full size of the wedge is not included. The specular return off the wedge face is less sensitive to the size of the model. This explains why much of the RCS patterns for the mid-size model match the measurement magnitudes. Despite the qualitative match, more quantitative comparisons are complicated by the amount of error in the calibration results as well as approximations used in interpreting the model.

There are a number of factors that could influence the measurement results. As the wedge sample ages, wear and tear will cause some of the dimensions to change. Any compression or shifting in the dielectric foam would impact the periodicity of the structure. A parametric study could be implemented using the computational models to determine the impact that wear and tear have on the results. Such a study is discussed in Chapter V. The close similarities between the measurement and model results show that the simulation techniques used in this thesis would be effective for this kind of study. To specifically study the factors impacting the resonance band, the frequency solver should be used as it appears to better match the measurement results.

## 4.5 Stripline Measurement Procedures and Theory

While there are different techniques available to measure  $S$ -parameters for a material sample, this thesis uses time-domain reflectometry. Here a Time-Domain Reflectometer (TDR) connected to a stripline stimulates the sample with a voltage step. The signal reflected from and transmitted through the sample are measured using an oscilloscope. Figure 101 shows the equipment used for these measurements. The TDR module is an Agilent 54754A, the oscilloscope is an Agilent 86100B, and the stripline is the same one described in Section 3.6.



**Figure 101. Equipment used for stripline measurements. The waveguide is the large stripline described in Section 3.6.3. TDR measurements are taken using an Agilent 86100B Wide-Bandwidth Oscilloscope with an Agilent 54754A Differential TDR Module.**

The  $S$ -parameters of a network are the ratio of voltage waves and are defined in the frequency-domain. Mainly, this research effort focuses on  $S_{11}$  and  $S_{21}$  because the metamaterial samples produce the same results measured forward or reverse in the stripline (i.e.,  $S_{22} = S_{11}$  and  $S_{12} = S_{21}$ ).  $S_{11}$  and  $S_{21}$  are defined by the frequency-domain impulse voltage response received at port 1 ( $V_1^-$ ), received at port 2 ( $V_2^-$ ), and transmitted at port 1 ( $V_1^+$ ) by [36, 221]

$$S_{11}(f) = \frac{V_1^-(f)}{V_1^+(f)}, \quad (55a)$$

$$S_{21}(f) = \frac{V_2^-(f)}{V_1^+(f)}. \quad (55b)$$

$S$ -parameters are calculated with the impulse response [29]. Since the TDR module produces a step-output, the first step in the process of calculating  $S$ -parameters

is to convert the step output to an impulse response by taking the first derivative with respect to time. Taking the FFT of the resulting impulse responses converts the signals to the frequency domain. Calculating the  $S$ -parameters requires the measurement of an electrical short, an empty stripline, and the material sample to ensure proper normalization. Defining the reflected signal at port 1 from the electrical short measurement, the transmitted signal at port 2 from the empty stripline measurement, the reflected signal at port 1 from the material sample measurement, and the transmitted signal at port from the material sample measurement as  $V_1^{sh}$ ,  $V_2^{th}$ ,  $V_1^s$ , and  $V_2^s$  respectively,  $S_{11}$  and  $S_{21}$  for the material sample are calculated using [30]

$$S_{11}(f) = -\frac{V_1^s(f)}{V_1^{sh}(f)}, \quad (56a)$$

$$S_{21}(f) = \frac{V_2^s(f)}{V_2^{th}(f)} e^{jk_0 d_s}. \quad (56b)$$

Taking into account the relationships between the time-domain measurements and the frequency-domain  $S$ -parameters, the basic procedure for taking stripline measurements for a material sample is:

1. measure reflected signal for the electrical short ( $V_1^{sh}$ ) in time-domain,
2. measure transmitted signal for the stripline with nothing in it except any sample holders ( $V_2^{th}$ ),
3. measure reflected and transmitted signals for sample ( $V_1^s$  and  $V_2^s$ ),
4. convert all measurements to impulse responses by taking the first derivative with respect to time,
5. apply time-domain gating to remove unwanted reflections (e.g., reflections from the stripline connectors),

6. convert all measurements to the frequency-domain using the FFT, and
7. apply Equation (56) to calculate  $S_{11}$  and  $S_{21}$ .

Once  $S_{11}$  and  $S_{21}$  for the sample have been determined, the material parameters  $n$ ,  $z$ ,  $\epsilon_r$ , and  $\mu_r$  can be determined.

A MATLAB<sup>TM</sup> script was developed to convert the TDR measurements to  $S$ -parameters. The script is described in Appendix C.

## 4.6 AFIT Metamaterial Design Stripline Measurements

The structures measured in this section are the same non-adaptive metamaterial structures modeled in Section 3.6. Unfortunately, samples of the adaptive metamaterial structure were not available for measurement before publication of this thesis. However, the results of the passive metamaterial measurements validate the computer models.

### 4.6.1 Large Scale Non-adaptive Design.

As mentioned in Section 3.6.3, prototypes of larger scale non-adaptive versions of the AFIT design are fabricated using the laser etcher. Figure 102 shows the etching process and the samples. The original scale designs are too small for the laser etcher, but the etcher can produce accurate prototypes of the large scale designs if the maximum resolution (1200 DPI) is used. The etching process is considerably faster than the surface micromachining process used to construct the adaptive structures making it ideal for rapid prototyping.

The 4.0 and 4.9 scale structures are loaded into the stripline as shown in Figure 103. The required electrical short and through measurements are also performed. For the through measurement, the foam used to hold the metamaterial samples is inserted into the stripline.

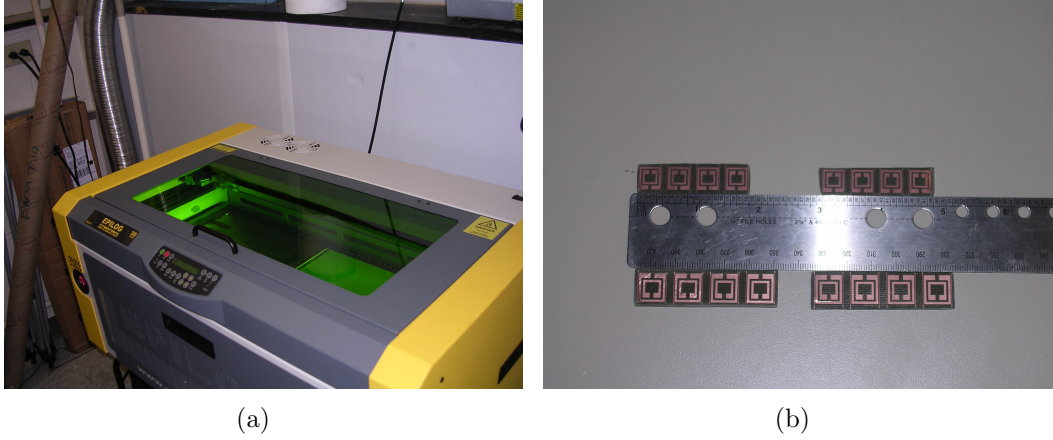


**Figure 102.** Fabrication of the passive large scale metamaterial test samples. (a) The samples are etched into a copper-coated FR4 circuit card material using a laser etcher. (b) The 4.0 scale samples are shown above the ruler while the 4.9 scale samples are shown below.

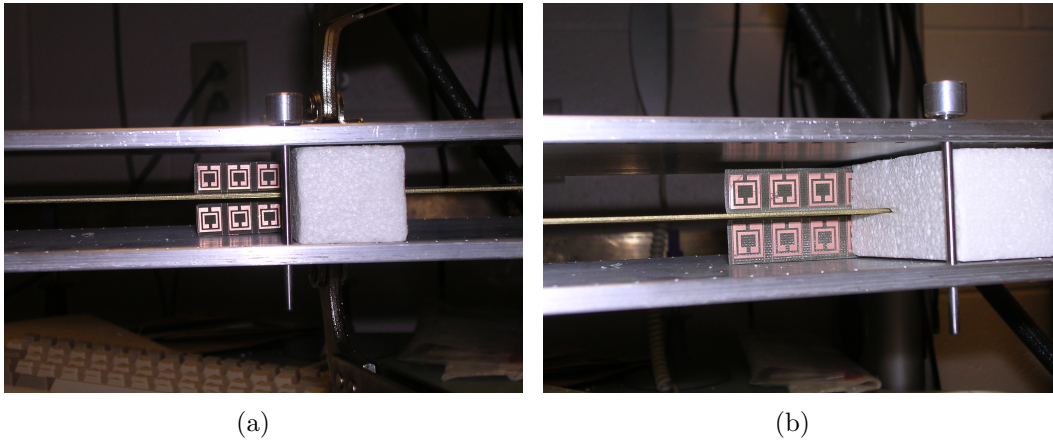


**Figure 103.** Testing of the passive large scale metamaterial samples. Foam is used to hold the 4.0 (a) and 4.9 (b) scale samples in the stripline.

Figure 104 shows the  $S$ -parameter results from the measurements. The magnitudes of  $S_{11}$  and  $S_{21}$  show behavior consistent with the presence of multiple modes beyond 3.5 GHz. Resonant frequencies are evident near 2.5 GHz for the 4.0 scale device and 2 GHz for the 4.9 scale device. As expected, the resonant frequency of the 4.9 scale device is lower than the resonant frequency of the 4.0 scale device.

The results in Figure 104 agree with the results from the computer model (see Figure 82). The measured resonant frequencies appear to be slightly lower than the

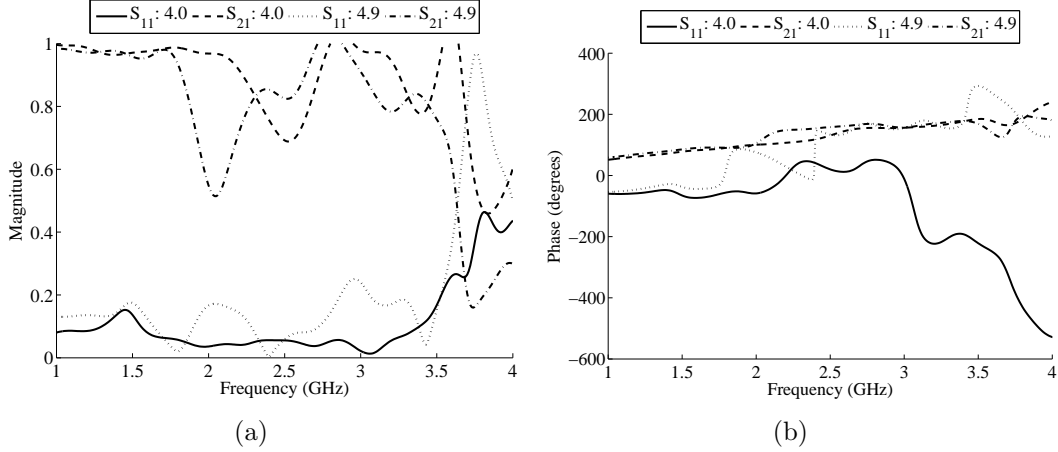


**Figure 104. Measurement results for the large scale passive metamaterial samples. (a) The magnitude of  $S_{11}$  and  $S_{21}$  show resonant frequencies at about 2.5 and 2 GHz for the 4.0 and 4.9 scale factors, respectively. (b) The phases of  $S_{11}$  and  $S_{21}$  for the 4.0 and 4.9 scale factors.**

resonant frequencies from the model. The biggest difference appears in the magnitudes of the  $S$ -parameters at resonance. The computer model shows much stronger resonant behavior than the measurements.

For the next measurement, a total of four strips are loaded into the stripline for each measurement: two strips above the center conductor and two strips below the center conductor. This will help determine the effect of coupling between the non-coplanar unit cells. Figure 105 shows the measured  $S$ -parameters for these measurements. The locations of the resonance bands are the same as the two-strip measurements. However, the resonance effects appear stronger in these measurements.

Like the two-strip measurement, the results in Figure 105 agree with the corresponding computer model (see Figure 83). The locations of the resonance bands vary only slightly between the model and measurement. Again, the key difference appears to be the strength of the  $S$ -parameters in the resonance band.

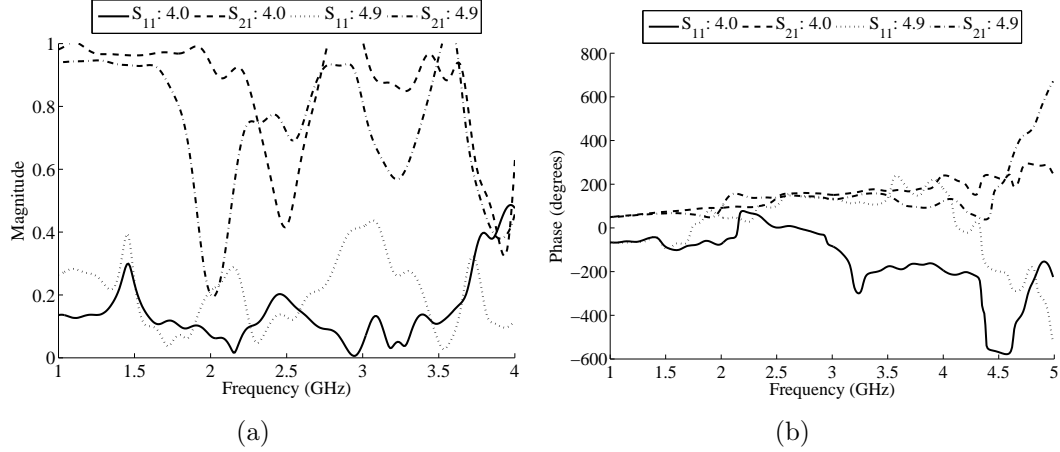


**Figure 105.** Measurement results for the large scale passive metamaterial samples. Four strips are loaded into the stripline for each measurement. (a) The magnitudes of  $S_{11}$  and  $S_{21}$  show resonant frequencies of approximately 2.5 and 2 GHz for the 4.0 and 4.9 scale models, respectively. (b) The phases of  $S_{11}$  and  $S_{21}$ .

#### 4.6.2 Stripline Measurement Conclusions.

As mentioned previously, samples of the metamaterial structure with the MEMS capacitor were not available for measurement before publication of this thesis. The measurement results presented in this chapter, however, show useful results. The locations of the measured resonant frequencies match the resonant frequencies from the computational models. Furthermore, the magnitudes of the measured  $S$ -parameters agree well with the computer simulations outside of the resonance band. The measurement results show that the resonance effects are stronger when more strips are placed into the stripline. This is also consistent with the computer simulations. These similarities demonstrate the validity of the passive metamaterial computer models and increase confidence in the results of the adaptive metamaterial models.



## V. Conclusions and Recommendations

### 5.1 Passive Metamaterial Characterization Summary

The research in this thesis is unable to settle the debate between effective medium and FSS theory. The only phenomena of scattering from the metamaterial wedge in the resonance band that is clearly distinguishable is specular reflection off the wedge face. Any return due to transmission through the wedge and reflection off the plate is too weak to see in the data. This is most likely due to the large amount of losses in the wedge at resonance. The large amount of losses are predicted by both effective medium and FSS theory.

The extracted index of refraction for the metamaterial wedge contains a large imaginary component at resonance. Thus, according to effective medium theory, any fields that propagate through the wedge will be attenuated. This would make determination of negative refraction very difficult to see with the reflection measurement technique used in this thesis since the field would propagate through the wedge twice. The results do show that the specular reflection off of the wedge face is reduced at resonance. This indicates that energy is being transmitted into the wedge.

Using the geometry of the measurements performed in this thesis, Equation (13) yields complex transmission angles for the higher order Floquet modes. According to FSS theory, the grating lobes for the metamaterial structure are trapped. Therefore, the only frequency-dependent scattering from the metamaterial wedge is due to residual currents. The angle of the lobes from residual currents are difficult to predict, but they tend to be small in amplitude. It is not determined in this thesis if residual currents are responsible for the scattering from the metamaterial wedge at resonance.

For the most part, the results from the CST MWS® models match the measurement results very well. A comparison of the results is in Section 4.4.3. Much

of the same phenomena that occurs in the models can be found in the measurement results. The models and the measurement data show that the specular return from the wedge face is attenuated in the resonance band. The computational models show why: energy is being transmitted into and absorbed by the metamaterial wedge.

As noted in Section 4.4.3, a key difference between the models and the measurement results is the location of the resonance band. The measured resonance band is about 12.8 to 14.5 GHz. The frequency solver in CST MWS® produced a very similar frequency band, especially in the unit cell model. On the other hand, the resonance band from the transient solver is about 1 GHz lower. More investigation is necessary to determine why the difference between the frequency and transient solver exists, but part of the difference could be a loss of accuracy with the FFT employed by the transient solver.

On the whole, this research effort shows that using full-wave electromagnetic solvers to model the entire metamaterial’s geometry provides the most accurate solution. Because calculations employing techniques like the FIT are so complex, this does place a limit on the size of the model. However, as computers and computational techniques advance, this drawback becomes less restricting.

## 5.2 Adaptive Metamaterial Summary

Several computational models of the AFIT adaptive metamaterial design are included in this thesis. The most relevant models are the two- and four-strip models with the stripline cross-section. Despite their increased complexity, the simulation time is tolerable (see Table 17 in Appendix A), and they provide results that can be directly compared to stripline measurements.

The computational models of the original-scale metamaterial structure show that the variable capacitor has little effect on the resonant frequency of the device. They

also show that the original-scale structures have no resonances below 4 GHz. Thus, they are not the correct size for AFIT’s large stripline. Increasing the size of the metamaterial structures lowers the resonant frequency, and it is shown in Section 3.6.3 that scale factors between 4.0 and 4.9 are well suited for the large stripline. Structures larger than 4.9 times the original scale will not fit between the center and outer conductors of the stripline.

Simulation results show that the passive metamaterial structure with an FR4 substrate has resonant frequencies of about 2.5 and 2 GHz for the 4.0 and 4.9 scale factors, respectively. The model results also show that coupling between non-coplanar cells does not affect the resonant frequency, but does have an impact on the magnitude of the resonant effects. The non-coplanar cells cause the structure to behave more like a bulk media and increase the magnitude of the resonant effects. The stripline measurements presented in Section 4.6 confirm the model results.

Samples of the adaptive metamaterial design were not available for measurement before the publication of this thesis, but several computational models of the adaptive design are included in Chapter III. As mentioned above, the models show that the resonant frequency of the original-scale structure is not very responsive to changes in the variable capacitor. This is because the equivalent capacitance of the structure is dominated by the capacitance between the inner and outer SRR particles. At the larger capacitances, the capacitance between the inner and outer SRR particles is increased, so the variable capacitor has more influence on the resonant frequency. There is a strong relationship between frequency adaptability and the size of the metamaterial structure, and the model results show that the 4.0 and 4.9 scale structures’ resonant frequency can be highly influenced by the AFIT MEMS capacitor design.

### **5.3 Recommendations for Future Research**

The proposals for expansion of this research fall into two categories: passive metamaterial characterization and adaptive metamaterial recommendations.

#### **5.3.1 Passive Metamaterial Characterization Recommendations.**

The results from the passive metamaterial characterization portion of this research effort effectively demonstrate a new way to measure and characterize bulk metamaterial structures. This new method takes advantage of computing resources and measurement capabilities AFIT already possesses. Expansion of this effort may lead to new discoveries in metamaterials including a possible measurement setup that can distinguish between negative refraction and surface wave effects. The recommendations presented here work towards that goal.

##### **5.3.1.1 Modeling Process Improvements.**

In order to make better comparisons between simulated and measured data for the metamaterial wedge, a study of key parameters should be performed. The purpose is to determine how changes in the wedge structure impact the response. Particular emphasis should be given to parameters impacted by the fabrication of the wedge as well as parameters that could change over time. As a minimum, this study should look at the alignment and spacing between non-coplanar unit cells to determine the impact of the expansion/compression and shifts in the foam.

##### **5.3.1.2 Measurement Process Improvements.**

The measured return from the metamaterial wedge in the resonance band shows the expected attenuation. However, calibration problems with the equipment cast a shadow of doubt on the results, especially in amplitude. Careful analysis of the

calibration data reveals no obvious problems with the radar system, but the amount of calibration error present is greatly dependent on the bistatic receiver angle. At certain angles, there are patterns that could indicate the presence of interference. Further investigation should be performed to determine if there is something wrong with the radar system. Also, the use of different calibration standards may improve the results. For example, square plates could be used instead of the short, squat cylinders.

Another issue plaguing the RCS measurements is the interaction with the range equipment. The global range data for the metamaterial wedge and plate (see Section 4.4.2.2) show a periodic pattern at about -20 inches downrange at  $0^\circ$  that sweeps upwards as the bistatic angle increases. This phenomenon is present and identical at all incident angles and is believed to be caused by some sort of interaction with the range itself. Attempts to remove this feature with postprocessing proved unsuccessful. It is interesting to note that this phenomenon does not appear in the metamaterial wedge measurements without the plate, but it does appear in the measurements with the metal plate and the calibration standards. For the final metamaterial wedge measurements, the bistatic arm was covered with foam absorber (see Figure 96). A next step to improve the RCS measurements is to determine the cause of this phenomenon. If this is caused by interaction with the range, eliminating or reducing its effects may also help with the calibration issue discussed earlier.

To augment the RCS measurements, the focus beam system should be used to directly measure transmission through the wedge. The directions of the scattering lobes can be determined by moving the receiving lens and antenna. This allows for a more straightforward calculation of the wedge's index of refraction and can help distinguish some of the scattering phenomena seen in the RCS measurements. It should be noted, however, that losses coupled with the wedge-shape of the metamaterial

sample are going to lead to a shift in the beam towards the negative refraction side. This is discussed in Section 2.4 and [40].

Once the measurement techniques have been further refined, different bulk metamaterial samples should be measured. Reduction of the losses at resonance is a key area to be investigated. The losses obscure the results at resonance and make it difficult to determine what scattering mechanisms are taking place. To address this issue, reducing the depth of the metamaterial wedge plays a key role since the transmitted fields must propagate through the wedge twice in the RCS measurements. The effect of reducing the depth of the wedge can be seen by comparing the results of the mid-sized wedge model to the full-sized wedge model. The results from the mid-sized model show some interesting lobes in the resonance band that are not present in the full-sized wedge model results.

Different bulk sample geometries should also be investigated. For measurements with the focus beam system, the wedge geometry helps to create the oblique incidence that is necessary to see negative refraction. Unfortunately, the wedge geometry coupled with the losses in the metamaterial cause an uneven distribution of energy on the metal plate behind the wedge. This may influence the results by making the radiation from one side of the wedge stronger than the other side of the wedge. With the bistatic RCS measurements, the oblique incidence is created by rotating the pylon to different incidence angles. The wedge geometry is no longer necessary and a rectangular geometry eliminates the problem of uneven field attenuation.

### **5.3.2 Adaptive Metamaterial Recommendations.**

Stripline measurements of the passive metamaterial structure confirm the validity of the modeling approach used in this thesis. To improve the modeling fidelity, longer stripline geometries may be beneficial. The stripline geometries used in this thesis

are three times longer than the metamaterial structure. Thus, the space between the end of the metamaterial sample and the second port is equal to the length of the metamaterial sample. This geometry may not allow enough space for any higher-order modes introduced by the metamaterial structure to attenuate properly. It is especially important for the original-size metamaterial structure model that the spacing be increased.

As is shown in this thesis, the original size of the AFIT metamaterial design is not well-suited to measurement in the large metamaterial structure. The 20 GHz stripline is harder to use and the center conductor tends to flex quite a bit. The larger stripline is more consistent and easier to use, but multimode operation beyond 4 GHz makes finding resonance bands an impossible task for the original-size structure. It is shown in this thesis that scaling the structure 4 to 4.9 times larger than the original size works well with AFIT's large stripline.

The capacitance measurements performed in [39] are performed at low frequencies. Higher frequency operation may change the capacitance values, but the samples that have been made are not compatible with the high-frequency probes. Testing pads should be included in the next mask of the adaptive metamaterial structure. These testing pads should be spaced appropriately for use with the high-frequency probes. Once these are included, capacitance measurements can be performed using a high-frequency impedance analyzer or network analyzer. Measurements above 1 GHz should be accomplished.

The models of the larger structures with the capacitance values from [39] show much more control of the resonant frequency with the MEMS capacitor than the original-scale structures. The relationship between the size of the metamaterial structure and the influence of the MEMS capacitor is critical. New adaptive metamaterial samples should be constructed at the 4.0 and/or 4.9 scale factors. An attempt should

be made to keep the capacitance of the MEMS capacitor as close to the same as possible. Once these samples are constructed, stripline measurements should be performed. These stripline measurements should show much greater variation in the resonant frequency as the state of the MEMS capacitor changes.



## Appendix A. Computation Mesh Figures and Statistics

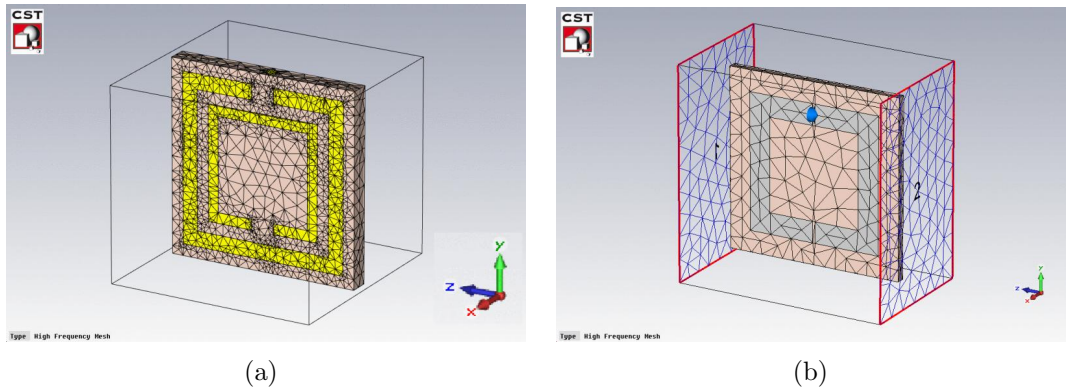


Figure 106. The high frequency tetrahedral meshes generated by CST MWS® for the comparison studies. (a) The mesh generated for the model of the structure in [47]. (b) The mesh generated for the model of structure in [17].

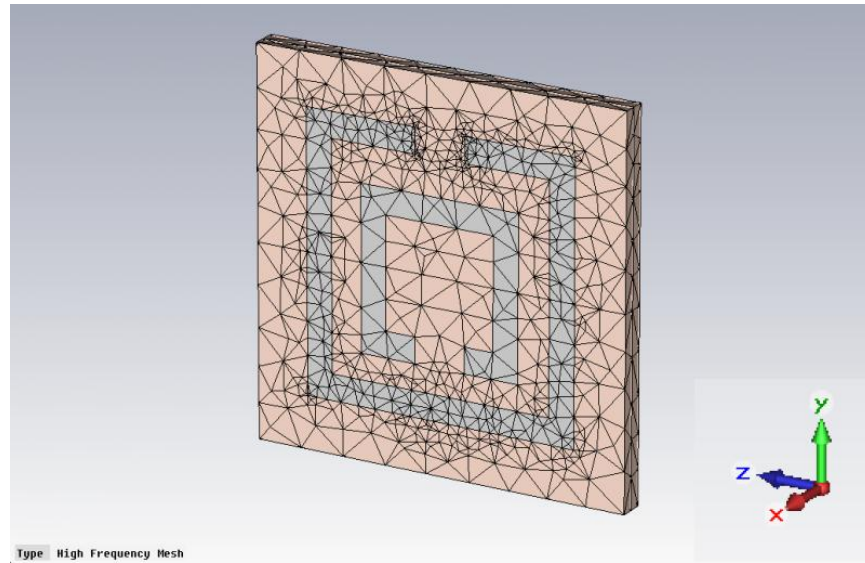


Figure 107. The high frequency tetrahedral mesh generated by CST MWS® for the metamaterial wedge unit cell model.

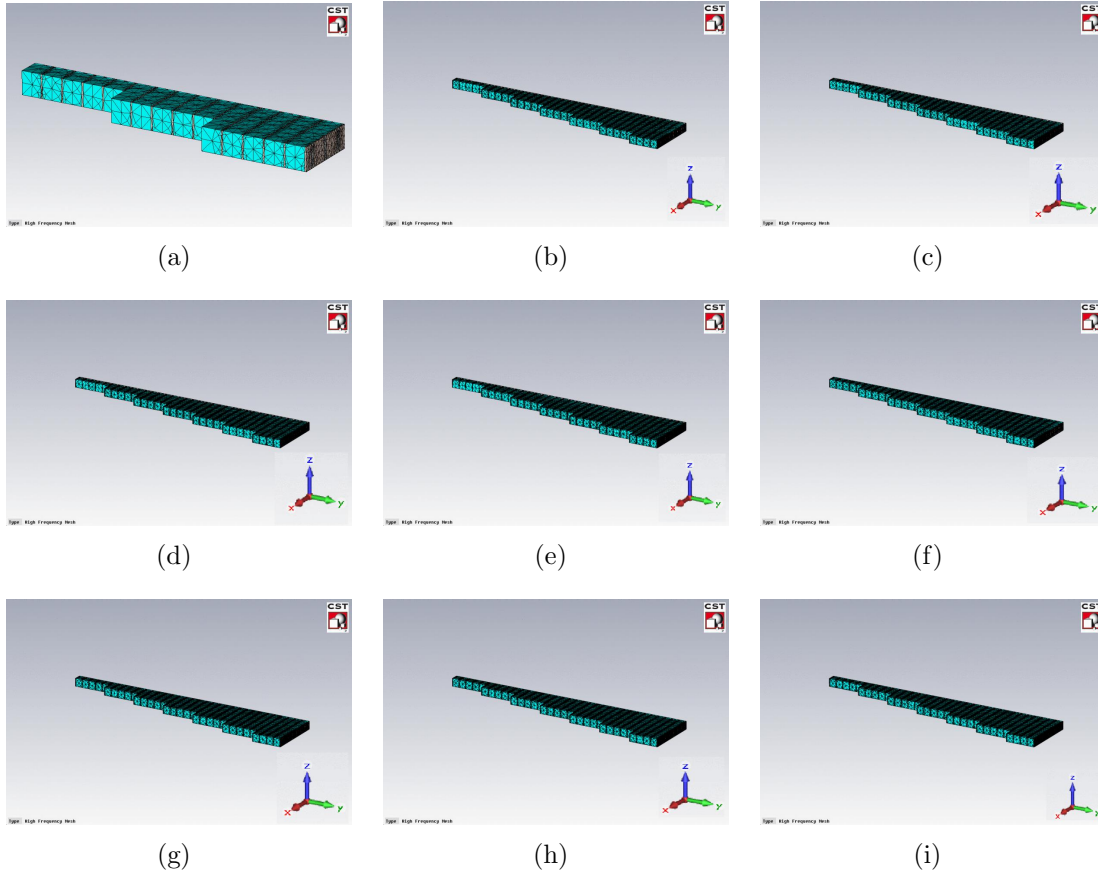
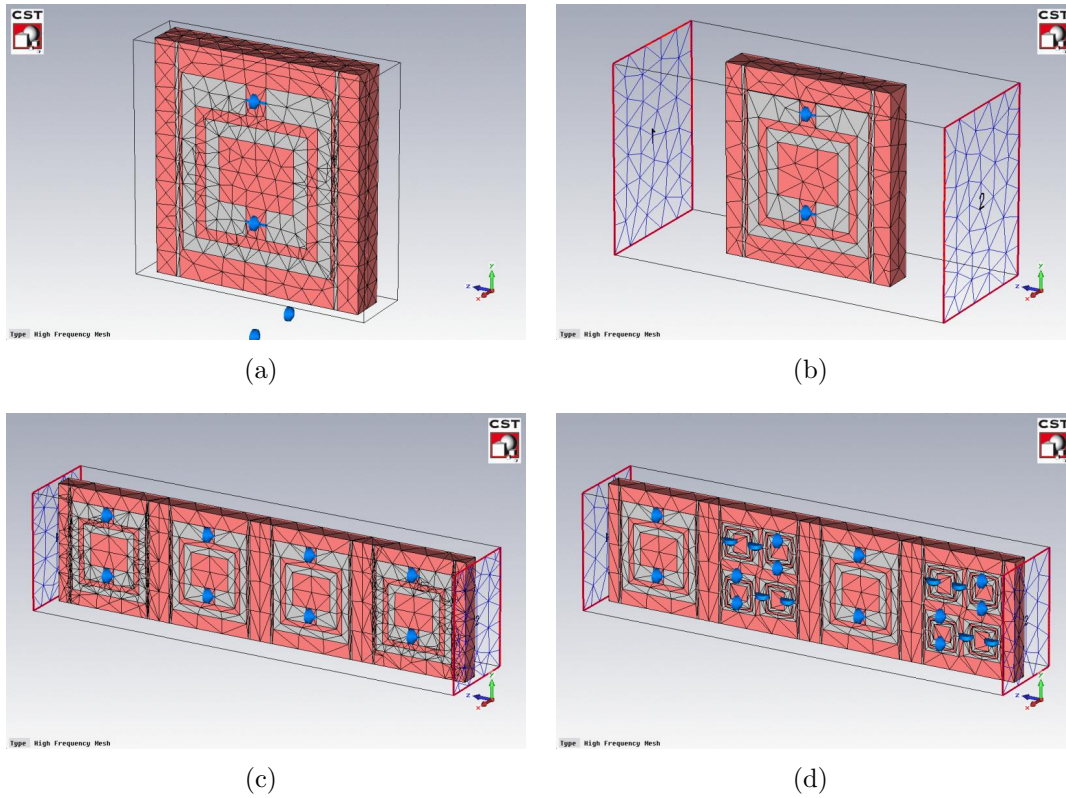


Figure 108. The high frequency tetrahedral meshes generated by CST MWS® for the metamaterial wedge models. The mesh for the (a) simple wedge model, (b) mid-sized metamaterial wedge model at an incident angle of  $0^\circ$ , (c) mid-sized wedge model at an incident angle of  $15^\circ$ , (d) mid-sized wedge model at an incident angle of  $30^\circ$ , (e) mid-sized wedge model at an incident angle of  $45^\circ$ , (f) mid-sized wedge without the plate at an incident angle of  $0^\circ$ , (g) mid-sized wedge without the plate at an incident angle of  $15^\circ$ , (h) mid-sized wedge without the plate at an incident angle of  $30^\circ$ , and (i) the mid-sized wedge without the plate at an incident angle of  $45^\circ$ .

Table 14. Full 2-D metamaterial wedge model mesh summary

Model	Mesh Step		Number Mesh Lines			Number of Mesh Cells
	Min	Max	$x$ -axis	$y$ -axis	$z$ -axis	
Wedge with plate	0.1275	0.90911	220	392	12	941,919
Wedge without plate	0.1275	0.707327	262	446	14	1,509,885



**Figure 109.** The high frequency tetrahedral meshes generated by CST MWS® for the AFIT adaptive metamaterial models. (a) The mesh generated for the single cell periodic model. (b) The mesh generated for the one cell non-periodic model. (c) The mesh generated for the four cell, single geometry SRR metamaterial structure with waveguide-like boundary conditions. (d) The mesh generated for the four cell, double geometry SRR metamaterial structure with waveguide-like boundary conditions.

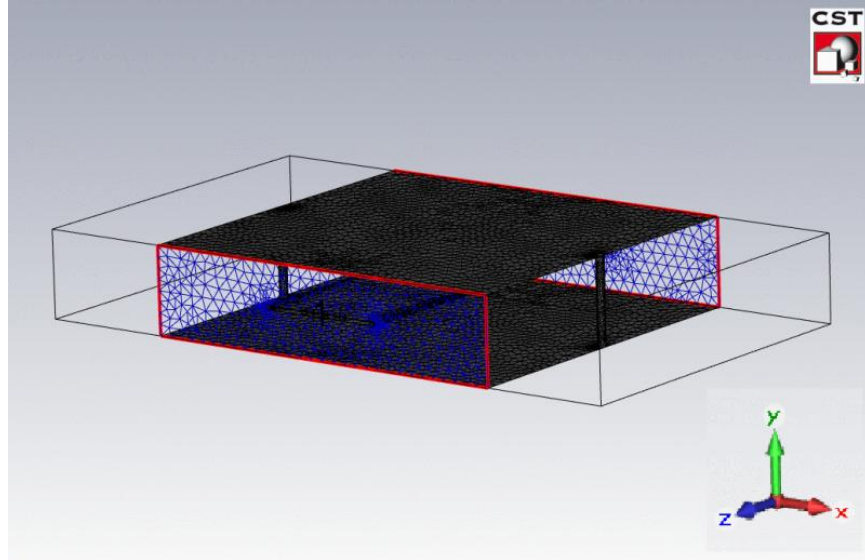


Figure 110. High frequency tetrahedral mesh generated for the empty stripline model.

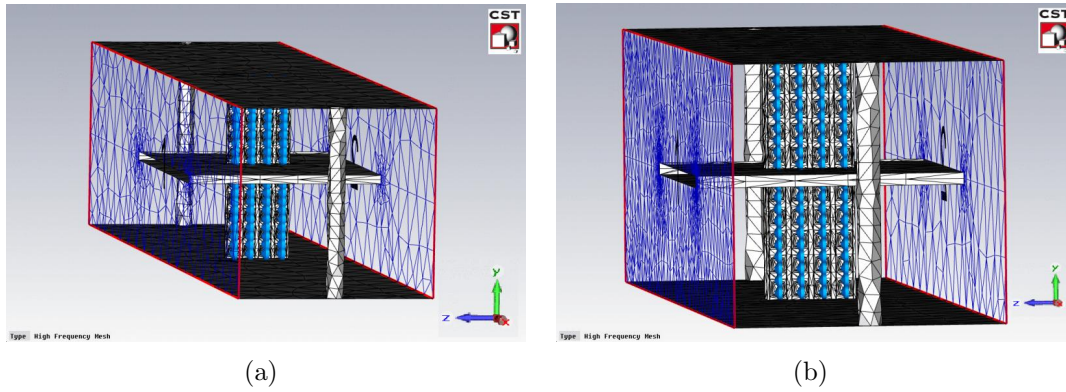
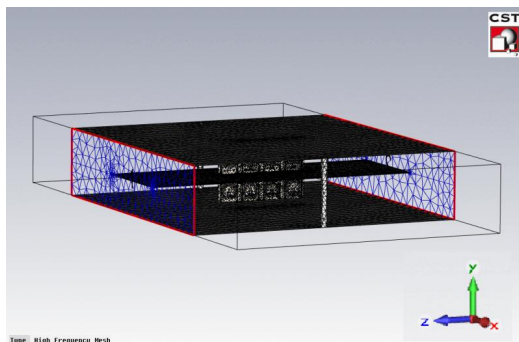
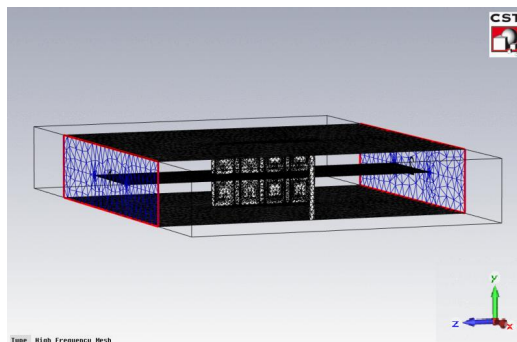


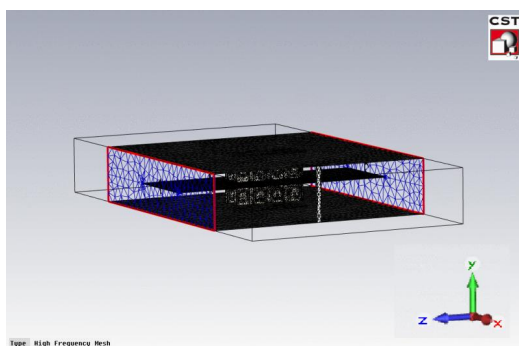
Figure 111. High frequency tetrahedral meshes generated for the advanced AFIT adaptive metamaterial models. The meshes shown are for a lumped capacitance value of 0.12 pF; other capacitance values generate similar meshes. (a) The mesh generated for the original size AFIT adaptive metamaterial model. (b) The mesh generated for the original size AFIT adaptive model with four metamaterial strips.



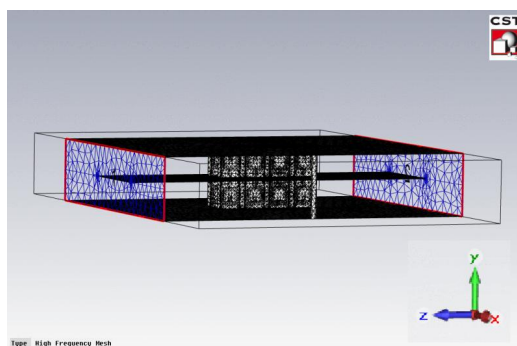
(a)



(b)



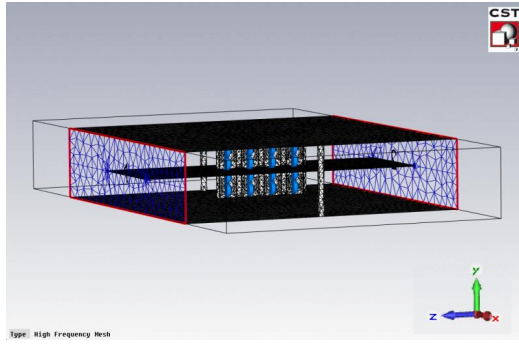
(c)



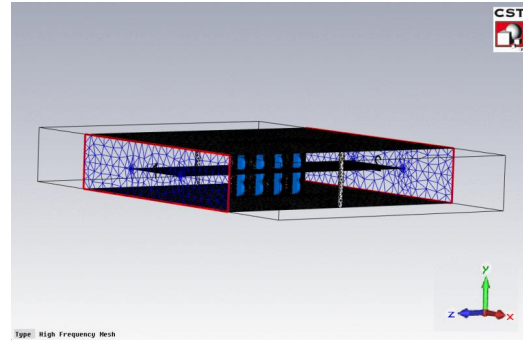
(d)

**Figure 112.** High frequency tetrahedral meshes generated by CST MWS® for the advanced AFIT large non-adaptive metamaterial models. (a) The mesh generated for the 4.0 scale model. (b) The mesh generated for the 4.9 scale model. (c) The mesh generated for the 4.0 scale, 4-strip model. (d) The mesh generated for the 4.9 scale, 4-strip model.

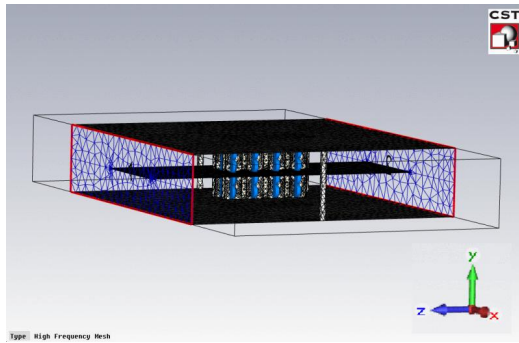




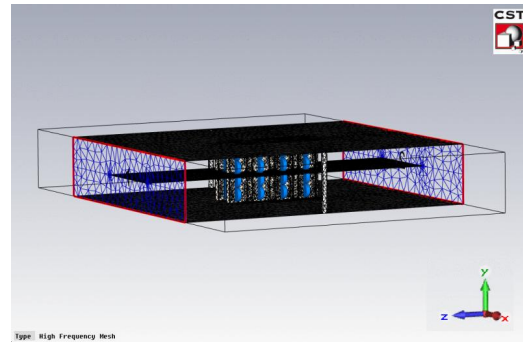
(a)



(b)



(c)



(d)

**Figure 113.** High frequency tetrahedral meshes generated for the advanced AFIT large adaptive metamaterial models. The meshes are shown for a lumped capacitance value of 0.12 pF; other lumped capacitance values generate similar meshes. (a) The mesh generated for the 4.0 scale model. (b) The mesh generated for the 4.9 scale model. (c) The mesh generated for the 4.0 scale, 4-strip model. (d) The mesh generated for the 4.9 scale, 4-strip model.

**Table 15. Metamaterial wedge frequency-solver mesh statistics**

Model	Tetrahedrons	Edge Length (mm)		Quality		
		Min	Max	Min	Max	Average
Wedge unit cell <sup>1</sup>	22,729	0.00831916	0.714566	0.10481	0.929698	0.447036
Simple wedge	56,391	0.028844	3.7	0.0479391	0.968559	0.407962
Mid-size wedge (0°incidence)	251,109	0.0378145	5.2248	0.0348697	0.949018	0.410025
Mid-size wedge (15°incidence)	250,502	0.0312864	5.2248	0.0334889	0.95497	0.410859
Mid-size wedge (30°incidence)	250,114	0.026268	5.30601	0.0278241	0.946134	0.410242
Mid-size wedge (45°incidence)	250,034	0.0406529	5.49743	0.0290624	0.950988	0.411101
Mid-size wedge, no plate (0°incidence)	257,127	0.0268994	5.49743	0.0384358	0.954558	0.411601
Mid-size wedge, no plate (15°incidence)	257,050	0.0231174	5.49743	0.0350923	0.981325	0.41171
Mid-size wedge, no plate (30°incidence)	255,755	0.0156015	5.49743	0.0353087	0.951797	0.411499
Mid-size wedge, no plate (45°incidence)	255,510	0.041592	5.2248	0.0353086	0.951303	0.411313

<sup>1</sup> Statistics are for 0° incidence; other incident angles produce similar meshes.

Table 16. AFIT metamaterial design frequency-solver mesh statistics

Model	Tetrahedrons	Edge Length (mm)		Quality		
		Min	Max	Min	Max	Average
Empty stripline	42,544	0.0694028	8.24068	0.0286122	0.94	0.50526
AFIT metamaterial advanced model Adaptive, original scale <sup>1</sup>	11,622	0.020274	13.73763	0.00326661	0.940384	0.3158
AFIT metamaterial advanced model Adaptive, original scale, 4 strips <sup>1</sup>	21,131	0.0145241	13.70961	0.00293801	0.94346	0.264348
AFIT metamaterial advanced model 4.0 scale, FR4 substrate <sup>2</sup>	67,167	0.0272273	10.97131	0.00355992	0.95286	0.417839
AFIT metamaterial advanced model 4.9 scale, FR4 substrate <sup>2</sup>	89,036	0.0218796	10.98022	0.00371147	0.953431	0.414323
AFIT metamaterial advanced model 4.0 scale, FR4 substrate, 4 strips <sup>2</sup>	91,280	0.00799138	10.9743	0.00547826	0.964973	0.398186
AFIT metamaterial advanced model 4.9 scale, FR4 substrate, 4 strips <sup>2</sup>	121,132	0.0187622	10.99104	0.0116254	0.952318	0.391853
AFIT metamaterial advanced model 4.0 scale, quartz substrate <sup>1</sup>	38,774	0.0407323	10.97307	0.00119568	0.939231	0.456589
AFIT metamaterial advanced model 4.9 scale, quartz substrate <sup>1</sup>	86,232	0.0168685	10.98597	0.00391981	0.968027	0.413631
AFIT metamaterial advanced model 4.0 scale, quartz substrate, 4 strips <sup>1</sup>	70,478	0.0266177	10.98775	0.0102308	0.96457	0.396182
AFIT metamaterial advanced model 4.9 scale, quartz substrate, 4 strips <sup>1</sup>	112,317	0.0143396	10.97588	0.00483358	0.965794	0.386898

<sup>2</sup> Statistics are for 0.12 pF lumped capacitance; other lumped capacitance values produce similar meshes.

<sup>3</sup> Statistics are for large scale, non-adaptive model.



**Table 17. Solution time**

Model	Time		
	Hours	Minutes	Seconds
Metamaterial wedge unit cell <sup>1</sup>	1	41	28
Simple metamaterial wedge	0	29	56
Mid-sized metamaterial wedge <sup>1</sup>	16	31	42
Mid-sized metamaterial wedge without plate <sup>1</sup>	17	13	59
Full metamaterial wedge <sup>1</sup>	34	27	35
Full metamaterial wedge without plate <sup>1</sup>	28	12	39
Empty stripline	0	9	30
AFIT metamaterial advanced, original scale <sup>2</sup>	1	8	22
AFIT metamaterial advanced, original scale, 4 strips <sup>2</sup>	2	35	11
AFIT metamaterial advanced, FR4 substrate <sup>3</sup>	1	52	46
AFIT metamaterial advanced, FR4 substrate, 4 strips <sup>3</sup>	2	53	38
AFIT metamaterial advanced, quartz substrate <sup>4</sup>	9	3	46
AFIT metamaterial advanced, quartz substrate, 4 strips <sup>4</sup>	15	16	25

<sup>1</sup> Total includes simulations at 0°, 15°, 30°, and 45° incidence angles.

<sup>2</sup> Total includes simulations at six different lumped capacitance values (see Table 9 in Section 3.6.2).

<sup>3</sup> Total includes simulations at 4.0 and 4.9 scale factors.

<sup>4</sup> Total includes simulations for six different lumped capacitances (see Table 9 in Section 3.6.2) at two different scale factors (4.0 and 4.9).

## Appendix B. Radar Cross Section Measurement Data

This appendix contains RCS measurement data that was not specifically referenced in the previous chapters. For the most part, the data presented in the previous chapters are considered to be representative of the outcomes from the measurements, and this data are presented for completeness.

### B.1 Initial Metamaterial Wedge Measurements

The test matrix for the initial metamaterial wedge RCS measurements taken on 15 Aug 09 is shown in Table 18. The data from the first low frequency calibration measurements (PM2, PM4, and PM6) are unusable because the frequency range on the radar acquisition system was improperly set. However, the second low frequency calibration measurements (PM14, PM16, and PM18) were successfully accomplished.

**Table 18. Test matrix for initial metamaterial wedge measurements**

Meas. ID	Target	Frequency (GHz)	Pylon Angle (deg)	Receiver $\phi$ (deg)
PM1	375 cal cylinder	6-18	NA	45
PM2	375 cal cylinder	3-6	NA	45
PM3	450 cal cylinder	6-18	NA	45
PM4	450 cal cylinder	3-6	NA	45
PM5	Calibration background	6-18	NA	45
PM6	Calibration background	3-6	NA	45
PM7	Metamaterial wedge	6-18	-45	0-145
PM8	Metamaterial wedge	3-6	-45	0-145
PM9	PEC plate	6-18	-45	0-145
PM10	PEC plate	3-6	-45	0-145
PM11	Target mount	6-18	-45	0-145
PM12	Target mount	3-6	-45	0-145
PM13	375 cal cylinder	6-18	NA	45
PM14	375 cal cylinder	3-6	NA	45
PM15	450 cal cylinder	6-18	NA	45
PM16	450 cal cylinder	3-6	NA	45
PM17	Calibration background	6-18	NA	45
PM18	Calibration background	3-6	NA	45

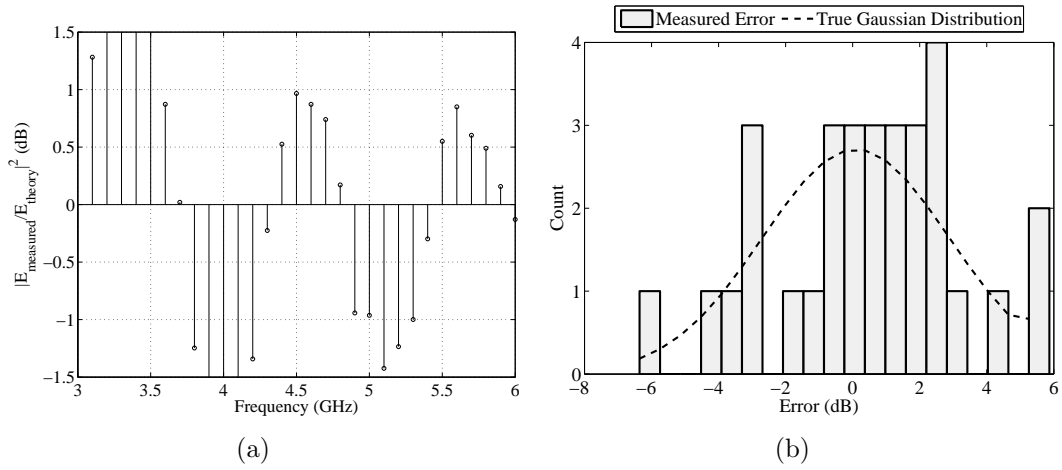
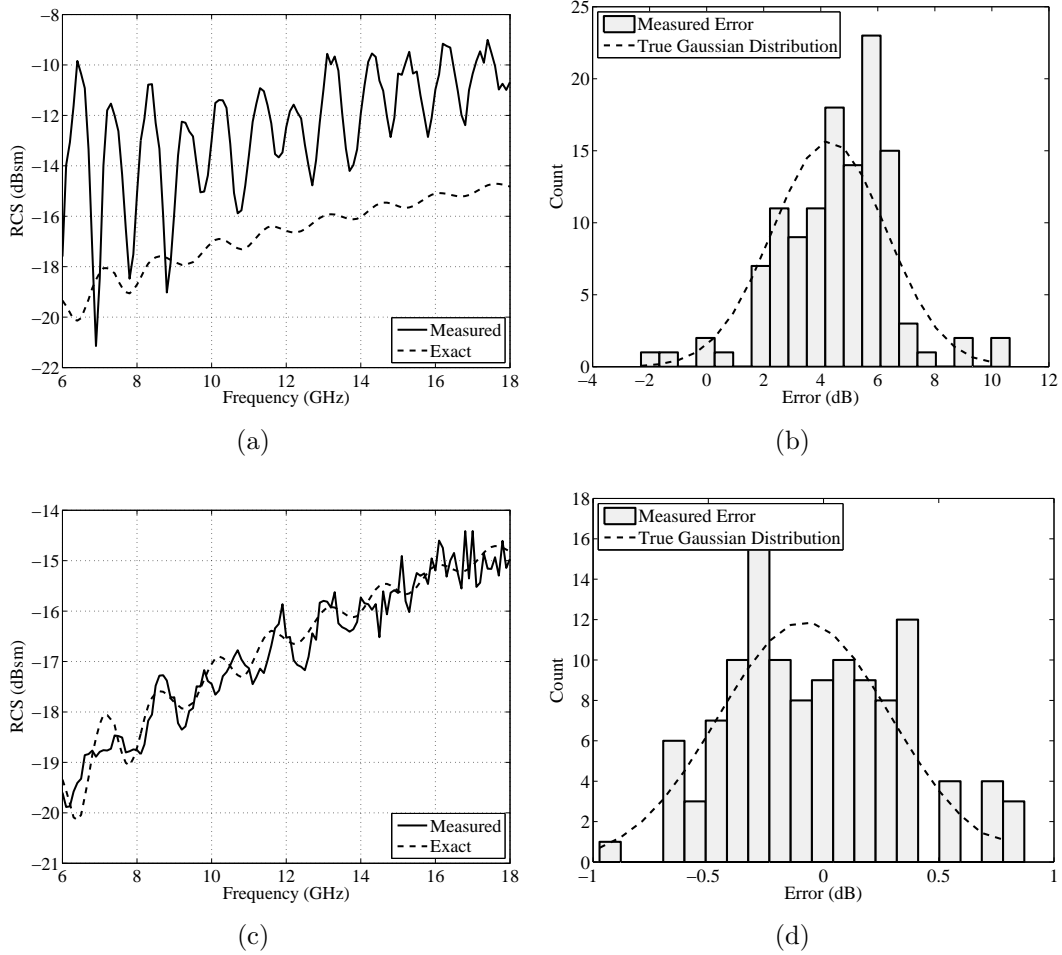
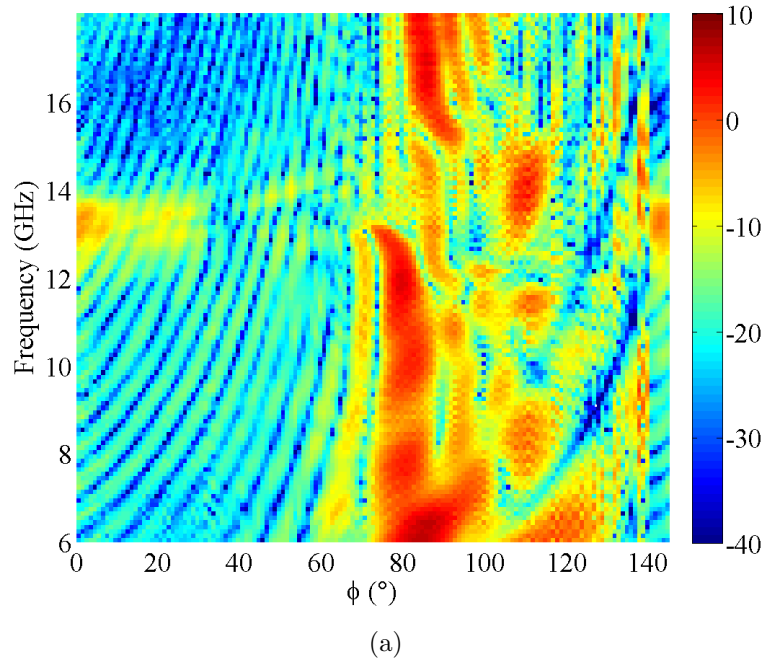


Figure 114. The calibration error for the second calibration measurement at the 3 to 6 GHz frequency band in the vertical polarization. (a) The calibration error appears larger than the 6 to 18 GHz measurements at individual frequency samples. This is because the 375 and 450 calibration standards are too small for the 3 to 6 GHz frequency range. (b) The histogram of the calibration error shows that while the mean error is similar to the measurement in the 6 to 18 GHz band, the standard deviation is much larger indicating much more variation in the accuracy of the 3 to 6 GHz measurements. Note that the  $pp$ -polarization was not measured.



**Figure 115. Histograms of the calibration measurement errors in the  $pp$ -polarization.** (a) The calibration verification for the first data set. (b) A histogram of the error in the first calibration. The dashed line shows a Gaussian distribution using the mean and standard deviation calculated from the data. The data appear normally distributed. (c) The calibration verification for the second data set. (d) A histogram of the error in the second calibration. The data appear normally distributed.



**Figure 116.** Measured global RCS patterns in the 6 to 18 GHz frequency band for the metamaterial wedge in the  $pp$ -polarization. The  $pp$ -polarization demonstrates the same specular return at  $90^\circ$  as the horizontal polarization, but there is less energy diffracting from the rear edge of the metal plate beyond  $90^\circ$ .

## B.2 Final Metamaterial Wedge Measurements

The test matrix for the final metamaterial wedge RCS measurements is shown in Table 19. In this test, 6 to 18 GHz is the only frequency band measured.

**Table 19. Test matrix for final metamaterial wedge measurements**

Meas. ID	Date	Target	Pylon Angle (deg)	Receiver $\phi$ (deg)
WM1	10 Nov 09	Calibration background	NA	-45-135
WM2	10 Nov 09	375 cal cylinder	NA	-45-135
WM3	10 Nov 09	450 cal cylinder	NA	-45-135
WM4	10 Nov 09	Metamaterial Wedge w/ Plate	0	-45-90
WM5	10 Nov 09	Metamaterial Wedge w/ Plate	-15	-45-105
WM6	10 Nov 09	Metamaterial Wedge w/ Plate	-30	-45-120
WM7	10 Nov 09	Metamaterial Wedge w/ Plate	-45	-45-135
WM8	10 Nov 09	Plate	0	-45-90
WM9	10 Nov 09	Plate	-15	-45-120
WM10	10 Nov 09	Plate	-30	-45-105
WM11	10 Nov 09	Plate	-45	-45-90
WM12	10 Nov 09	Calibration background	NA	-45-135
WM13	10 Nov 09	375 cal cylinder	NA	-45-135
WM14	10 Nov 09	450 cal cylinder	NA	-45-135
WM15	10 Nov 09	Calibration background	NA	-45-135
WM16	10 Nov 09	375 cal cylinder	NA	-45-135
WM17	10 Nov 09	450 cal cylinder	NA	-45-135
WM18	11 Nov 09	Target Background	0	-45-90
WM19	11 Nov 09	Target Background	-15	-45-105
WM20	11 Nov 09	Target Background	-30	-45-120
WM21	11 Nov 09	Target Background	-45	-45-135
WM22	11 Nov 09	Metamaterial Wedge no Plate	0	-45-90
WM23	11 Nov 09	Metamaterial Wedge no Plate	-15	-45-105
WM24	11 Nov 09	Metamaterial Wedge no Plate	-30	-45-120
WM25	11 Nov 09	Metamaterial Wedge no Plate	-45	-45-135
WM26	10 Nov 09	Calibration background	NA	-45-135
WM27	10 Nov 09	375 cal cylinder	NA	-45-135
WM28	10 Nov 09	450 cal cylinder	NA	-45-135

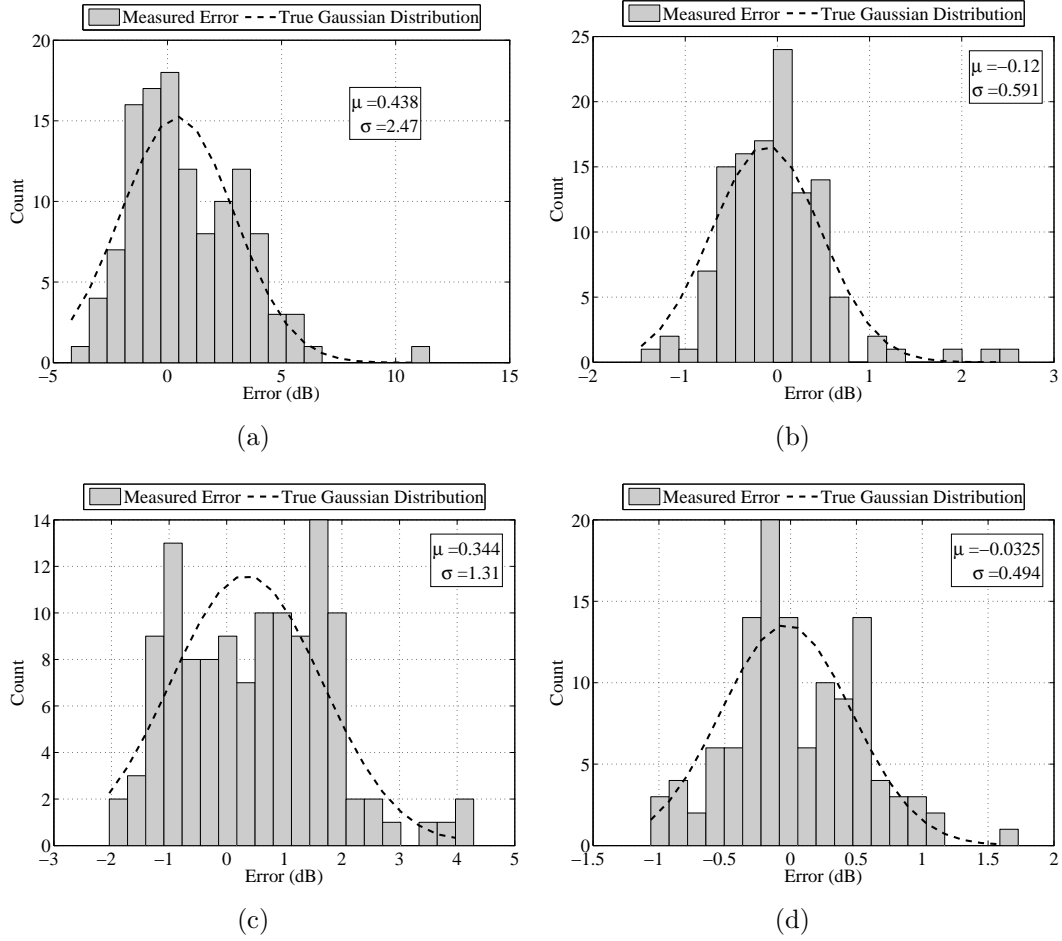


**Figure 117.** Calibration histograms for the  $pp$ -polarized data for the final metamaterial wedge RCS measurements. Shown are the first calibration on day one (a), second calibration on day one (b), first calibration on day two (c), and second calibration on day two (d).

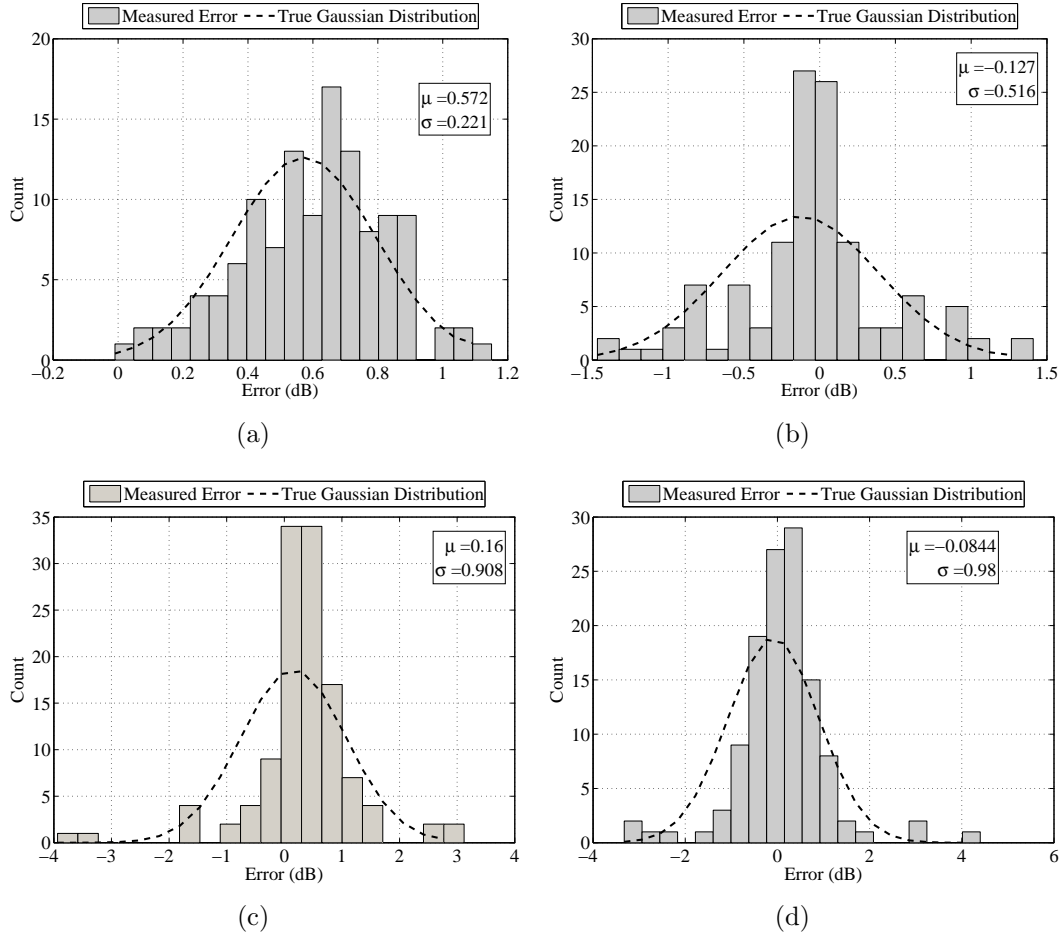


**Figure 118.** Calibration histograms for the  $tt$ -polarized data for the final metamaterial wedge RCS measurements. Shown are the first calibration on day one (a), second calibration on day one (b), first calibration on day two (c), and second calibration on day two (d).



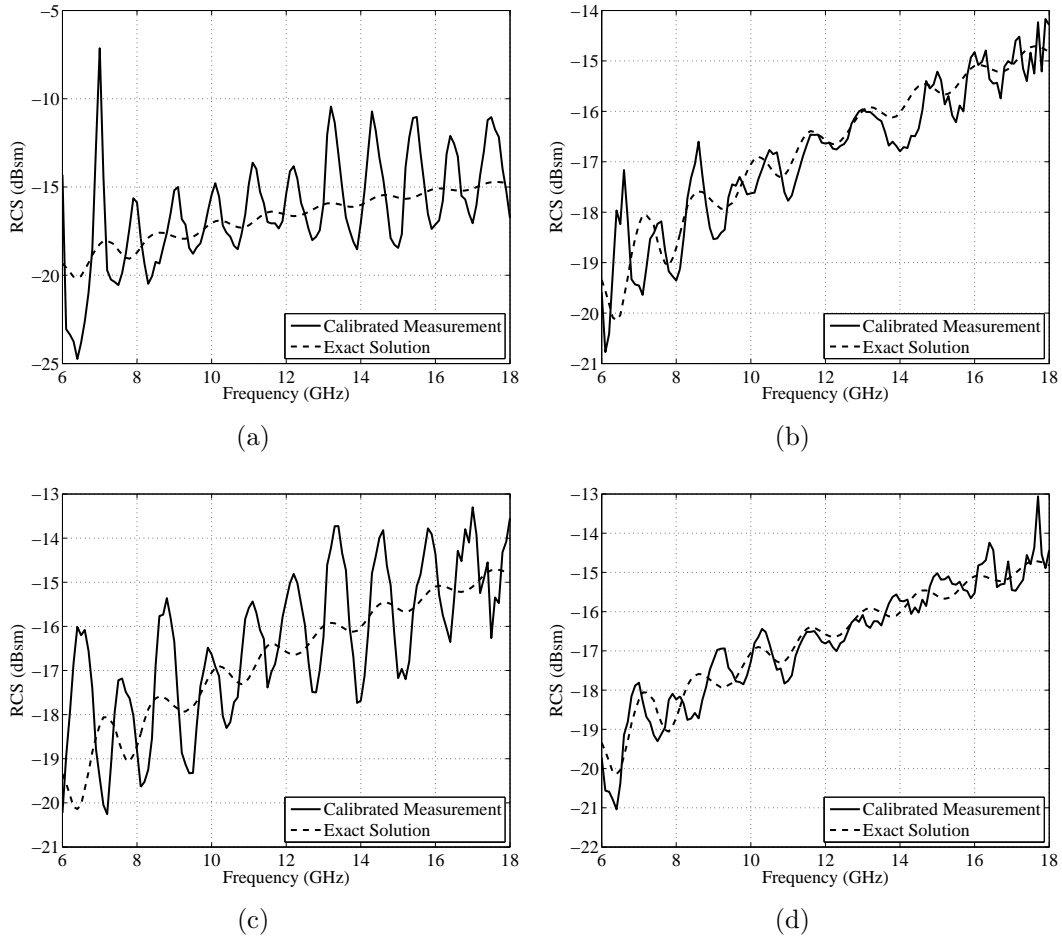


**Figure 119.** Calibration comparison of the  $pp$ -polarized data for the final metamaterial wedge RCS measurements. Shown are the first calibration on day one (a), second calibration on day one (b), first calibration on day two (c), and second calibration on day two (d).

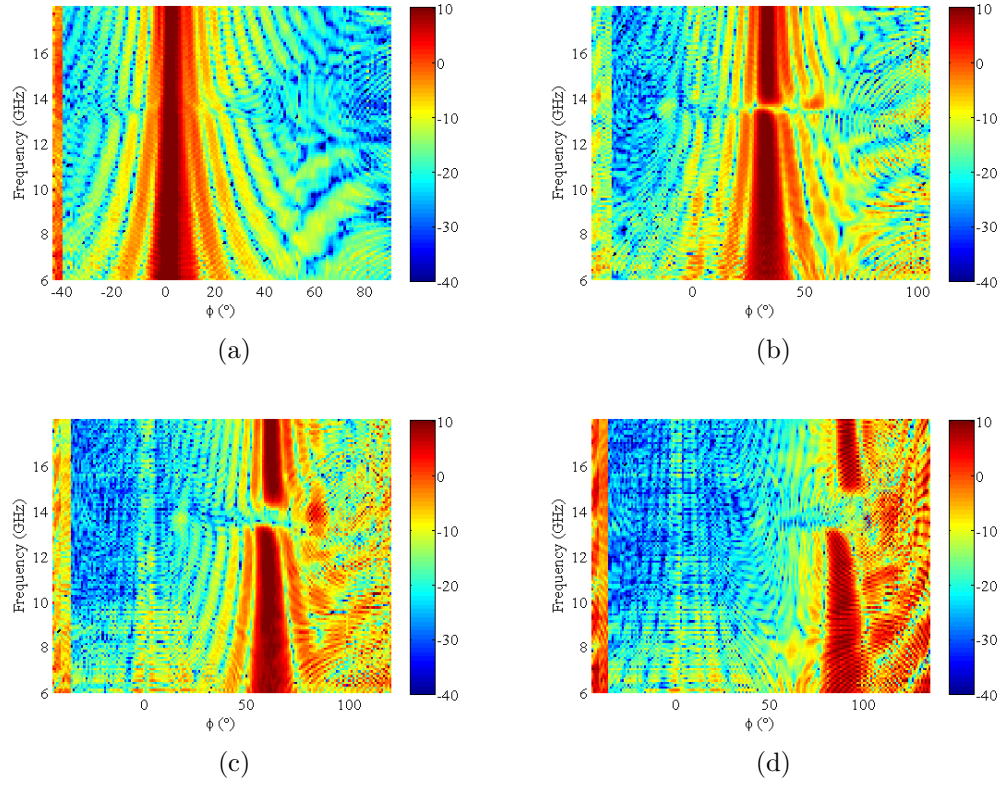


**Figure 120.** Global RCS patterns from the final metamaterial wedge measurements in the *pp*-polarization. (a) Global RCS pattern for an incident angle of 0°. (b) Global RCS pattern for an incident angle of 15°. (c) Global RCS pattern for an incident angle of 30°. (d) Global RCS pattern for an incident angle of 45°.

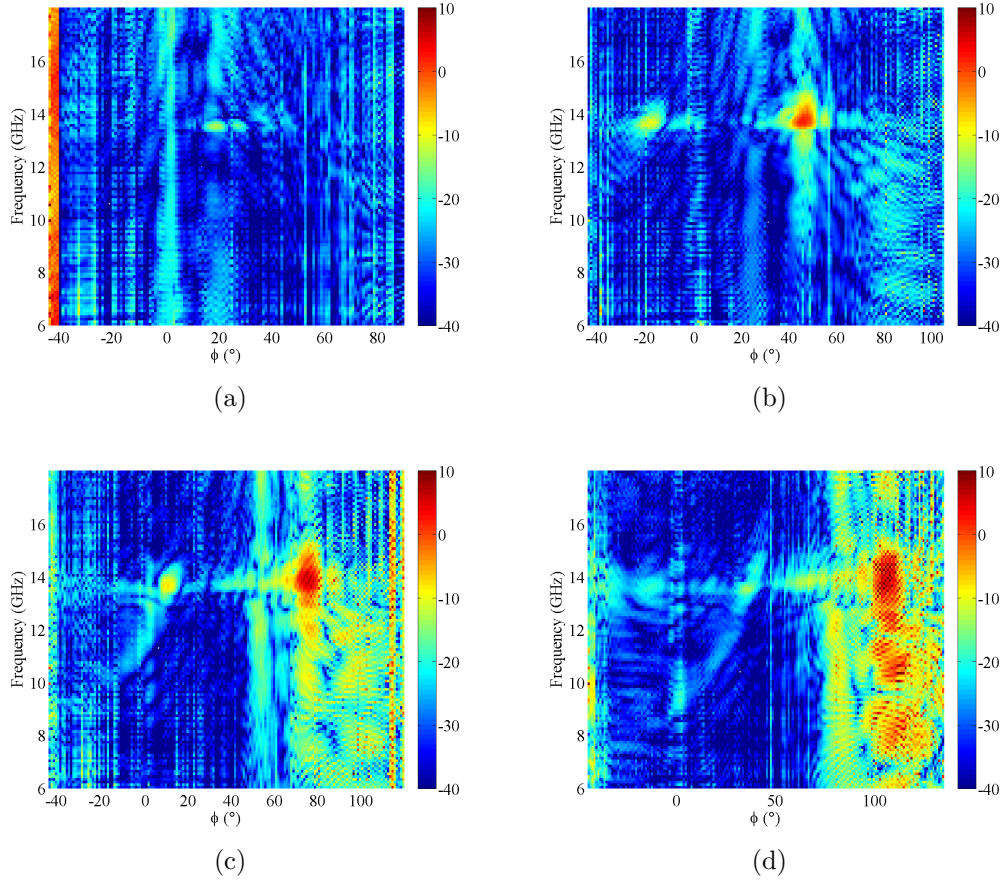


**Figure 121.** Global RCS patterns from the final metamaterial wedge measurements without the metal plate in the  $pp$ -polarization. (a) Global RCS pattern for an incident angle of  $0^\circ$ . (b) Global RCS pattern for an incident angle of  $15^\circ$ . (c) Global RCS pattern for an incident angle of  $30^\circ$ . (d) Global RCS pattern for an incident angle of  $45^\circ$ .

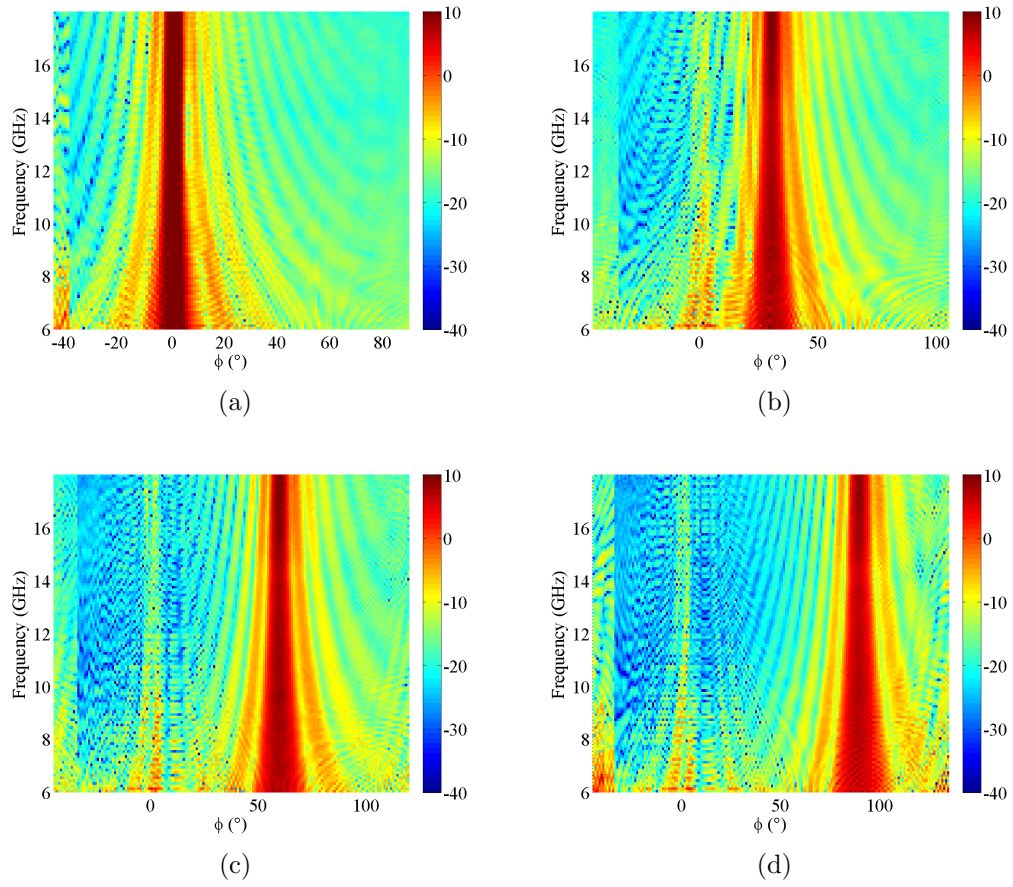


**Figure 122.** Global RCS patterns from the final measurements of the metal plate in the  $tt$ -polarization. (a) Global RCS pattern for an incident angle of  $0^\circ$ . (b) Global RCS pattern for an incident angle of  $15^\circ$ . (c) Global RCS pattern for an incident angle of  $30^\circ$ . (d) Global RCS pattern for an incident angle of  $45^\circ$ .

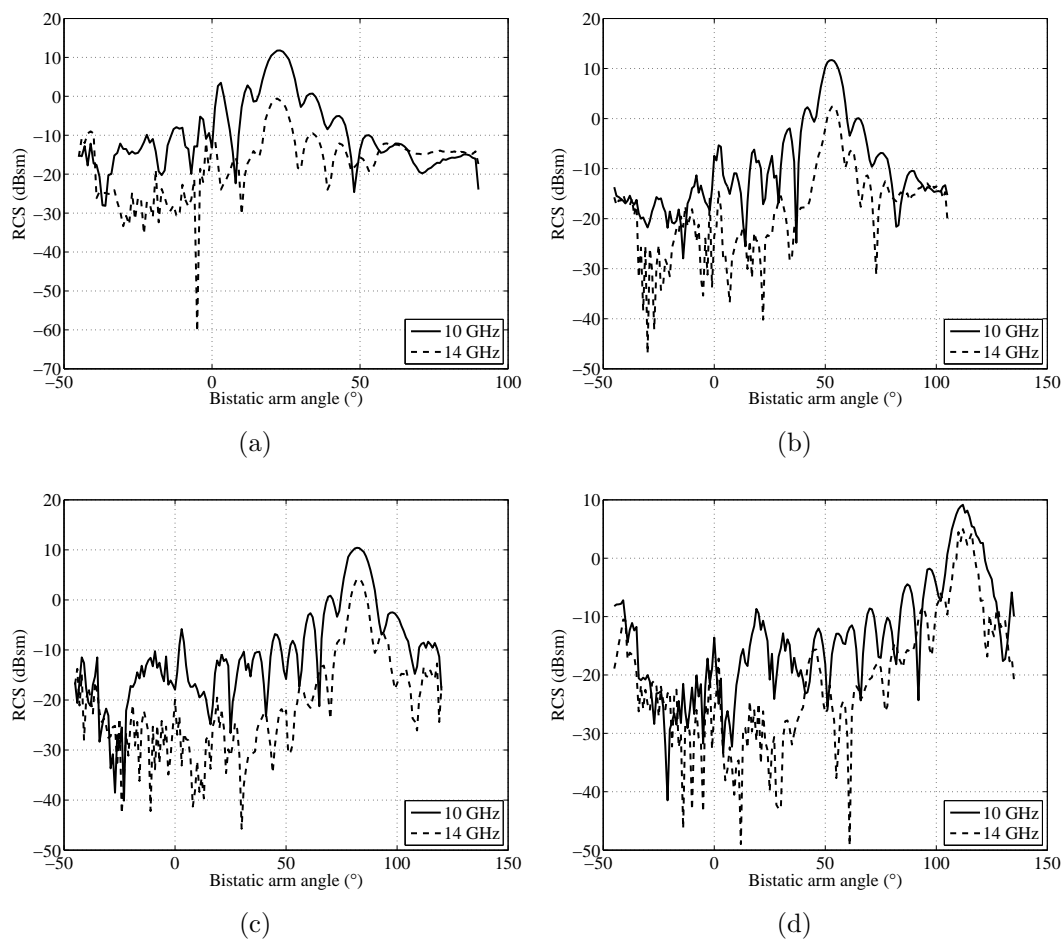


**Figure 123.** RCS patterns for the final RCS measurements of the metamaterial wedge with plate at 10 GHz (out of the resonance band) and 14 GHz (in the resonance band) for incident angles of  $0^\circ$  (a),  $15^\circ$  (b),  $30^\circ$  (c), and  $45^\circ$  (d).

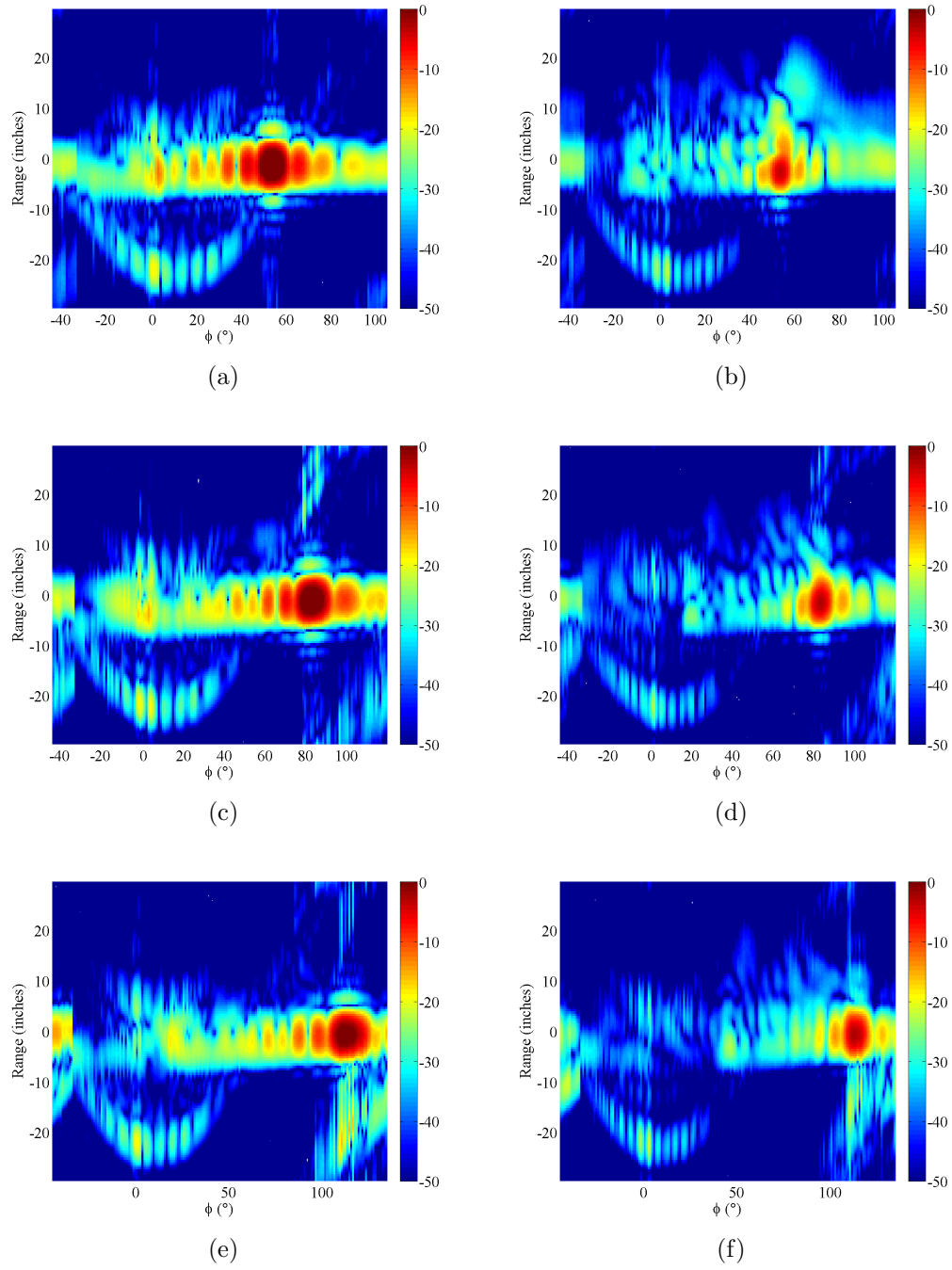


Figure 124. Global range patterns from the final measurements of the metamaterial wedge with plate. (a) The global range pattern for  $15^\circ$  incidence with a center frequency of 10 GHz. (b) The global range pattern for  $15^\circ$  incidence with a center frequency of 14 GHz. (c) The global range pattern for  $30^\circ$  incidence with a center frequency of 10 GHz. (d) The global range pattern for  $30^\circ$  incidence with a center frequency of 14 GHz. (e) The global range pattern for  $45^\circ$  incidence with a center frequency of 10 GHz. (f) The global range pattern for  $45^\circ$  incidence with a center frequency of 14 GHz.

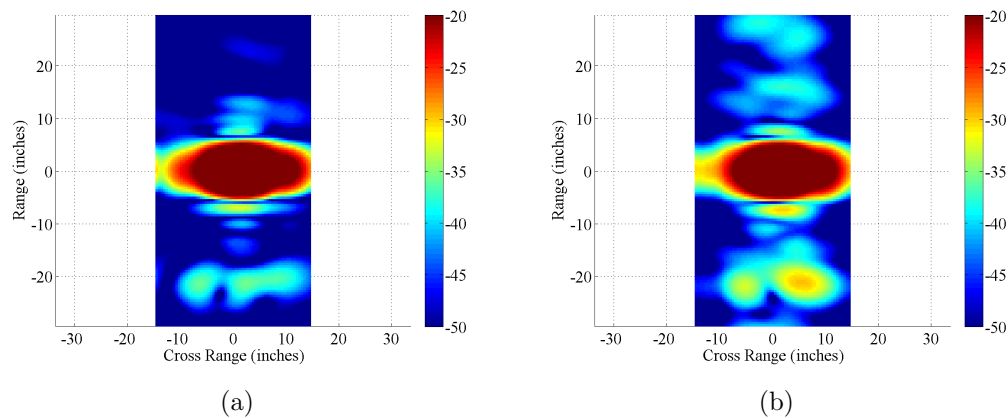
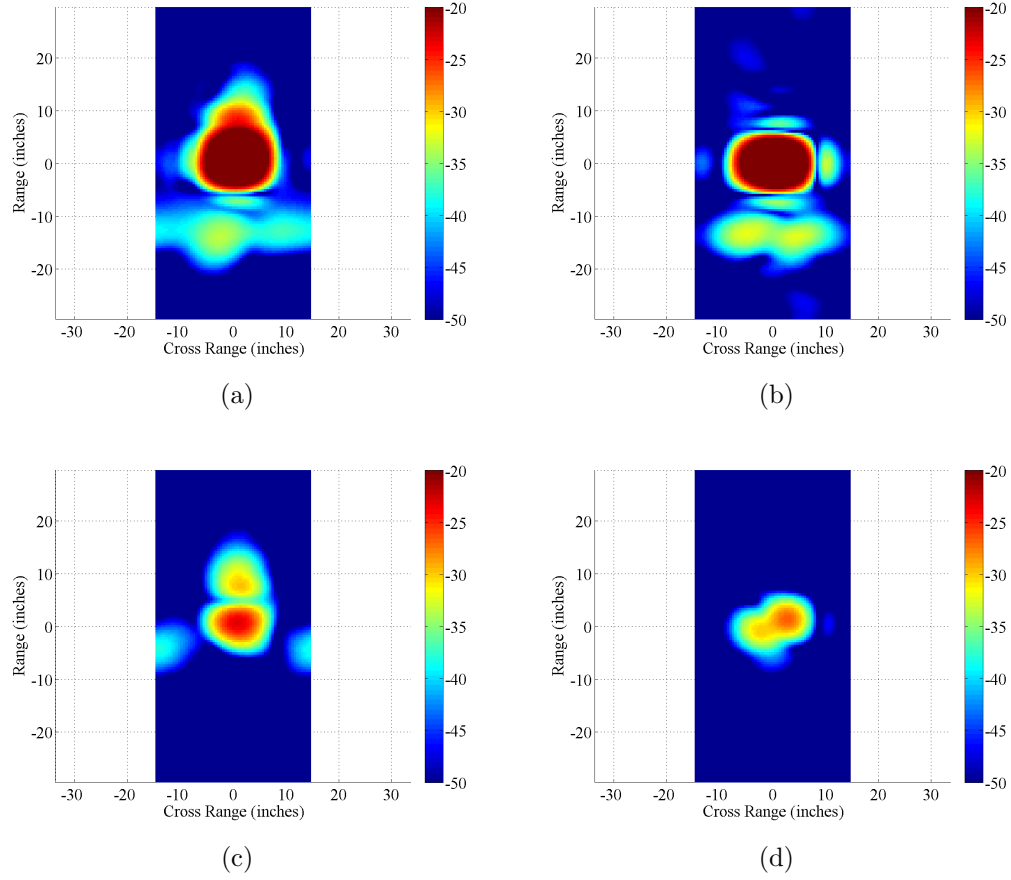
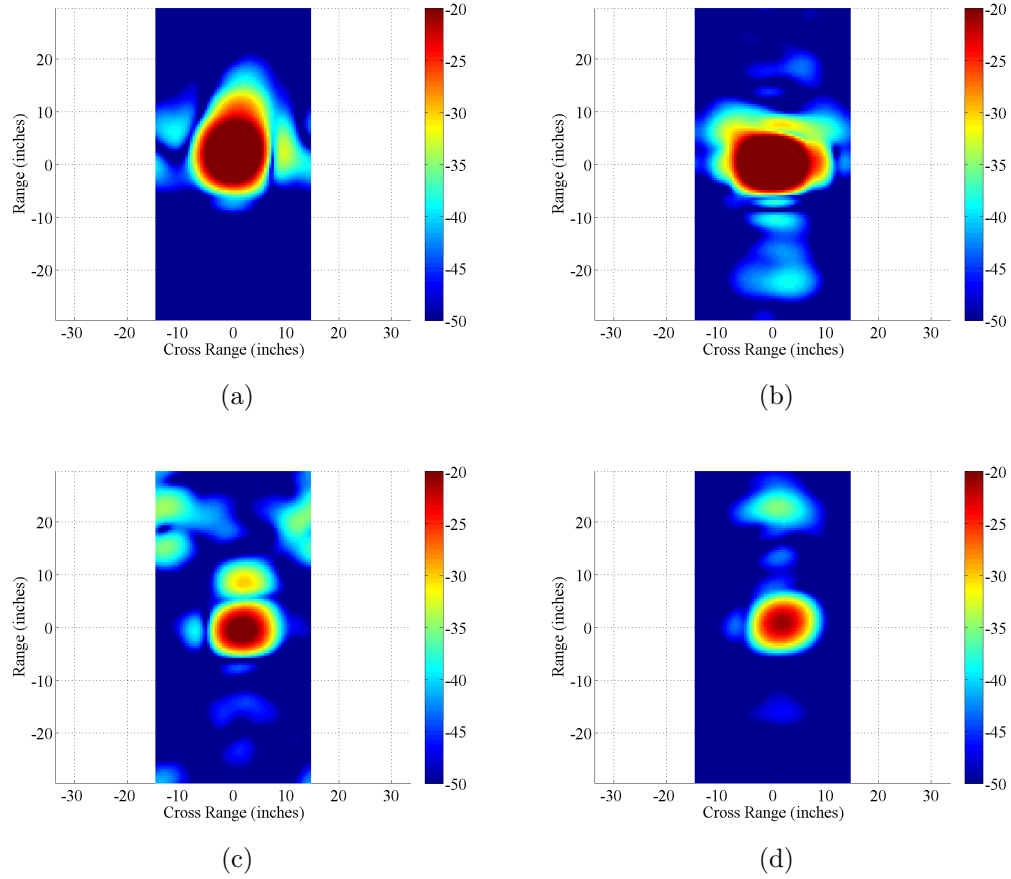


Figure 125. ISAR imagery from the final RCS measurements of the metamaterial wedge with the plate at  $0^\circ$  incidence. The frequency windows are 2 GHz wide and are centered at 13 GHz (a) and 17 GHz (b). The angular windows are both centered at  $0^\circ$  and chosen to be wide enough to make the cross range resolution match the downrange resolution.



**Figure 126.** ISAR imagery from the final RCS measurements of the metamaterial wedge with the plate at  $15^\circ$  incidence. All angular windows are wide enough such that the cross range resolution matches the downrange resolution. (a) The ISAR image with a 2 GHz frequency window centered at 13 GHz and an angular window centered at  $30^\circ$ . (b) The ISAR image with a 2 GHz frequency window centered at 17 GHz and an angular window centered at  $30^\circ$ . (c) The ISAR image with a 2 GHz frequency window centered at 13 GHz and an angular window centered at  $54^\circ$ . (d) The ISAR image with a 2 GHz frequency window centered at 17 GHz and an angular window centered at  $54^\circ$ .





**Figure 127.** ISAR imagery of the metamaterial wedge with the plate at 30° incidence from the final measurements. All angular windows are wide enough such that the cross range resolution matches the downrange resolution. (a) The ISAR image with a frequency window centered at 13 GHz and an angular window centered at 60°. (b) The ISAR image with a frequency window centered at 17 GHz and an angular window centered at 60°. (c) The ISAR image with a frequency window centered at 13 GHz and an angular window centered at 84°. (d) The ISAR image with a frequency window centered at 17 GHz and an angular window centered at 84°.

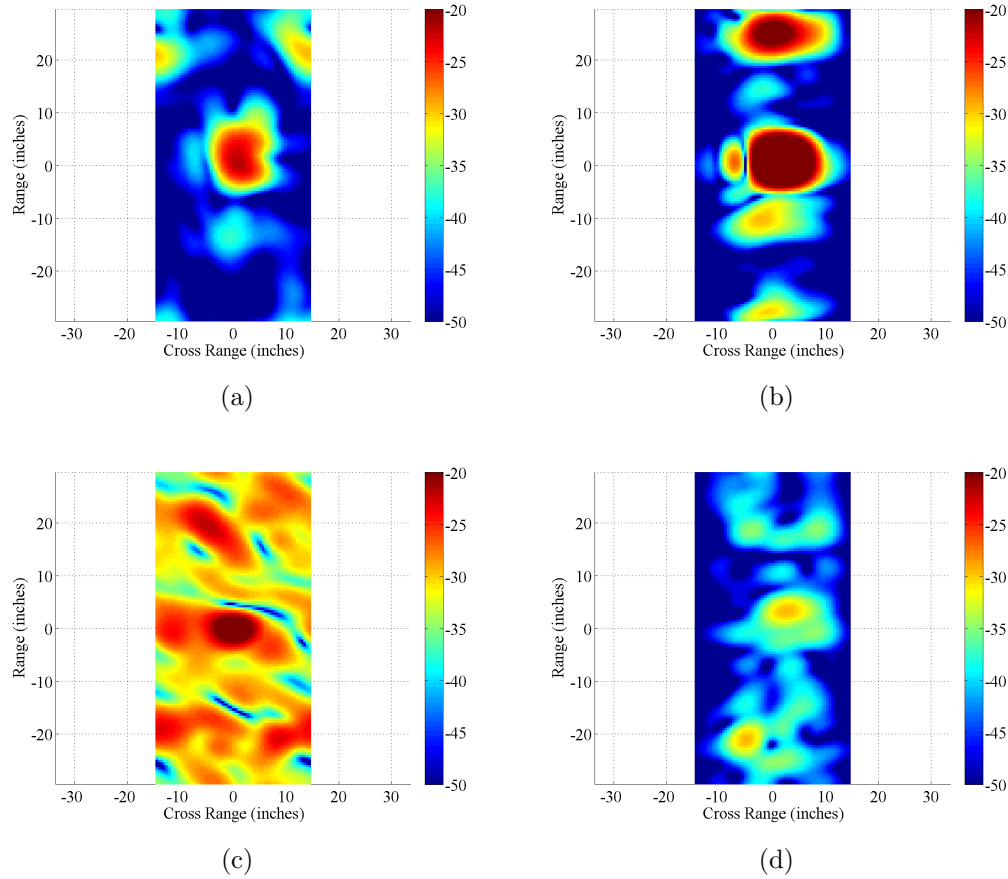


**Figure 128.** ISAR imagery from the final RCS measurements of the metamaterial wedge with the plate at  $45^\circ$  incidence. All angular windows are wide enough such that the cross range resolution matches the downrange resolution. (a) The ISAR image with a 2 GHz frequency window centered at 13 GHz and an angular window centered at  $90^\circ$ . (b) The ISAR image with a 2 GHz frequency window centered at 17 GHz and an angular window centered at  $90^\circ$ . (c) The ISAR image with a 2 GHz frequency window centered at 13 GHz and an angular window centered at  $115^\circ$ . (d) The ISAR image with a 2 GHz frequency window centered at 17 GHz and an angular window centered at  $115^\circ$ .

## Appendix C. Theory of Operation for Computer Scripts

This appendix contains operational descriptions of the computer code written for this thesis effort.

### C.1 Material Parameter Extraction Script

A MATLAB<sup>TM</sup> script was created for this research effort to extract the material parameters  $n$ ,  $z$ ,  $\epsilon_r$ , and  $\mu_r$  from  $S_{11}$  and  $S_{21}$ . Figure 129 shows a flow diagram for the script. Help for this function is available by typing “help mtmextract” at the MATLAB<sup>TM</sup> command line. The main function is invoked in MATLAB<sup>TM</sup> using the command “model\_out=mtmextract(model\_in)” where “model\_in” is a structure containing information about the computer model or measurement and “model\_out” is the structure that will contain the extracted material parameters along with the information in “model\_in”. The structure for “model\_in” and “model\_out” contain the following fields:

- fnames: structure that defines the various filenames for the raw data and is divided into the following fields:
  - S11mag, S12mag, S21mag, and S22mag: strings containing the filenames for the magnitudes of  $S_{11}$ ,  $S_{12}$ ,  $S_{21}$ , and  $S_{22}$ ,
  - S11arg, S12arg, S21arg, and S22arg: strings containing the filenames for the arguments of  $S_{11}$ ,  $S_{12}$ ,  $S_{21}$ , and  $S_{22}$ , and
  - TDR1 and TDR2: strings containing the filenames for the channels 1 and 2 data from the TDR;
- signal: structure that defines various signals and is divided into the following fields:

- V11t and V21t: vectors containing the raw TDR data from channels 1 and 2,
  - V11p and V21p: vectors containing the time-domain impulse response calculated from channels 1 and 2,
  - V11pg and V21pg: vectors containing the gated time-domain impulse response calculated from channels 1 and 2,
  - V11f and V21f: vectors containing the gated frequency-domain impulse response calculated from channels 1 and 2, and
  - t: vector containing the time values in seconds;
- len: number containing the sample length in meters;
  - Frq: vector containing the frequency values in Hertz;
  - k0: vector containing the freespace wavenumber in the waveguide;
  - t: vector containing the time values in seconds;
  - S11, S12, S21, and S22: vectors containing  $S_{11}$ ,  $S_{12}$ ,  $S_{21}$  and  $S_{22}$  in the frequency-domain;
  - z, n, eps, and mu: vectors containing the  $z$ ,  $n$ ,  $\epsilon_r$ , and  $\mu_r$  in the frequency-domain;
  - epsg and mug: numbers containing initial guesses for  $\epsilon_r$  and  $\mu_r$ ; and
  - header: string containing descriptive information about the sample.

The basic theory behind the design of the script is discussed in Section 2.3.5. The function is fed values for  $S_{11}$  and  $S_{21}$  that can be determined through simulation, direct measurement with a network analyzer, or calculated from TDR measurements.

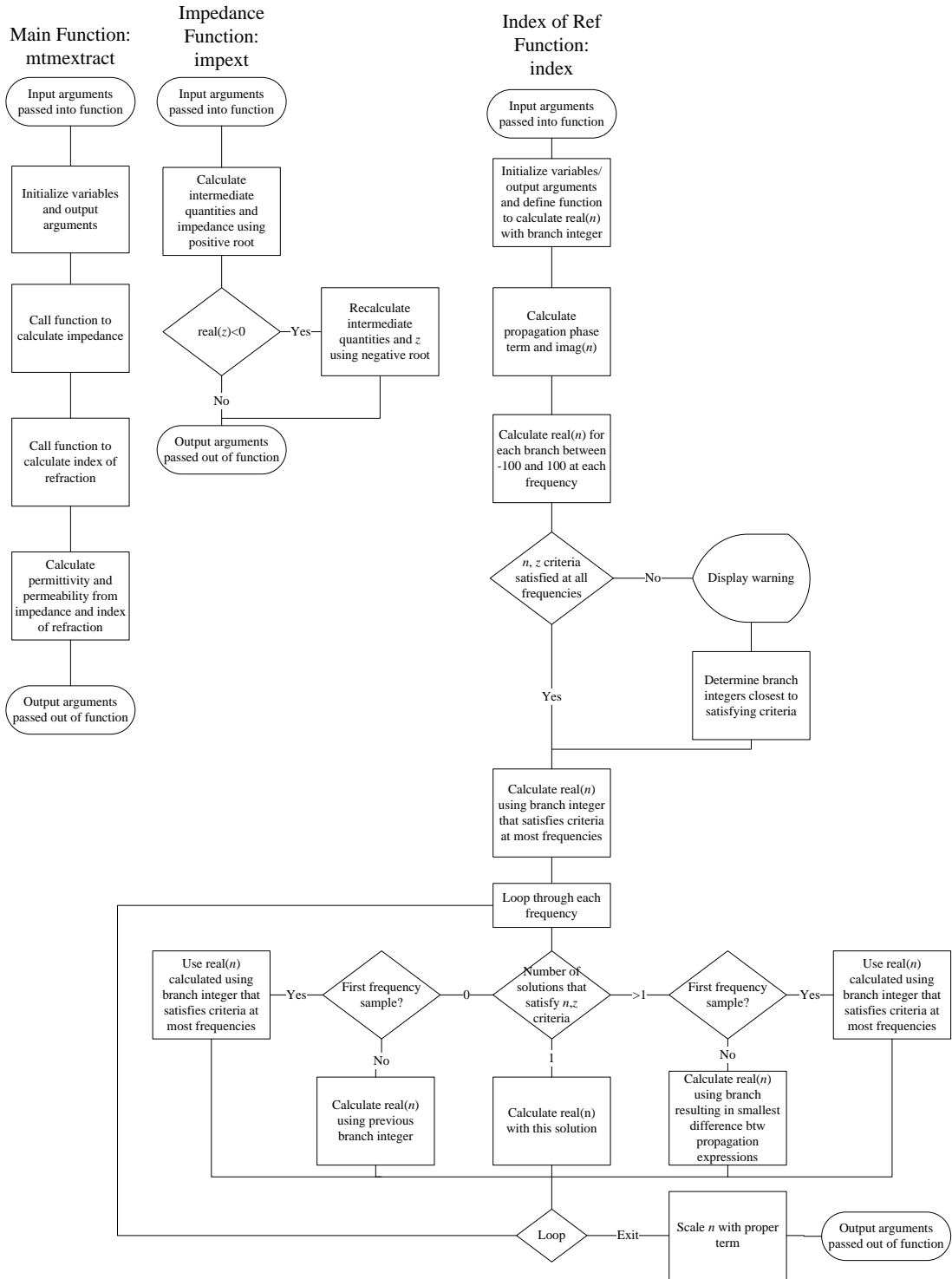


Figure 129. Flow diagram for material parameter extraction MATLAB™ script.

The script first uses traditional methods to calculate  $z$ . Then, it uses  $z$  to determine which branch to use to determine  $n$ . Once  $z$  and  $n$  are determined,  $\epsilon_r$  and  $\mu_r$  can be calculated in a straightforward manner.

## C.2 Time-Domain Reflectometry Script

MATLAB<sup>TM</sup> was used to create a script for calculating  $S_{11}$  and  $S_{21}$  in the frequency-domain from TDR measurements. Flow diagrams for this function are shown in Figures 130 and 131. Help for this function is available by typing “help calcSfromTDR” at the MATLAB<sup>TM</sup> command line. The main function is invoked by typing “[out,short,thru]=calcSfromTDR(in,short,thru,wguide,gate>window)” at the MATLAB<sup>TM</sup> command line. The input arguments “in”, “short”, and “thru” are structures that contain data about the sample, electrical short, and empty stripline measurements, respectively. The output argument “out” contains the same information as “in” along with the addition of the time- and frequency-domain signals including  $S_{11}$ ,  $S_{21}$ , and the frequency values. Similarly, the optional output arguments “short” and “thru” contain the same information as the input arguments with the same name along with the addition of the time- and frequency-domain signals. If the output arguments “short” and “thru” are not specified, their signals are assumed to already be contained in the corresponding input arguments and will not be calculated. The data structure for the input arguments “in”, “short”, and “thru”, and output arguments “out”, “short”, and “thru” is identical to the structure of “model\_in” described in Section C.1. The input argument “wguide” is a data structure that defines certain parameters of the stripline and contains the following fields:

- kc: number containing the cutoff wavenumber of the waveguide (set equal to 0 for stripline measurements),
- min: number containing the minimum frequency in Hertz where the results

from the waveguide can be trusted, and

- max: number containing the maximum frequency in Hertz where the results from the waveguide can be trusted.

The input argument “gate” is a structure that defines the start and stop time-values for time-domain gating and contains the fields “min” defining the signal to start the gate (i.e., the minimum time-value to include in the gated signal), and “max” defining the time to stop the gate (i.e., the maximum time-value to include in the gated signal).

The basic theory behind the operation of this script is described in Section 4.5. The function is fed three data structures that contain the data for the short, through, and sample measurements. The data structures contain either only channel 1 data (in the case for a short measurement), only channel 2 data (in the case of a through measurement), or both channel 1 and channel 2 data (in the case of a sample measurement). The script then converts the step data from channel 1 and/or 2 into an impulse response by taking the first derivative with respect to time. Time-domain gating is applied to block out unwanted portions of the signal (for example, reflections from the connectors). The gated time-domain signal is then transformed into the frequency-domain using the FFT. Windowing can be applied to the frequency-domain signals if desired. Finally,  $S_{11}$  and  $S_{21}$  are calculated using Equation (56).

### C.3 Farfield Data Export Script

For this thesis, analysis of the farfield data calculated by CST MWS® is performed using the AFIT Processing Code Suite© in MATLAB™. This facilitates comparison between simulation and measurement results. For the modules in the AFIT Processing Code Suite© to work, however, they need the RCS data with phase information as calculated with Equation (26) (see Section 2.3.3.2).

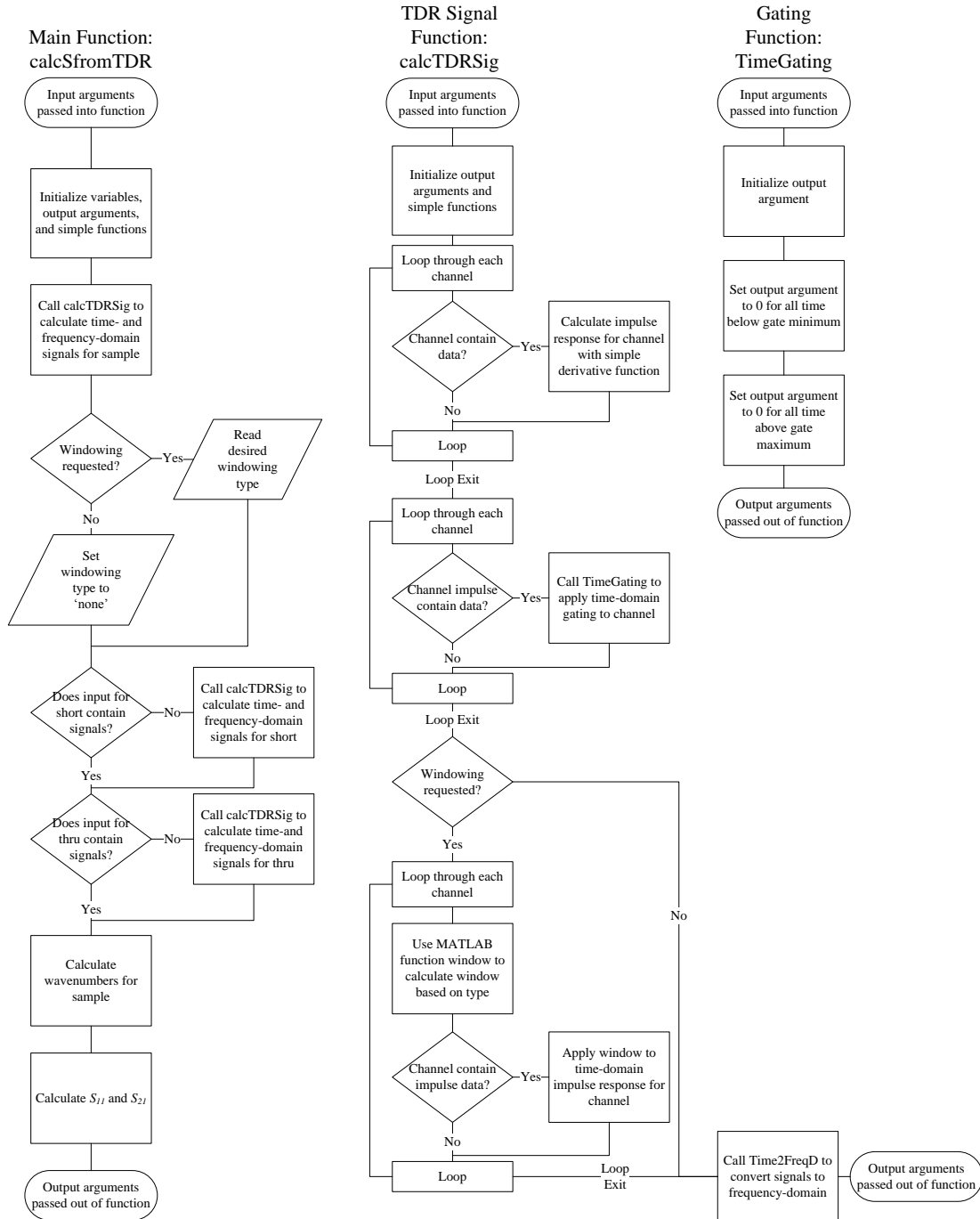


Figure 130. Flow diagram for the TDR MATLAB™ script.



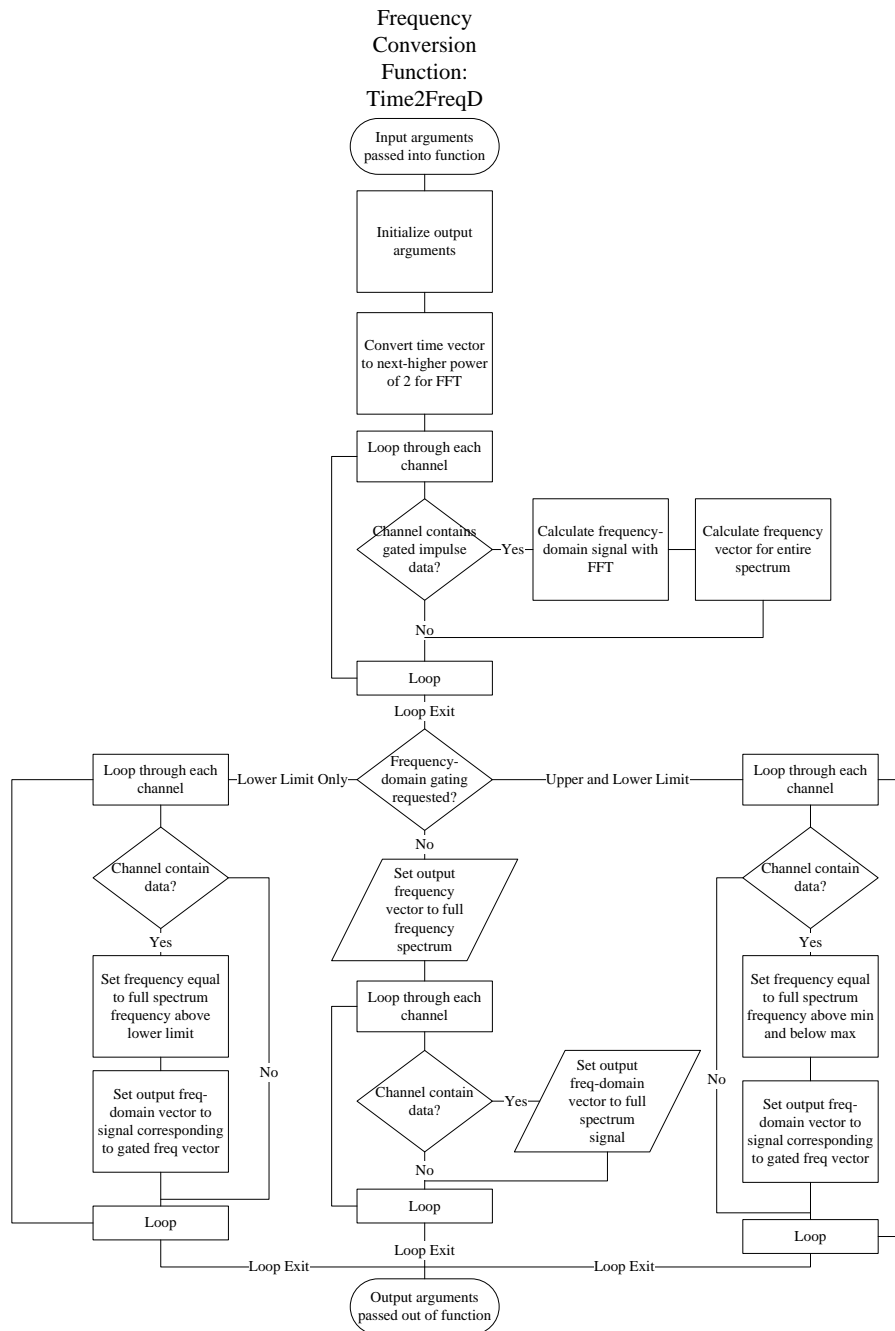


Figure 131. Flow diagram for the TDR MATLAB™ script (cont.).

CST MWS® does have broadband farfield RCS monitors, but they are not compatible with the frequency-domain solver. Thus, to get farfield data over a frequency band, many single-frequency farfield monitors must be defined. To automate this procedure, CST MWS® includes a built-in macro named “Broadband Farfield Monitors” that will create multiple single-frequency farfield monitors between two frequencies at a given frequency sampling.

Exporting RCS data without the phase information at a single frequency is simple to do with CST MWS® since that feature is built-in. To get the phase information is a bit more complicated. To get the farfield data with phase information at multiple frequencies in a single text file requires a Visual BASIC (VB) script. CST MWS® has built-in support for the VB language.

The text file created by the farfield data export script contains six header lines: the name of the CST MWS® project, the date of export, a line stating the file contains a global RCS data table, the incident polarization, the problem dimension (2-dimensional or 3-dimensional), and the column headings for the data table. The entries in the file are separated by a comma. The data table contains seven columns (from left to right):

1. the frequency,
2. the receiver angle in  $\theta$ ,
3. the receiver angle in  $\phi$ ,
4. the magnitude of  $E_\theta$ ,
5. the phase of  $E_\theta$ ,
6. the magnitude of  $E_\phi$ , and
7. the phase of  $E_\phi$ .

A flow diagram for this script is shown in Figure 132. The script reads the farfield results from the result tree in CST MWS® and writes the data to a text file.

The basic theory of operation behind this script is straightforward. The script first prompts the user for information about the problem. While the script could read some of the information from the parameter list, that would require the parameters be in the same order for each simulation. Once the script has written the header information to the file, it then loops through each of the monitors in the CST MWS® navigation tree. When it finds a farfield monitor, the frequency of the monitor is read into a list. The script then goes through each of the farfield result tree items. For each farfield item, it builds a list of  $\theta$  and  $\phi$  angles for CST MWS® to calculate according to the user inputs. Once the list is build, the script then sets the desired results to electric field, changes the scale from dB to linear, and tells CST MWS® to not include the sidewalls of the unit cell in the calculation. For periodic structures, this last setting is important since CST MWS® by default includes the unit sidewalls as if there were only one unit cell present. After the settings have been changed, the script then tells CST MWS® to calculate the farfields for the list of  $\theta$  and  $\phi$  angles that have been built. Batch computing the farfield results for each frequency is faster than calculating the farfield results at each angle individually. Once the calculation is complete, the script writes the data into the text file and moves on to the next result set. Once the script has written the farfield results for each of the farfield monitors it found earlier, the loop terminates, and the script closes the text file.

## C.4 Farfield Data Import Script

Section C.3 described a VB script that exports farfield data from CST MWS® to a text file. This section describes a script that imports the farfield data from the file into MATLAB™. The resulting data will be in the correct format for use in the

**Main Function:**  
export\_ff\_monitors

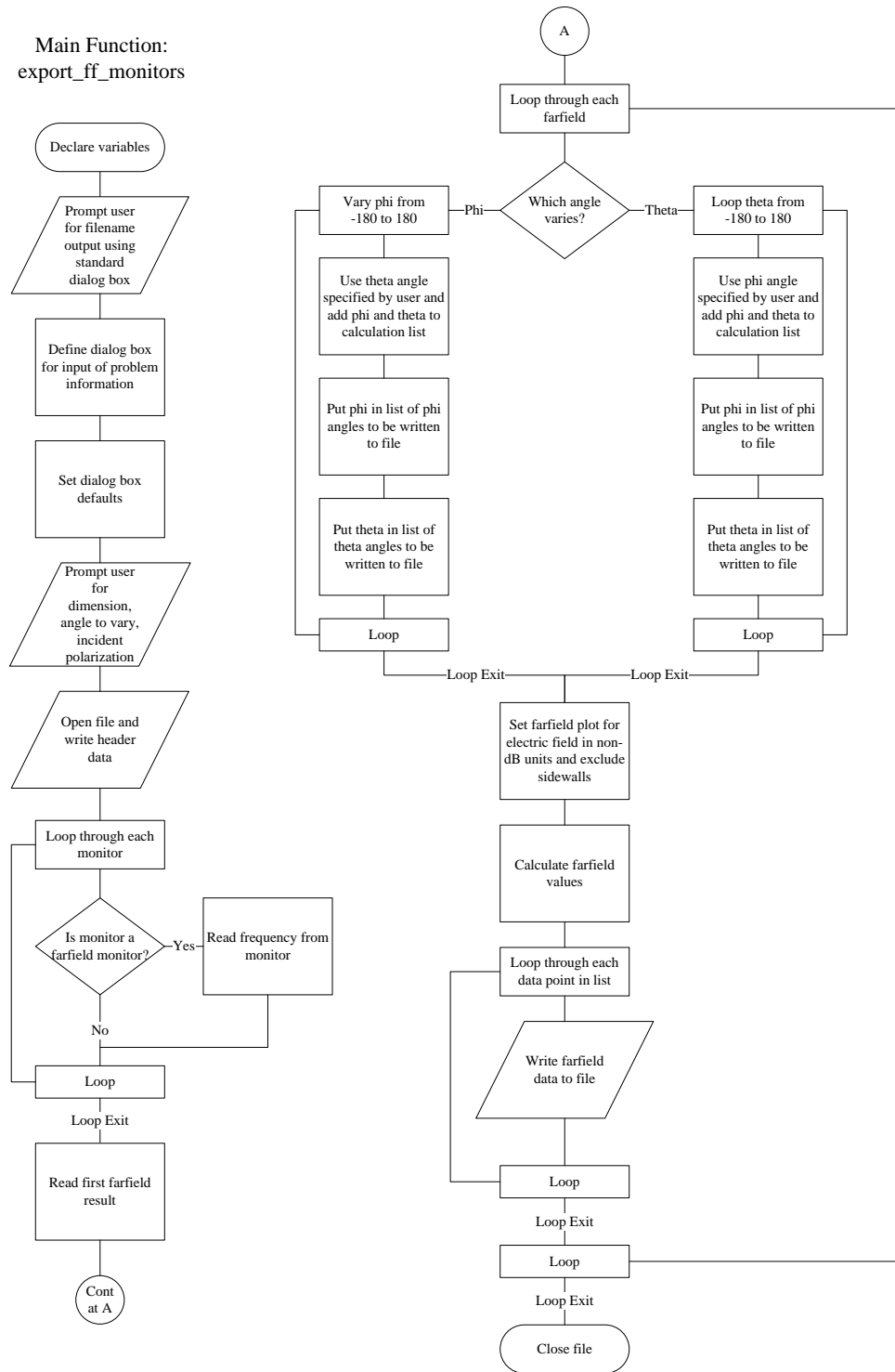


**Figure 132.** Flow diagram for script to export farfield data from CST MWS® to a text file.

AFIT Code Processing Suite©.

The name for this function is “readCSTGlobalRCS.” Help for this function is available by typing “help readCSTGlobalRCS” at the MATLAB<sup>TM</sup> command line. The main function is invoked by typing “data=readCSTGlobalRCS(filename,height)” at the MATLAB<sup>TM</sup> command line, where “filename” is a string containing the path and name of the file containing the data to import and height is a number containing the height in meters of the unit cell in the periodic dimension. Both input arguments are optional.

Figure 133 shows a flow diagram for the script. The format of the data file is described in the previous section. The output data will be put into a structure that contains many different fields that can describe various RCS measurements. The key data fields in the structure that this script affects are:

- frq: array of frequency values in GHz,
- ph: array of observation angles in  $\phi$  in degrees,
- th: array of observation angles in  $\theta$  in degrees,
- tt, pp, tp, pt: arrays or matrices containing *tt*-, *pp*-, *tp*-, or *pt*-polarized, complex RCS data, and
- header: structure that contains fields of strings that describe the data.

Most of the header fields are set to the standard values by the script. The following fields are set to special values:

- FILENAME: set to the name of the data file (if the file contains scattering width data, the string “(Scattering Width)” will be added to the end of this field),

- DATE: set to the date in the header of the data file,
- COMMENT: set to the name of the CST MWS® project (this is the first line of the data file), and
- COMMENT2: set to the string “Bistatic data”.

The data file from CST MWS® contains data describing  $E_\theta$  and  $E_\phi$  in the farfield. If the appropriate header line in the data file indicates that the CST MWS® model is three-dimensional (that is, it does not have periodic boundary conditions in any direction), this script calculates the square root of RCS according to Equation (26). If the data is two-dimensional (that is, it does have periodic boundary conditions) and the user specifies the height of the periodic cell in the model, this script calculates the square root of RCS and converts it to scattering width by inverting Equation (27). Note that this approximation becomes worse as the model gets smaller in the periodic dimension.

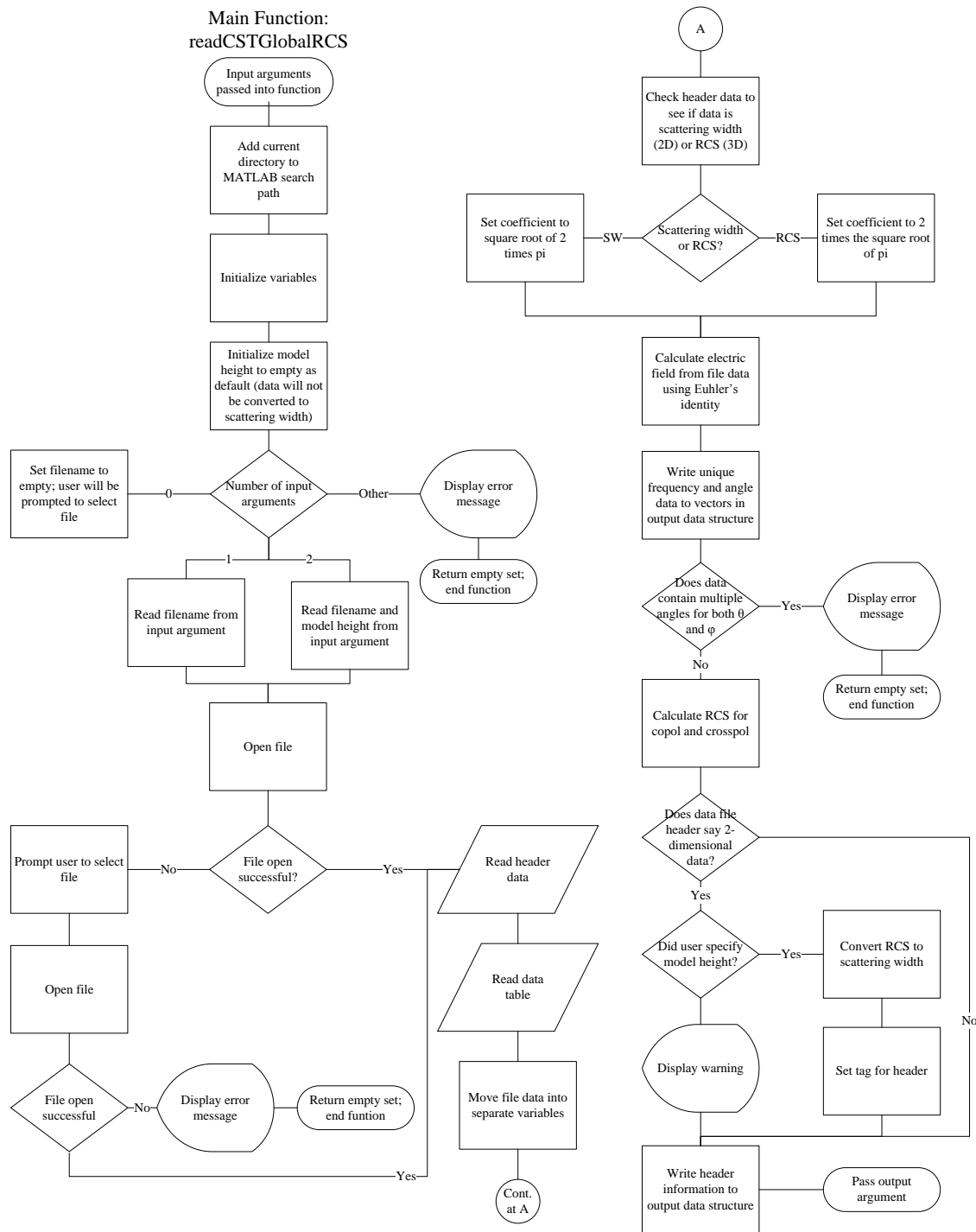


Figure 133. Flow diagram for script to import farfield data into MATLAB™.

## Bibliography

- [1] Balanis, Constantine A. *Advanced Engineering Electromagnetics*. Wiley, New York, 1989.
- [2] Benningfield, Damond. “Now You See It, Now You Don’t: Can science make aircraft invisible?” *Air & Space Smithsonian*, 24(5):20–23, Nov. 2009.
- [3] Bérenger, J. P. “Perfectly matched layer for the FDTD solution of wave-structure interaction problems”. *IEEE Trans. Antennas Propag.*, 44(1):110–117, 1996.
- [4] Born, Max and Emil Wolf. *Principles of Optics*. Cambridge University Press, Cambridge; New York, 1999.
- [5] Bradley, Christopher J., Peter J. Collins, Joaquim Fortuny-Guasch, Michael Larkin Hastriter, Giuseppe Nesti, Andrew J. Terzuoli Jr., and Kelce S. Wilson. “An investigation of bistatic calibration techniques”. *IEEE Trans. Geosci. Remote Sens.*, 43(10):2185–2190, 2005.
- [6] Chen, Xudong, Tomasz M. Grzegorzczuk, Bae-Ian Wu, Joe Pacheco, and Jin Au Kong. “Robust method to retrieve the constitutive effective parameters of metamaterials”. *Phys. Rev. E: Stat. Nonlinear Soft Matter Phys.*, 70(1):016608, July 2004.
- [7] Clemens, M., E. Gjonaj, P. Pinder, and T. Weiland. “Numerical Simulation of Coupled Transient Thermal and Electromagnetic Fields with the Finite Integration Method”. *IEEE Trans. Magn.*, 36(4):1448, Jul. 2000.
- [8] Cummer, Steven, Bogdan-Ioan Popa, David Schurig, David R. Smith, and John B. Pendry. “Full-wave simulations of electromagnetic cloaking structures”. *Phys. Rev. E: Stat. Nonlinear Soft Matter Phys.*, 74(3), 2006.
- [9] Eleftheriades, G. V. and K. G. Balmain. *Negative-Refractive Metamaterials: Fundamental Properties and Applications*. J. Wiley, Hoboken, NJ, 2005.
- [10] Engheta, N. and Richard W. Ziolkowski. *Metamaterials: Physics and Engineering Explorations*. Wiley, Hoboken, N.J., 2006.
- [11] “Farfield overview”. CST Microwave Studio® help file, 2008.
- [12] Garcia, N. and M. Nieto-Vesperinas. “Is there an experimental verification of a negative index of refraction yet?” *Opt. Lett.*, 27(11):885–887, 2002.
- [13] Gil, I., J. García-García, J. Bonache, F. Martín, M. Sorolla, and R. Marqués. “Varactor-loaded split ring resonators for tunable notch filters at microwave frequencies”. *Electron. Lett.*, 40(21):1–2, Oct. 2004.



- [14] Gollub, Jonah N., David R. Smith, and Juan D. Baena. “Hybrid resonant phenomenon in a metamaterial structure with integrated resonant magnetic material”. *Opt. Express*, 17(4):2122–2131, 2008.
- [15] Hambling, David. “Metamaterial miracles”. *Popular Mechanics*, 186(9):18–18, Sept. 2009.
- [16] Han, Jiaguang, Akhlesh Lakhtakia, and Cheng-Wei Qiu. “Terahertz metamaterials with semiconductor split-ring resonators for magnetostatic tunability”. *Opt. Express*, 16(19):14390–14396, 2008.
- [17] Hand, T. and S. Cummer. “Characterization of tunable metamaterial elements using MEMS switches”. *IEEE Antennas Wireless Propag. Lett.*, 6:401–404, Jan. 2007.
- [18] Hayt, William Hart and Jack E. Kemmerly. *Engineering Circuit Analysis*. McGraw-Hill, New York, 5th edition, 1993.
- [19] Hecht, Eugene. *Optics*. Addison-Wesley, Reading, Mass., 2002.
- [20] Hirtenfelder, F. and G. Lubkowski. “3D field simulations using FI time domain technique of wedge- and parabolic-shaped left handed materials (LHM)”. *2007 3rd International Workshop on Antenna Technology: Small and Smart Antennas MetaMaterials and Applications*. IEEE, Jan. 2007.
- [21] Knott, Eugene F., John F. Shaeffer, and Michael T. Tuley. *Radar Cross Section*. Artech House, Boston, 1993.
- [22] Lapine, M. and S. Tretyakov. “Contemporary notes on metamaterials”. *IET Microwaves Antennas Propag.*, 1(1):3–11, Feb. 2007.
- [23] Leonhardt, Ulf. “Optical conformal mapping”. *Science*, 312(5781):1777–1780, June 2006.
- [24] McGuirk, Jeffrey S. *Electromagnetic Field Control and Optimization Using Metamaterials*. Ph.D. thesis, Air Force Institute of Technology, Air University, Wright Patterson AFB OH, 2009. (ADA506707).
- [25] Mensa, Dean L. *High Resolution Radar Cross-Section Imaging*. Artech House, Boston, 1991.
- [26] Munk, Ben A. *Frequency Selective Surfaces: Theory and Design*. John Wiley, New York, 2000.
- [27] Munk, Ben A. *Metamaterials: Critique and Alternatives*. John Wiley, Hoboken, N.J., 2009.

- [28] Munk, Ben A., Dan S. Janning, Jonothan B. Pryor, and Ronald J. Marhefka. “Scattering from surface waves on finite FSS”. *IEEE Trans. Antennas Propag.*, 49(12):1782–1793, 2001.
- [29] Nicolson, A. M. “Broad-band microwave transmission characteristics from a single measurement of the transient response”. *IEEE Trans. Instrum. Meas.*, 17(4):395–402, Dec. 1968.
- [30] Nicolson, A. M. and G. F. Ross. “Measurement of the intrinsic properties of materials by time-domain techniques”. *IEEE Trans. Instrum. Meas.*, 19(4):377–382, Nov. 1970.
- [31] Pendry, J. B. “Negative Refraction Makes a Perfect Lens”. *Phys. Rev. Lett.*, 85(18):3966–3969, Oct. 2000.
- [32] Pendry, J. B., A. J. Holden, D. J. Robbins, and W. J. Stewart. “Magnetism from conductors and enhanced nonlinear phenomena”. *IEEE Trans. Microw. Theory Tech.*, 47(11):2075–2084, Nov. 1999.
- [33] Pendry, J. B., A. J. Holden, W. J. Stewart, and I. Youngs. “Extremely low frequency plasmons in metallic mesostructures”. *Phys. Rev. Lett.*, 76(25):4773–4776, June 1996.
- [34] Pendry, J. B., D. Schurig, and D. R. Smith. “Controlling electromagnetic fields”. *Science*, 312(5781):1780–1781, June 2006.
- [35] Peterson, Andrew F., Scott L. Ray, and Raj Mittra. *Computational Methods for Electromagnetics*. IEEE Press; Oxford University Press, New York; Oxford, 1998.
- [36] Pozar, David M. *Microwave Engineering*. Addison-Wesley, Reading, Mass., 1990.
- [37] Radcliff, Roger D. and Constantine A. Balanis. “Modified Propagation Constants for Nonuniform Plane Wave Transmission through Conducting Media”. *IEEE Trans. Geosci. Remote Sens.*, GE-20(3):408–411, July 1982.
- [38] Ran, L., J. Huangfu, H. Chen, X. Zhang, K. Cheng, T. M. Grzegorzczuk, and J. A. Kong. “Experimental study on several left-handed metamaterials”. *Progress in Electromagnetics Research*, PIER 51:249–279, 2005.
- [39] Rederus, Luke. *A MEMS Multi-Cantilever Variable Capacitor on Metamaterial*. Master’s thesis, Air Force Institute of Technology, Air University, Wright Patterson AFB OH, 2009. (ADA497157).
- [40] Sanz, M., A. C. Papageorgopoulos, W. F. Egelhoff, M. Nieto-Vesperinas, and N. García. “Transmission measurements in wedge-shaped absorbing samples: an experiment for observing negative refraction”. *Phys. Rev. E: Stat. Nonlinear Soft Matter Phys.*, 67(6):067601, June 2003.

- [41] Schuhmann, R. and T. Weiland. “Efficient calculation of effective material parameters in metamaterials using FDTD and a modal approach”. *Microwave Symposium Digest, 2002 IEEE MTT-S International*, volume 3, 2037–2040. 2002.
- [42] Shadrivov, Ilya V., Alexander B. Kozyrev, Daniel W. van der Weide, and Yuri S. Kivshar. “Tunable transmission and harmonic generation in nonlinear metamaterials”. *Appl. Phys. Lett.*, 93:161903, 2008.
- [43] Shadrivov, Ilya V., Steven K. Morrison, and Yuri S. Kivshar. “Tunable split-ring resonators for nonlinear negative-index metamaterials”. *Opt. Express*, 14:9344, 2006.
- [44] Shelby, R. A., D. R. Smith, and S. Schultz. “Experimental Verification of a Negative Index of Refraction”. *Science*, 292(5514):77, Apr. 2001.
- [45] Simovski, Constantin R., Pavel A. Belov, and Sailing He. “Backward wave region and negative material parameters of a structure formed by lattices of wires and split-ring resonators”. *IEEE Trans. Antennas Propag.*, 51(10):2582–2591, 2003.
- [46] Smith, D. R., W. J. Padilla, D. C. Vier, S. Nemat-Nasser, and S. Schultz. “Composite medium with simultaneously negative permeability and permittivity”. *Phys. Rev. Lett.*, 84(18):4184–4187, May 2000.
- [47] Smith, D. R., D. C. Vier, Th Koschny, and C. M. Soukoulis. “Electromagnetic parameter retrieval from inhomogeneous metamaterials”. *Phys. Rev. E: Stat. Nonlinear Soft Matter Phys.*, 71(3):036617/1–036617/11, 2005.
- [48] Sui, Qiang and Fang Li. “Experimental study of composite medium with simultaneously negative permeability and permittivity”. *Sci. China, Ser. G*, 47(1):64–78, 2004.
- [49] Tretyakov, Sergei. “On geometrical scaling of split-ring and double-bar resonators at optical frequencies”. *Metamaterials*, 1(1):40–43, Mar. 2007.
- [50] Tsitsos, S., A. A. P. Gibson, and A. H. I. McCormick. “Higher order modes in coupled striplines: prediction and measurement”. *IEEE Trans. Microw. Theory Tech.*, 42(11):2071–2077, Nov. 1994.
- [51] Varadan, V. V. and Ji Liming. “Does a negative refractive index always result in negative refraction? - Effect of loss”. *Microwave Symposium Digest, 2009 IEEE MTT-S International*, 61–64. June 2009.
- [52] Veselago, V. G. “The electrodynamics of substances with simultaneously negative values of  $\epsilon$  and  $\mu$ ”. *Phys. Usp.*, 10(4):509–514, Jan. 1968.
- [53] Veselago, V. G. “Electrodynamics of materials with negative index of refraction”. *Phys. Usp.*, 46(7):764–768, July 2003.

- [54] “Waveguide port overview”. CST Microwave Studio® help file, 2008.
- [55] Weiland, T., R. Schuhmann, R. B. Gregor, C. G. Parazzoli, A. M. Vetter, D. R. Smith, D. C. Vier, and S. Schultz. “Ab initio numerical simulation of left-handed metamaterials: comparison of calculations and experiments”. *J. Appl. Phys.*, 90(10):5419–5419, 2001.
- [56] Weiland, T., M. Timm, and I. Munteanu. “A practical guide to 3-D simulation”. *IEEE Microwave Mag.*, 9(6):62–75, Dec. 2008.
- [57] Zwillinger, Daniel. *CRC Standard Mathematical Tables and Formulae*. CRC Press, Boca Raton, Florida, 1996.

## Vita

Capt Christopher Lundell was born in Akron, Ohio. After graduating with honors from North Canton Hoover High School, he studied Electrical Engineering at the University of Cincinnati. While a student at the University of Cincinnati, he held co-op engineering jobs with Ethicon Endo-Surgery, Inc. (a Johnson and Johnson Company) and Ellis and Watts International, LLC. He graduated with his Bachelor's Degree in Electrical Engineering in June of 2002. After graduation, Capt Lundell enrolled at the University of Tennessee-Knoxville and earned a Master's Degree in Business Administration in December of 2003 with concentrations in marketing and operations management.

Capt Lundell commissioned into the United States Air Force in June of 2004 through Officer Training School (OTS) at Maxwell AFB, Montgomery, Alabama. Following OTS, he was assigned to Robins AFB, Georgia. While at Robins AFB, he first worked in the 542d Combat Sustainment Group (542 CBSG) as an engineer for an electronic warfare program. In 2006 he was moved to the 402d Electronics Maintenance Group (402 EMXG) as a test equipment engineer. Following his assignment at Robins AFB, he entered graduate school at the Air Force Institute of Technology (AFIT) in August of 2008 and is currently completing his Master's Degree. His anticipated follow-on assignment is to the Sensors Directorate of the Air Force Research Labs (AFRL/RY) at Wright-Patterson AFB, Ohio.

# REPORT DOCUMENTATION PAGE

Form Approved  
OMB No. 0704-0188

The public reporting burden for this collection of information is estimated to average 1 hour per response, including the time for reviewing instructions, searching existing data sources, gathering and maintaining the data needed, and completing and reviewing the collection of information. Send comments regarding this burden estimate or any other aspect of this collection of information, including suggestions for reducing this burden to Department of Defense, Washington Headquarters Services, Directorate for Information Operations and Reports (0704-0188), 1215 Jefferson Davis Highway, Suite 1204, Arlington, VA 22202-4302. Respondents should be aware that notwithstanding any other provision of law, no person shall be subject to any penalty for failing to comply with a collection of information if it does not display a currently valid OMB control number. **PLEASE DO NOT RETURN YOUR FORM TO THE ABOVE ADDRESS.**

<b>1. REPORT DATE (DD-MM-YYYY)</b> 25-03-2010			<b>2. REPORT TYPE</b> Master's Thesis		<b>3. DATES COVERED (From — To)</b> Aug 2008 — Mar 2010	
<b>4. TITLE AND SUBTITLE</b>  Characterization and Measurement of Passive and Active Metamaterial Devices					<b>5a. CONTRACT NUMBER</b>	
					<b>5b. GRANT NUMBER</b>	
					<b>5c. PROGRAM ELEMENT NUMBER</b>	
<b>6. AUTHOR(S)</b>  Lundell, Christopher A., Capt, USAF					<b>5d. PROJECT NUMBER</b> 10ENG142	
					<b>5e. TASK NUMBER</b>	
					<b>5f. WORK UNIT NUMBER</b>	
<b>7. PERFORMING ORGANIZATION NAME(S) AND ADDRESS(ES)</b> Air Force Institute of Technology Graduate School of Engineering and Management (AFIT/EN) 2950 Hobson Way Wright-Patterson AFB, OH 45433-7765					<b>8. PERFORMING ORGANIZATION REPORT NUMBER</b>  AFIT/GE/ENG/10-15	
<b>9. SPONSORING / MONITORING AGENCY NAME(S) AND ADDRESS(ES)</b> Air Force Research Lab, Materials and Manufacturing Directorate Attn: Katie Thorp 2941 Hobson Way Wright-Patterson AFB, OH 45433-7750 (937) 255-9145, katie.thorp@wpafb.af.mil					<b>10. SPONSOR/MONITOR'S ACRONYM(S)</b> AFRL/RX	
					<b>11. SPONSOR/MONITOR'S REPORT NUMBER(S)</b>	
<b>12. DISTRIBUTION / AVAILABILITY STATEMENT</b>  APPROVED FOR PUBLIC RELEASE; DISTRIBUTION UNLIMITED.						
<b>13. SUPPLEMENTARY NOTES</b>						
<b>14. ABSTRACT</b> This document addresses two major obstacles facing metamaterial development: uncertainty in the characterization of electromagnetic field behavior in metamaterial structures and the relatively small operational bandwidth of metamaterial structures. To address the first obstacle, a new method to characterize electromagnetic field behavior in a metamaterial is presented. This new method is a bistatic radar cross section (RCS) measurement technique. RCS measurements are well-suited to measuring bulk metamaterial samples because they show frequency dependence of scattering angles and offer common postprocessing techniques that can be useful for visualizing results. To address the second obstacle, this document characterizes the effectiveness of an adaptive metamaterial design that incorporates a microelectromechanical systems (MEMS) variable capacitor. Applying voltages to the MEMS device changes the resonant frequency of the metamaterial. In this research, computational models show that the size of the adaptive metamaterial unit cell should be increased to improve the responsiveness of the resonant frequency to changes in the MEMS capacitor.						
<b>15. SUBJECT TERMS</b> Metamaterials, Bistatic RCS Measurements, Computational Electromagnetics, MEMS Devices, Frequency Adaptive Metamaterials, Stripline Measurements						
<b>16. SECURITY CLASSIFICATION OF:</b>			<b>17. LIMITATION OF ABSTRACT</b>	<b>18. NUMBER OF PAGES</b>	<b>19a. NAME OF RESPONSIBLE PERSON</b>	
<b>a. REPORT</b>	<b>b. ABSTRACT</b>	<b>c. THIS PAGE</b>			Dr. Peter J. Collins	
U	U	U	U	242	<b>19b. TELEPHONE NUMBER (include area code)</b> (937) 255-3636, x7256; peter.collins@afit.edu	